

Martyn P. Nash · Adam Wittek ·
Poul M. F. Nielsen · Magdalena Kobielarz ·
Anju R. Babu · Karol Miller *Editors*

Computational Biomechanics for Medicine

Towards Automation and Robustness
of Computations in the Clinic

 Springer

Computational Biomechanics for Medicine

Martyn P. Nash · Adam Wittek ·
Poul M. F. Nielsen · Magdalena Kobielarz ·
Anju R. Babu · Karol Miller
Editors

Computational Biomechanics for Medicine

Towards Automation and Robustness
of Computations in the Clinic

 Springer

Editors

Martyn P. Nash
Auckland Bioengineering Institute
University of Auckland
Auckland, New Zealand

Poul M. F. Nielsen
Auckland Bioengineering Institute
University of Auckland
Auckland, New Zealand

Anju R. Babu
Department of Biotechnology and Medical
Engineering
National Institute of Technology Rourkela
Rourkela, India

Adam Wittek
Intelligent Systems for Medicine
Laboratory
Department of Mechanical Engineering
The University of Western Australia
Perth, WA, Australia

Magdalena Kobielarz
Department of Mechanics, Materials
and Biomedical Engineering
Wroclaw University of Science
and Technology
Wroclaw, Poland

Karol Miller
Intelligent Systems for Medicine
Laboratory
Department of Mechanical Engineering
The University of Western Australia
Perth, WA, Australia

ISBN 978-3-031-34905-8 ISBN 978-3-031-34906-5 (eBook)
<https://doi.org/10.1007/978-3-031-34906-5>

© The Editor(s) (if applicable) and The Author(s), under exclusive license to Springer Nature Switzerland AG 2023

This work is subject to copyright. All rights are solely and exclusively licensed by the Publisher, whether the whole or part of the material is concerned, specifically the rights of translation, reprinting, reuse of illustrations, recitation, broadcasting, reproduction on microfilms or in any other physical way, and transmission or information storage and retrieval, electronic adaptation, computer software, or by similar or dissimilar methodology now known or hereafter developed.

The use of general descriptive names, registered names, trademarks, service marks, etc. in this publication does not imply, even in the absence of a specific statement, that such names are exempt from the relevant protective laws and regulations and therefore free for general use.

The publisher, the authors, and the editors are safe to assume that the advice and information in this book are believed to be true and accurate at the date of publication. Neither the publisher nor the authors or the editors give a warranty, expressed or implied, with respect to the material contained herein or for any errors or omissions that may have been made. The publisher remains neutral with regard to jurisdictional claims in published maps and institutional affiliations.

This Springer imprint is published by the registered company Springer Nature Switzerland AG
The registered company address is: Gewerbestrasse 11, 6330 Cham, Switzerland

Contents

Patient-Specific Model Generation

Generation of Patient-Specific Structured Hexahedral Mesh of Aortic Aneurysm Wall 3
Farah Alkhatib, George C. Bourantas, Adam Wittek, and Karol Miller

Workflow for Generating Personalised Anatomical Models of the Skeleton and the Skin Surface of the Upper Torso 23
Fangchao Pan, Kejia Khoo, Thiranjia P. Babarenda Gamage, Gonzalo Maso Talou, Poul M. F. Nielsen, and Martyn P. Nash

Automated Modeling of Brain Bioelectric Activity Within the 3D Slicer Environment 33
Saima Safdar, Benjamin Zwick, George Bourantas, Grand Joldes, Damon Hyde, Simon Warfield, Adam Wittek, and Karol Miller

Solid Biomechanics

Rapid Prediction of Breast Biomechanics Under Gravity Loading Using Surrogate Machine Learning Models 49
Max Dang Vu, Gonzalo D. Maso Talou, Huidong Bai, Poul M. F. Nielsen, Martyn P. Nash, and Thiranjia Prasad Babarenda Gamage

Effect of Analyst Segmentation Variability on Computed AAA Stress Distributions 63
Tim Hodge, Jasper C. Y. Tan, Paddy H. Koh, Eli Storer, Andy Huynh, Farah Alkhatib, Karol Miller, and Adam Wittek

The Effects of the Spine on the Analysis of Peak Wall Stress in Abdominal Aortic Aneurysms 79
Michael D. Liddelow, Farah Alkhatib, Adam Wittek, and Karol Miller

Analysis of Head Protection Performance of Bicycle Helmets by Full-Scale Computational Biomechanics Modelling of Real-World Car-to-Cyclist Accidents	95
Fang Wang, Ke Peng, Jiajie Yin, Shenghui Hu, Fan Li, and Lin Hu	
Fluid Biomechanics	
Modelling the Blood Flow and Drug Transport in an Anatomically Accurate Rat Liver	117
Harvey Ho, Chong Sheng Chuah, and Uta Dahmen	
Numerical Simulation of Blood Flow Under High Shear Forces in Experimental and Clinical Applications	125
Przemysław Kurtyka, Magdalena Kopernik, Ievgenii Altyntsev, Maciej Gawlikowski, Roman Kustos, Małgorzata Pomorska, Christoph Hofstetter, Juergen M. Lackner, and Roman Major	
Effect of Mechanical Aortic Valves on Coronary Artery Flow in a Patient Suffering from Ischemic Heart Disease	145
Anna Nieroda, Krzysztof Jankowski, and Marek Pawlikowski	
New Applications	
Stump Length Effect on Pelvic Tilt in Transfemoral Amputees Assessed by Statistical Parametric Mapping	161
Vít Nováček, Simona Bartošová, Bohumír Chládek, Pavel Jedlička, Alberto Sanchez-Alvarado, Ondřej Vyhnal, Tomáš Železný, Jiří Křen, and Luděk Hynčák	
Assessment of Obstructive Sleep Apnea Phenotypes from Routine Sleep Studies: A New Approach to Precision Medicine	173
Raichel M. Alex, Khosrow Behbehani, and Donald E. Watenpaugh	
Index	193

Patient-Specific Model Generation

Generation of Patient-Specific Structured Hexahedral Mesh of Aortic Aneurysm Wall



Farah Alkhatib, George C. Bourantas, Adam Wittek, and Karol Miller

Abstract Abdominal aortic aneurysm (AAA) is an enlargement in the lower part of the main artery “Aorta” by 1.5 times its normal diameter. AAA can cause death if rupture occurs. Elective surgeries are recommended to prevent rupture based on measurement of AAA diameter and diameter growth rate. Reliability of these geometric parameters to predict the AAA rupture risk has been questioned, and biomechanical assessment has been proposed to distinguish between patients with high and low risk of AAA rupture. Stress in aneurysm wall is the main variable of interest in such assessment. Most studies use finite element method to compute AAA stress. This requires discretising patient-specific geometry (aneurysm wall and intraluminal thrombus ILT) into finite elements/meshes. Tetrahedral elements are most commonly used as they can be generated in seemingly automated and effortless way. In practice, however, due to complex aneurysm geometry, the process tends to require time-consuming mesh optimisation to ensure sufficiently high quality of tetrahedral elements. Furthermore, ensuring solution convergence requires large number of tetrahedral elements, which leads to relatively long computation times. In this study, we focus on generation of hexahedral meshes as they are known to provide converged solution for smaller number of elements than tetrahedral meshes. We limit our investigation to already existing algorithms and software packages for mesh generation. Generation of hexahedral meshes for continua with complex/irregular geometry, such as aneurysms, requires analyst interaction. We propose a procedure for generating high-quality patient-specific hexahedral discretisation of aneurysm wall using the algorithms available in commercial software package for mesh generation. We demonstrate, for the actual aneurysms, that the procedure facilitates patient-specific mesh generation within timeframe consistent with clinical workflow while requiring only limited input from the analyst.

F. Alkhatib (✉) · G. C. Bourantas · A. Wittek · K. Miller
Intelligent Systems for Medicine Laboratory, The University of Western Australia, Perth, Western Australia, Australia
e-mail: farah.alkhatib@research.uwa.edu.au

K. Miller
Harvard Medical School, Boston, MA, USA

Keywords Abdominal aortic aneurysm · Structured hexahedral elements · Patient-specific aneurysm wall

1 Introduction

Abdominal aortic aneurysm (AAA) is a permanent and irreversible enlargement in the lower part of the aorta [1], the main artery that pumps blood from the heart to the rest of human body. It is a chronic vascular disease of elderly men (over 65 years old). Prevalence is regarded as negligible before the age of 55–60 years [2]. AAA prevalence in women is up to 4–6 times less than in men [3].

AAA is usually diagnosed incidentally by unrelated examination as it is a symptomless disease [2]. The most fatal event of AAA is rupture, where mortality rate can reach up to 90% [4] leading to 200,000 deaths annually worldwide [5] and around 1500 deaths yearly in Australia and the Oceania region [6].

According to current AAA management, patients undergo elective surgical intervention if their maximum aortic diameter is more than 55 mm for men and 50 mm for women [7, 8]. Below these recommended thresholds, patients are placed on surveillance program that monitors the aneurysm growth rate. The surgery is recommended if the growth rate exceeds 10 mm/year. Australia has a high rate of AAA repairs below these recommended thresholds compared to other Western countries. However, the probability for aneurysms with aortic diameter of 40–50 mm under surveillance to rupture is only 0.4% per year, which is lower than the risk of death due to the postoperative complications [2].

This raises the question of how to best manage AAAs as there is a balance between interventions to prevent AAA rupture versus overtreatment that may cause harm to patients and incur non-essential medical cost. Over the last 25 years, researchers introduced different AAA biomechanical rupture risk indicators or indices to identify patients at high risk of AAA rupture [9–13] and conversely those at low risk for whom surgical intervention can be avoided. Evaluation of such indices is beyond the scope of this study. Biomechanical indices for evaluating the AAA rupture risk strongly rely on computation of AAA wall stress [9]. Finite element method (FEM) dominates such computations. It requires discretising patient-specific geometry (aneurysm wall and intraluminal thrombus ILT) into finite elements/meshes to create a computational grid.

Patient-specific tetrahedral meshes are often used in computational biomechanics analysis of AAA as it is believed that such meshes can be created automatically with high element quality by analysts without expertise in computational grid generation [13, 14]. In a study by Miller et al. [15], AAA (aneurysm wall and ILT) finite element models contained more than 1 million tetrahedral elements. This high number of elements ensures convergent solution but tends to result in relatively long computational times. Furthermore, automated elimination of poor-quality tetrahedral elements typically requires application of mesh optimisation procedures. From our experience, presence of even small number of poor-quality elements may lead

to very long optimisation times (up to around 40–50 minutes of a personal computer with Intel quad-core i7 processor). Therefore, we focus on hexahedral meshes as they require a smaller number of elements than tetrahedral meshes [16]. For aneurysm walls discretised using 30,000–50,000 hexahedral elements, around 500,000 tetrahedral elements were needed to achieve similar geometric discretisation accuracy [17].

Generation of high-quality structured (mapped) hexahedral finite element meshes of healthy blood vessel walls can be done automatically by defining the vessels centre-lines [18–20] using freely available software such as pyFormex (<https://github.com/dladd/pyFormex>) and Gmsh (<https://gmsh.info/>). This, however, does not extend to complex/irregular geometry of AAAs. Generation of structured hexahedral meshes of AAAs tends to require expert's knowledge of finite element meshing procedures and substantial manual effort of the analyst. Specialised mesh generation code developed by Tarjuelo-Gutierrez et al. [21] facilitates construction of hexahedral meshes for aneurysm wall and thrombus including the bifurcations. It relies on connecting the extracted axial and longitudinal lines in the aneurysm from the manual magnetic resonance imaging (MRI) segmentation and the calculated aneurysm centreline. Need for substantial effort of the analyst was also reported in the studies using well-established commercial mesh generators. Application of CEM CFD 14.5 (Ansys Inc., USA) to create patient-specific hexahedral finite element meshes of aneurysm wall required 4–8 h of analyst's work per case [12, 22]. Mayr et al. [23] used CUBIT mesh generator (<https://cubit.sandia.gov/>) to create hexahedral elements for aortic aneurysms for fluid-structure interaction simulation. Distinct advantage of CUBIT is that it can automatically partition complex geometries into mappable volumes to build structured hexahedral mesh. CUBIT is available for the US government use only. However, its commercial version, Coreform Cubit (<https://coreform.com/products/coreform-cubit/free-meshing-software/>), has no such restriction. A4Clinics VASCOPS (<http://www.vascops.com>) software to biomechanically analyse AAA rupture risk creates a hexahedral aneurysm wall with a minimal user interaction. Their meshing algorithm limits any mesh refinement along the circumferential and axial directions of aneurysm wall and ILT, which creates one layer through wall thickness and coarse elements for thick ILT [24]. However, in several studies it has been argued that at least two elements across the AAA wall thickness are needed for converged solution in terms of stress computation [25]. Zhang et al. [16, 26] have successfully created unstructured hexahedral meshes from volumetric data (medical images as an example). Automated unstructured hexahedral elements for aneurysm wall and ILT using Harpoon (<http://www.sharc.co.uk/index.htm>) were done by Maier et al. [27]. Our experience indicates that unstructured hexahedral meshes may contain some poor-quality elements, in particular elements with very low (close to zero or even negative) Jacobian quality measure [26, 28].

In this study, we demonstrate a procedure to create a high-quality patient-specific structured hexahedral mesh of aortic aneurysm wall models using commercially

available mesh generators for stress computation in the aneurysm wall. We use tetrahedral elements for the intraluminal thrombus (ILT) because of its complex geometry. Accurate ILT stress analysis is not a variable of interest as an indicator of AAA rupture risk, further justifying the use of tetrahedral elements.

2 Methods

2.1 Patient's Data and Patient-Specific AAA Geometry

A contrast-enhanced computed tomography angiography (CTA) image data set of four abdominal aortic aneurysm (AAA) patients with an average maximum aortic diameter of 55 mm (standard deviation = 9 mm) was used to demonstrate the meshing techniques proposed and used in this work. The CTA images were acquired at Fiona Stanley Hospital (Murdoch, Western Australia, Australia) using SOMATOM Definition Flash CT Scanner (Siemens Healthineers AG, Forchheim, Germany). The spatial resolution (voxel size) of the CTA images is $0.625 \times 0.625 \times 1.5 \text{ mm}^3$. Patients gave their informed consent before acquiring the images according to the Declaration of Helsinki.

The patient-specific AAA geometries were segmented from the CTA images using the open-source medical image analysis package, 3D Slicer (<https://www.slicer.org/>) [29]. The contrast-enhanced images allowed an automated segmentation for the lumen (blood channel) using the threshold algorithm in 3D Slicer segmentation module. The aneurysm (wall and the intraluminal thrombus "ILT") needed some manual work to distinguish between the aneurysm and surrounding tissues. Figure 1 shows the segmented AAA for a Patient 1; the aneurysm wall is shaded in blue, and the ILT is in red. We assumed constant wall thickness of 1.5 mm for the aneurysm wall, as there is no reliable method to accurately determine AAA wall thickness solely from CTAs has been developed yet [30].

2.2 Generation of Patient-Specific AAA Computational Grids

2.2.1 Patient-Specific AAA Meshes

Different meshing tools and algorithms can be used to generate patient-specific hexahedral meshes of aneurysm wall as stated in Introduction. We initially attempted to use an in-house algorithm (implemented using MATLAB) that reconstructs the aneurysm geometry using the aortic centreline and maximum distances from this centreline to the aortic wall. This algorithm defines subdivided circles and ellipses orthogonal to the centreline ready to be connected using splines to form surface quadrilateral meshes. We faced two main issues with this early-stage algorithm, (1)

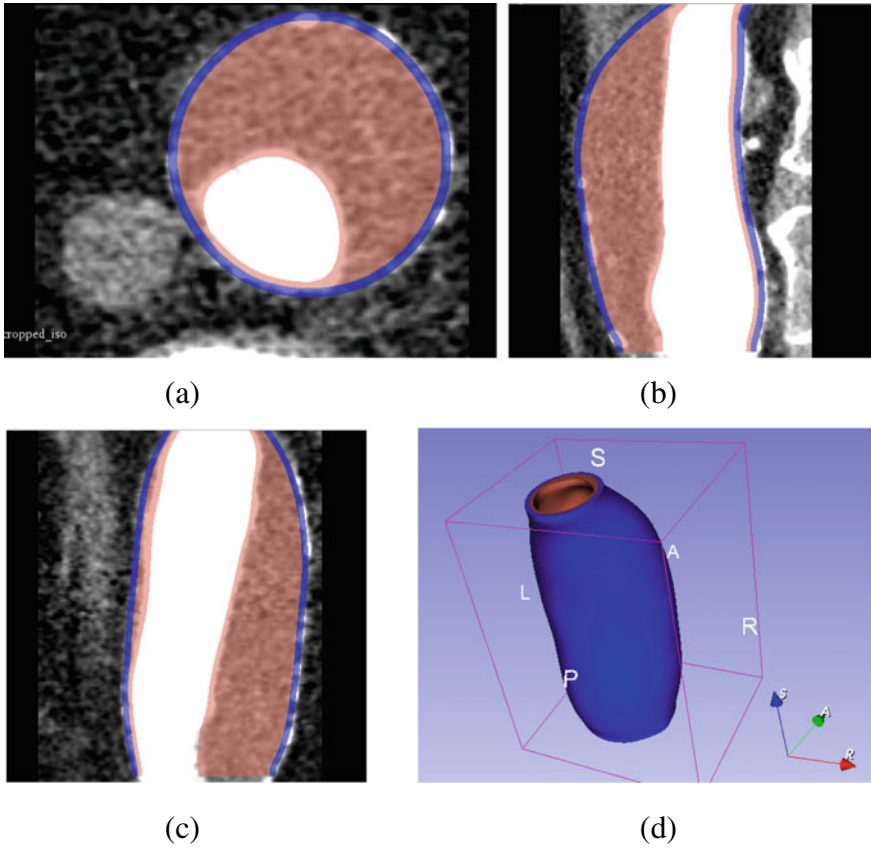
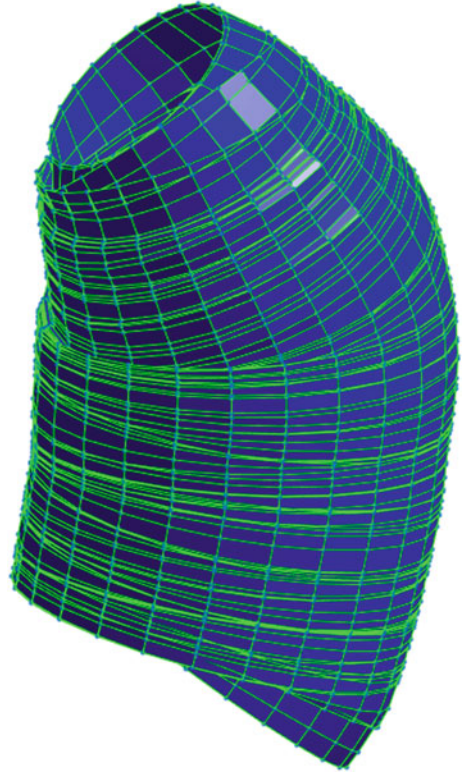


Fig. 1 Patient-specific abdominal aortic aneurysm (AAA) geometry obtained by segmentation of computed tomography angiography (CTA) images using 3D Slicer. The segmented aneurysm wall (constant thickness of 1.5 mm is assumed) is shown in blue, and the segmented intraluminal thrombus (ILT) is shown in red; **a** a slice from the axial view of AAA, **b** a slice from the sagittal view of AAA, **c** a slice from the coronal view of AAA, and **d** the 3D rendered AAA

the circles and ellipses may overlap in the locations that have a large change in wall curvature (Fig. 2), and (2) a smoothing technique (Laplace smoothing as an example [31]) should be used to improve the elements shape and mesh quality.

Fully automated hexahedral meshing was not possible for the aneurysm wall using known to us open-source and commercial mesh generators because of its irregular and asymmetrical shape. We initially used the mesh generator available in ABAQUS/CAE (<https://www.3ds.com/products-services/simulia/products/abaqus/>) finite element pre-processor. It provides high-quality element generation. However, it strongly relies on the user's expertise and requires substantial input (manual mesh generation work) from the user as the AAA geometry needs to be subdivided into many partitions in order to create a structured hexahedral mesh. In this study, we

Fig. 2 Example of surface meshing (2D quadrilateral elements) using a prototype in-house code showing the overlapped circles (green circles) created while defining the AAA geometry based on centrelines (Patient 1)



used the industrially applied mesh generation software Altair HyperMesh (<https://www.altair.com/hypermesh>) to create a high-quality hexahedral mesh of AAA wall. Our Intelligent Systems for Medicine Laboratory (ISML) team has many years of experience in using HyperMesh, and HyperMesh can be applied to generate high-quality meshes from computer-aided design (CAD) and image-derived geometries.

We imported the geometry of AAA wall extracted from the CTA images in stereo lithography (STL) format. Because of the irregular geometry of AAA, partitioning was needed to create the structured (mapped meshing) hexahedral mesh. Figure 3 shows the four aneurysm wall geometries meshed in this study.

The 3D hexahedral mesh (Fig. 4a) was created by sweeping the 2D meshed ring (Fig. 4b) along the aneurysm wall. The created 2D top ring of quadrilateral elements in the aneurysm wall defines the element size and number of hexahedral layers (elements) through wall thickness. We used two elements (size of 0.75 mm) through the wall thickness.

We created tetrahedral elements for the aneurysm intraluminal thrombus (ILT) using HyperMesh because of its complex shape. The transition between the quadrilateral surface meshes to tetrahedral volume meshes was important to create the shared conformal surface between the hexahedral aneurysm wall and the tetrahedral

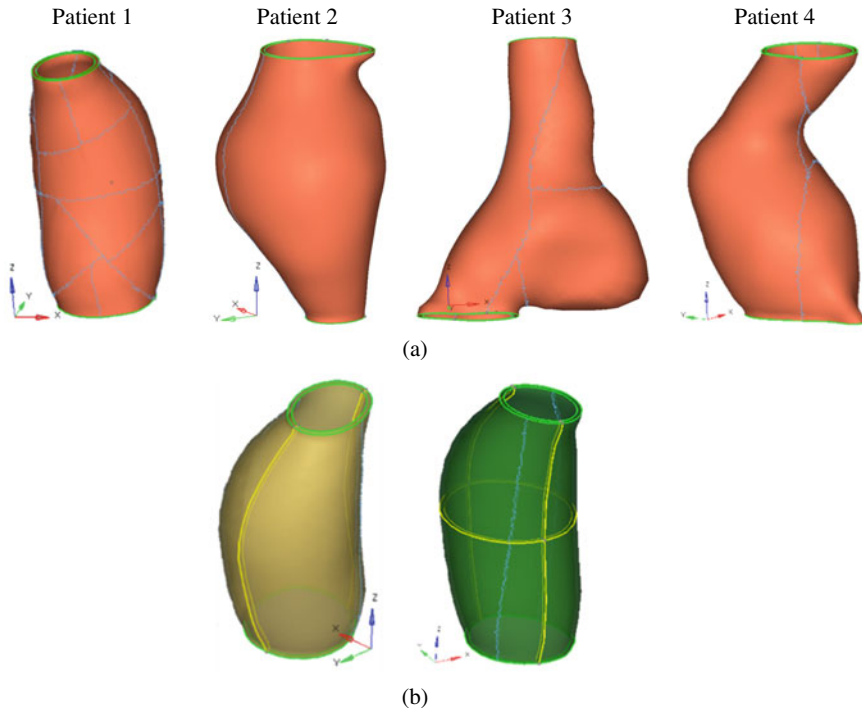


Fig. 3 **a** Aneurysm wall geometries for four patients extracted from computed tomography angiography (CTA) images and imported to HyperMesh finite element mesh generator in STL format. At least one partition was required before these geometries could be discretised (meshed) using hexahedral elements; **b** Partitioned aneurysm wall geometry (Patient 1) ready for mapped (structured) meshing: yellow shading—partition using one plane and green shading—partition using two planes. Bright yellow lines indicate the partitioning planes

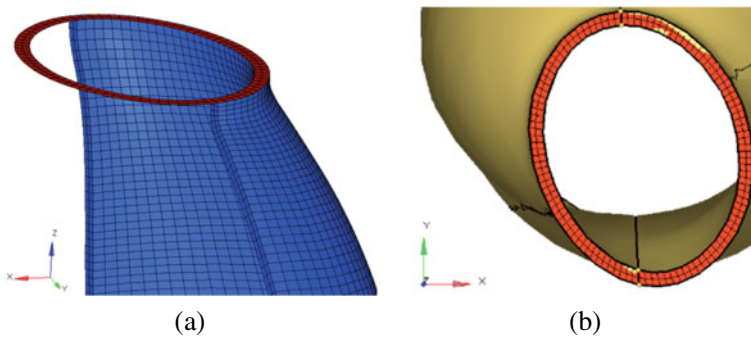


Fig. 4 Hexahedral meshing of aneurysm wall, **a** section of aneurysm wall (blue elements) showing the hexahedral meshes created by sweeping the quadrilateral 2D ring (red elements), and **b** top view of the aneurysm wall geometry that has the generated 2D top ring of quadrilateral elements used to create the 3D volume wall (hexahedral elements), element size is 0.75 mm

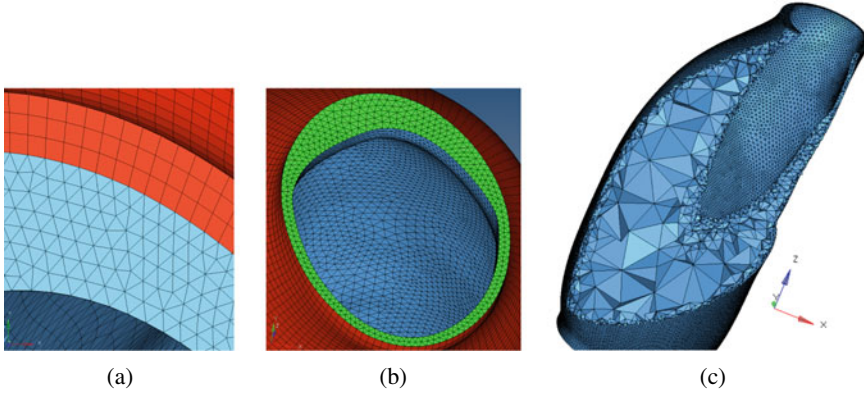


Fig. 5 Generation of tetrahedral intraluminal thrombus (ILT) mesh. **a** The top view of abdominal aortic aneurysm (AAA) showing the wall in red and ILT in blue, **b** 2D top edge created (green) to close the volume of ILT and generate the tetrahedral mesh, and **c** section view of the meshed ILT

ILT (Fig. 5a). We used the inner wall surface topology (nodes location) to create the outer surface of the ILT (triangular elements). We imported the inner surface of the ILT (the surface of the lumen segmented in 3D Slicer) and created a dummy mesh to close the top and bottom edges of the ILT creating water-tight surface assembly that defines the ILT (Fig. 5b). ILT tetrahedral mesh was then generated automatically while allowing the meshing algorithm to increase the element size in the areas distance from the surfaces defining the ILT boundary. This, in turned, reduced the number of elements and, hence, the computation time. We kept the nodes on the surfaces of wall and ILT fixed while allowing the splitting of quadrilaterals into triangles to avoid pyramid elements. The upper and lower edges (dummy mesh) were designated as freely adjustable nodes. A section view of the ILT tetrahedral mesh created in this study is shown in Fig. 5c.

2.2.2 Element Quality

Hexahedral meshes We used the following two measures to evaluate quality of hexahedral elements: (1) normalised/scaled Jacobian [26, 28] (a Jacobian value of 0.6 and higher is recommended [32]) and (2) the minimum and maximum allowable interior angles of a quadrilateral face (the suggested limits are between 45° and 135° [32])—see Fig. 6a for definition. Both measures need to be used as we found that some elements have high Jacobian, but their maximum or minimum interior angles are out of the recommended range. Figure 6a shows an example of such poor-quality element. We confirmed that such elements could be avoided by increasing the number of partitions or sections of the AAA geometry and by decreasing the element size.

Tetrahedral meshes We analysed quality of tetrahedral elements using the following two measures: (1) maximum and minimum allowable interior angle for

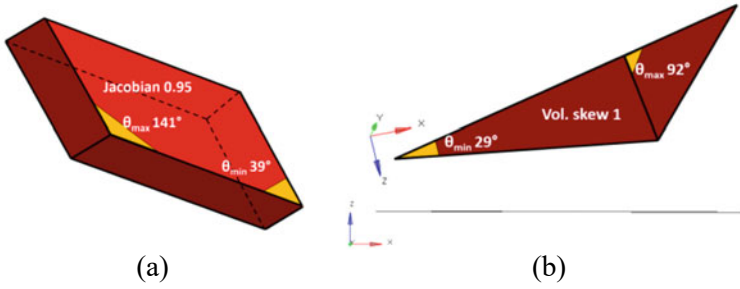


Fig. 6 Examples of poor-quality elements: **a** hexahedral element with Jacobian of 0.95, but with minimum interior angle of 39.25° and maximum interior angle of 141.36° that are out of the recommended allowable range of 45°–135° [1]; and **b** two views of a “flat” tetrahedral element degenerated to triangle. Volumetric skew of this element equals one. Interior angles are highlighted in yellow

triangles [32] and (2) the volumetric skew [33]:

$$\text{Volumetric skew} = 1 - \frac{\text{Actual tetrahedron volume}}{\text{Ideal tetrahedron volume}}, \tag{1}$$

where ideal tetrahedron is an equilateral tetrahedron with the same circumradius of the actual tetrahedron (i.e. circumradius is radius of a sphere passing through the four vertices of the tetrahedron).

The recommended interior angles range between 30° and 120°. Volumetric skew of 1 means a tetrahedral element degenerated to triangle (Fig. 6b). Volumetric skew of 0 means an ideal (equilateral) tetrahedron.

We found that, for both hexahedral and tetrahedral mesh, all poor-quality elements were located at the top or bottom (aortic bifurcation) edges of the AAA. These edges are rigidly constrained in the AAA biomechanical models (including the models created and used in this study) [13] and therefore are of limited interest for the AAA stress analysis.

2.3 Stress Computation in AAA Wall

Following our previous studies [13, 34], we used linear static finite element analysis implemented in ABAQUS/standard finite element code [35] (<https://www.3ds.com/products-services/simulia/products/abaqus/>) to calculate the AAA wall stress. This approach has been used in the freely available open-source software platform *BioPARR—Biomechanics-based Prediction of Aneurysm Rupture Risk* (<https://bioparr.mech.uwa.edu.au/>) for biomechanical analysis of AAA [13]. It relies on the observation that as patient images show the deformed (due to loading by the blood pressure) AAA geometry, the internal forces on the blood vessel wall that balance the

applied pressure can be calculated from the principles of statics [13, 34]. This implies that if the computational biomechanics simulations are set up in such a way that the deformed AAA geometry remains unchanged when loaded by blood pressure, one should obtain the stress field in the AAA wall that balances the pressure [34]. Such field is for practical purposes independent of the material properties of aorta tissue if the material is homogenous [34, 36].

For both aortic wall and ILT, we used nearly incompressible (Poisson’s ratio of 0.49) linear elastic material model. Following [15], the ILT was defined as 20 times more compliant than the AAA wall. To construct hexahedral meshes, we used hybrid 20-noded quadratic hexahedral element with reduced integration (eight integration points)—element C3D20RH in ABAQUS finite element code. For tetrahedral meshes, we used hybrid ten-noded quadratic tetrahedral element—element C3D10H in ABAQUS finite element codes. Application of hybrid formulation, that prevents volumetric locking for the nearly incompressible materials, was used.

The aneurysm was uniformly loaded at the internal surface of the ILT by the patient-specific blood pressure measured 5 minutes before acquiring the CT images [12, 37, 38]. We used mean arterial blood pressure (MAP) that is calculated from the systolic and diastolic pressures ($\text{MAP} = 1/3 \text{ systolic pressure} + 2/3 \text{ diastolic pressure}$). Top and bottom surfaces “caps” (i.e. top and bottom surfaces closing the aneurysm volume) of the aneurysm were rigidly constrained.

We analysed the maximum principal stress in the aneurysm walls as it provides indication of the internal forces within the aorta that balance the blood pressure [13]. The residual stresses in the aorta were not considered in this study as we focus on the method of generating high-quality hexahedral meshes for aneurysm wall rather than the AAA rupture assessment through stress computation.

We compared the contours of the maximum principal stress and distribution of the 99th percentile of the maximum principal stress in the aneurysm wall obtained using the hexahedral and tetrahedral finite meshes. We used 99th percentile rather the peak values to eliminate the artefacts and uncertainties due to the AAA segmentation and AAA geometry discretisation when generating the finite element meshes [39].

3 Results

3.1 Computational Grid (Finite Element Mesh) Convergence

We performed a mesh convergence study for one of the analysed AAAs (Patient 1) to ensure that computation of stress in aneurysm wall is independent of mesh size. We created three finite element models of the aneurysm of this patient using hexahedral meshes with different number of elements: Model 1 with two layers of hexahedral elements through the aneurysm wall thickness; Model 2 with three layers of hexahedral elements, and Model 3 with four layers of hexahedral. Following the approach used in BioPARR open-source software platform for biomechanical AAA

analysis, we calculated the maximum principal stress in the aneurysm wall using the linear finite element algorithm from ABAQUS/standard executed on Intel(R) Core (TM) i7-5930 K CPU @3.50 GHz with 64 GB of RAM running Windows 8 operating system. The finite element models used when analysing the mesh convergence did not include the ILT. The inner surface of the AAA wall was loaded with 12 kPa (MAP, mean arterial pressure for Patient 1).

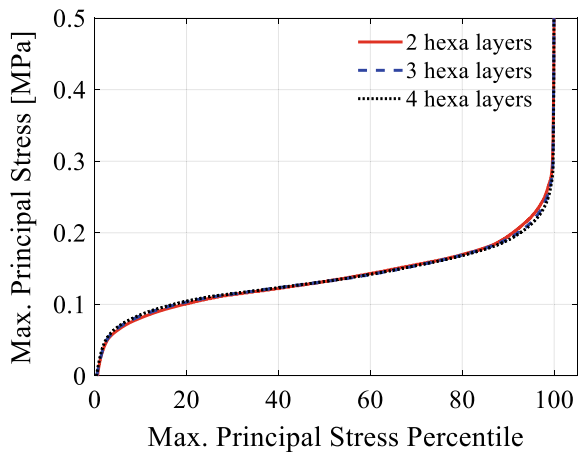
Table 1 summarises the mesh characteristics of each studied finite element model. It also includes the peak and 99th percentile values of maximum principal stress for the three models. The peak stress values typically occur at the fixed (rigidly constrained) nodes of the top and bottom edges of the aneurysm wall, which can be regarded as a modelling artefact. Therefore, we compared 99th percentile of the maximum principal stress.

Figure 7 shows the maximum principal stress for the three studied models with respect of a percentile rank of the stress values. We refer to Fig. 7 as the maximum principal stress percentile plot. For all three models, the maximum principal stress percentile plots are very close.

Table 1 Mesh characteristics, maximum principal stress (peak value and 99th percentile), and finite element models computation time when conducting the mesh convergence analysis

	Model 1	Model 2	Model 3
No. of hexahedral elements through wall thickness	2	3	4
Element size (mm)	0.75	0.5	0.375
No. of elements	27,972	95,190	225,676
No. of nodes	154,734	477,787	1,075,083
Peak of maximum principal stress (MPa)	0.5300	0.6070	0.6831
99th percentile of maximum principal stress (MPa)	0.2700	0.2620	0.2557
Computation time (sec)	23	103	568

Fig. 7 Percentile plot of the maximum stress in the aneurysm wall of Patient 1 obtained using finite element models with different number of hexahedral elements (as indicated by the number of hexahedral elements through the aneurysm wall thickness). The results indicate that the calculated stress is mesh independent (i.e. the solution converged for two layers of hexahedral elements through the aneurysm wall thickness)



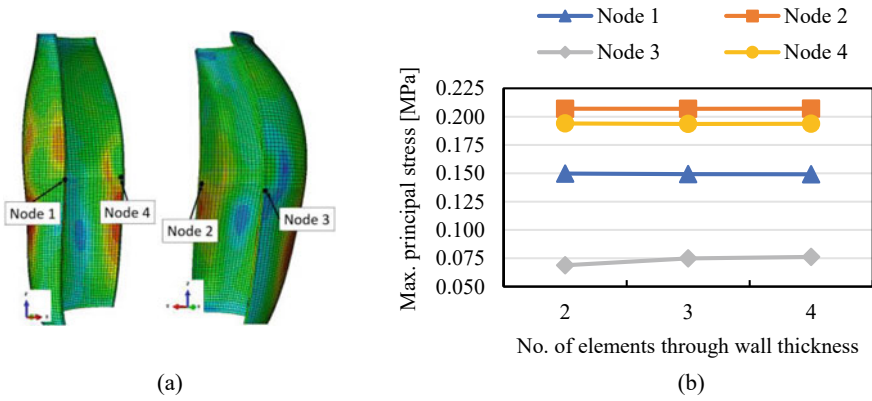


Fig. 8 **a** Location of the four selected nodes used to analyse convergence of computing the maximum principal stress in the aneurysm wall, and **b** convergence analysis of the computation of the maximum principal stress in the aneurysm wall when varying the number of elements through the wall

We selected four nodes in the three aneurysm wall models to compare the maximum principal stress. The selected nodes were in the middle of the aneurysm wall, two of them were on the outer surface of the wall and two on the inner surface (Fig. 8a). The four nodes had the same location/coordinates for all three studied aneurysm wall models. Figure 8b shows convergence of the computed stress at the four selected nodes. We conclude that two layers of hexahedral elements through the aneurysm wall thickness are sufficient to ensure converged stress computation.

3.2 Computational Grids and Element Quality

The created computational grids (hexahedral finite element meshes) for four patients analysed in this study are shown in Fig. 9. These meshes were generated using two hexahedral elements through wall thickness and element size of 0.75 mm.

Table 2 reports the number of poor-quality elements according to the quality measures used, Jacobian and minimum/maximum interior allowable angles for hexahedral elements, and volumetric skew and minimum/maximum interior allowable angles for tetrahedral elements. We noticed that poor-quality tetrahedral elements in AAA are located at the top and bottom edges of the aneurysm model, where the aneurysm is fully supported. They account for a very small fraction (less than 0.02% of the total number of elements in the AAA model).

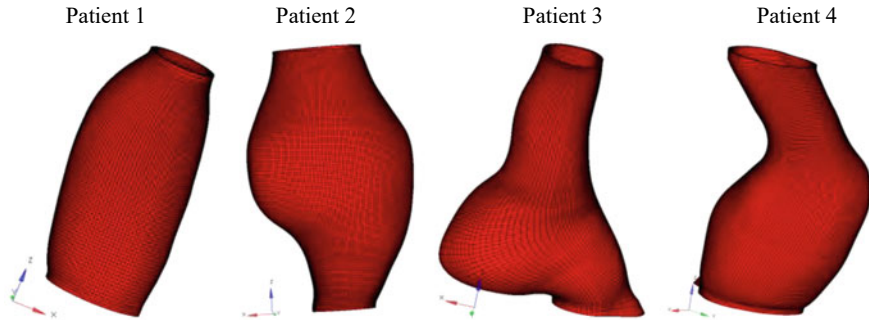


Fig. 9 Hexahedral meshes of the aneurysm wall created using HyperMesh with an element size of 0.75 mm

Table 2 Summary of poor-quality elements according to the used quality measures for the AAA wall (hexahedral mesh) and ILT (tetrahedral elements) models for four AAA patients analysed in this study

Part	Patient 1		Patient 2		Patient 3		Patient 4	
	Wall	ILT	Wall	ILT	Wall	ILT	Wall	ILT
No. of elements	21,090	290,924	35,616	180,162	27,072	90,571	46,472	234,976
No. of nodes	116,883	251,506	197,160	309,160	149,648	168,802	256,780	391,362
No. of elements failed to Jacobian	0	N/A	0	N/A	5	N/A	0	N/A
Min. Jacobian	0.86	N/A	0.73	N/A	0.57	N/A	0.72	N/A
No. of elements failed to volumetric skew	N/A	3	N/A	0	N/A	84	N/A	147
Max. vol. skew	N/A	1	N/A	0.93	N/A	1	N/A	1
No. of elements failed to min/max angle	0	41	4	37	67	105	50	163
Min angle	50°	0.5°	45°	9°	26°	6°	37°	5°
Max angle	131°	179°	140°	136°	162°	155°	146°	160°

N/A: not applicable measure for the specific case

3.3 Aneurysm Wall Stress

Figure 10 shows the maximum principal stress contour plots for the aneurysms analysed in this study. Table 3 compares the peak and 99th percentile of maximum principal stress for the models using hexahedral and tetrahedral meshes. There are only minor differences between the results obtained using hexahedral and tetrahedral meshes. However, the number of elements (over 1 million) in tetrahedral meshes is

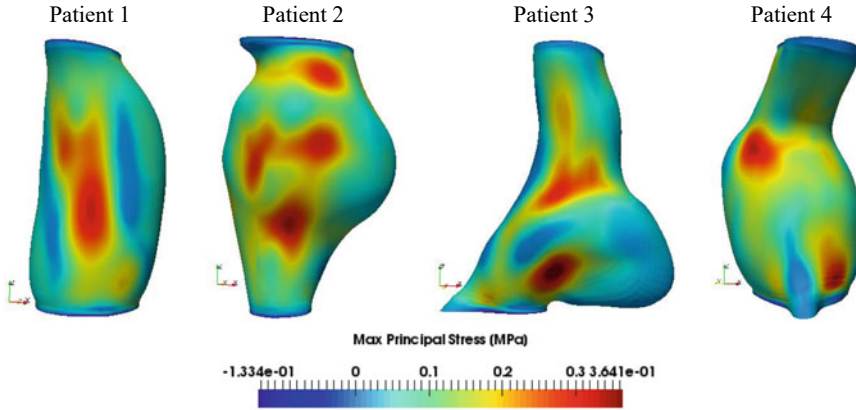


Fig. 10 Contour plots of the maximum principal stress in aneurysm wall for four patients analysed in this study obtained from patient-specific finite element models using hexahedral meshes of the aneurysm wall (two hexahedral elements through the aneurysm wall thickness)

appreciably larger than in hexahedral meshes (around 35,000 elements, Table 2). Consequently, more than fivefold reduction in computation time is observed for the models using hexahedral meshes. The time required to assemble the stiffness matrix and the finite element models computation time for both grids is reported using Intel(R) Core (TM) i7-5930 K CPU @3.50 GHz with 64 GB of RAM running Windows 8 operating system (Table 3). Additionally, we used the percentile plots (Fig. 11) to show the stress distribution between the hexahedral and tetrahedral meshed walls in terms of a percentile rank (in the population of all nodes in the AAA finite element model of a given patient).

4 Discussion

Hexahedral meshing of aneurysm wall is not a trivial and straightforward problem. In this study, we present a procedure to build hexahedral mesh of abdominal aortic aneurysm (AAA) wall using commercial (industrially applied) HyperMesh mesh generator. The procedure requires 20–30 minutes of analyst’s time to create a high-quality patient-specific mesh of the AAA wall. In the future, these steps can be automated using the HyperMesh programming script to further reduce the need for the analyst involvement. Poor-quality hexahedral elements could not be completely avoided (see Table 2, Patients 3 and 4) because of complex and irregular geometry of AAAs. However, the number of such elements did not exceed 0.2% of the total number of hexahedral elements in the patient-specific AAA model. From the results obtained in this study, it can be concluded that mesh refinement (increasing the number of elements) could further improve the mesh quality. This, however, increases

Table 3 Comparison of the peak values and 99th percentile of the maximum principal stress obtained using hexahedral (hexa) and tetrahedral (tetra) meshes of the aneurysm wall for the four patients analysed in this study

		Patient 1	Patient 2	Patient 3	Patient 4
Applied pressure/load (kPa)		12	13	13	14
No. of elements in the finite element model	AAA wall Hexa mesh	166,701	215,778	117,643	281,448
	AAA wall Tetra mesh	1,256,654	1,515,460	1,418,616	1,326,264
No. of integration points in the finite element model	AAA wall Hexa mesh	1,333,608	1,726,224	941,144	2,251,584
	AAA wall Tetra mesh	5,026,616	6,061,840	5,674,464	5,305,056
No. of nodes in the finite element model	AAA wall Hexa mesh	368,389	506,320	318,450	648,142
	AAA wall Tetra mesh	1,961,363	2,378,646	2,203,917	2,086,393
Peak of max. principal stress (MPa)	AAA wall Hexa mesh	0.3641	0.4543	0.4383	0.5048
	AAA wall Tetra mesh	0.3880	0.3953	0.4755	0.6074
	Relative absolute difference%	6.6%	12.9%	8.5%	20.3%
99th percentile of max. principal stress (MPa)	AAA wall Hexa mesh	0.2310	0.2859	0.3037	0.2437
	AAA wall Tetra mesh	0.2034	0.2554	0.2487	0.2176
	Relative absolute difference%	11.9%	10.7%	18.1%	10.7%
Stiffness matrix assembly time (sec)	AAA wall Hexa mesh	18	27	19	38
	AAA wall Tetra mesh	96	118	109	151
Finite element model computation time (sec)	AAA wall Hexa mesh	157	296	133	1355
	AAA wall Tetra mesh	880	1641	1196	3048

All finite element models included the ILT and were executed using a computer with Intel(R) Core (TM) i7-5930 K CPU @3.50 GHz processor and 64 GB of RAM running Windows 8 operating system

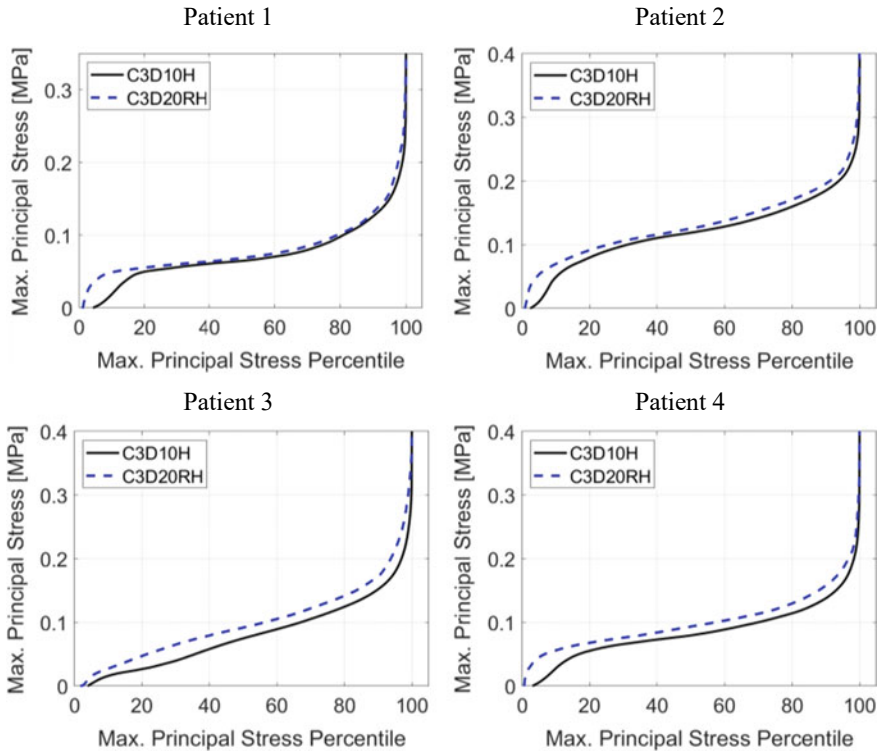
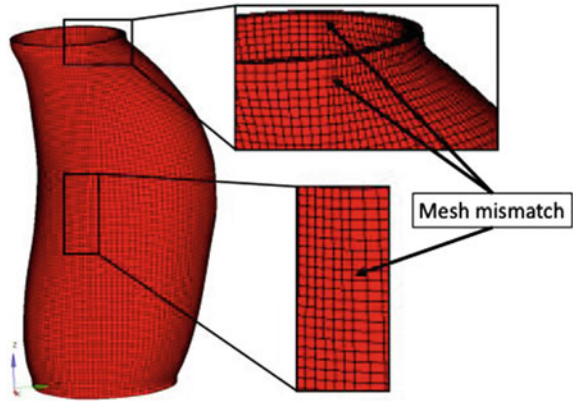


Fig. 11 Percentile plots of the maximum principal stress in the AAA wall for the four patients analysed in this study when varying the finite element type. C3D10H is a ten-noded quadratic tetrahedral hybrid element, and C3D20RH is a 20-noded quadratic hexahedral hybrid element with reduced integration

the computation time with only negligible changes in the computed stress. Therefore, we conclude that two hexahedral elements through wall thickness are sufficient to ensure convergence of stress computation.

We were also able to create high-quality hexahedral meshes (minimum Jacobian of 0.71) of AAA wall using ABAQUS/CAE mesh generator (see Sect. 2.2.1). Although from Fig. 12, the mesh density mismatch was obvious because of the inflexibility of defining partition planes in ABAQUS/CAE. Maximum principal stress contour plots and peak values of the maximum principal stress showed very good agreement for the models using the hexahedral meshes created using ABAQUS/CAE meshing tool and HyperMesh. The difference in the peak value of maximum principal stress between these models was only up to 0.0479 MPa. However, HyperMesh required less partitioning (and less analyst's time) than ABAQUS/CAE meshing tool to create mapped hexahedral meshes.

Fig. 12 Hexahedral mesh of the abdominal aortic aneurysm AAA wall generated using ABAQUS/CAE meshing tool



Acknowledgements The authors acknowledge funding of the Australian Government through the National Health and Medical Research Council NHMRC Ideas Grant, Ideas grant no. APP2001689. This research was carried out while the first author F. A. was in receipt of an “Australian Government Research Training Program Scholarship at The University of Western Australia”. The first author acknowledges Ms. Kiara Beinart of the University of Western Australia’s Intelligent System for Medicine Laboratory for her contribution in obtaining the ethics approval and support of Ms. Giuliana D’Aulerio of the University of Western Australia’s Medical School Division of Surgery. Contributions of Christopher Wood and Jane Polce, radiology technicians at Medical Imaging Department, Fiona Stanley Hospital (Western Australia) in patient (abdominal aortic aneurysm) CT image acquisition are gratefully acknowledged. We also thank Fiona Stanley Hospital, Perth, Western Australia, for providing the patient CT images.

References

1. Johnston, K.W., Rutherford, R.B., Tilson, M.D., Shah, D.M., Hollier, L., Stanley, J.C.: Suggested standards for reporting on arterial aneurysms. *J. Vasc. Surg.* **13**(3), 452–458 (1991)
2. Wanhainen, A., Verzini, F., Van Herzele, I., Allaire, E., Bown, M., Cohnert, T., Dick, F., van Herwaarden, J., Karkos, C., Koelemay, M., Kölbel, T., Loftus, I., Mani, K., Melissano, G., Powell, J., Szeberin, Z., Committee, E.G., de Borst, G.J., Chakfe, N., Debus, S., Hinchliffe, R., Kakkos, S., Koncar, I., Kolh, P., Lindholt, J.S., de Vega, M., Vermassen, F., Document, R., Björck, M., Cheng, S., Dalman, R., Davidovic, L., Donas, K., Earnshaw, J., Eckstein, H.-H., Golledge, J., Haulon, S., Mastracci, T., Naylor, R., Ricco, J.-B., Verhagen, H.: Editor’s choice – European society for vascular surgery (ESVS) 2019 clinical practice guidelines on the management of abdominal aorto-iliac artery aneurysms. *Euro. J. Vascul. Endovasc. Surg.* **57**(1), 8–93 (2019)
3. Martufi, G., Christian Gasser, T.: Review: the role of biomechanical modeling in the rupture risk assessment for abdominal aortic aneurysms. *J. Biomech. Eng.* **135**(2) (2013)
4. Upchurch, G.R., Schaub, T.A.: Abdominal aortic aneurysm. *Am. Acad. Family Phys.* **73**(7), 1198–1204 (2006)
5. Global, regional, and national age–sex specific all-cause and cause-specific mortality for 240 causes of death, 1990–2013: a systematic analysis for the global burden of disease study 2013. *The Lancet* **385**(9963), 117–171 (2015)

6. Lancet-2017: The lancet, global burden of disease. <https://www.thelancet.com/gbd/gbd-compare-visualisation>
7. Scott, R., Group, M.A.S.S.: The multicentre aneurysm screening study (MASS) into the effect of abdominal aortic aneurysm screening on mortality in men: a randomised controlled trial. *The Lancet* **360**(9345), 1531–1539 (2002)
8. Powell, J.T., Brady, A.R.: Detection, management, and prospects for the medical treatment of small abdominal aortic aneurysms. *Arterioscler. Thromb. Vasc. Biol.* **24**(2), 241–245 (2004)
9. Vande Geest, J., Di Martino, E., Bohra, A., Makaroun, M.S., Vorp, D.A.: A Biomechanics-based rupture potential index for abdominal aortic aneurysm risk assessment: demonstrative application. *Ann. N. Y. Acad. Sci.* **1085**, 11–21 (2006)
10. Gasser, T.C., Auer, M., Labruto, F., Swedenborg, J., Roy, J.: Biomechanical rupture risk assessment of abdominal aortic aneurysms: model complexity versus predictability of finite element simulations. *Eur. J. Vasc. Endovasc. Surg.* **40**(2), 176–185 (2010)
11. Gasser, T.C., Nchimi, A., Swedenborg, J., Roy, J., Sakalihan, N., Böckler, D., Hyhlik-Dürr, A.: A novel strategy to translate the biomechanical rupture risk of abdominal aortic aneurysms to their equivalent diameter risk: method and retrospective validation. *Eur. J. Vasc. Endovasc. Surg.* **47**(3), 288–295 (2014)
12. Polzer, S., Gasser, T.C.: Biomechanical rupture risk assessment of abdominal aortic aneurysms based on a novel probabilistic rupture risk index. *J. R. Soc. Interface* **12**(113), 20150852 (2015)
13. Joldes, G.R., Miller, K., Wittek, A., Forsythe, R.O., Newby, D.E., Doyle, B.J.: BioPARR: a software system for estimating the rupture potential index for abdominal aortic aneurysms. *Sci. Rep.* **7**(1), 4641 (2017)
14. Raut, S.S., Liu, P., Finol, E.A.: An approach for patient-specific multi-domain vascular mesh generation featuring spatially varying wall thickness modeling. *J. Biomech.* **48**(10), 1972–1981 (2015)
15. Miller, K., Mufty, H., Catlin, A., Rogers, C., Saunders, B., Sciarrone, R., Fourneau, I., Meuris, B., Tavner, A., Joldes, G.R., Wittek, A.: Is there a relationship between stress in walls of abdominal aortic aneurysm and symptoms? *J. Surg. Res.* **252**, 37–46 (2020)
16. Zhang, Y.J.: Chapter 6: image-based quadrilateral and hexahedral meshing. In: *Geometric Modeling and Mesh Generation from Scanned Images*, pp. 193–228. Chapman and Hall/CRC, New York (2018)
17. Wittek, A., Alkhatib, F., Vitásek, R., Polzer, S., Miller, K.: On stress in abdominal aortic aneurysm: linear versus non-linear analysis and aneurysm rupture risk. *Int. J. Numerical Meth. Biomed. Eng.* **38**(2), e3554 (2022)
18. De Santis, G., Mortier, P., De Beule, M., Segers, P., Verdonck, P., Verheghe, B.: Patient-specific computational fluid dynamics: structured mesh generation from coronary angiography. *Med. Biol. Eng. Comput.* **48**(4), 371–380 (2010)
19. Trachet, B., Renard, M., De Santis, G., Staelens, S., De Backer, J., Antiga, L., Loeys, B., Segers, P.: An integrated framework to quantitatively link mouse-specific hemodynamics to aneurysm formation in angiotensin II-infused ApoE $-/-$ mice. *Ann. Biomed. Eng.* **39**(9), 2430–2444 (2011)
20. Marchandise, E., Geuzaine, C., Remacle, J.F.: Cardiovascular and lung mesh generation based on centerlines. *Int. J. Numer. Meth. Biomed. Eng.* **29**(6), 665–682 (2013)
21. Tarjuelo-Gutierrez, J., Rodriguez-Vila, B., Pierce, D.M., Fastl, T.E., Verbrugge, P., Fourneau, I., Maleux, G., Herijgers, P., Holzapfel, G.A., Gomez, E.J.: High-quality conforming hexahedral meshes of patient-specific abdominal aortic aneurysms including their intraluminal thrombi. *Med. Biol. Eng. Comput.* **52**(2), 159–168 (2014)
22. Joldes, G.R., Noble, C., Polzer, S., Taylor, Z.A., Wittek, A., Miller, K.: A simple method of incorporating the effect of the uniform stress hypothesis in arterial wall stress computations. *Acta Bioeng. Biomech.* **20**(3), 59–67 (2018)
23. Mayr, M., Wall, W.A., Gee, M.W.: Adaptive time stepping for fluid-structure interaction solvers. *Finite Elem. Anal. Des.* **141**, 55–69 (2018)
24. Auer, M., Gasser, T.C.: Reconstruction and finite element mesh generation of abdominal aortic aneurysms from computerized tomography angiography data with minimal user interactions. *IEEE Trans. Med. Imaging* **29**(4), 1022–1028 (2010)

25. Polzer, S., Bursa, J., Gasser, T.C., Staffa, R., Vlachovsky, R.: A numerical implementation to predict residual strains from the homogeneous stress hypothesis with application to abdominal aortic aneurysms. *Ann. Biomed. Eng.* **41**(7), 1516–1527 (2013)
26. Zhang, Y., Bajaj, C.: Adaptive and quality quadrilateral/hexahedral meshing from volumetric data. *Comput. Meth. Appl. Mech. Eng.* **195**(9–12), 942–960 (2006)
27. Maier, A., Gee, M.W., Reeps, C., Pongratz, J., Eckstein, H.H., Wall, W.A.: A comparison of diameter, wall stress, and rupture potential index for abdominal aortic aneurysm rupture risk prediction. *Ann. Biomed. Eng.* **38**(10), 3124–3134 (2010)
28. Ito, Y., Shih, A.M., Soni, B.K.: Octree-based reasonable-quality hexahedral mesh generation using a new set of refinement templates. *Int. J. Numer. Meth. Eng.* **77**(13), 1809–1833 (2009)
29. Fedorov, A., Beichel, R., Kalpathy-Cramer, J., Finet, J., Fillion-Robin, J.-C., Pujol, S., Bauer, C., Jennings, D., Fennessy, F., Sonka, M., Buatti, J., Aylward, S., Miller, J.V., Pieper, S., Kikinis, R.: 3D slicer as an image computing platform for the quantitative imaging network. *Magn. Reson. Imag.* **30**(9), 1323–1341 (2012)
30. Huynh, A.T., Miller, K.: Towards accurate measurement of abdominal aortic aneurysm wall thickness from CT and MRI. In: *Computational Biomechanics for Medicine - Towards Translation and Better Patient Outcomes*. Springer International Publishing (2022)
31. Bern, M., Plassmann, P., Sack, J.R., Urrutia, J.: Chapter 6 - mesh generation. In: *Handbook of Computational Geometry*, pp. 291–332. North-Holland, Amsterdam (2000)
32. Yang, K.H.: Chapter 3 - isoparametric formulation and mesh quality. In: Yang, K.-H. (ed.) *Basic Finite Element Method as Applied to Injury Biomechanics*, pp. 111–149. Academic Press (2018)
33. AltairEngineering: Altair HyperMesh. https://2022.help.altair.com/2022.1/hwdesktop/hm/topics/chapter_heads/tutorials_r.htm (2022)
34. Joldes, G.R., Miller, K., Wittek, A., Doyle, B.: A simple, effective and clinically applicable method to compute abdominal aortic aneurysm wall stress. *J. Mech. Behav. Biomed. Mater.* **58**, 139–148 (2016)
35. Abaqus: Abaqus 6.14 Documentation. 2018. Dassault Systèmes Simulia Corp. <https://www.3ds.com/support/documentation/> (2018)
36. Lu, J., Zhou, X., Raghavan, M.L.: Inverse elastostatic stress analysis in pre-deformed biological structures: demonstration using abdominal aortic aneurysms. *J. Biomech.* **40**(3), 693–696 (2007)
37. Inzoli, F., Boschetti, F., Zappa, M., Longo, T., Fumero, R.: Biomechanical factors in abdominal aortic aneurysm rupture. *Eur. J. Vasc. Surg.* **7**(6), 667–674 (1993)
38. Vorp, D.A., Mandarino, W.A., Webster, M.W., Gorcsan, J.: Potential influence of intraluminal thrombus on abdominal aortic aneurysm as assessed by a new non-invasive method. *Cardiovasc. Surg.* **4**(6), 732–739 (1996)
39. Speelman, L., Bosboom, E.M.H., Schurink, G.W.H., Hellenthal, F.A.M.V.I., Buth, J., Breeuwer, M., Jacobs, M.J., van de Vosse, F.N.: Patient-specific AAA wall stress analysis: 99-percentile versus peak stress. *Eur. J. Vasc. Endovasc. Surg.* **36**(6), 668–676 (2008)

Workflow for Generating Personalised Anatomical Models of the Skeleton and the Skin Surface of the Upper Torso



Fangchao Pan, Kejia Khoo, Thiranja P. Babarenda Gamage, Gonzalo Maso Talou, Poul M. F. Nielsen, and Martyn P. Nash

Abstract Breast cancer is the leading cause of cancer-related death in women worldwide. Diagnostic imaging such as 3D magnetic resonance imaging (MRI) is acquired with patients positioned in the prone orientation with arms either above their heads or by their sides. However, treatment procedures such as surgery are performed in the supine position. Differences in the skeletal pose, and the large deformations that the breast undergoes during repositioning, make it challenging to localise breast lesions during treatment procedures. To address this issue, biomechanical modelling workflows have been proposed to simulate breast tissue deformation following patient repositioning. A key step in these workflows is the automated construction of personalised anatomical models to describe the geometry of the individual's breast tissues. Previous workflows have focused on modelling the soft tissue boundaries near the breast region without considering the individual's pose and skeletal joint positions. The proposed workflow uses a human body model as a template to obtain an initial estimate of each individual's shape before performing local refinement. The workflow is being designed to model data from multiple poses, and it incorporates skeletal information enabling more realistic boundary conditions to be applied during breast biomechanics simulations.

Keywords Breast cancer imaging · Breast biomechanics · Breast anatomical modelling · Multi-body modelling · Automated medical image analysis

F. Pan · K. Khoo · T. P. Babarenda Gamage (✉) · G. Maso Talou · P. M. F. Nielsen · M. P. Nash
Auckland Bioengineering Institute, University of Auckland, Auckland, New Zealand
e-mail: psam012@aucklanduni.ac.nz

P. M. F. Nielsen · M. P. Nash
Department of Engineering Science, University of Auckland, Auckland, New Zealand

1 Introduction

Breast cancer is the leading cause of cancer-related death in females, affecting one in every ten women worldwide [1]. During treatment, the patient usually lies in a supine position, whereas the diagnostic image of the breast is typically acquired in a prone position. The relative change in gravity loading can cause significant deformation in the breast tissues, creating ambiguity for the surgeon in locating tumour positions. To address this issue, biomechanical models have been developed to simulate breast deformation due to gravity and changes in pose. One of the key steps for biomechanical simulation is to construct a personalised anatomical model that provides descriptions of the geometry of the breast tissues. Many studies have focused on creating personalised anatomical models to represent the soft tissue boundaries of the breast (e.g. [2–6]). However, existing biomechanical models typically consider only the region surrounding the breasts without considering the individual’s skeletal pose. The joint positions of the arms and shoulders need to be considered as they influence the shape and stretch level of the pectoral muscles upon which the breast sits. During the imaging process, the subject’s arm and shoulder can be placed in a variety of positions, significantly altering the shape of the pectoral muscles and impacting the position and deformation of the breast. Articulated human body models are used in the computer graphics field to generate realistic-looking 3D human body surfaces. These parameterised human body models were trained using large datasets to model the variation in body shapes and pose-related deformation on the skin surface. They are widely adopted for their robustness, controllability, flexibility, and efficiency. Some of the most successful human body models include SCAPE [7], SMPL [8], and STAR [9]. Numerous studies [10, 11] have been conducted to register such human body models to 3D scans of the entire human body. However, current human body models rely on very naive and anatomically unrealistic representations of the human skeleton, in contrast to anatomically accurate multi-body skeletal models that are widely adopted in the field of biomechanics analysis [12–14].

This manuscript aims to describe an automated workflow for the generation of personalised anatomical meshes of the torso that incorporates anatomically accurate models of the skeleton for biomechanics simulations. A multi-body model is developed and personalised using the OpenSim software [15] to model the relevant skeletal joints for each individual. We employ an articulated human body model as the template model to obtain an initial estimate for the skin surface. The initial estimate is then locally refined to capture more details on the skin surface. The workflow assimilates 3D medical data from multiple positions.

Incorporating skeletal modelling into the workflow enables personalised boundary conditions to be applied during breast biomechanics simulations. The constructed meshes also provide a basis for statistical shape analysis of the torso in multiple poses.

Table 1 List of manually identified landmarks in the MR image and their definition

Landmarks	Definition for manual identification
Sternal notch	The most superior, anterior point at the centreline of the manubrium
SC	The most anterior, superior point at the medial end of the clavicle
AC	The most posterior, lateral point on the acromion of the scapula
GH	Centre of the humeral head

2 Methods

This section will describe the methods used to generate personalised anatomical surface meshes of the skeleton and the skin surface of upper torso. Section 2.1 will introduce the data used to test and evaluate the workflow. Sections 2.2 and 2.3 will introduce the personalisation process of the skeleton and skin surface models, respectively.

2.1 Image Acquisition and Pre-Processing

This workflow was tested and evaluated using MR images in a dataset acquired by the Breast Biomechanics Research Groups at The Auckland Bioengineering Institute (ABI). The full dataset consists of high resolution (1 mm^3) $T1$ - and $T2$ -weighted MR images that were acquired from 110 healthy participants in prone and supine positions at the University of Auckland's Centre for Advanced Magnetic Resonance Imaging (CAMRI). Landmarks on relevant skeletal joints were manually placed on the MR images (See Table 1 for a complete list of the identified landmarks and their definition). Meshlab software was used to generate triangulated surface meshes (hereinafter referred to as data meshes) from the manually segmented skin surface boundaries observed in the prone MR images.

2.2 Skeletal Model Personalisation

A multi-body model of the torso developed in OpenSim [14] was used as the template model for the skeleton. The model has 23 degrees of freedom, parameterised on the sternum, sternoclavicular (SC), acromioclavicular (AS), glenohumeral (GH), humeroulnar, and ulnoradial joints. The template model is in a standard anatomical position, which is defined as standing erect, looking forward, with the feet close and parallel to each other, the arms at the side and the palms facing forward [16].

Personalisation of the template model is achieved through scaling each component (e.g. each bone) of the model to match joint landmark positions identified in the MR images (See Table 1) for a given subject. The optimal scaling factor was computed

using Scipy version 0.24 [17]. Specifically, the objective function quantifying the distance error between joint landmarks is defined as

$$F(\mathbf{s}) = \frac{\sum_{p=1}^P \sum_{i=1}^N \|z_{i,p}(\mathbf{s})\|}{P}, \quad (1)$$

where \mathbf{s} is the vector of scaling parameters in each of the x , y , and z axes to be optimised, $\|z_{i,p}(\mathbf{s})\|$ is the Euclidean distance between the corresponding i th joint centre point on the template model and MRI data in the p th body position, N is the number of joints, and P is the number of body positions (e.g. prone or supine). Once the scale parameters were identified, the joint angles were subsequently determined using the inverse kinematic solver provided in the Python API of OpenSim 4.0 [15]. The objective function to minimise is the energy defined as

$$E_\phi = \|\mathbf{J}_{\text{MRI}} - \mathbf{J}_\mathcal{O}(\phi)\|_F, \quad (2)$$

where ϕ are the joint angles in the template model with respect to the standard anatomical position and $\mathbf{J}_\mathcal{O}$ and \mathbf{J}_{MRI} are matrices related with the joint positions in the template model and MRI data, respectively. Specifically, $\mathbf{J} = [\mathbf{j}_1^T, \dots, \mathbf{j}_K^T]$, where the three-element vector \mathbf{j}_k represents the 3D coordinates of the k th joint. In our workflow, $K = 7$. The optimised joint angles describe the pose of the individual seen in the MRI (see Fig. 1).

2.3 Skin Surface Model Personalisation

To deal with the complex geometry of the human skin surface in multiple poses, an articulated human body model was used as a template model to generate an initial estimate of the geometry of the skin surface. The template model used in this workflow is a female version of the skinned multi-person linear model (SMPL) model [8]. SMPL is an articulated human body model that uses joint angles θ and body shapes descriptors β as input parameters and generates triangulated skin surface mesh of the human body based on population information (See Fig. 2a). The fitting process follows the concept of the functional automatic registration method (FARM) [11].

The personalised multi-body model estimated in the previous section is used to constrain key joint positions of the SMPL model. The template model was linearly scaled and aligned to match the position of shoulder joints in SMPL and those defined in the personalised skeleton model. We modified this model to only include vertices from the neck to the base of the thorax and upper sections of the arms. Note that the multi-body model has two joints to represent the kinematic movement of shoulders (glenohumeral and acromioclavicular), whereas SMPL uses only one joint. Thus, the midpoints of glenohumeral joints and acromioclavicular joints in the multi-body model were considered as the shoulder joint for optimisation.

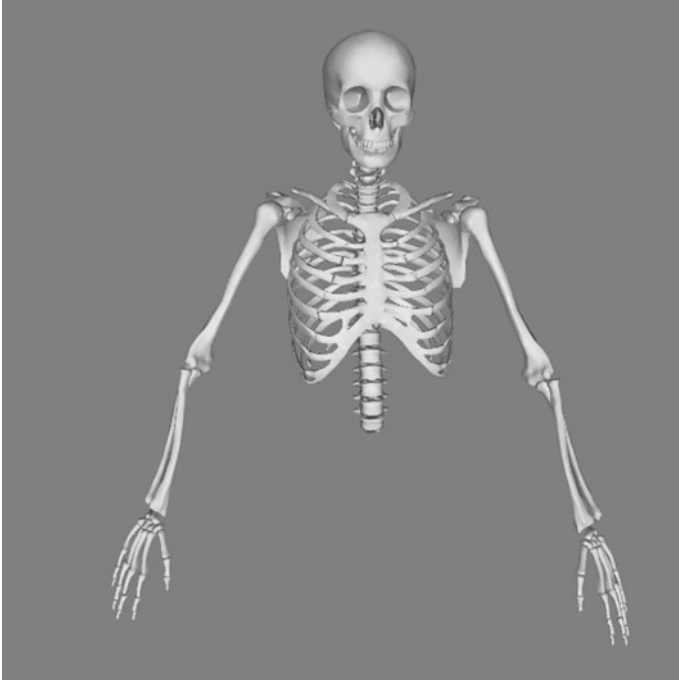


Fig. 1 Personalised multi-body skeleton model generated using the proposed workflow for a volunteer in the prone position

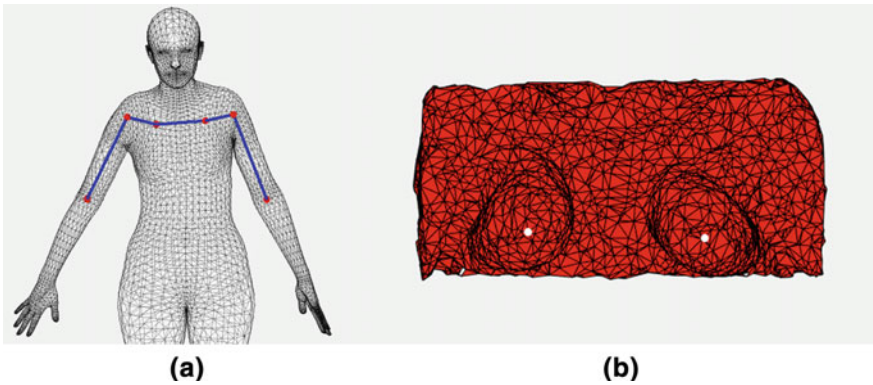


Fig. 2 SMPL **a** is employed as the template model in this workflow, where red points are the estimated joint positions. **b** is the data mesh generated from segmented MR data using Meshlab software, where white dots are landmarks placed on the nipples

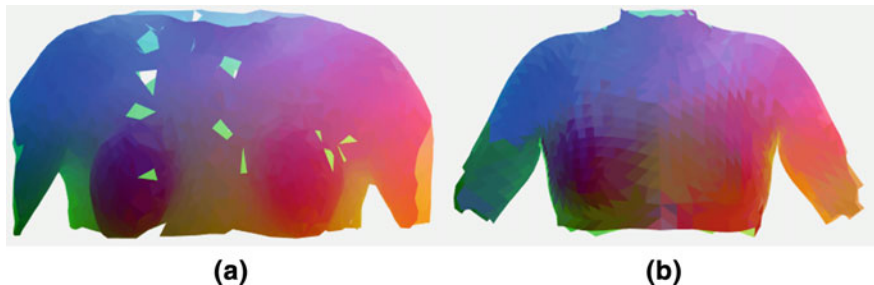


Fig. 3 Dense correspondences between the **a** data mesh and **b** template model. Computed correspondences are displayed in the same colour

The template model was non-rigidly registered to the data mesh generated from the manually segmented skin surface boundaries observed in the prone MR image (see Sect. 2.1), obtaining an initial estimate of the individual’s shape. The registration process can be described as follows. To initialise the process, left and right nipple landmarks were placed on the data mesh (see Fig. 2b) and template model. Specifically, the landmarks are placed on the most anterior point of each breast. Dense correspondences between the template model and the data mesh were computed using the functional map approach. The goal is to compute a point-wise map

$$\pi : \mathcal{N} \rightarrow \mathcal{M}, \quad (3)$$

where operator π maps points on the data mesh domain \mathcal{N} to the corresponding points on the template model domain \mathcal{M} (See Fig. 3a and b). Functional map approach uses real-valued functions defined on each shape, such as the eigenfunctions of its Laplace–Beltrami operator, to obtain a more compact representation of a map between two shapes. The original map π can be reconstructed from the functional representation. We refer the readers to the references [11, 18] for the details. The map π will constrain the non-rigidly fit of the template model to the data mesh.

The initial estimate of the skin surface is obtained by minimising the following energy:

$$\mathcal{E}(\beta, \theta) = w_V E_V(\beta, \theta) + w_L E_L(\beta, \theta) + w_\beta E_\beta(\beta) \quad (4)$$

with respect to the shape β and pose θ parameters in the SMPL model that instantiate the template model domain \mathcal{M} . Here, E_V is the term measuring the alignment error between surface vertices of the two shapes

$$E_V = \|\mathbf{X}_{\mathcal{M}} - \pi(\mathbf{X}_{\mathcal{N}})\|_F, \quad (5)$$

where $\mathbf{X}_{\mathcal{M}}$ are the vertices on the template model and $\pi(\mathbf{X}_{\mathcal{N}})$ are the corresponding points identified by the mapping π . Similarly, E_L represents the discrepancies between landmarks on the model and data

$$E_L = \|\mathbf{L}_{\mathcal{M}} - \mathbf{L}_{\mathcal{N}}\|_F, \quad (6)$$

where $\mathbf{L}_{\mathcal{M}}$ and $\mathbf{L}_{\mathcal{N}}$ are the positions of landmarks placed on the model and data mesh, respectively. E_β is defined as

$$E_\beta = \|\beta\|^2 \quad (7)$$

which regularises the shape parameter. Regularisation weights, w , in the workflow are set to $w_V = 1$, $w_L = 1$, and $w_\beta = 0.05$.

Until this step, all optimisations are with respect with SMPL parameters β and θ . Since SMPL can only model human body shape within the span of its training set, the model is at our disposal, and further local refinement can be applied directly. In this workflow, an as-rigid-as-possible (ARAP) algorithm [19] is employed in conjunction with a nearest neighbour energy to get the locally refined mesh.

3 Result and Discussion

Personalisation of the multi-body skeleton model was applied to MR images of 12 individuals in the dataset. To quantify the fitting accuracy, we define an error metric as the distance between the modelled joint positions and the landmarks placed in the MR images. Applying the multiple pose optimisation method results in a mean error of 2.4 ± 2.3 mm.

The main source of error is the uncertainty incurred in manual identification of landmarks in MR images. Repeatability in landmark identification was investigated by selecting the landmarks for each volunteer ten times. The order of landmarks was randomised and performed over two sessions. Standard deviation is used to measure the uncertainties of landmark placement. The uncertainties in the placement of landmarks are 2.3, 1.9, 2.6, and 0.9 mm for the sternal notch, SC, AC, and GH joints, respectively. The uncertainties in the landmark placement process could lead to significant inaccuracies during the personalisation of the multi-body model. The accuracy of kinematic models depends on how well the underlying model matches the subject's anthropometric data. However, previous studies have shown that the linear scaling method has a higher error when compared to statistical shape modelling scaling [20].

Due to the lack of manually segmented data and poor visibility of key joint landmarks in the MR image, the personalisation of skin surface was applied to MR images of three individuals in the dataset. See Fig. 4a and b for an example of the fitted mesh. Hausdorff distance between the skin surface segmented from the MRI and the fitted skin surface was used to quantify the performance of the workflow. The mean Hausdorff distances for three individuals are 5.1, 4.9, and 7.8 mm. The mesh shows noticeable poor fits around the sternum region because the template model

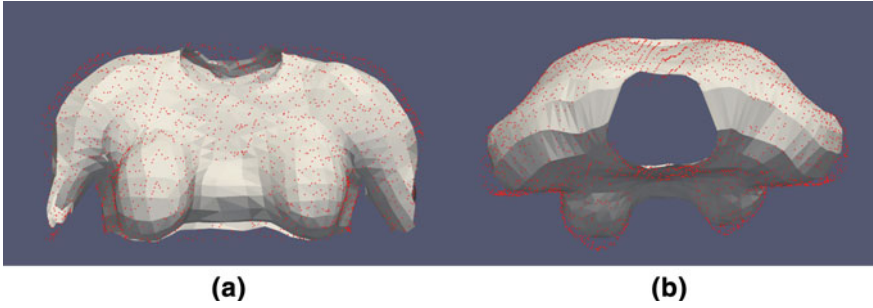


Fig. 4 Refined mesh from the **a** anterior view and **b** superior view, where points are the segmented point clouds from a MR image acquired in the prone position

being employed in the workflow was trained using clothed people in upright positions. The workflow is also sensitive to data partiality, as missing parts may cause shape matching between the data and the template to fail.

The proposed workflow for the skin surface is automatic and requires minimal manual intervention. The functional map algorithm matches correspondences on the template model and the data without regarding the individual’s body size, pose, and orientation. The template model patches small holes and fixes minor artefacts on the segmented data. This approach also uses population information on female body shapes, since SMPL is the first human body model that used the entire CAESAR [21] dataset for training. However, one of the key limitations of this workflow is that the training data of SMPL (as well as other human body models in the field) consists of scanned people who are wearing tight clothing and standing in an upright position. This makes the template model unable to capture anatomical details on bare breasts when the individual is in the prone position, leading to poor initial estimates and will subsequently destabilise the process of local refinement.

Although the approach is automatic, the correspondence matching algorithm employed in the workflow is vulnerable to any change of topology. A major limitation of this workflow is the partiality of data, where the data observed in the MR image is a subset of the template model. The inconsistency of the field of view causes difficulties in the model fitting process. For example, a template model with the neck included may not be suitable for those data without the neck region segmented since the correspondences on the neck region do not exist. Moreover, shoulder joints are only visible in less than 40% of the MR images in our dataset due to limited field of view. Extending the field of view would allow more skeletal joint to be identified, providing more constraints for skin surface mesh construction.

In the future, a mapping algorithm that specialises in matching partial shapes will be deployed. A partial map enables the alignment of whole-body models without considering the completeness of the input data. Furthermore, the robustness of this workflow will be quantitatively assessed by fitting it to a larger cohort. It should be remarked that the SMPL representation of joints does not accurately represent the

anatomical structure of the human skeleton. A better mapping between the multi-body and human body models to align the template models is within the scope of future works. Alternatively, the 1D multi-body skeleton model can be replaced with a more representative statistical shape model, potentially providing a more accurate estimate of joint positions compared to the linear scaling of the multi-body model.

4 Conclusion

This study proposed a workflow to generate skin surface meshes of the female torso from medical imaging. In contrast to previous works which mainly focused on regions near the breast without regarding the skeletal pose, this workflow is being designed to account for multiple poses. Additionally, the workflow incorporates anatomically accurate models of the skeleton. The constructed skin surface meshes provide a basis for statistical shape analysis of the torso in multiple poses.

Acknowledgements The authors are grateful for financial support from the New Zealand Government Ministry for Business, Innovation and Employment (UOAX1004), the University of Auckland Foundation (F-IBE-BIP), and the New Zealand Breast Cancer Foundation (R1704).

References

1. Bray, F., Ferlay, J., Soerjomataram, I., Siegel, R.L., Torre, L.A., Jemal, A.: Global cancer statistics 2018: GLOBOCAN estimates of incidence and mortality worldwide for 36 cancers in 185 countries. *CA Cancer J. Clin.* **68**(6), 394–424 (2018)
2. Han, L., Hipwell, J.H., Eiben, B., et al.: A nonlinear biomechanical model based registration method for aligning prone and supine MR breast images. *IEEE Trans. Med. Imag.* **33**(3), 682–694 (2013)
3. Mira, A., Carton, A.K., Muller, S., Payan, Y.: A biomechanical breast model evaluated with respect to MRI data collected in three different positions. *Clin. Biomech.* **60**, 191–199 (2018)
4. Babarenda Gamage, T.P., Malcolm, D.T.K., Maso TalouTalou, G., et al.: An automated computational biomechanics workflow for improving breast cancer diagnosis and treatment. *Interface Focus.* **9**(4), 20190034 (2019)
5. Eiben, B., Han, L., Hipwell, J., et al.: Biomechanically guided prone-to-supine image registration of breast MRI using an estimated reference state. In: 2013 IEEE 10th International Symposium on Biomedical Imaging, pp. 214–217. IEEE (2013)
6. Han, L., Hipwell, J.H., Tanner, C., et al.: Development of patient-specific biomechanical models for predicting large breast deformation. *Phys. Med. Biol.* **57**(2), 455 (2011)
7. Anguelov, D., Srinivasan, P., Koller, D., Thrun, S., Rodgers, J., Davis, J.: SCAPE: shape completion and animation of people. In: ACM SIGGRAPH Papers on - SIGGRAPH '05, pp. 408. ACM Press (2005)
8. Loper, M., Mahmood, N., Romero, J., Pons-Moll, G., Black, M.J.: SMPL: a skinned multi-person linear model. *ACM Trans. Graph.* **34**(6), 1–16 (2015)
9. Osman, A.A.A., Bolkart, T., Black, M.J.: STAR: sparse trained articulated human body regressor. *ArXiv200808535 Cs.* **12351**, 598–613 (2020)

10. Zuffi, S., Black, M.J.: The stitched puppet: a graphical model of 3D human shape and pose. In: 2015 IEEE Conference on Computer Vision and Pattern Recognition (CVPR), pp.3537–3546. IEEE (2015)
11. Marin, R., Melzi, S., Rodolà, E., Castellani, U.: FARM: functional automatic registration method for 3D human bodies. *Comput. Graph. Forum.* **39**(1), 160–173 (2020)
12. Chadwick, E.K., Blana, D., Kirsch, R.F., van den Bogert, A.J.: Real-time simulation of three-dimensional shoulder girdle and arm dynamics. *IEEE Trans. Biomed. Eng.* **61**(7), 1947–1956 (2014)
13. Bruno, A.G., Boussein, M.L., Anderson, D.E.: Development and validation of a musculoskeletal model of the fully articulated thoracolumbar spine and rib cage. *J. Biomech. Eng.* **137**(8), 081003 (2015)
14. Khoo, K.: Personalised Skeletal Modelling of the Female Torso from Multiple Loaded States. M.S. Thesis. The University of Auckland (2021)
15. Delp, S.L., Anderson, F.C., Arnold, A.S., et al.: OpenSim: open-source software to create and analyze dynamic simulations of movement. *IEEE Trans. Biomed. Eng.* **54**(11), 1940–1950 (2007)
16. Nikita, E.: The human skeleton. In: *Osteoarchaeology*, pp.1–75. Elsevier (2017)
17. Virtanen, P., et al.: SciPy 1.0: fundamental algorithms for scientific computing in python. *Nat. Meth.* **17** (2020)
18. Ovsjanikov, M., Ben-Chen, M., Solomon, J., Butscher, A., Guibas, L.: Functional maps: a flexible representation of maps between shapes. *ACM Trans. Graph.* **31**(4), 1–11 (2012)
19. Chao, I., Pinkall, U., Sanan, P., Schröder, P.: A simple geometric model for elastic deformations. *ACM Trans. Graph. TOG.* **29**(4), 1–6 (2010)
20. Bahl, J.S., Zhang, J., Killen, B.A., et al.: Statistical shape modelling versus linear scaling: effects on predictions of hip joint centre location and muscle moment arms in people with hip osteoarthritis. *J. Biomech.* **85**, 164–172 (2019)
21. Robinette, K.M., Daanen, H., Paquet, E.: The CAESAR project: a 3-D surface anthropometry survey. In: *Second International Conference on 3-D Digital Imaging and Modeling (Cat. No. PR00062)*, pp. 380–386. IEEE (1999)

Automated Modeling of Brain Bioelectric Activity Within the 3D Slicer Environment



Saima Safdar, Benjamin Zwick, George Bourantas, Grand Joldes, Damon Hyde, Simon Warfield, Adam Wittek, and Karol Miller

Abstract Electrocorticography (ECoG) or intracranial electroencephalography (iEEG) monitors electric potential directly on the surface of the brain and can be used to inform treatment planning for epilepsy surgery when paired with numerical modeling. For solving the inverse problem in epilepsy seizure onset localization, accurate solution of the iEEG forward problem is critical which requires accurate representation of the patient's brain geometry and tissue electrical conductivity. In this study, we present an automatic framework for constructing the brain volume conductor model for solving the iEEG forward problem and visualizing the brain bioelectric field on a deformed patient-specific brain model within the 3D Slicer environment. We solve the iEEG forward problem on the predicted postoperative geometry using the finite element method (FEM) which accounts for patient-specific inhomogeneity and anisotropy of tissue conductivity. We use an epilepsy case study to illustrate the workflow of our framework developed and integrated within 3D Slicer.

Keywords Epilepsy · Framework · Modeling · Biomechanics · Finite element method · Patient-specific

1 Introduction

Techniques for building patient-specific models of brain bioelectric activity and solving such models accurately and efficiently are important enablers for neuroscience and neurology. The application of such modeling and simulation techniques to the

S. Safdar · B. Zwick · G. Bourantas · G. Joldes · A. Wittek · K. Miller (✉)
Intelligent Systems for Medicine Laboratory, The University of Western Australia, 35 Stirling
Highway, Perth, WA, Australia
e-mail: karol.miller@uwa.edu.au

D. Hyde · S. Warfield · K. Miller
Harvard Medical School, Boston, MA, USA

D. Hyde · S. Warfield
Computational Radiology Laboratory, Boston Children's Hospital, Boston, MA, USA

© The Author(s), under exclusive license to Springer Nature Switzerland AG 2023
M. P. Nash et al. (eds.), *Computational Biomechanics for Medicine*,
https://doi.org/10.1007/978-3-031-34906-5_3

identification of epileptic seizure onset zones (SOZ) that consider the brain at length scales accessible by medical imaging and electrodes is of particular interest.

Epilepsy is a chronic brain disorder that causes unpredictable and recurrent electrical activity in the brain (seizures). It affects 65 million people worldwide, making it one of the most common neurological diseases globally [1]. It is estimated that about 70% of the people living with epilepsy can be cured if diagnosed and treated properly [2]. One such treatment option is surgical resection of the area of the brain where seizures occur. During epilepsy surgery planning using iEEG, placement of electrode grids and strips, and the body's inflammatory response to craniotomy, displace and deform the brain relative to its undeformed configuration observed in the preoperative MRI. This brain shift must be accurately modeled after insertion of electrode grids to enable precise localization of the SOZ with respect to preoperative MRI and postoperative CT. The geometry of the patient's brain and the electrical conductivity distribution within the patient's head must be accurately represented for appropriate SOZ localization [3].

The methodology used to compute the brain shift has been extensively validated in our previous studies [4–10]. For brain bioelectric activity modeling, continuum models based on partial differential equations are the most dominant models. The governing equations of the iEEG forward problem can be solved numerically using finite element (FEM) [11–14], finite volume (FVM) [15], finite difference (FDM) [16–19], or boundary element methods (BEM) [20–22]. In our previous study [23], we used the FEM with a mesh coinciding with the voxel structure of the image to obtain a forward solution to the problem on a deformed patient-specific head model.

In this study, we integrate the various components of our framework in the form of independent modules within 3D Slicer for automatically generating the patient-specific head model for solving the iEEG forward problem. We demonstrate the application of our framework by solving the iEEG forward problem for an epilepsy case study using patient data obtained from Boston Children's Hospital. We solve the iEEG forward problem on the deformed (predicted postoperative) image obtained after using the framework of biomechanical brain modeling [24–26] and compute the brain shift with methods extensively validated in our previous research [4–10].

The paper is organized as follows. In Sect. 2, we describe the framework and workflow, and the methods used in each stage of the framework, for automatically constructing the patient-specific head volume conductor model for solving iEEG forward problem. In Sect. 3, we demonstrate the application of our framework to the solution of the iEEG forward problem. Section 4 contains discussion and conclusion.

2 Methods

The framework architecture follows a modular approach, as presented in Fig. 1. Our automatic system for generating a patient-specific head model and for solving the iEEG forward problem consists of the following features: (1) image preprocessing; (2) constructing a patient-specific head model based on deformed predicted post-

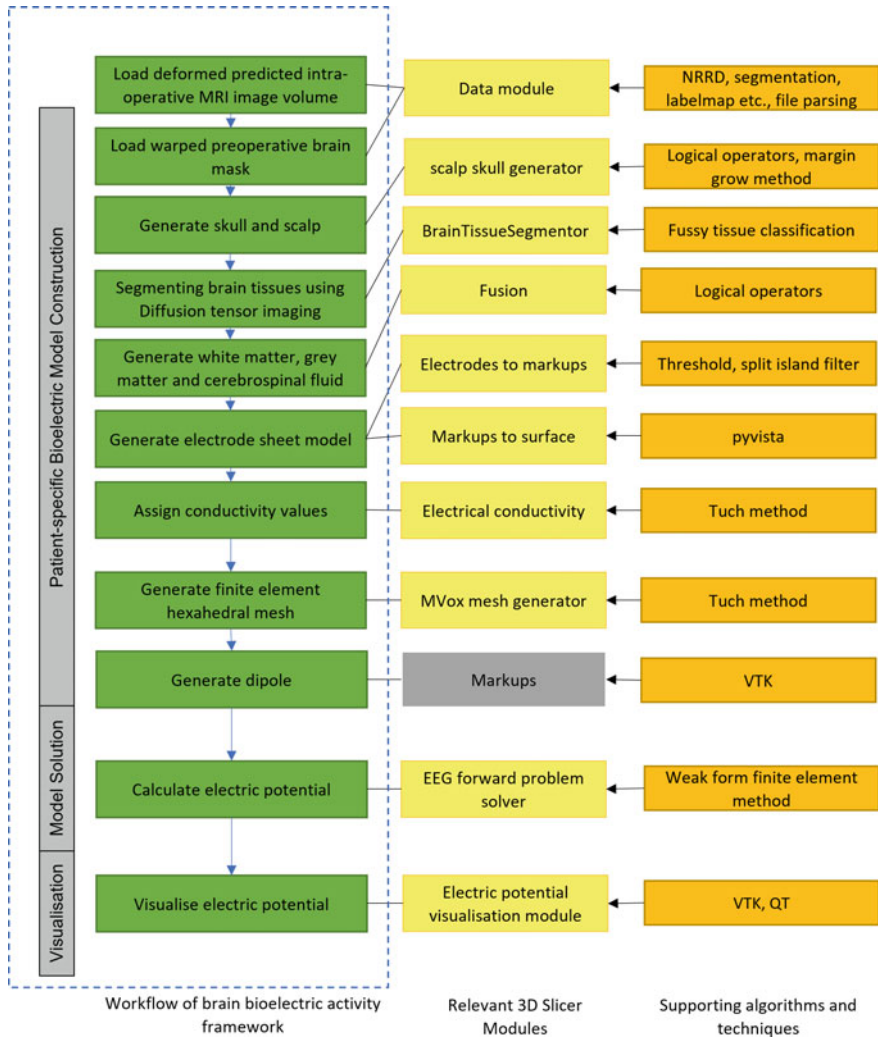


Fig. 1 System workflow diagram of the automatic framework along with relevant 3D Slicer modules and supporting algorithms and techniques for patient-specific bioelectric modeling. Yellow blocks represent our developed modules and gray blocks represent the 3D Slicer modules

operative MRI [23]; (3) generating electrode sheet model after extracting electrode locations from postoperative CT with electrodes implanted; (4) assigning patient-specific electrical conductivities to brain tissues; (5) generating a patient-specific voxel-based hexahedral mesh; (6) defining current dipole; (7) patient-specific model solution for iEEG forward problem; and (8) visualization of electric potential within patient-specific head model.

The framework features are implemented as a combination of multiple 3D Slicer command-line interface (CLI) modules and scripted modules, bundled as one downloadable extension (<https://github.com/SlicerCBM/SlicerCBM>). Each module is independent, addressing only a specific requirement (see Fig. 1). This modularization makes development and maintenance much easier compared to working with a monolithic code base. Section 2.2 to 2.4 describes the workflow of our system for generating a patient-specific head model based on the predicted deformed postoperative MRI by our biomechanics system [4–10, 24–26] for an epilepsy case studied in our previous research, and then solving a forward problem on the generated head model using our developed 3D Slicer extensions.

2.1 The iEEG Forward Problem

The partial differential equation underlying the iEEG forward problem can be derived by introducing the quasi-static approximation of Maxwell’s equations [27, 28]. For a spatial domain ($\Omega \in \mathbb{R}^3$) with boundary ($\partial\Omega = \overline{\Gamma_D} \cup \overline{\Gamma_N}$) and outward unit normal (\mathbf{n}), Poisson’s equation for the iEEG forward problem can be written as follows:

$$-\nabla \cdot (C(\nabla u)) = f \text{ in } \Omega, \quad (1)$$

$$\mathbf{n} \cdot (C(\nabla u)) = g \text{ on } \Gamma_N, \quad (2)$$

$$u = h \text{ on } \Gamma_D, \quad (3)$$

where u is the unknown scalar potential and C is the (symmetric positive semi-definite) conductivity tensor. The low conductivity of air outside the scalp ($C = 0$) for all ($x \notin \Omega$) implies that a zero-flux Neumann boundary condition $g = 0$ can be applied on the surface Γ_N . Dirichlet boundary conditions (h) on the surface Γ_D are typically applied by setting the potential to zero at a node corresponding to a reference electrode. Loading can be applied to the model either by prescribing the potential (u) at certain nodes or by applying a current source ($f = \nabla \cdot \mathbf{j}$), with (\mathbf{j}) being a dipole source vector. The epileptic seizure onset source is typically modeled as a current dipole [29].

2.2 Image Preprocessing

In this study, extracting the brain volume and removing the skull is performed using FreeSurfer software (<http://surfer.nmr.mgh.harvard.edu/>). It is an open-source software suite for processing and analyzing human brain medical resonance images (MRIs) [30]. We used the Watershed algorithm in FreeSurfer to extract the brain portion from T1-weighted MRI [31]. The Watershed algorithm uses preflooding height factor to adjust the boundaries of the brain to be included in the extracted

brain volume (set of brain MRI slices without skull). After extracting the brain volume, we applied a threshold filter (Otsu's method) [32] to the brain volume which selects the brain parenchyma and produces a brain mask. The computed parameter value of Otsu's method was 48.96 for thresholding the brain volume. The resulting brain mask is used to reconstruct the brain geometry further in the pipeline.

2.3 Patient-specific Head Model Construction for Solving *iEEG Forward Problem*

Segmenting brain tissues using diffusion tensor imaging: A fuzzy c-means clustering algorithm is used to classify brain tissues using diffusion tensor imaging (DTI) [23]. In the first step, mean diffusivity is used to separate the cerebrospinal fluid (CSF) from the rest of the brain. In the second step, fractional anisotropy is used to separate the white matter (WM) from the gray matter (GM). The threshold values for mean diffusivity and fractional anisotropy obtained using fuzzy c-means clustering were $0.00137 \text{ mm}^2/\text{s}$ and 0.263, respectively. The results of DTI-based image segmentation are shown for a deformed DTI in Fig. 2.

Constructing patient-specific skull and scalp segments: Segmenting the skull from CT is difficult due to artifacts caused by the implanted electrodes and requires time consuming manual segmentation, which is not compatible with a clinical workflow. Therefore, instead of realistic representation of the skull geometry, we simplified the construction of the skull geometry by offsetting the extracted brain volume by 4 voxels. In a similar manner, we constructed a simplified model of the scalp by offsetting the skull model by 4 voxels. For constructing the simplified skull and scalp models, we developed a module "Scalp Skull Generator," in 3D Slicer for automatically generating skull and scalp models. The module requires extracted brain volume, and two different growing margin numbers (in mm) as an input and it outputs brain, skull and scalp masks (mask is a separate label set of slices comprising the particular tissue type). The margin number defines the thickness of the skull and the scalp. We used the following set of procedures to create the scalp, skull, and

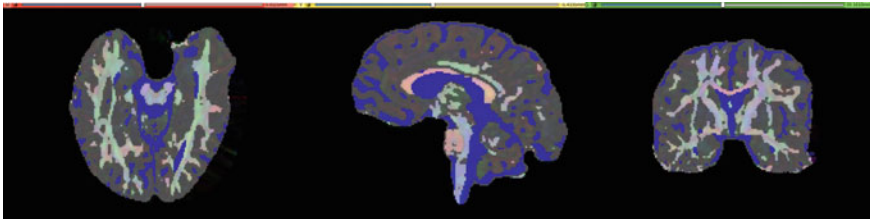


Fig. 2 Results of DTI-based image segmentation for a deformed DTI image. Gray represents gray matter, dark blue represents CSF and remaining represents white matter. The segmentation of the tissues (white matter, gray matter, and CSF) is overlaid with the DTI image

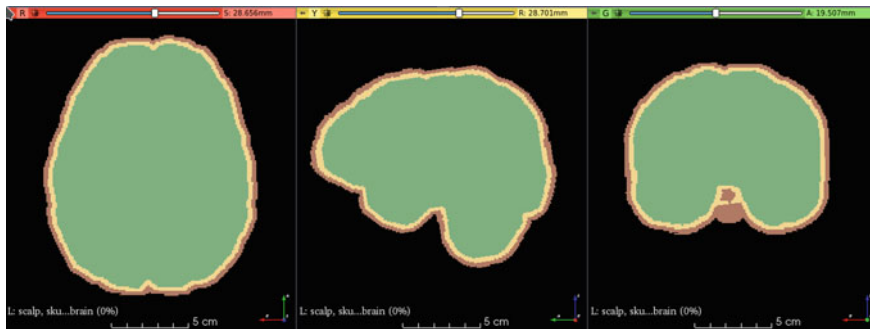


Fig. 3 Scalp (light brown), skull (yellow), and brain (green) label maps within 3D Slicer

brain masks: (1) threshold the extracted brain volume; (2) copy the thresholded brain volume to create a new brain volume segment; (3) grow the new brain volume with a specified margin size (thickness in mm) to obtain the skull segment; (4) subtract brain volume from skull segment to create skull mask; (5) grow the skull mask with a specified margin size (mm) to create a new segment scalp; and (6) subtract the skull and brain from the scalp segment to get the scalp. We applied logical operators and margin grow methods of segment editor [32] to construct the scalp, skull, and the brain masks (see Fig. 3).

Combining patient-specific brain tissue segments: We developed the “Fusion” module within 3D Slicer to combine brain tissue segments (i.e., white matter, gray matter, and CSF) with skull, scalp, and electrode sheet segments. This module can combine a variety of tissue segments to produce the following models: (1) undeformed model based on preoperative MRI image (with or without electrode sheet model); and (2) deformed model based on predicted postoperative MRI (obtained by warping the preoperative MRI), with or without electrode sheet model. We used logical operators (union) procedure of 3D Slicer segment editor module to combine all the segments. We used the brain mask generated in Sect. 2.2 to fill any gaps in the CSF mask. Figure 4 shows tissue label maps based on deformed postoperative image data by insertion of electrodes within 3D Slicer (Fig. 5).

Generating an electrode sheet model: ECoG strip and grid electrodes are typically composed of an array of platinum electrodes embedded into a sheet of plastic material. Our automated procedure for reconstructing the electrode sheet geometry from the postoperative CT image is as follows: (1) extract electrode locations from postoperative CT image and (2) create the electrode sheet model. In step 1, we extract the electrode coordinates from the segmented electrode volume (image set containing electrode segmentations) using our procedure implemented as a 3D Slicer module “Electrodes To Markups.” The postoperative (post-implantation) electrode positions were extracted (via segmentation) from the CT image rigidly aligned to the preoperative MRI. We used the rigid registration algorithm of the “GeneralRegistration (BRAINS)” module of 3D Slicer [33] to rigidly align the CT image to the

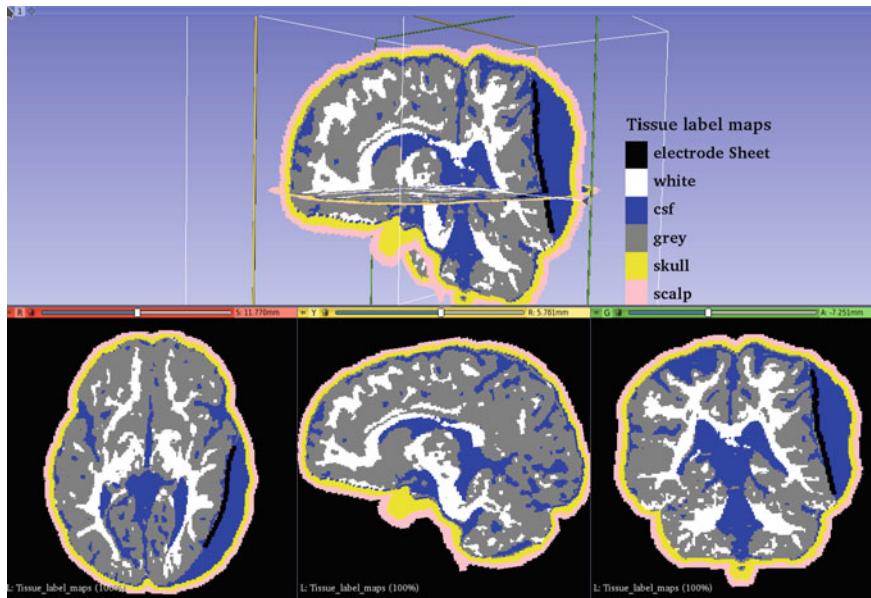


Fig. 4 Tissue label maps based on deformed by insertion of electrodes postoperative image data (predicted postoperative MRI) within 3D Slicer (axial, sagittal, coronal, and 3D view). Tissue classes are colored as follows: scalp (pink); skull (yellow); GM (gray); WM (white); and CSF (blue). The location of the electrode grid array can be identified by the line of black voxels in the vicinity of the right temporal and parietal lobes

preoperative MRI. The steps involved in extracting electrode locations using our procedure are as follows: (1) create a binary label volume from segmented electrode volume using auto thresholding; (2) split the binary label volume to individual segments corresponding to each electrode; and (3) add a point at the centroid of each electrode segment. The conversion from segmented electrode volume to binary label volume [step (1)] is performed using PolySeg [34], a software library that provides automatic conversions between different geometry representations (e.g., label map, surface) [34]. Splitting the binary label volume [step (2)] is performed using “split island into segments” and then “segment statistics” of segment editor effect module [step (3)] is used to get the centroids (center of mass of the segment) [34]. In step 2, we used electrode locations to create an electrode sheet model by means of PolyData algorithm [35], which creates a triangulated surface. We then used delaunay method to construct an electrode sheet model based on triangulated surface [36].

Assigning patient-specific electrical conductivities: We assigned isotropic conductivities to the scalp, skull, CSF, electrode grid array substrate, and gray matter regions [23, 29, 37]. We assigned anisotropic conductivity to the white matter region. We estimated the anisotropic conductivity values using the fractional methods directly from the diffusion tensors [23, 38].

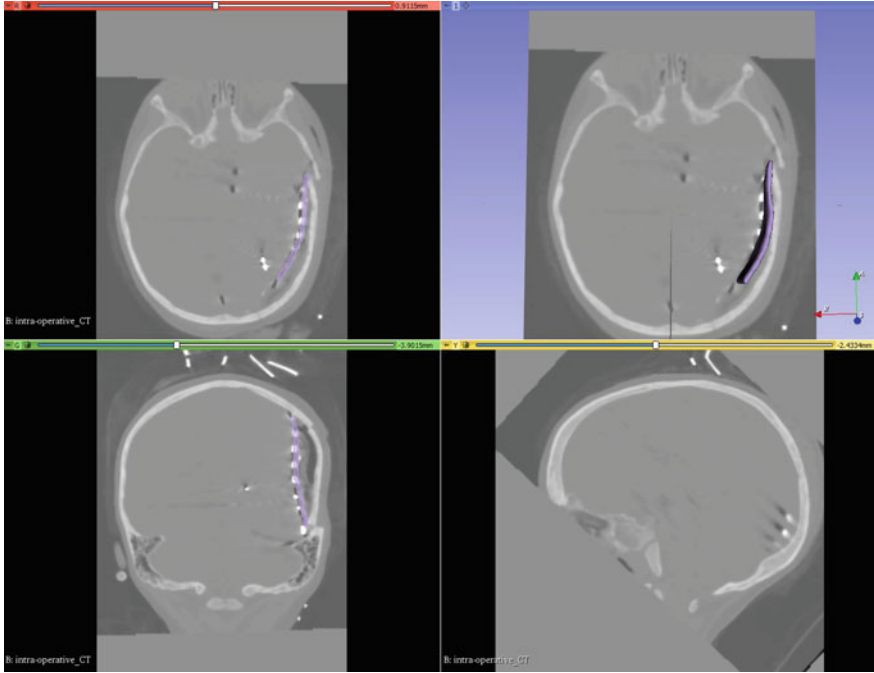
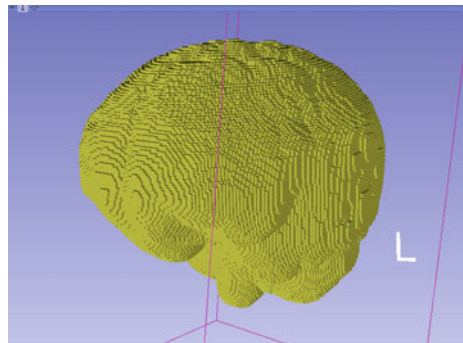


Fig. 5 3D electrode sheet model overlaid with postoperative CT in axial, sagittal, coronal, and 3D window within 3D Slicer

Fig. 6 3D patient-specific regular hexahedral mesh in 3D window within 3D Slicer



Generating patient-specific voxel-based hexahedral mesh: We used the MVox mesh generator (<https://github.com/benzwick/mvox>) to generate a regular hexahedral finite element mesh (Fig. 6) corresponding to the voxels of the 3D conductivity tensor image. Each nonzero voxel in the input image is converted to a hexahedral element centered at the voxel’s centroid. MVox is implemented using the open-source MFEM library [39]. It supports a variety of input and output file formats. We integrated MVox as the “MVox Mesh Generator” module within 3D Slicer.

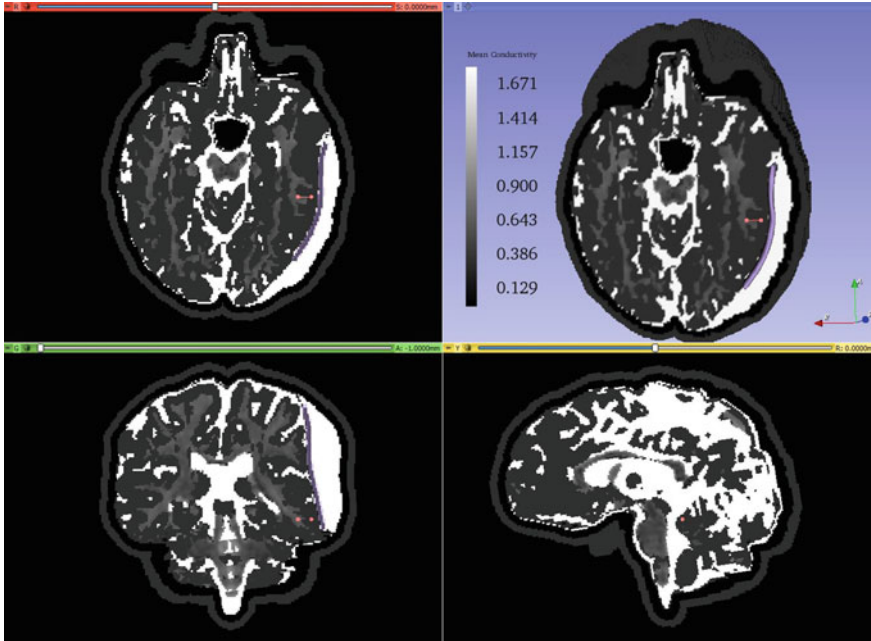


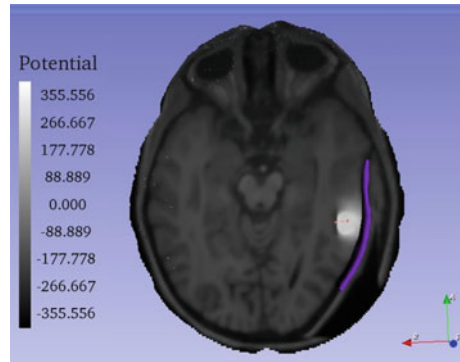
Fig. 7 Mean conductivity of the deformed model based on image data deformed by implantation of electrodes shown in axial, sagittal, and coronal view overlaid with deformed MRI and 3D brain model in 3D window within 3D Slicer. The current dipole moment vector is denoted by the pink line with two fiducial points. The electrode sheet is denoted by the purple color

Defining a dipole: We used the “Markups” module of 3D Slicer [32] to generate a `vtkMRMLMarkupsLineNode` to define the dipole in the gray matter region of the brain tissue. It is represented as two 3D control points in the 3D plane (see Fig. 7)

2.4 Model Solution for EEG Forward Problem

We used the finite element method with a regular hexahedral mesh that corresponds to the voxel structure of the image [14, 23, 40, 41]. We assigned conductivity tensors directly from image voxels to integration points in the elements of the hexahedral mesh. We refer to this approach of assigning the values from image voxels to elements as the “image as a model” approach, as the finite element mesh used to solve problem directly corresponds to image data. All elements in a regular hexahedral mesh are cubes with perfect element quality. We used a finite element mesh with 1,618,745 nodal points and 1,565,095 linear hexahedral elements for solving the EEG forward problem. We implemented the solution to the EEG forward problem using the open-source MFEM library [42] (<https://mfem.org>) and integrated into 3D Slicer as a separate module. We used continuous Galerkin formulation with linear hexahedral

Fig. 8 Electric potential in the brain generated by a current dipole predicted by the deformed model based on image data deformed by implantation of electrodes. The current dipole moment vector is denoted by the pink line with two fiducial points. The electrode sheet model is denoted by the purple color



elements for spatial discretization of the potential and for computing the electric field [23]. We used the full subtraction approach to model the current dipole source [11]. We solved the discretized equations using the conjugate gradient (CG) method with an algebraic multigrid (AMG) preconditioner from the HYPRE library of linear solvers (<http://www.llnl.gov/casc/hypre>).

3 Results

We demonstrate the application of our framework by solving an iEEG forward problem. We solved the iEEG forward problem with a current dipole source using the deformed image data with the actual electrode locations. We put a dipole in the gray matter of the brain with a dipole moment of $100 \mu \text{ Amm}$ to replicate a current dipole set up by cortical neurons. Figure 7 shows mean conductivity of the deformed model based on image data deformed by implantation of electrodes. Figure 8 shows the predicted distribution of electric potential within the brain computed using the model based on the deformed image data with the actual electrode positions. We used deformed image data with actual electrode positions to avoid the error introduced by using incorrect tissue geometry. As discussed in our previous study [23], the correct geometry can reduce the effect of inaccuracy of source localization.

4 Discussion

In this paper, we presented an automated framework for constructing a patient-specific head volume conductor model and computing the brain bioelectric activity within the 3D Slicer environment. To demonstrate the application of our framework, we used the predicted postoperative MRI with implanted intracranial electrodes obtained from our previous study [23, 24] of a real, patient-specific case from Boston Children's Hospital.

The generation of the patient-specific computational model for the iEEG forward problem which include image preprocessing, segmentation of electrodes and electrode sheet generation, scalp and skull generation, brain tissue classification and fusion of brain tissues, scalp, skull and electrode sheet, conductivity tensor estimation and generation of the finite element mesh, can take approximately 10 min per patient. The time to generate a patient-specific computational model for the iEEG forward problem using our workflow system is acceptable in the research environment and could be considered to be sufficient for clinical applications. We have automated all of the modeling stages in preparation for use in a clinical setting. We demonstrated the applicability of the developed framework by solving the iEEG forward problem. We showed the electric potential of the model of the brain with current dipole using the deformed (predicted postoperative) image data.

We have developed the modules to automate the modeling tasks to reduce the time required to construct a patient-specific model for solving the iEEG forward problem and support the medical practitioners by providing an easy to use graphical user interface (GUI). This can also make the solution of the iEEG inverse problem feasible as we intend to combine the framework described in this paper with an appropriate method for solving the iEEG inverse problem to enable accurate source localization for epilepsy patients who have undergone invasive electrophysiological monitoring. We use a modular approach to develop our system which makes it easy to integrate existing frameworks or components. We plan to take advantage of this in the future by integrating other freely available open-source frameworks (e.g., FreeSurfer, DUNEuro, etc.) within our system.

Acknowledgements A. Wittek and K. Miller acknowledge the support by the Australian Government through National Health and Medical Research Project Grant no. APP1162030.

References

1. Thurman, D.J., Beghi, E., Begley, C.E., Berg, A.T., Buchhalter, J.R., Ding, D., Hesdorffer, D.C., Hauser, W.A., Kazis, L., Kobau, R., et al.: Standards for epidemiologic studies and surveillance of epilepsy. *Epilepsia* **52**, 2–26 (2011)
2. Engel, J.: A greater role for surgical treatment of epilepsy: why and when? *Epilepsy Curr.* **3**(2), 37–40 (2003)
3. Castaño-Candamil, S., Höhne, J., Martínez-Vargas, J.D., An, X.W., Castellanos-Domínguez, G., Haufe, S.: Solving the EEG inverse problem based on space–time–frequency structured sparsity constraints. *NeuroImage* **118**, 598–612 (2015). Sep
4. Garlapati, R.R., Roy, A., Joldes, G.R., Wittek, A., Mostayed, A., Doyle, B., Warfield, S.K., Kikinis, R., Knuckey, N., Bunt, S., et al.: More accurate neuronavigation data provided by biomechanical modeling instead of rigid registration. *J. Neurosurg.* **120**(6), 1477–1483 (2014)
5. Miller, K., Horton, A., Joldes, G.R., Wittek, A.: Beyond finite elements: a comprehensive, patient-specific neurosurgical simulation utilizing a meshless method. *J. Biomech.* **45**(15), 2698–2701 (2012)
6. Miller, K., Joldes, G.R., Bourantas, G., Warfield, S.K., Hyde, D.E., Kikinis, R., Wittek, A.: Biomechanical modeling and computer simulation of the brain during neurosurgery. *Int. J. Numer. Methods Biomed. Eng.* **35**(10), e3250 (2019)

7. Mostayed, A., Garlapati, R.R., Joldes, G.R., Wittek, A., Roy, A., Kikinis, R., Warfield, S.K., Miller, K.: Biomechanical model as a registration tool for image-guided neurosurgery: evaluation against b-spline registration. *Ann. Biomed. Eng.* **41**(11), 2409–2425 (2013)
8. Wittek, A., Miller, K., Kikinis, R., Warfield, S.K.: Patient-specific model of brain deformation: application to medical image registration. *J. Biomech.* **40**(4), 919–929 (2007)
9. Wittek, A., Hawkins, T., Miller, K.: On the unimportance of constitutive models in computing brain deformation for image-guided surgery. *Biomech. Model. Mechanobiol.* **8**, 77–84 (2009)
10. Wittek, A., Joldes, G., Couton, M., Warfield, S.K., Miller, K.: Patient-specific non-linear finite element modelling for predicting soft organ deformation in real-time; application to non-rigid neuroimage registration. *Prog. Biophys. Mol. Biol.* **103**, 292–303 (2010)
11. Drechsler, F., Wolters, C.H., Dierkes, T., Si, H., Grasedyck, L.: A full subtraction approach for finite element method based source analysis using constrained delaunay tetrahedralisation. *NeuroImage* **46**(4), 1055–1065 (2009). Jul
12. Marin, G., Guerin, C., Baillet, S., Garnero, L., Meunier, G.: Influence of skull anisotropy for the forward and inverse problem in EEG: simulation studies using FEM on realistic head models. *Hum. Brain Mapp.* **6**(4), 250–269 (1998)
13. Pursiainen, S., Sorrentino, A., Campi, C., Piana, M.: Forward simulation and inverse dipole localization with the lowest order Raviart–Thomas elements for electroencephalography. *Inverse Prob.* **27**(4), 045003 (2011). Mar
14. Schimpf, P.H., Ramon, C., Haueisen, J.: Dipole models for the EEG and MEG. *IEEE Trans. Biomed. Eng.* **49**(5), 409–418 (2002). May
15. Cook, M.J.D., Koles, Z.J.: A high-resolution anisotropic finite-volume head model for EEG source analysis. In: 2006 International Conference of the IEEE Engineering in Medicine and Biology Society. pp. 4536–4539 (Aug 2006)
16. Bourantas, G.C., Zwick, B.F., Warfield, S.K., Hyde, D.E., Wittek, A., Miller, K.: A Flux-Conservative Finite Difference Scheme for Anisotropic Bioelectric Problems. In: Miller, K., Wittek, A., Joldes, G.R., Nash, M.P., Nielsen, P.M.F. (eds.) *Computational Biomechanics for Medicine*, pp. 135–146. Springer International Publishing, Cham (2020)
17. Hyde, D.E., Duffy, F.H., Warfield, S.K.: Anisotropic partial volume CSF modeling for EEG source localization. *NeuroImage* **62**(3), 2161–2170 (2012). Sep
18. Saleheen, H., Ng, K.: New finite difference formulations for general inhomogeneous anisotropic bioelectric problems. *IEEE Trans. Biomed. Eng.* **44**(9), 800–809 (1997). Sep
19. Wendel, K., Narra, N.G., Hannula, M., Kauppinen, P., Malmivuo, J.: The influence of CSF on EEG sensitivity distributions of multilayered head models. *IEEE Trans. Biomed. Eng.* **55**(4), 1454–1456 (2008). Apr
20. Acar, Z.A., Makeig, S.: Neuroelectromagnetic forward head modeling toolbox. *J. Neurosci. Methods* **190**(2), 258–270 (2010). Jul
21. Meijs, J., Weier, O., Peters, M., Van Oosterom, A.: On the numerical accuracy of the boundary element method (EEG application). *IEEE Trans. Biomed. Eng.* **36**(10), 1038–1049 (1989). Oct
22. Stenroos, M., Sarvas, J.: Bioelectromagnetic forward problem: isolated source approach revis(it)ed. *Phys. Med. Biol.* **57**(11), 3517–3535 (2012). May
23. Zwick, B.F., Bourantas, G.C., Safdar, S., Joldes, G.R., Hyde, D.E., Warfield, S.K., Wittek, A., Miller, K.: Patient-specific solution of the electrocorticography forward problem in deforming brain. *NeuroImage* **263**, 119649 (2022). <http://arxiv.org/abs/2109.07164>. <https://doi.org/10.1016/j.neuroimage.2022.119649>
24. Safdar, S., Zwick, B., Bourantas, G., Joldes, G., Warfield, S.K., Hyde, D.E., Wittek, A., Miller, K.: Automatic framework for patient-specific biomechanical computations of organ deformation: an epilepsy (eeg) case study. In: *Computational Biomechanics for Medicine—Towards translation and better patient outcomes*. Springer, Berlin (2022)
25. Safdar, S., Joldes, G., Zwick, B., Bourantas, G., Kikinis, R., Wittek, A., Miller, K.: *Automatic Framework for Patient-Specific Biomechanical Computations of Organ Deformation*, pp. 3–16. Springer, Berlin (2021)
26. Yu, Y., Safdar, S., Bourantas, G., Zwick, B., Joldes, G., Kapur, T., Frisken, S., Kikinis, R., Nabavi, A., Golby, A., et al.: Automatic framework for patient-specific modelling of tumour resection-induced brain shift. *Comput. Biol. Med.* 105271 (2022)

27. Hämäläinen, M., Hari, R., Ilmoniemi, R.J., Knuutila, J., Lounasmaa, O.V.: Magnetoencephalography-theory, instrumentation, and applications to noninvasive studies of the working human brain. *Rev. Mod. Phys.* **65**(2), 413 (1993)
28. Brette, R., Destexhe, A.: *Handbook of neural activity measurement*. Cambridge University Press (2012)
29. Hallez, H., Vanrumste, B., Grech, R., Muscat, J., De Clercq, W., Vergult, A., D'Asseler, Y., Camilleri, K.P., Fabri, S.G., Van Huffel, S., Lemahieu, I.: Review on solving the forward problem in EEG source analysis. *J. NeuroEng. Rehabil.* **4**(1), 46 (2007). Nov
30. Dale, A.M., Fischl, B., Sereno, M.I.: Cortical surface-based analysis: i segmentation and surface reconstruction. *NeuroImage* **9**(2), 179–194 (1999). Feb
31. Ségonne, F., Dale, A.M., Busa, E., Glessner, M., Salat, D., Hahn, H.K., Fischl, B.: A hybrid approach to the skull stripping problem in mri. *NeuroImage* **22**(3), 1060–1075 (2004)
32. Fedorov, A., Beichel, R., Kalpathy Cramer, J., Finet, J., Fillion Robin, J.C., Pujol, S., Bauer, C., Jennings, D., Fennessy, F., Sonka, M., Buatti, J., Aylward, S., Miller, J., Pieper, S., Kikinis, R.: 3D slicer as an image computing platform for the quantitative imaging network. *Magn. Reson. Imaging* **30**(9), 1323–41 (2012)
33. Johnson, H., Harris, G., Williams, K., et al.: Brainsfit: mutual information rigid registrations of whole-brain 3d images, using the insight toolkit. *Insight J.* **57**(1), 1–10 (2007)
34. Pinter, C., Lasso, A., Fichtinger, G.: Polymorph segmentation representation for medical image computing. *Comput. Methods Programs Biomed.* **171**, 19–26 (2019)
35. Sullivan, C., Kaszynski, A.: PyVista: 3D plotting and mesh analysis through a streamlined interface for the visualization toolkit (VTK). *J. Open Source Softw.* **4**(37), 1450 (2019)
36. Valette, S., Chassery, J.M., Prost, R.: Generic remeshing of 3d triangular meshes with metric-dependent discrete voronoi diagrams. *IEEE Trans. Visual. Comput. Graph.* **14**(2), 369–381 (2008)
37. Vorwerk, J., Cho, J.H., Rampp, S., Hamer, H., Knösche, T.R., Wolters, C.H.: A guideline for head volume conductor modeling in EEG and MEG. *NeuroImage* **100**, 590–607 (2014). Oct
38. Tuch, D.S., Wedeen, V.J., Dale, A.M., George, J.S., Belliveau, J.W.: Conductivity tensor mapping of the human brain using diffusion tensor MRI. *Proc. Nat. Acad. Sci.* **98**(20), 11697–11701 (2001). Sep
39. Anderson, R., Andrej, J., Barker, A., Bramwell, J., Camier, J.S., Cerveny, J., Dobrev, V., Dudouit, Y., Fisher, A., Kolev, T., et al.: Mfem: a modular finite element methods library. *Comput. Math. Appl.* **81**, 42–74 (2021)
40. Wolters, C.H., Anwander, A., Berti, G., Hartmann, U.: Geometry-adapted hexahedral meshes improve accuracy of finite-element-method-based EEG source analysis. *IEEE Trans. Biomed. Eng.* **54**(8), 1446–1453 (2007). Aug
41. Rullmann, M., Anwander, A., Dannhauer, M., Warfield, S.K., Duffy, F.H., Wolters, C.H.: EEG source analysis of epileptiform activity using a 1 mm anisotropic hexahedra finite element head model. *NeuroImage* **44**(2), 399–410 (2009). Jan
42. Anderson, R., Andrej, J., Barker, A., Bramwell, J., Camier, J.S., Cerveny, J., Dobrev, V., Dudouit, Y., Fisher, A., Kolev, T., Pazner, W., Stowell, M., Tomov, V., Akkerman, I., Dahm, J., Medina, D., Zampini, S.: MFEM: a modular finite element methods library. *Comput. Math. Appl.* (Jul 2020)

Solid Biomechanics

Rapid Prediction of Breast Biomechanics Under Gravity Loading Using Surrogate Machine Learning Models



Max Dang Vu, Gonzalo D. Maso Talou, Huidong Bai, Poul M. F. Nielsen, Martyn P. Nash, and Thiranja Prasad Babarenda Gamage

Abstract Identifying and localising breast tumours is challenging due to differing patient positions between clinical examination and treatment procedures. Individual-specific, physics-driven models of the breast can help clinicians track and co-locate information between medical images acquired from different modalities but are unsuitable for real-time intervention. We present a surrogate machine learning model that predicts the breast's mechanical behaviour under gravity loading in near real time. Synthetic data was generated from a physics-driven finite element (FE) model simulating material point displacements \mathbf{d} of the breast, using a reference geometry and combinations of a constitutive material parameter C_1 and the relative orientation of the breast with respect to gravity \mathbf{g} . The best-trained surrogate model produced an error of $0.13 \text{ mm} \pm 0.03 \text{ mm}$ with respect to the L_2 -norm of the FE model's displacement field in model validation. This model can predict the material point displacement of the breast in clinically relevant positions (e.g. prone and supine) with a maximum root mean squared error of 1.04 mm (SD 1.08 mm). The computations took around $2.0\text{--}2.1 \text{ s}$, up to 82.5 times faster than the equivalent FE models on a CPU. The proposed approach is therefore promising for developing augmented reality tools to aid with real-time clinical navigation of soft tissues.

Keywords Surrogate modelling · Breast biomechanics · Large deformation mechanics · Machine learning · Neural networks

M. Dang Vu · G. D. Maso Talou · H. Bai · P. M. F. Nielsen · M. P. Nash · T. P. Babarenda Gamage (✉)
Auckland Bioengineering Institute, University of Auckland, Auckland, New Zealand
e-mail: psam012@aucklanduni.ac.nz

P. M. F. Nielsen · M. P. Nash
Department of Engineering Science, University of Auckland, Auckland, New Zealand

1 Introduction

Approximately 2.3 million women are diagnosed with breast cancer, and another 685,000 women die from the disease annually [1]. Early detection and removal of tumours help improve patient outcomes [2]. Tumour positions are identified and analysed across medical images acquired from X-ray mammography, magnetic resonance imaging (MRI), and second-look ultrasound (US) (Fig. 1). However, patient position differs between these imaging modalities and treatment, complicating the matching and localisation of lesions, limiting successful tumour removal. In such cases, patients undergo re-operation which ranges from 19 to 22% of patients who underwent breast-conserving surgery in New Zealand [3, 4] and across the world [5–8]. Re-operation is associated with increased morbidity, treatment duration, cost of care, and worsened cosmetic outcomes [5].

Such clinical challenges have motivated the development of physics-driven computational models to track and collocate lesions during procedures accurately and efficiently. These models use the finite element method (FEM) to predict breast tissue deformation from prone (position in MRI) to supine (position in surgery) under gravity loading [9–11]. However, this approach is computationally expensive for simulating large nonlinear deformations [12]. State-of-the-art FE breast models take at least 30 s to solve [13], which makes clinical translation difficult.

We have developed a surrogate modelling framework for cardiac mechanics to avoid the need for retraining [14]. An intrinsic learning domain was created using diffeomorphic mapping to preserve the geometry’s topology, ensuring that the surrogate model was application agnostic. The validated model, trained using Siamese neural networks, took 0.7 s to predict the left ventricular displacement during passive filling (62 times faster than the FE model) and approximately 9 s to estimate one constitutive parameter of the model [15]. This work documents the application of this surrogate modelling framework to rapidly predict the material point displacement of a personalised breast biomechanical model subjected to gravity loading in multiple orientations, which represents patient positioning. Note that material point



Fig. 1 Breast cancer diagnostic images acquired using **a** mammography in the standing position, followed by **b** MRI in the prone position and **c** US in the supine-tilted position. Image a (monkey business—stock.adobe.com), Image b (siemens.com/press), Image c (Luisandres—stock.adobe.com)

displacement refers to the displacement of nodes in a FE model and their equivalents in the surrogate model.

The manuscript is structured as follows. Section 2 details the development of the surrogate model and the training and performance evaluation results. Section 3 presents the predicted material displacements and the surrogate model's accuracy and efficiency compared to the equivalent FE model results. Section 4 discusses the findings and the surrogate model's future developments. Section 5 provides concluding remarks.

2 Methods

This section presents a sequential modelling framework (see Fig. 2) to generate and benchmark surrogate models using a physics model of the breast. Ground truth data for training the surrogate model was obtained from a FE model of the breast under gravity loading implemented in OpenCMISS [11, 17].

The geometry of the physics model was segmented from the prone T2-weighted MR image of a healthy 49-year-old volunteer at the University of Auckland's Centre for Advanced Magnetic Resonance Imaging (CAMRI). The breast geometry in the undeformed state was estimated from this prone-loaded geometry using methods described in [18]. The undeformed geometry was then discretised into a FE mesh containing cubic Lagrange elements for the simulation (Fig. 3) [19].

The FE model assumes that breast tissue is incompressible, isotropic, and homogeneous and has a material density of 900 kg m^{-3} [9, 16, 20]. The mechanical behaviour of breast tissues was simulated using a neo-Hookean hyperelastic strain energy function $W = C_1 (I_1 - 3)$, where C_1 is the constitutive material parameter and I_1 is the first invariant of the right Cauchy-Green deformation tensor [21]. Homogeneous Dirichlet boundary conditions were applied on the outer rib boundary to approximate the rigid attachment between the breast and the anterior chest wall [22, 23].

Synthetic breast displacement data $\mathbf{d} = [dx, dy, dz]$ was generated from the FE model using a reference geometry (with coordinates x, y, z), a value of C_1 and

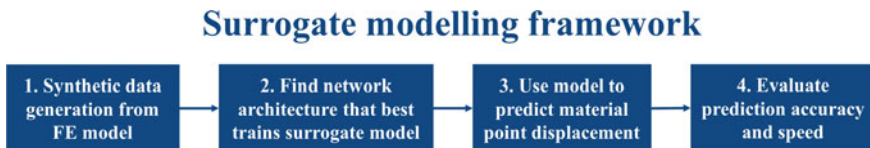


Fig. 2 Several surrogate models were trained using synthetic ground truth data from a FE model that simulates the material point displacement of the breast for a given constitutive material parameter, orientation with respect to gravity, and reference geometry. Several network architectures were used for training. The network that yielded the surrogate model with the lowest validation error with respect to the L_2 -norm of the FE model's displacement field was selected for training. This model's prediction accuracy and runtime compared to the FE model were evaluated to assess its performance

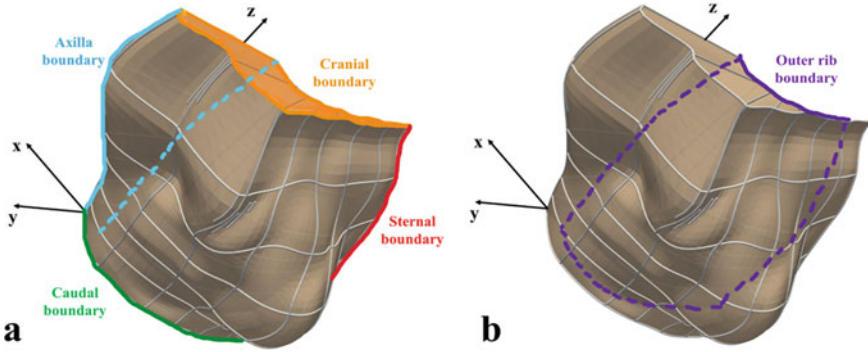


Fig. 3 **a** Breast model was segmented from the anatomical model of a torso, and the cranial, caudal, sternal, and axilla surfaces were defined as the model boundaries. **b** The breast geometry is the FE domain of interest, and the outer rib boundary is the posterior surface of the breast [19]

the orientation of the gravity body force ($\mathbf{g} = [g_x, g_y, g_z]$) in m s^{-2} . \mathbf{g} is defined in spherical coordinates as, $([g_x, g_y, g_z] = 9.81[\cos \Phi, \sin \Phi \cos \theta, \sin \Phi \sin \theta])$, where r is the magnitude (9.81 ms^{-2}), Φ is the elevation angle, and θ is the azimuth angle (Fig. 4). Six hundred and eighty-eight mechanical set-ups were evaluated using the FE model, and each sampled 3545 material points in the domain, yielding a total of 2,438,960 samples for the data set (Table 1). These samples were partitioned as 80% for training, 10% for testing, and 10% for validating the surrogate model.

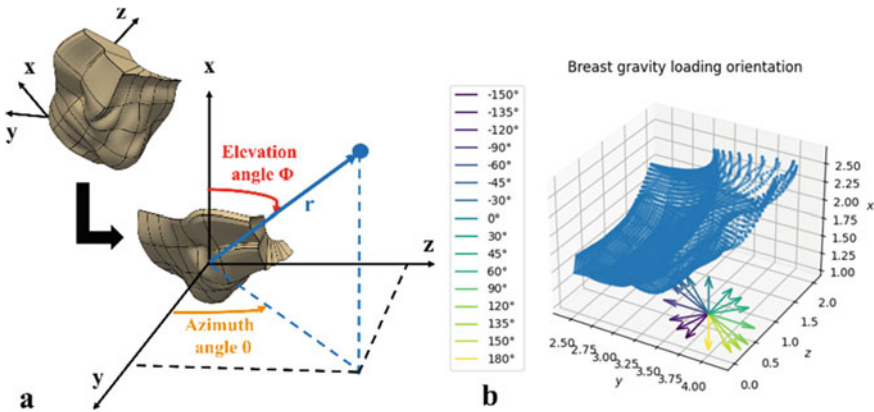


Fig. 4 **a** Orientation of gravity \mathbf{g} with respect to the breast was defined in spherical coordinates. The combination of $\Phi = 0^\circ$ and $\theta = 0^\circ$ represents the gravity body force orientation on the breast in the supine position, while $\Phi = 180^\circ$ and $\theta = 0^\circ$ represent the gravity body force orientation on the breast in the prone position. **b** The arrows indicate the \mathbf{g} orientation where Φ varies between -150° and 180° , and θ was fixed at 0° to simulate the torso rotation about the craniocaudal (z) axis direction. Note that the breast model point cloud has been down sampled 100 times for illustration purposes in this figure

Table 1 Sampling of the mechanical parameters used to generate the synthetic data set

Parameter	Step	Range	Samples
C_1 (kPa)	0.1	[0.8, 5.0]	43
Φ (degrees, °)	Variable	[- 150, 180]	16

The surrogate model was trained using a Siamese neural network [24] and implemented using TensorFlow v2.1 [25]. One network trains the domain nodes (non-boundary nodes) to predict the material point displacement, while the other trains the boundary nodes to enforce the Dirichlet boundary condition. The network architecture consists of hidden dense layers containing neurons and a single final output layer. All neurons are connected to those on the successive layer to increase the network's capacity. The output layer has three neurons to predict dx , dy , and dz , respectively. The error between the ground truth data set and the surrogate prediction is computed using a loss function L that combines the L^2 -norm error of the domain and boundary networks. $L = \sum_{u_d \in B_d} \|u_d - \hat{u}_d\|_2 + \alpha \sum_{u_b \in B_b} \|u_b - \hat{u}_b\|_2$, where u is the predicted displacement, \hat{u} is the FE model displacement, B is a set of points in the domain or boundary, and the subindices b and d denote points on the boundary or the domain, respectively. A penalisation factor α applied on the boundary network helps to enforce the boundary conditions. Weights of the trained network are obtained when the loss function is minimised.

The network was trained using the ADAM algorithm [26] with network weights of 0.5 and 0.9, respectively, a learning rate of 0.01 and a batch size of 8000 samples during 200 epochs at maximum. A patience parameter of 20 stops training when the validation loss function does not improve after 20 epochs. The network was trained with nine different architectures to investigate the sensitivity of training accuracy to network architecture. These networks contain 2, 3, and 4 identical layers with 32, 64, and 128 neurons each. The network architecture with the lowest error (or loss function output) during validation was selected as the best-trained network for further training of the surrogate model.

The trained and validated surrogate model was used to predict the material point displacement of presented cases. The prediction error was quantified using the root mean squared (RMS) error $\varepsilon = \frac{\sum_{i=1}^N \sqrt{(u_{i,x} - \hat{u}_{i,x})^2 + (u_{i,y} - \hat{u}_{i,y})^2 + (u_{i,z} - \hat{u}_{i,z})^2}}{N}$ between the FE model results and the surrogate model predictions over N sampled points on both models. Secondly, the prediction speed of the surrogate model was compared against the solution time for the FE model using the average wall clock time, and the distribution of such times over repeated experiments was analysed.

3 Results

Here, we showcase (1) the neural network architecture that best trained a surrogate model using synthetic data from the FE model; (2) how accurately this surrogate model predicted the material point displacements compared to the synthetic data; and (3) the relative times taken to perform the task.

The surrogate model was trained using nine different Siamese neural network architectures to find the network that achieved the lowest prediction error (see Table 2). The model was trained five times with each architecture on an NVIDIA Tesla V100 GPU. The mean and standard deviation of validation error was reported, alongside the training time for each architecture. Preliminary findings show that the best-ranked surrogate model was trained with a network architecture of three hidden layers and 32 neurons per layer (lowest validation error of $0.13 \text{ mm} \pm 0.03 \text{ mm}$), and model training took approximately $3155 \text{ s} \pm 60 \text{ s}$ (between 51 and 54 min).

We used the best-trained surrogate model to predict material displacements of the breast for clinically relevant positions, i.e. gravity body force orientations representing the prone and supine patient positions. Figure 5 demonstrates the ability of the surrogate model to predict material point displacements for a breast under gravity loading in these two positions. We used C_1 values of 1.0 and 5.0 kPa to demonstrate the model's ability to predict a variety of nonlinear deformation fields and the associated prediction errors. These predictions are compared quantitatively to the FE model results in Table 3. Compared to supine, the surrogate model's performance seems to improve with large C_1 values and gravity loading in prone. The prediction that incurred the largest possible error (RMS error of 1.04 mm [SD 1.08 mm]) was the 1.0 kPa case with the breast under gravity loading in supine.

The FE and surrogate models were executed using an 11th Gen Intel Core i7 CPU at 2.30 GHz. As shown in Table 4, the surrogate models were approximately 70–82.5 times faster than the FE framework for simulating breast deformations for the soft models ($C_1 = 1.0 \text{ kPa}$) and about 37–41 times faster for stiff models ($C_1 = 5.0 \text{ kPa}$).

Table 2 Prediction errors of surrogate models trained using Siamese neural networks with a varying number of hidden layers and neurons per hidden layer

Architecture (layers \times n_i)	Mean \pm SD validation error (mm)	Mean \pm SD training time (s)
2 \times 32	0.31 \pm 0.06	2663 \pm 110
2 \times 64	0.21 \pm 0.06	2632 \pm 98
2 \times 128	0.27 \pm 0.10	2715 \pm 105
3 \times 32	0.13 \pm 0.03	3155 \pm 60
3 \times 64	1.27 \pm 0.26	1171 \pm 168
3 \times 128	1.43 \pm 0.60	1414 \pm 982
4 \times 32	1.15 \pm 0.56	1842 \pm 1051
4 \times 64	0.92 \pm 0.77	2420 \pm 1175
4 \times 128	1.14 \pm 0.19	1390 \pm 164

4 Discussion

This manuscript presents the development and training of a surrogate model to predict breast tissue displacement under different orientations with respect to gravity. We generated synthetic data using a physics-based FE model of the breast implemented in OpenCMISS and used these data to train, test, and evaluate the surrogate modelling approach. We analysed 688 biomechanical FE models of the breast,

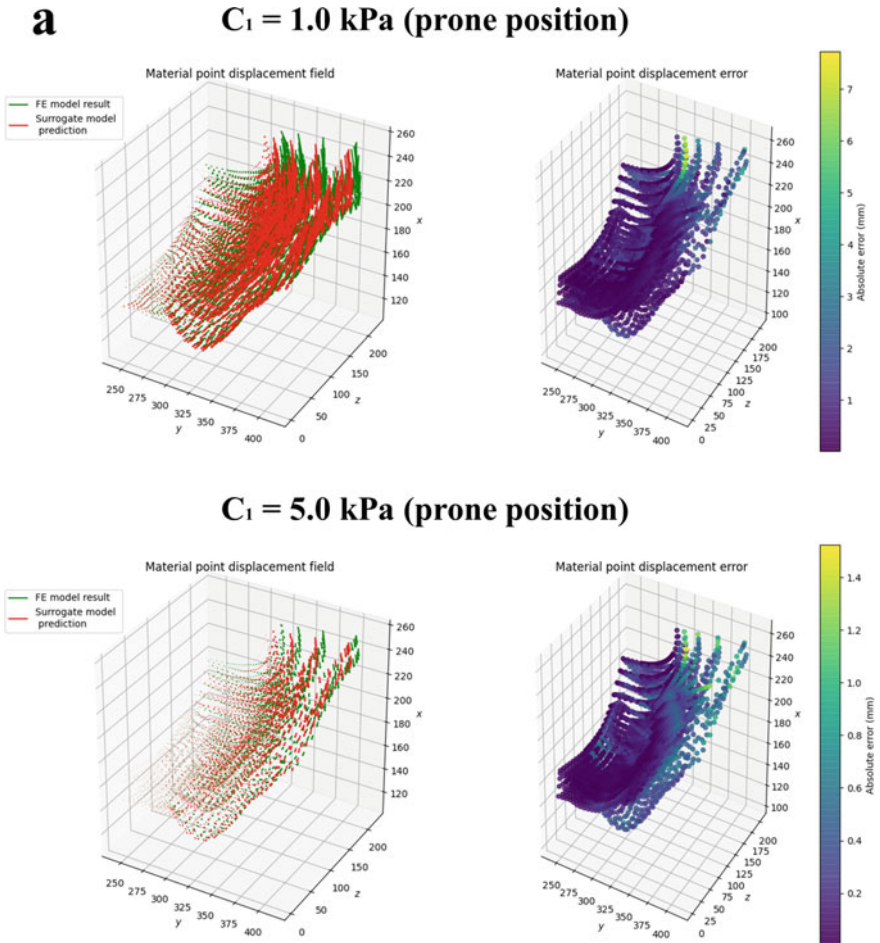
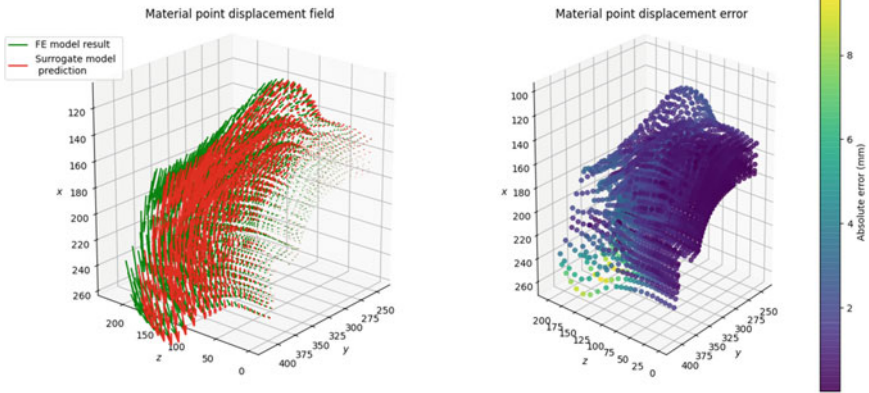
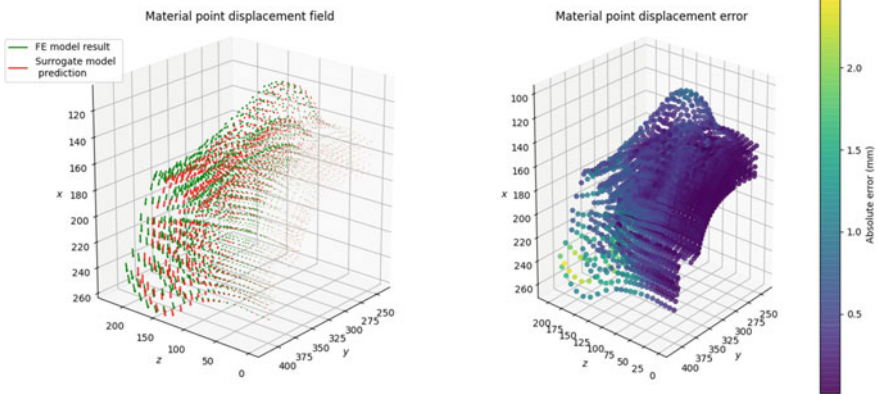


Fig. 5 Material point displacement field prediction and RMS error with C_1 values of 1.0 and 5.0 kPa for breast models in the **a** prone and **b** supine orientations. The surrogate model’s predictions incurred smaller errors at the outer rib boundaries and the areas surrounding the nipple and were more prominent for the softer models with $C_1 = 1.0$ kPa. The largest prediction errors were located around the shoulder regions (maximum error of 7.73 mm in the prone orientation for 1.0 kPa. and 9.50 mm in the supine orientation for 1.0 kPa)

b **$C_1 = 1.0$ kPa (supine position)** **$C_1 = 5.0$ kPa (supine position)****Fig. 5** (continued)

with different material parameters and gravity body force orientations, yielding ~ 2.4 million samples. We chose $C_1 \in [0.8, 5.0]$ kPa at 0.1 kPa intervals, as the FE model underwent significant deformations in this range. The elevation angles, Φ , of the gravity body force vector were sampled between -150° and 180° to represent rotations about the craniocaudal axis, with sample points that were clustered about the poles ($\Phi = 0^\circ, 180^\circ$) and comparatively sparse about the equator ($\Phi = \pm 90^\circ$) of a unit sphere [27] (Fig. 4b). Future work could consider setting the probability of placing an arbitrary point proportional to the region's area on the circular cross section to place more points around the equator [28].

We reported errors observed during validation for surrogate models trained using the nine architectures reported in Maso Talou's study [14]. In that case, a 4×64 architecture achieved the lowest error ($0.044 \text{ mm} \pm 0.029 \text{ mm}$), whereas in the

Table 3 Mean displacements and displacement ranges for the prone and supine orientations computed using the FE and surrogate models

Model	Metrics	Prone orientation		Supine orientation	
		$C_1 = 1.0$ kPa	$C_1 = 5.0$ kPa	$C_1 = 1.0$ kPa	$C_1 = 5.0$ kPa
FE	Mean displacement (mm)	3.21	0.62	3.16	0.62
	Displacement range (mm)	[0, 37.2]	[0, 7.2]	[0, 38.4]	[0, 7.3]
Surrogate	Mean displacement (mm)	3.0	0.58	2.6	0.42
	RMSE \pm SD (mm)	0.70 ± 0.68	0.19 ± 0.18	1.04 ± 1.08	0.30 ± 0.29
	Displacement range (mm)	[0.01, 35.7]	[0.01, 7.3]	[0.00, 36.2]	[0.01, 6.7]

The RMS errors for the surrogate model predictions (compared to the FE models) are also reported to showcase the ranges of errors involved

Table 4 Average wall clock time for solving breast models with C_1 values of 1.0 and 5.0 kPa in the prone and supine positions

Model	Prone simulation time (s)		Supine simulation time (s)	
	$C_1 = 1.0$ kPa	$C_1 = 5.0$ kPa	$C_1 = 1.0$ kPa	$C_1 = 5.0$ kPa
FE	154 ± 11	80.0 ± 1.7	152 ± 4	82.6 ± 1.6
Surrogate	2.02 ± 0.02	2.06 ± 0.03	2.02 ± 0.01	2.08 ± 0.03

present study, a 3×32 architecture performed best ($0.13 \text{ mm} \pm 0.03 \text{ mm}$) (Table 2). Using a wider, deeper network may have led to overtraining of the model, as variations in breast deformations due to variations in gravity loading are generally less complex than cardiac deformations, and the present study used significantly less training data than the cardiac problem (~ 6 million samples). To confirm this, the training step could be repeated by feeding more data to the network to test whether the higher-capacity networks can improve the training performance. We could also increase the number of epochs and the patience parameter to ensure comprehensive model training. An intrinsic breast domain for training has not yet been considered—we could consider using a rectangular domain for the breast topology to check for training performance improvement.

The surrogate model's prediction accuracy was better for the stiffer models (Table 3). The large nonlinear deformations for the soft breast models (maximum of 37.2 mm for C_1 of 1.0 kPa) were computationally expensive and challenging to solve with the FE model. Nevertheless, the surrogate modelling prediction errors were within an average of 1.04 mm (SD 1.08 mm) of the FE model results, which is promising for such large deformations. Similarly to Martinez-Martinez [29], predictions of the proposed model fall within the 5 mm error range accepted clinically, whereas Mendizabal's validation studies on a breast phantom averaged a target registration

error of 6.2 mm [30]. The large prediction errors associated with the deformations in the shoulder region near the axilla boundary are a potential concern. Unlike previous works [22, 31], the axilla boundary was not fixed for the simulation as we assumed, for this study, that it does not significantly affect the deformation of the breast region. However, these errors are exaggerated for an extremely low C_1 and reduces as C_1 increases (Fig. 5).

The surrogate model was around 70–82.5 times faster at computing mechanics of the softer models than the FE model. The speed-up factor reduces to 37–41 times for the stiffer models, because surrogate models are time-insensitive to C_1 . In contrast, FE models are not (solving FE models with smaller C_1 values are generally more computationally intensive). The observed speed-up factors are comparable to [14], which produced surrogate model predictions 62 times faster than equivalent FE models. However, the cardiac model solved within 0.7 s, whereas these breast models took about 2.0–2.1 s. A possible reason for this was that training could be improved by gathering more data or using an intrinsic domain, as discussed earlier. Another contributing factor is that the surrogate cardiac model was executed on a GPU, not on a CPU like the breast model. The proposed surrogate model's speed is slower than similar studies of breast mechanics [29, 30]. However, it was noted that the previous models were designed for different loading conditions and used different machine learning techniques. To the best of our knowledge, no similar model has been implemented for gravity loading of the breast.

Future aims of this work involve estimating the constitutive parameters of the surrogate breast models rapidly and validating the framework using a silicone breast phantom under gravity loading. This will build on related studies for identifying the mechanical properties of soft materials [11, 32, 33]. These steps are essential for the development of a software platform [34] that integrates fast physics-driven biomechanical models with augmented reality technology [35, 36] and state-of-the-art visualisation techniques [37] to align diagnostic images with 3D holograms of biomechanical models. This platform aims to extend our automated breast cancer image analysis workflow [18] by providing clinicians with real-time navigational guidance during breast cancer imaging and treatment procedures (Fig. 6).

5 Conclusion

We presented a surrogate modelling framework that predicts the material point displacement of a personalised breast model under gravity loading and varying constitutive material parameters efficiently in about 2.0–2.1 s. The surrogate model was trained with 688 FE models representing different biomechanical set-ups and achieved errors of 0.13 mm \pm 0.03 mm compared to the FE model solutions. The surrogate models predictions were about 70–82.5 times faster than the FE model, and the maximum prediction errors averaged at only 1.04 mm (SD 1.08 mm) for soft

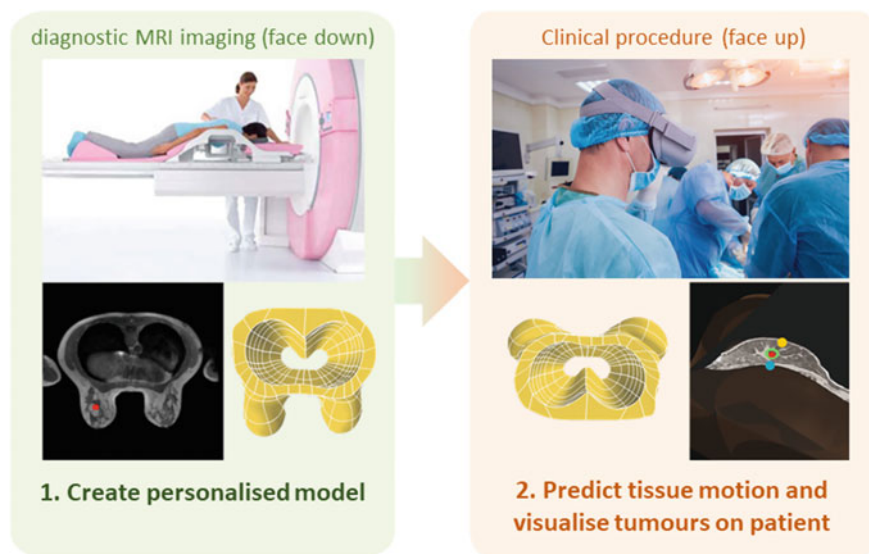


Fig. 6 Proposed augmented reality platform will leverage an automated clinical workflow for breast cancer image analysis. The workflow builds personalised biomechanical models of the breast from diagnostic MRI and visualises breast tissue deformation in near real time during clinical procedures performed in the supine position. Some images were obtained from Romaset—stock.adobe.com

models of the breast. This represents a promising development towards applying real-time, personalised biomechanical models to help improve breast cancer diagnosis and treatment practices.

Acknowledgements The authors are grateful for financial support from the New Zealand Government’s Ministry for Business, Innovation and Employment (UOAX1004), the New Zealand Breast Cancer Foundation (R1704), and the University of Auckland Foundation (F-IBE-BIP). Max Dang Vu is supported by a University of Auckland Doctoral Scholarship. We also thank Mr Stephen Creamer and Mr Chinchien Lin for their valuable contributions to this study.

References

1. Sung, H., et al.: Global cancer statistics 2020: GLOBOCAN estimates of incidence and mortality worldwide for 36 cancers in 185 countries. *CA Cancer J. Clin.* **71**(3), 209–249 (2021). <https://doi.org/10.3322/caac.21660>
2. Abrahimi, M.S., Elwood, M., Lawrenson, R., Campbell, I., Tin Tin, S.: Associated factors and survival outcomes for breast conserving surgery versus mastectomy among New Zealand women with early-stage breast cancer. *Int. J. Environ. Res. Public. Health* **18**(5), 2738 (2021). <https://doi.org/10.3390/ijerph18052738>
3. Ooi, C., Campbell, I., Kollias, J., de Silva, P.: National breast cancer audit: overview of invasive breast cancer in New Zealand. *N. Z. Med. J. Online* **125**(1359), 7–16 (2012)

4. Gautier, A., Harvey, V., Kleinsman, S., Knowlton, N., Lasham, A., Ramsaroop, R.: 30,000 Voices: Informing a Better Future for Breast Cancer in Aotearoa New Zealand. Breast Cancer Foundation National Register 2003–2020. Breast Cancer Foundation NZ (2022)
5. Tamburelli, F., et al.: Reoperation rate after breast conserving surgery as quality indicator in breast cancer treatment: a reappraisal. *Breast* **53**, 181–188 (2020). <https://doi.org/10.1016/j.breast.2020.07.008>
6. van Leeuwen, M.T., et al.: Reoperation after breast-conserving surgery for cancer in Australia: statewide cohort study of linked hospital data. *BMJ Open* **8**(4), e020858 (2018). <https://doi.org/10.1136/bmjopen-2017-020858>
7. Isaacs, A.J., Gemignani, M.L., Pusic, A., Sedrakyan, A.: Association of breast conservation surgery for cancer with 90-day re-operation rates in New York state. *JAMA Surg.* **151**(7), 648 (2016). <https://doi.org/10.1001/jamasurg.2015.5535>
8. Jeevan, R., et al.: Re-operation rates after breast conserving surgery for breast cancer among women in England: retrospective study of hospital episode statistics. *BMJ* **345**(Jul 12 2), e4505–e4505 (2012). <https://doi.org/10.1136/bmj.e4505>
9. Rajagopal, V., Chung, J.H., Bullivant, D., Nielsen, P.M.F., Nash, M.P.: Determining the finite elasticity reference state from a loaded configuration. *Int. J. Numer. Methods Eng.* **72**(12), 1434–1451 (2007). <https://doi.org/10.1002/nme.2045>
10. Lee, A.W.C.: Breast image fusion using biomechanics. PhD, The University of Auckland, Auckland Bioengineering Institute (2011)
11. Babarenda Gamage, T.P.: Constitutive parameter identifiability and the design of experiments for applications in breast biomechanics. PhD, The University of Auckland, Auckland Bioengineering Institute (2016)
12. Phellan, R., Hachem, B., Clin, J., Mac-Thiong, J.M., Duong, L.: Real-time biomechanics using the finite element method and machine learning: review and perspective. *Med. Phys.* **48**(1), 7–18 (2021). <https://doi.org/10.1002/mp.14602>
13. Han, L., et al.: A nonlinear biomechanical model based registration method for aligning prone and supine MR breast images. *IEEE Trans. Med. Imaging* **33**(3), 682–694 (2014). <https://doi.org/10.1109/TMI.2013.2294539>
14. Maso Talou, G.D., Babarenda Gamage, T.P., Sagar, M., Nash, M.P.: Deep learning over reduced intrinsic domains for efficient mechanics of the left ventricle. *Front. Phys.* **8**, 1–14 (2020). <https://doi.org/10.3389/fphy.2020.00030>
15. Maso Talou, G.D., Babarenda Gamage, T.P., Nash, M.P.: Efficient ventricular parameter estimation using AI-surrogate models. *Front. Physiol.* **12**(24), 1–14 (2021). doi: <https://doi.org/10.3389/fphys.2021.732351>
16. Chung, J.H., Rajagopal, V., Nielsen, P.M.F., Nash, M.P.: A biomechanical model of mammographic compressions. *Biomech. Model. Mechanobiol.* **7**(1), 43–52 (2008). <https://doi.org/10.1007/s10237-006-0074-6>
17. Bradley, C., et al.: OpenCMISS: a multi-physics & multi-scale computational infrastructure for the VPH/Physiome project. *Prog. Biophys. Mol. Biol.* **107**(1), 32–47 (2011). <https://doi.org/10.1016/j.pbiomolbio.2011.06.015>
18. Babarenda Gamage, T.P., et al.: An automated computational biomechanics workflow for improving breast cancer diagnosis and treatment. *Interf. Focus* **9**(4), 1–12 (2019). <https://doi.org/10.1098/rsfs.2019.0034>
19. Babarenda Gamage, T.P., Baluwala, H.Y., Nash, M.P., Nielsen, P.M.F.: Registration of prone and supine breast MRI for breast cancer treatment planning. In: Wittek, A., Joldes, G., Nielsen, P.M.F., Doyle, B.J., Miller, K. (eds.) *Computational Biomechanics for Medicine*, pp. 123–134. Springer International Publishing, Cham (2017). doi: https://doi.org/10.1007/978-3-319-54481-6_11
20. Babarenda Gamage, T.P., Rajagopal, V., Ehrgott, M., Nash, M.P., Nielsen, P.M.F.: Identification of mechanical properties of heterogeneous soft bodies using gravity loading. *Int. J. Numer. Methods Biomed. Eng.* **27**(4), 391–407 (2011). <https://doi.org/10.1002/cnm.1429>
21. Holzapfel, G.A.: *Nonlinear Solid Mechanics: A Continuum Approach for Engineering*, 1st ed. Wiley, Chichester, New York (2000)

22. Babarenda Gamage, T.P., Boyes, R., Rajagopal, V., Nielsen, P.M.F., Nash, M.P.: Modelling prone to supine breast deformation under gravity loading using heterogeneous finite element models. *Comput. Biomech. Med. Deform. Flow* 29–38 (2012). <https://doi.org/10.1007/978-1-4614-3172-5>
23. McGhee, D.E., Steele, J.R.: Breast biomechanics: what do we really know? *Physiology* **35**(2), 144–156 (2020). <https://doi.org/10.1152/physiol.00024.2019>
24. Chicco, D.: Siamese neural networks: an overview. In: Cartwright, H. (ed.) *Artificial Neural Networks*, vol. 2190, pp. 73–94. Springer, New York, NY (2021). https://doi.org/10.1007/978-1-0716-0826-5_3
25. Abadi, M., et al.: TensorFlow: A system for large-scale machine learning. In: 12th USENIX Symposium on Operating Systems Design and Implementation (OSDI 16), pp. 265–283. Savannah, GA, Nov. 2016. <https://www.usenix.org/conference/osdi16/technical-sessions/presentation/abadi>
26. Kingma, D.P., Lei Ba, J.: ADAM: a method for stochastic optimisation. *Int. Conf. Learn. Represent.* **3**, 1–15 (2015)
27. Weisstein, E.W.: Sphere point picking. In: *Sphere Point Picking—From MathWorld—A Wolfram Web Resource* (2002). <https://mathworld.wolfram.com/SpherePointPicking.html>
28. Deserno, M.: How to generate equidistributed points on the surface of a sphere. *Polym. Ed.* **99**(2) (2004). https://www.cmu.edu/biolphys/deserno/pdf/sphere_equi.pdf
29. Martínez-Martínez, F., et al.: A finite element-based machine learning approach for modeling the mechanical behavior of the breast tissues under compression in real-time. *Comput. Biol. Med.* **90**(September), 116–124 (2017). <https://doi.org/10.1016/j.compbiomed.2017.09.019>
30. Mendizabal, A., Tagliabue, E., Brunet, J.-N., Dall’Alba, D., Fiorini, P., Cotin, S.: Physics-based deep neural network for real-time lesion tracking in ultrasound-guided breast biopsy. *Comput. Biomech. Med.* 3–45 (2020). https://doi.org/10.1007/978-3-030-42428-2_4
31. Lee, A.W.C., Rajagopal, V., Babarenda Gamage, T.P., Doyle, A.J., Nielsen, P.M.F., Nash, M.P.: Breast lesion co-localisation between X-ray and MR images using finite element modelling. *Med. Image Anal.* **17**(8), 1256–1264 (2013). <https://doi.org/10.1016/j.media.2013.05.011>
32. Rajagopal, V.: Modelling breast tissue mechanics under gravity loading. PhD, Auckland Bioengineering Institute, The University of Auckland (2007)
33. Chung, J.-H.: Modelling mammographic mechanics. PhD, Auckland Bioengineering Institute, The University of Auckland (2008)
34. Dang Vu, M.: Pinpointing Breast Cancer From a Bioengineering Perspective, vol. 2, no. 1, pp. 5–8. University of Auckland Scientific (2022)
35. Gouveia, P.F., et al.: Breast cancer surgery with augmented reality. *Breast* **56**, 14–17 (2021). <https://doi.org/10.1016/j.breast.2021.01.004>
36. Perkins, S.L., Lin, M.A., Srinivasan, S., Wheeler, A.J., Hargreaves, B.A., Daniel, B.L.: A mixed-reality system for breast surgical planning. In: *Adjunct. Proc. 2017 IEEE Int. Symp. Mix. Augment. Real. ISMAR-Adjunct. 2017*, pp. 269–274 (2017). <https://doi.org/10.1109/ISMAR-Adjunct.2017.92>
37. Laven, R.: Markerless tracking of highly deformable objects. M.S., Auckland Bioengineering Institute, The University of Auckland (2021)

Effect of Analyst Segmentation Variability on Computed AAA Stress Distributions



Tim Hodge, Jasper C. Y. Tan, Paddy H. Koh, Eli Storer, Andy Huynh, Farah Alkhatib, Karol Miller, and Adam Wittek

Abstract Abdominal Aortic Aneurysms (AAA) are a symptomless condition and are common in the geriatric population (over 65 years old). It is imperative for clinicians to identify regions of the AAA with greatest risk of rupture as well as overall rupture risk. A more dependable, patient-specific approach based on computational biomechanics which could prove useful. This research paper aims to identify and evaluate the extent of analyst variability during semi-automatic segmentation providing the geometry for a model. We used patient data obtained from Fiona Stanley Hospital in Perth, Western Australia, in the form of CT images at 80% through the cardiac cycle. Individual segmentations were performed by four analysts of similar experience with a repeat segmentation conducted four weeks later. Segmentations by different analysts produced different stress results and therefore affected the rupture potential prediction. Segmentations by the same analyst were not exactly reproducible. We recommend more stringent guidelines to guide analysts while utilising an automated segmentation process by edge detection may also prove to be feasible.

Keywords Computational biomechanics · Computed tomography · Aneurysms · Segmentation variability · Principal stresses · Canny edges

1 Motivations

An Abdominal Aortic Aneurysm (AAA) is clinically defined as the permanent and irreversible dilation of the abdominal region in the descending aorta. Aneurysm names are characterised by their location, for this project we have investigated aneurysms originating below the renal arteries and are appropriately referred to as infra-renal AAA's which can be illustrated in Fig. 1. This cardiovascular disease is a symptomless condition that is often discovered by coincidence when undertaking other clinical scans such as bladder screening, ultra-sonographies, or other

T. Hodge · J. C. Y. Tan · P. H. Koh · E. Storer · A. Huynh · F. Alkhatib · K. Miller (✉) · A. Wittek
Intelligent Systems for Medicine Laboratory, The University of Western Australia, Perth, Australia
e-mail: karol.miller@uwa.edu.au

radiography tests. In many cases, the discovery only takes place after rupture has taken place; hence, it is given the nickname “The Silent Killer” [27]. Rupture of the aneurysm is lethal, and even with swift medical attention and surgical intervention, the long-term post-operative mortality rates remain high between 30 and 45% [6, 12]. On a global scale, AAA’s cause approximately 200,000 deaths per year highlighting its severity [20]. The disease is more likely to occur if you have a family history of cardiovascular conditions as well as the typical lifestyle related factors consisting of high cholesterol, elevated blood pressure, obesity as well as excessive alcohol and tobacco consumption [28]. Studies have determined that males are more susceptible to incidence; however, females have a higher risk of rupture [2, 28].

The current gold-standard AAA rupture risk assessment method involves maximum diameter and diameter growth rate [28]. These criteria prove to be unreliable, as AAAs with diameters smaller than 5.5 cm have been shown to rupture, with rates between 7 and 23% [5], while larger AAAs have remained stable [7, 11]. This poses an issue; these guidelines rely on a one size fits all approach which has little physiological basis, as patient-specific information is unaccounted for. This

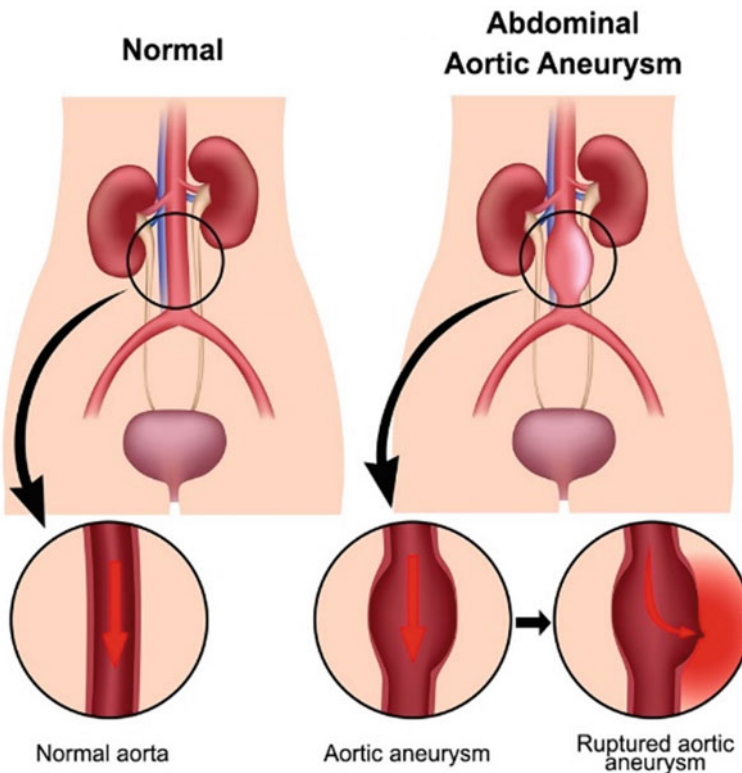


Fig. 1 Infra-renal AAA. Normal and healthy aorta (L). Dilated aortic aneurysm (R). Extracted from: [13]

points to the need for a more reliable indicator of AAA rupture risk that incorporates patient-specific biomechanics [15, 21, 22]. Our overall objective is to develop and verify a non-invasive, patient-specific biomechanics-based rupture risk assessment for AAA. It is these shortcomings associated with diameter-based assessments of AAAs that provided the initial motivations for this research direction.

This paper specifically aims to investigate and examine the effects of inter- and intra-analyst segmentation variability on the reproducibility of results from computational biomechanics models. To achieve this, a qualitative visual comparison with associated wall stress values will be observed.

2 Methods

Software utilised was constructed by Intelligent Systems for Medicine Laboratory (ISML) at The University of Western Australia, Biomechanics-based Prediction of Aneurysm Rupture Risk (BioPARR) [16] available from: <https://bioparr.mech.uwa.edu.au>.

2.1 Patient Demographic

The abdominal CT scan of one patient was obtained from Fiona Stanley Hospital in Perth, Western Australia for analysis. This CT scan was captured at 80% of the cardiac cycle, which corresponds to the diastolic phase in the abdominal aorta, as there is comparatively less noise in this portion. The patient's systolic and diastolic blood pressure was also recorded and will be used to calculate patient-specific mean arterial pressures (MAP). Ethical approvals were obtained from both Fiona Stanley Hospital and the University of Western Australia.

2.2 Image Segmentation

All image segmentations to extract the AAA wall geometry were performed in open source segmentation software, 3D Slicer [8]. Four analysts performed two segmentations each, with segmentations conducted four weeks apart. Stress analysis was performed on each geometry to assess intra- and inter-analyst differences in simulation results resulting from differences in segmentations. Semi-automatic segmentation process is detailed below.

ROI creation and lumen segmentation. We first defined the region of interest (ROI) of the AAA. This was achieved through cropping the CT images from the renal arteries to the iliac bifurcation. The voxels of this ROI were then made isotropic

at 0.625 mm to simplify smoothing. A threshold was applied to differentiate the lumen from surrounding tissue. As this threshold included areas of the spine and surrounding arteries, manual removal was required to ensure the label map only contained the aortic lumen. The resulting label map was Gaussian smoothed with a σ parameter of one.

AAA segmentation. The AAA including lumen was separated from the surrounding tissues through user-interpreted semi-automatic segmentation in the ROI. Using the Fast GrowCut [8] module in 3D Slicer, [8] an open-source medical image analysis package the AAA including lumen was separated from the surrounding tissues throughout the ROI. However, this model had some inaccuracies which had to be manually corrected to ensure the selected region is representative of the AAA. The resulting label map was Gaussian smoothed with an appropriate standard deviation, σ , of two to ensure the surface is optimal for the meshing algorithm without removing important AAA features.

AAA wall extraction. A blood masked label is created, which is the lumen label shrunk by four pixels. This blood masked label is subtracted from the AAA label previously created to obtain the AAA wall label. The resulting label is manually checked for errors and corrected. A 3D surface model of the AAA wall is created using the ModelMaker module in 3D Slicer, with 100 iterations of Laplacian smoothing and the decimate field set to 0.1. This model can be viewed in Paraview—an open source, multi-platform data analysis and visualisation application [3]. A visual process of this extraction can be seen in Fig. 2.

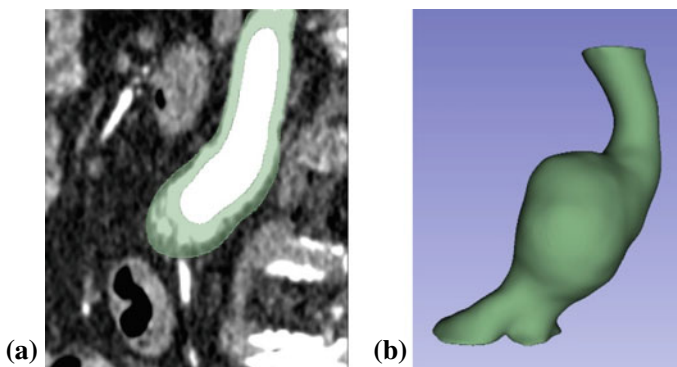


Fig. 2 AAA wall extraction—a CT image of AAA wall segmentation viewed in sagittal plane; **b** 3D label reconstruction of AAA wall. Viewed in 3D Slicer

2.3 Wall Thickness Specification

AAA wall thickness is an important factor affecting the stress magnitude within the wall. However, accurate determination of wall thickness from medical images remains problematic due to low image resolution and poor soft tissue contrast. Leading to inaccurate and unreliable wall thickness measurements from medical images. This is why previous authors utilised a constant AAA wall thickness in their studies [24, 26]. Therefore, a constant wall thickness of 1.5 mm is used here to ensure more reliable comparison of intra and inter-analyst segmentation differences on AAA wall stress. This constant wall thickness is applied by AAA rupture risk prediction software, BioPARR [16].

2.4 AAA Geometry Creation

The following steps are automated by BioPARR. The AAA surface model created in 3D Slicer contains elements of different sizes and poor aspect ratios, which will be problematic when creating the AAA wall and intraluminal thrombus (ILT) inner and outer surfaces. So, the surface mesh of the AAA model is re-meshed using mesh resampling software ACVDQ [25]. Then, a custom command line interface (CLI) 3D Slicer module is used to generate the AAA wall and ILT surfaces from the resampled geometry. The three surfaces generated are the external and internal AAA surface and the internal ILT surface. Thickness of the ILT is computed to ensure it has a minimum thickness of 1 mm. Local AAA wall and ILT thicknesses are used to compute the mesh element size ensuring the wall thickness can be represented by two layers of elements.

2.5 Mesh Generation for a Finite Element Model

Meshing of the AAA wall and ILT surfaces are performed using open source meshing software, Gmsh [10]. The surfaces are first meshed using the previously generated element size information. End surfaces are then generated between the external and internal AAA wall, and the internal AAA wall surface and ILT, to ensure that the surfaces of the geometry are closed and watertight. Using the previously generated element size information, a tetrahedral volumetric mesh is created throughout the geometry. Tetrahedral elements were selected as they well represent complex geometries, such as the bifurcations commonly found in AAAs. Very small tetrahedral elements are generated near the edges of the geometry to maintain geometry accuracy. While element size is increased in the thicker areas of the AAA wall and

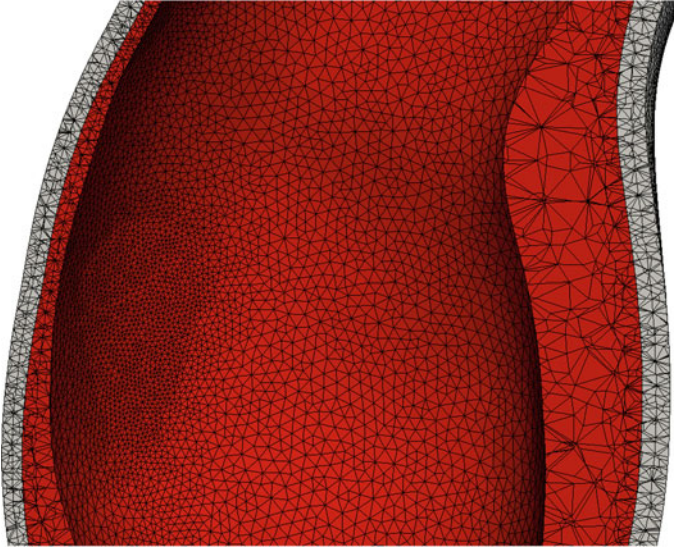


Fig. 3 Generated volume mesh with two layers of AAA wall. Minimum of two elements on ILT wall with larger element sizes inside ILT. Inner layer (red), outer layer (grey)

middle of the ILT to reduce element count and therefore computational cost of the finite element analysis. Figure 3 shows an example mesh which illustrates the range of element sizes encountered and its distribution.

2.6 *Finite Element Model Creation*

The previously created volumetric mesh files of the AAA wall and ILT are used to generate input files for commercial finite element software, Abaqus [1] called from within BioPARR, using a custom CLI 3D Slicer module. The input files contain the AAA wall and ILT meshes as parts, on which loads, and boundary conditions can be applied. Three loading scenarios are generated, which includes ILT pressure, wall pressure, and wall pressure with no ILT. These scenarios are represented in Fig. 4. Only results of the ILT pressure scenario will be presented, as this most closely resembles in vivo conditions. The load is the mean arterial pressure determined from patient-specific systolic and diastolic blood pressure. While the boundary conditions are that the AAA is tethered superiorly and inferiorly at the renal arteries and iliac bifurcation respectively to simulate in vivo conditions.

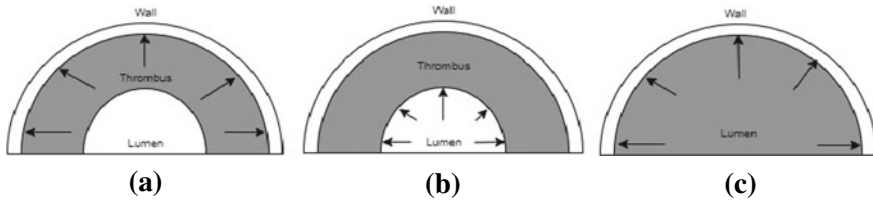


Fig. 4 Loading scenarios used in BioPARR pipeline **a** ILT pressure; **b** wall pressure; **c** no ILT

2.7 Finite Element Analysis

BioPARR calls on ABAQUS to perform finite element analysis of the previously created scenarios, following the procedure of Joldes et al. [15]. As the geometry extracted from the CT image is the AAA deformed under patient-specific blood pressure, the stress within the AAA wall balances the blood pressure load in that deformed configuration. Therefore, the computed stresses depend on geometry and load, but only very weakly on patient-specific wall material properties as demonstrated in Joldes et al. [15], Miller and Lu [18]. In essence, results of Joldes et al. [15], Miller and Lu [18] demonstrate that an AAA seen in a deformed configuration is approximately a statically determinate structure. This means the stress within the AAA wall balances the blood pressure load, while only being very weakly dependent on patient-specific wall material properties. BioPARR ensures the deformed AAA geometry is unchanged under realistic blood pressure load by specifying an aortic Young's modulus of 100 MPa.

Residual stress incorporation. According to the uniform stress hypothesis, residual stress arises from the continual remodelling of arteries and works to make stress distribution within the vessel wall more uniform under normal conditions [9]. To incorporate residual stresses, the previously extracted max principal stress is averaged over the AAA wall thickness [17]. This is performed for each node on the AAA wall surface to extract the max wall stress under the uniform stress hypothesis.

99th percentile max principal stress. After extraction of max principal wall stress, the 99th percentile max principal stress is calculated via MATLAB. The 99th percentile is an arbitrary number used to remove any inaccurate peak stresses due to meshing artefacts [23]. These 99th percentile values will be used to compare intra and inter-analyst variability.

2.8 *Evaluating Intra- and Inter-analyst Segmentation Variability*

To evaluate the differences in inter-analyst segmentation, all four analysts individually segmented one patient, as a control. The completed segmentations followed the same protocols defined in 2.2 to generate geometry and compute wall stresses. The maximum principal stress of each geometry is extracted, from which the peak and 99th percentile max principal stresses are computed and graphically visualised in MATLAB and Paraview. These stress values allow comparison of each geometry, its segmentation, and their effects on computed AAA wall stress, which may be clinically significant. Two sets of data per analyst was obtained, as each analyst performed the process four weeks apart. From these two sets of data per analyst, the intra-analyst segmentation variability and its effects on computed stress can be assessed. The segmentations were input to BioPARR to compute AAA wall stress. The wall stress was used as a metric to compare the effects of segmentation variability arising from the same analyst on the same patient.

3 Results

3.1 *Inter-analyst Segmentation*

Tables 1 and 2 present results of the patient from segmentations by four different analysts. The peak 99th percentile and average maximum principal stresses are presented along with the number of nodes per geometry. From these tables we can appreciate a difference of 0.125 MPa between the greatest and lowest 99th percentile maximum principal stresses. For segmentation 1, the 99th percentile stresses diverged from the average by 23.79% for E34, 34.28% for J34, 5.84% for P34 and 4.64% for T34. Interestingly from the percentile plots of Figs. 6 and 7, graphically, there is a larger spread of inter-analyst results in the first segmentation than is shown in the second segmentation. Figure 5 presents regions of high wall stress of the AAA, which are all localised to the same regions for all analysts. These regions of high stress are localised to the high curvature areas across all geometries despite their stress value differences.

3.2 *Intra-analyst Segmentation*

Between Tables 1 and 2 and Figs. 5, 6 and 7, we are also able to observe the results the two segmentations conducted four weeks apart. Peak 99th percentile and average maximum principal stresses are presented along with the number of nodes. The largest differences in 99th percentile stresses were of E34 and J34, of

Table 1 Peak 99th percentile and average maximum principal stresses of the first inter-analyst segmentations

Segmentation 1						
Analyst	Peak stress (MPa)	99th percentile stress		Average stress (MPa)	No. of nodes	
		Value (MPa)	Difference (%)		Value	Difference (%)
E34	0.4229	0.2669	23.79	0.1008	146,808	7.93
J34	0.2479	0.1417	-34.28	0.0691	145,892	7.26
P34	0.7766	0.2282	5.84	0.0696	101,252	-25.56
T34	0.3445	0.2256	4.64	0.0853	150,125	10.37
Average		0.2156			136,019	

Number of nodes contained in the geometry are also presented. Percentage differences are calculated relative to the means of each metric

Table 2 Peak 99th percentile and average maximum principal stresses of the second inter-analyst segmentations

Segmentation 2						
Analyst	Peak stress (MPa)	99th percentile stress		Average stress (MPa)	No. of nodes	
		Value (MPa)	Difference (%)		Value	Difference (%)
E34	0.2568	0.1416	-27.40	0.0691	145,663	6.44
J34	0.2253	0.1682	-13.77	0.0776	148,862	8.77
P34	0.6440	0.2548	30.63	0.0750	103,846	-24.12
T34	0.3627	0.2156	10.54	0.0845	149,042	8.91
Average		0.1951			136,853	

Number of nodes contained in the geometry are also presented. Percentage differences are calculated relative to the means of each metric

which decreased by 30.67% and 8.55%, respectively, while P34 and T34 only exhibited small relative stress differences at 5.51% and 2.27%, respectively. The stress percentile plots of Figs. 6 and 7 demonstrate similar patterns for distribution of wall stress over percentiles for all four analysts. However, E34 and J34 presented large stress differences in segmentation two compared to segmentation one, while P34 and T34 remained very similar. Figure 5 also illustrates that high stress locations remain the same for both segmentations of E34 and J34, while the stress magnitudes differ considerably. Alternatively, P34 and T34 exhibit similar stress locations and stress magnitudes.

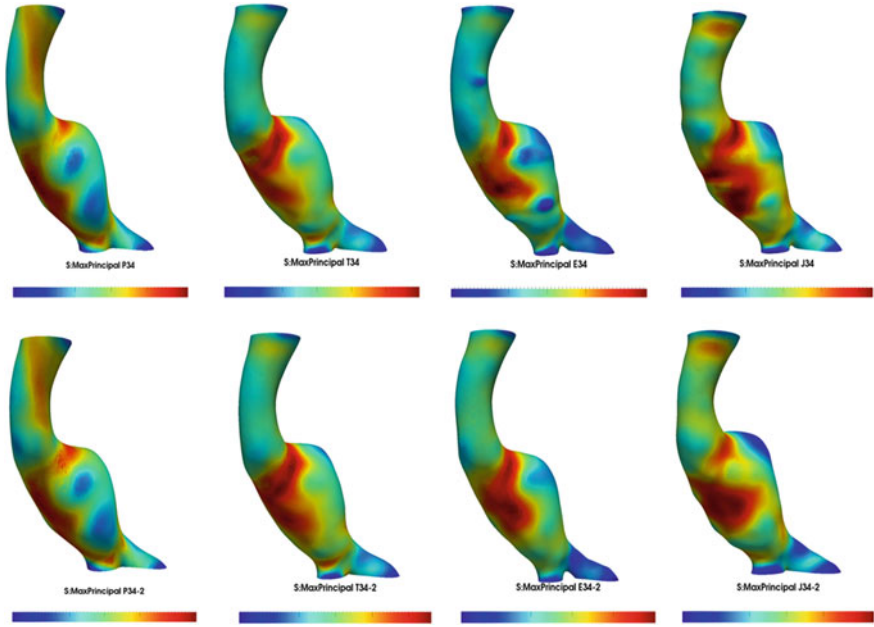


Fig. 5 Stress field contour plots of the analysed AAA patient on the same scale for each analyst. Attempt one (top) and second attempt (bottom). E34-1 has a significantly higher stress field than the other models. Regions of high stress are localised to high curvature areas that are similar across all geometries, although their stress values are different. All models viewed in Paraview

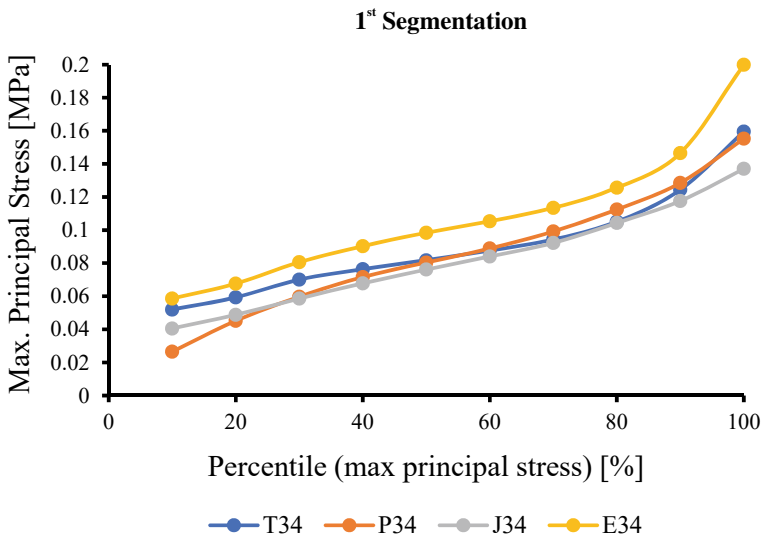


Fig. 6 Percentile plot of maximum principal stresses for 1st segmentation of the analysed AAA patient. Relative variability in stress values between analysts. 99th percentile values for T34 = 0.2256 MPa, P34 = 0.2282 MPa, J34 = 0.1417 MPa and E34 = 0.2669 MPa

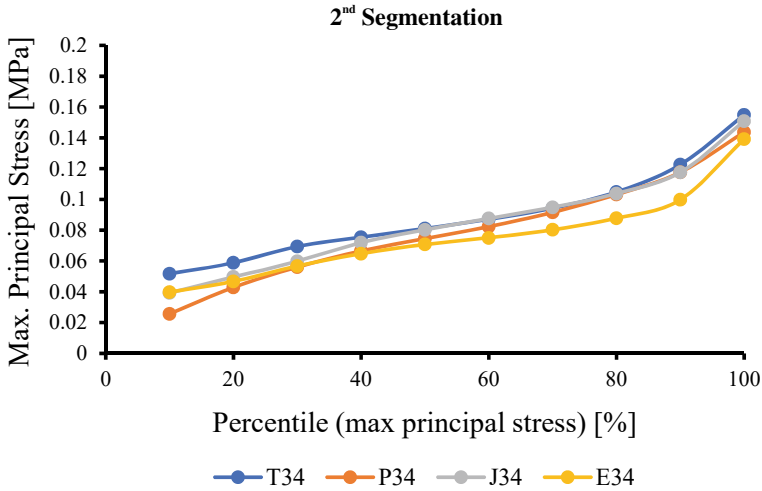


Fig. 7 Percentile plot of maximum principal stress for 2nd segmentation of the analysed AAA patient. Maximum value is T34 at 0.168 MPa. There still exists a relative difference in the stress values between analysts. 99th percentile values for T34 = 0.2156 MPa, P34 = 0.2548 MPa, J34 = 0.1682 MPa, and E34 = 0.1416 MPa

4 Discussion

The CT images that were segmented had voxel sizes of 0.625 mm cubed. By nature, CT imaging has difficulties capturing and visualising low-contrast structures like soft tissue. As the AAA is primarily made up of and surrounded by soft tissue, identification of the AAA compared to surrounding tissue may vary among analysts. Assuming an uncertainty of two pixels on each edge, there is a potential difference of up to 2.5 mm in model generation. While this may seem like a small value, it is important to consider that 3D-CT images contain a stack of 2D images which will compound on the uncertainty of each slice.

Considering that the generated 3D model is crucial for the results, it can be observed from Figs. 5, 6 and 7 that there is variability among analysts. This variability can cause influential differences in the resulting regions of wall stress. Additionally, the team decided to test if there was intra-analyst variability. After four weeks from the initial model generation, the team conducted another segmentation of the AAA from the same patient. The results from all four analysts are illustrated in Fig. 5 which shows the presence of intra-analyst variability for each team member. It is important to note that all team members are of relatively equal experience and followed the same protocol when producing segmentations. This further reinforces the need to have a standardised way to segment AAA models in patients to eliminate the variability that can arise from both inter- and intra-analyst sources.

There are limitations to this study, however. The first being that the computed stress values demonstrated here cannot be validated by realistic, in vivo results, as

no experimental results of AAA wall stress are available. Therefore, no conclusions can be made regarding the accuracy of the results obtained here. The wall stresses computed here are also potentially unreliable in AAA rupture risk prediction, as no patient-specific wall strength metric is available to compare local wall stresses and strengths. The assumption of a constant, 1.5 mm AAA wall thickness used here presents as a limitation, as it does not represent patient-specific AAA geometry. Inaccuracies of the computed stress in the AAA wall will arise, as maximum principal stresses are proportional to the wall thickness [19]. This study does verify however, the presence of analyst variability. While differences between the 99th percentile maximum principal stresses were very small (less than 8.55%) for three out of the four analysts, one analyst (E34) reported a 30.67% difference between computed stresses. In addition to this, two out of the four analysts reported slight changes in the locations of high stress on the AAA wall.

4.1 Canny Edge Detection—Future Implications

Edge detection algorithms are widely used in image processing and image analysis, especially when identifying objects within an image and preserving structural information about object boundaries. Most edge detection algorithms only require parametric user input to detect object boundaries and can be used as an alternative to semi-automatic free-hand segmentation such as Fast GrowCut within 3D Slicer. Although Fast GrowCut has the advantage of providing analysts with an interactive segmentation method that is effective and efficient over other manual methods, the method requires large amounts of user input by manually drawing seeds and background pixels to guide the segmentation [29] and may be a contributing factor to the intra- and inter-analyst variability. As such, edge detection algorithms such as Canny edge detection [4] where analysts are required to input parameters for Gaussian smoothing and thresholding instead of manual segmentation may reduce variability. Figure 8 shows a sample of the aortic wall detected by the Canny edge detection algorithm available in MATLAB. This method has been applied to previous work on detecting and measuring AAA wall thickness [14] and has the potential to be used as guidance in the form of object edge boundaries for image segmentation, reducing intra- and inter-analyst variability. Further advancements into edge detection needs to be investigated, with Canny edge detection being a simple, yet effective example of its application in medical imaging analysis.

5 Conclusions

This study verifies the workflow of AAA rupture risk prediction software, BioPARR, by analysing nine patients. The stresses computed by BioPARR and Abaqus present high stresses in region of large curvature. BioPARR was utilised to analyse the inter-

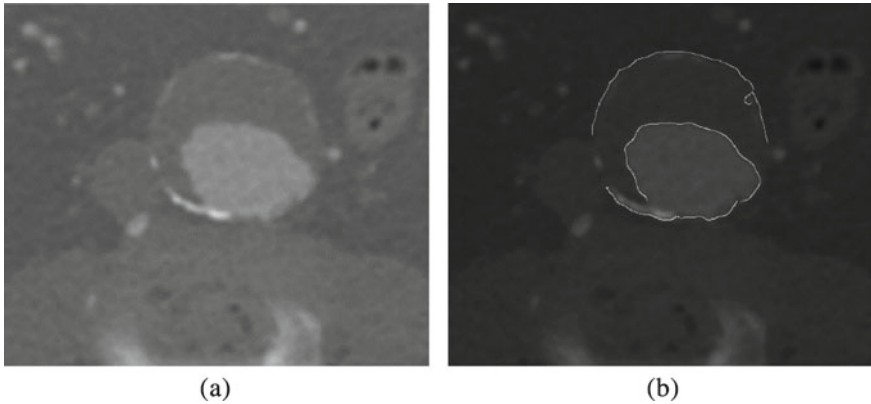


Fig. 8 Example of Canny edge detection for guiding image segmentation of the abdominal aortic aneurysm from CT scans. **a** Original axial CT slice **b** CT slice with Canny edges (in white)

and intra-analyst segmentation variability and its effects on computed stress fields. Differences were observed when comparing segmentations performed by the four analysts, with the number of nodes in the geometry being different. Additionally, the location of high stress areas differs slightly between the segmentations. These factors directly affect the prediction of rupture risk occurrence and location. Future studies are recommended to incorporate Bland and Altman's difference of mean methods and plots to obtain a more reliable comparison of intra- and inter-analyst segmentation differences and their effects on computed wall stresses. This paper also highlights the importance of the development of edge detection methods which reduce analyst variability altogether.

Acknowledgements The authors acknowledge funding of the Australian Government through the National Health and Medical Research Council NHMRC Ideas Grant, Ideas grant no. APP2001689. We also thank Fiona Stanley Hospital, Perth, Western Australia for providing the patient CT images. This research was carried out while the author F. Alkhatib was in receipt of the Australian Government Research Training Program Scholarship at the University of Western Australia.

References

1. Abaqus/CAE User's Manual (n.d.) 1174
2. Aggarwal, S., Qamar, A., Sharma, V., Sharma, A.: Abdominal aortic aneurysm: a comprehensive review. *Exp. Clin. Cardiol.* **16**(1), 11–15 (2011)
3. Ahrens, J., Geveci, B., Law, C.: ParaView: an end-user tool for large data visualization. In: *Visualization Handbook*. Elsevier (2005). ISBN-13: 978-0123875822
4. Canny, J.A.: Computational approach to edge detection. *IEEE Trans. Pattern Anal. Mach. Intell.* **8**(6), 679–698 (1986). <https://doi.org/10.1109/TPAMI.1986.4767851>

5. Darling, R.C., Messina, C.R., Brewster, D.C., Ottinger, L.W.: Autopsy study of unoperated abdominal aortic aneurysms. The case for early resection. *Circulation* **56**(3 Suppl), II161–164 (1977)
6. De Bruin, J.L., Baas, A.F., Buth, J., Prinssen, M., Verhoeven, E.L.G., Cuypers, P.W.M., van Sambeek, M.R.H.M., Balm, R., Grobbee, D.E., Blankensteijn, J.D.: Long-term outcome of open or endovascular repair of abdominal aortic aneurysm. *N. Engl. J. Med.* **362**(20), 1881–1889 (2010)
7. Droz, N.M., Miner, J., Pecchioni, L.: An 18-cm unruptured abdominal aortic aneurysm. *J. Vasc. Surg. Cases Innovations Tech.* **3**(1), 16–19 (2017)
8. Fedorov, A., Beichel, R., Kalpathy-Cramer, J., Finet, J., Fillion-Robin, J.-C., Pujol, S., Bauer, C., Jennings, D., Fennessy, F., Sonka, M., Buatti, J., Aylward, S., Miller, J.V., Pieper, S., Kikinis, R.: 3D Slicer as an image computing platform for the quantitative imaging network. *Magn. Reson. Imaging* **30**(9), 1323–1341 (2012). <https://doi.org/10.1016/j.mri.2012.05.001>
9. Fung, Y.C.: What are the residual stresses doing in our blood vessels? *Ann. Biomed. Eng.* **19**(3), 237–249 (1991). <https://doi.org/10.1007/BF02584301>
10. Geuzaine, C., Remacle, J.-F.: Gmsh: a 3-D finite element mesh generator with built-in pre- and post-processing facilities: the gmsh paper. *Int. J. Numer. Meth. Eng.* **79**(11), 1309–1331 (2009). <https://doi.org/10.1002/nme.2579>
11. Greenhalgh, R.M., Brown, L.C., Kwong, G.P.S., Powell, J.T., Thompson, S.G.: EVAR trial participants: Comparison of endovascular aneurysm repair with open repair in patients with abdominal aortic aneurysm (EVAR trial 1), 30-day operative mortality results: Randomised controlled trial. *Lancet* **364**(9437), 843–848 (2004). [https://doi.org/10.1016/S0140-6736\(04\)16979-1](https://doi.org/10.1016/S0140-6736(04)16979-1)
12. Greenhalgh, R.M., Brown, L.C., Powell, J.T., Thompson, S.G., Epstein, D., Sculpher, M.J.: Endovascular versus open repair of abdominal aortic aneurysm. *N. Engl. J. Med.* **362**(20), 1863–1871 (2010)
13. HealthDirect (2020) Aortic Aneurysm 2022. <https://www.healthdirect.gov.au/aortic-aneurysm>
14. Huynh, A., Miller, K.: Towards accurate measurement of abdominal aortic aneurysm wall thickness from CT and MRI. In: Nielsen, P.M.F., Nash, M., Li, X., Miller, K., Wittek, A. (eds.) *Computational Biomechanics for Medicine—Towards Translation and Better Patient Outcomes*. Springer International Publishing, Berlin (2022)
15. Joldes, G.R., Miller, K., Wittek, A., Doyle, B.: A simple, effective and clinically applicable method to compute abdominal aortic aneurysm wall stress. *J. Mech. Behav. Biomed. Mater.* **58**, 139–148 (2016). <https://doi.org/10.1016/j.jmbbm.2015.07.029>
16. Joldes, G.R., Miller, K., Wittek, A., Forsythe, R.O., Newby, D.E., Doyle, B.J.: BioPARR: a software system for estimating the rupture potential index for abdominal aortic aneurysms. *Sci. Rep.* **7**(1), 4641 (2017). <https://doi.org/10.1038/s41598-017-04699-1>
17. Joldes, G.R., Noble, C., Polzer, S., Taylor, Z., Wittek, A., Miller, K.: A simple method of incorporating the effect of the uniform stress hypothesis in arterial wall stress computations [PDF]. *Acta Bioeng. Biomech.* (2018). ISSN 1509-409X. <https://doi.org/10.5277/ABB-01143-2018-03>
18. Miller, K., Lu, J.: On the prospect of patient-specific biomechanics without patient-specific properties of tissues. *J. Mech. Behav. Biomed. Mater.* **27**, 154–166 (2013)
19. Miller, K., et al.: Maximum principal AAA wall stress is proportional to wall thickness. In: Nielsen, P., Wittek, A., Miller, K., Doyle, B., Joldes, G., Nash, M. (eds.) *Computational Biomechanics for Medicine*. Springer, Cham (2019). https://doi.org/10.1007/978-3-319-75589-2_5
20. Naghavi, M., et al.: Global, regional, and national age–sex specific all-cause and cause-specific mortality for 240 causes of death, 1990–2013: a systematic analysis for the global burden of disease study 2013. *Lancet* **385**(9963), 117–171 (2015)
21. Polzer, S., Gasser, T.C., Vlachovský, R., Kubiček, L., Lambert, L., Man, V., Novák, K., Slažanský, M., Burša, J., Staffa, R.: Biomechanical indices are more sensitive than diameter in predicting rupture of asymptomatic abdominal aortic aneurysms. *J. Vasc. Surg.* **71**(2), 617–626.e6. <https://doi.org/10.1016/j.jvs.2019.03.051>

22. Raghavan, M.L., Vorp, D.A.: Toward a biomechanical tool to evaluate rupture potential of abdominal aortic aneurysm: identification of a finite strain constitutive model and evaluation of its applicability. *J. Biomech.* **33**(4), 475–482 (2000)
23. Speelman, L., Bosboom, E.M.H., Schurink, G.W.H., Hellenhal, F.A.M.V.I., Buth, J., Breeuwer, M., Jacobs, M.J., van de Vosse, F.N.: Patient-specific AAA wall stress analysis: 99-percentile versus peak stress. *Eur. J. Vasc. Endovasc. Surg.* **36**(6), 668–676 (2008). <https://doi.org/10.1016/j.ejvs.2008.09.007>
24. Truijers, M., Pol, J.A., Schultzekool, L.J., van Sterkenburg, S.M., Fillinger, M.F., Blankensteijn, J.D.: Wall stress analysis in small asymptomatic, symptomatic and ruptured abdominal aortic aneurysms. *Eur. J. Vasc. Endovasc. Surg. Official J. Eur. Soc. Vasc. Surg.* **33**(4), 401–407 (2007). <https://doi.org/10.1016/j.ejvs.2006.10.009>
25. Valette, S.M.J., Prost, R.: ACVD: surface mesh coarsening and resampling. Sébastien Valette (2016). <https://www.creatis.insa-lyon.fr/~valette/public/project/acvd/0>
26. Vande Geest, J.P., Di Martino, E.S., Bohra, A., Makaroun, M.S., Vorp, D.A.: A biomechanics-based rupture potential index for abdominal aortic aneurysm risk assessment: demonstrative application. *Ann. N. Y. Acad. Sci.* **1085**, 11–21 (2006). <https://doi.org/10.1196/annals.1383.046>
27. Vascular, S.V.: Abdominal aortic aneurysms symptoms. The Silent Killer (2022). <https://www.southvalleyvascular.com/post/abdominal-aortic-aneurysms-symptoms-the-silent-killer#:~:text=An%20abdominal%20aortic%20aneurysm%20is,abdominal%20aortic%20aneurysm%20than%20women>
28. Wanhainen, A., et al.: Editor’s choice—European society for vascular surgery (ESVS) 2019 clinical practice guidelines on the management of abdominal aorto-iliac artery aneurysms. *Eur. J. Vasc. Endovasc. Surg.* **57**(1), 8–93 (2019)
29. Zhu, L., Kolesov, I., Gao, Y., Kikinis, R., Tannenbaum, A.: An effective interactive medical image segmentation method using fast GrowCut. In: International Conference on Medical Image Computing and Computer-Assisted Intervention. Workshop on Interactive Methods, vol. 17 (WS) (2014)

The Effects of the Spine on the Analysis of Peak Wall Stress in Abdominal Aortic Aneurysms



Michael D. Liddelow, Farah Alkhatib, Adam Wittek, and Karol Miller

Abstract Abdominal aortic aneurysms (AAA) are a chronic degenerative disease, affecting around 7% of men aged 65 years or over. Previous studies on AAA biomechanics either assume the effects of surrounding tissues to be negligible, or do not address the assumption. This study determines the potential for the spine to affect the AAA stress calculations and therefore influence the resulting risk assessment accuracy. Spinal contact boundary conditions on the AAA were manually chosen. Finite element analysis (FEA) was performed on two AAAs adapting the BioPARR workflow to calculate maximum principal stress (MPS) in the isolated AAA and the AAA with spinal contact. The 99th percentile MPS in the spine contact variant was 0.421 MPa, compared to 0.448 MPa in the isolated vessel (0.311 MPa vs. 0.345 MPa, for case 2, respectively). The mean absolute difference of the nodal MPS between variants for case 1 was 0.016 MPa and 0.014 MPa for case 2. Areas of stress on the posterior surface of the AAA in the isolated method appear to be overestimated. However, the overall stress maps of the two variants in both cases indicated almost identical locations of high and low stress. This study indicates that the effect of the spine on AAA biomechanics is mostly negligible, providing the first evidence to justify the common assumption that such impact can be ignored.

Keywords Aneurysm · Assumption · Patient-specific modelling (PSM) · Finite element method · External tissues · Maximum principal stress (MPS)

M. D. Liddelow · F. Alkhatib · A. Wittek · K. Miller (✉)
Intelligent Systems for Medicine Laboratory, The University of Western Australia, Perth, WA,
Australia
e-mail: karol.miller@uwa.edu.au

1 Introduction

Abdominal aortic aneurysm (AAA) is a chronic degenerative disease, characterised by the permanent dilation of the lower part of the descending aorta. It occurs in around 7% of men aged 65 years or over [10] and affects 4–6 times more men than women [21]. The disease is known as the ‘Silent Killer’ since the aneurysm can rupture or dissect with no prior symptoms, resulting in a high mortality [1, 24]. The rates of mortality after rupture are around 80–90% without surgery [11].

The most common technique used to determine rupture threat is the geometrical approach, associated with the aortic maximum diameter and its growth with time [10]. To determine the risk of rupture, the maximum anterior–posterior or transverse aortic diameter is measured [10]. A high risk of rupture is indicated for diameters ≥ 5.5 cm in men and ≥ 5.0 cm in women [25]. The growth rate guidelines consider a high risk of rupture with an aortic diameter increase of > 1 cm/year [34]. These measurements are commonly taken using computed tomography angiography (CTA) or ultrasound. The identification of a high risk of rupture leads to the decision to perform treatment, which currently includes endovascular aneurysm repair and open surgical repair [34].

This current identification method is not an optimal solution as it does not take into account relevant comorbidities, the risk of intra-operative mortality, or the height and weight of the patient. AAA ruptures have occurred in patients with AAA maximum diameters of < 5 cm (less than the recommended threshold) [26]. Conversely, larger aneurysms have remained stable, with diameters reaching 15 cm [3, 28]. The unnecessary AAA repair is an issue since there is 4–8% mortality rate related to the suggested AAA treatment repairs [34]. Additionally, very few diagnosed aneurysms actually rupture, with annual rupture rates of 3.5% for 5.5–6.0 cm, 4.1% for 6.1–7.0 cm, and 6.3% for > 7.0 cm of aortic diameters of [27]. This presents the need for a patient-specific way to measure AAA disease progression and assess the rupture risk more accurately. Computational biomechanics is used to create a non-invasive patient-specific modelling tool to indicate rupture and the progression of the disease. This method focuses on the stress being the variable of interest in specific areas of the AAA, to identify areas of high stress as a biomarker for rupture likelihood [15]. The aneurysm stress can be determined in the Biomechanics-based Prediction of Aneurysm Rupture Risk (*BioPARR*) programme using the patient CTA scans and median arterial blood pressure [15].

In many previous studies, the effects of external tissues on AAA biomechanics were assumed to be negligible [8, 14, 15]. Conversely, other recent studies computed biomechanics on the isolated AAA, not including any external tissues, and did not mention the surrounding tissue non-contact assumption [2, 4, 9, 13, 20, 22, 24, 32]. Reeps et al. [29] discuss the impact of various AAA model assumptions, but do not mention the effects of surrounding tissues. The members at Intelligent Systems for

Medicine Laboratory (ISML) believe that external tissues may in fact affect the AAA biomechanics, and therefore, the accuracy of risk assessments associated with these biomechanical analyses may have the potential to be improved.

The purpose of this paper is to analyse the biomechanics of two AAA cases, taking into account their interaction with the spine. This research forms a precedent to determine whether surrounding tissues affect the biomechanics of the AAA and therefore influence the resulting risk assessment accuracy. This was assessed by comparing the calculated maximum principal stress (MPS) in two variants: the isolated AAA (spine is not included in the analyses) and the AAA with contact from the rigid spine. The relevant AAA and surrounding tissues were segmented using the 3D Slicer programme, and subsequent finite element analysis was performed on the two variants in BioPARR [15] and ABAQUS (Version 6.20; RI, USA, 2020) finite element code.

2 Methodology

2.1 Patient Data

Here we analysed two cases of AAA from Fiona Stanley Hospital in Perth, Western Australia. The patients received a 4D-CT exam. Case 1 was an 86-year-old overweight (BMI 29.1) female with a controlled blood pressure of 178/81 mmHg and no other comorbidities. Case 2 was a 79-year-old normal weighted (BMI 24.7) male, with a controlled blood pressure of 163/101 mmHg and no other comorbidities. The mean arterial blood pressure for case 1 was 15.1 kPa and 16.2 kPa for case 2. The data consists of ten phases of 3D-CT scans, showing the region of interest over the entire cardiac cycle. The scan chosen for analysis was taken at the diastolic phase of the cardiac cycle (at the 80% point), since it produced the clearest image (fewest artefacts). Maximum AAA diameter was measured in the axial view, anteroposterior axis of the CT scans [17]. The measured maximum AAA diameter for case 1 was 60 mm and 48 mm for case 2.

2.2 Patient-Specific AAA and Spine Model Creation

To find the AAA geometry, we first created a 3D reconstruction using the open-source software 3D Slicer [5]. The steps include defining and cropping a region of interest, below the renal arteries up until the iliac bifurcation (including all the surrounding organs). This is followed by segmenting both the AAA and ILT using the ‘Fast GrowCut’ algorithm to create segmentations of the AAA [35]. Manual corrections were also performed to smooth the segmentation [15]. The internal

AAA wall structure was then segmented and distinguished from the intraluminal thrombus [15].

The internal wall of the AAA was identified with relative ease since the patient was given a contrasting agent prior to imaging. CT creates contrast through differences in x-ray attenuation. Bone and calcifications have high atomic numbers and density, resulting in increased attenuation and therefore a higher pixel intensity in CT images [19]. This means that it is relatively easy to create a spinal segmentation since the bone creates higher contrast compared to the surrounding tissues. The spine was therefore segmented using pixel intensity thresholding, followed by manual corrections, and Gaussian smoothing.

The spine does not directly contact the aneurysm, as seen in Fig. 1. This is due to soft tissues anterior to the spine that are not segmented resulting from a lack of contrast. Tissues in front of the spine in the abdomen region include the following anatomical structures; suspensory muscle of the duodenum, the diaphragmatic crura, the anterior longitudinal ligament, ascending veins, and branching arteries [6]. These structures have a frictional effect between the spinal contact boundary conditions. It is difficult to determine the frictional coefficients between these structures, the aneurysm and spine. Therefore, in order to create the maximum level of interaction between the spine and aneurysm, the nodes that would be in close contact with the spine were fixed, simulating maximum interaction strength. If the worst-case scenario boundary condition does not significantly alter the maximum principal stress calculated throughout the wall, then all other frictional interaction cases will be covered, and the assumption is supported.

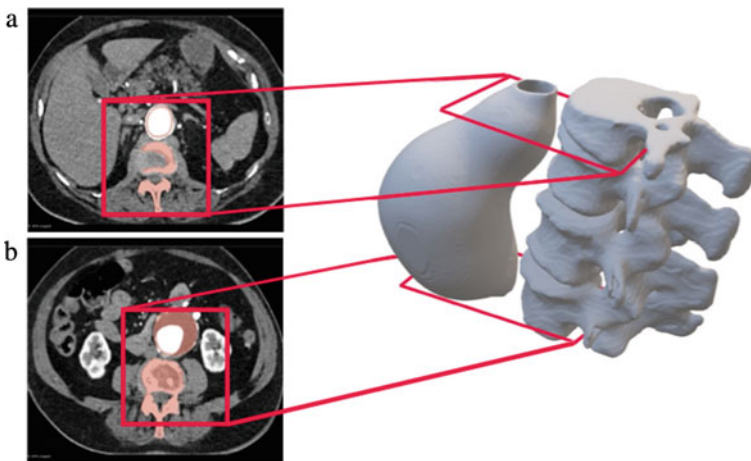


Fig. 1 Diagram of aneurysm and spine contacting areas corresponding to radiological data. **A** Superior axial slice, showing the gap between aneurysm and spine, separated by the suspensory muscle of the duodenum, diaphragmatic crura, and anterior longitudinal ligament. **B** Inferior axial slice, showing the lower gap between aneurysm and spine, separated by the anterior longitudinal ligament, branching arteries, and ascending veins

Finite element mesh was generated in three stages using the BioPARR custom command files that utilise Gmsh (Version 4.8.4; MA, USA, 2021) software. This creates hybrid tetrahedral elements, with quadratic shape functions. Firstly, the surface is meshed using the generated element size information, where further constraints can be made on the element size. Secondly, generated end surfaces form boundaries to create the AAA wall and ILT volumes. The VTK toolkit [16], used in stage 1 does not guarantee closed surfaces; thus, the end surfaces are necessary for a closed watertight surface. Finally, a tetrahedral volumetric mesh was created to ensure a conforming mesh between the ILT and AAA wall, and the meshes are saved as .vtk files [15]. For case 1, the AAA (aneurysm wall and ILT) mesh contained 665,344 elements (1,156,395 nodes), and the ILT mesh contained 792,849 elements (1,364,086 nodes). For case 2, the AAA mesh contained 346,521 elements (603,507 nodes), and the ILT mesh 880,285 elements (1,362,108 nodes).

2.3 Finite Element Analysis

Finite element analysis was performed using a direct linear procedure, as described by Joldes et al. [15] for the *BioPARR* workflow. The ILT pressure analysis chosen involves the AAA with both the aneurysm wall and the ILT, where blood pressure is applied to the inner surface of the ILT. The wall and ILT were modelled with linear elastic material. The solution relies only on AAA geometry and internal blood pressure and is very weakly related to material properties [14]. This is because the imaged AAA is in a deformed state, in which stress distribution depends on loading and geometry (i.e. in the deformed state, the AAA can be regarded as approximately statically determinant). A statically determinant structure has satisfied equilibrium equations meaning that the internal stresses are balanced with the externally applied forces [30]. The non-reliance on material properties is important since this is a patient-specific analysis, and it is extremely difficult to obtain tissue material properties in vivo, as described in Miller and Lu [23]. Thus, this method avoids the use of population-based properties that are taken by many researchers using the Vande Geest et al. [33] statistical model, which would cause the analysis to no longer be patient specific.

The wall and ILT were given material properties in accordance with the *BioPARR* procedure. Isotropic linearly elastic material was used for both tissues with a Poisson's ratio of 0.49. The Young's moduli for the two materials were chosen to be very stiff, relative to the blood pressure load of 15–16 kPa. This is to ensure the already deformed geometry does not change under loading, creating infinitesimal strains [14]. The Young's modulus for the wall was 1000 and 50 MPa for the ILT. The ILT was kept at 20 times less stiff than the wall, in accordance with Miller et al. [24].

Features of the AAA wall and ILT geometry were defined, fixing both the top and bottom lumen edges of the AAA. The spinal contact nodes were also fixed in place for the spinal contact simulation. The internal surface of the aneurysm wall

and the external surface of the ILT were tied together using a tie constraint. Finally, a uniform pressure load was placed against the internal surface of the ILT, with a magnitude equal to the patient-specific mean arterial blood pressure. We calculated stress at each node by taking the average of the stress tensor components from every element that had a vertex at that specific node [18]. The maximum principal stress was then examined in *Paraview* (<https://www.paraview.org/download/>) and exported as a .csv file to be post-processed in *MATLAB*.

2.4 Contact Node Identification

Spinal contact nodes were identified in relation to spinal location, with the outer surface nodes of the AAA wall being considered, as seen in Fig. 2. These nodes were manually selected to be fixed.

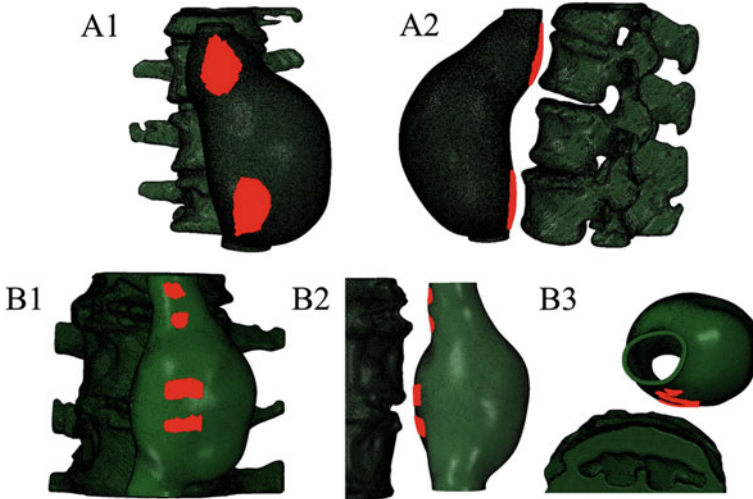


Fig. 2 Manually selected areas of spinal contact. **A** Case 1 fixed contact nodes. **B** Case 2 fixed contact nodes. **A1** Anterior view (note: contact nodes are on the posterior surface of the AAA). **A2** Left view. **B1** Anterior view. **B2** Right view. **B3** Superior view. All contact nodes were individually selected on the outer surface of the AAA wall in relation to spinal location. Red nodes were fixed in position for analysis using the *Encastré* command in the *ABAQUS* finite element code

2.5 *Quantitative Comparison of Isolated and Spine-Contacted Models*

A number of methods were used to calculate the similarity in maximum principal stress between the isolated aneurysm and spinal contacted aneurysm. This included finding the 99th and 99.9th percentile, the percentile difference between nodes in regions of high stress, mean absolute difference (MD), and root mean squared error (RMSE). Both 99th and 99.9th percentile maximum principal stress were taken in order to determine the value in which 99 and 99.9% of stress values fall below. Fixed nodes at the top and bottom of the lumen, as well as the spinal contact nodes, cause high stress artefacts, seen clearly in A2 of Fig. 3. Speelman et al. [31] found that the 99th percentile AAA wall stress improved reproducibility compared to the peak wall stress, due to localised artefacts in computational grids. The 99.9th percentile has relevance since these artefacts only cause a small number of nodes to have high stress on the outer edge of the wall, near the fixed nodes.

3 Results

Arterial wall maximum principal stress was visualised using contour plots (Figs. 3 and 4). The areas of high stress remained almost identical between the isolated aneurysm wall and spine-contacted aneurysm wall, with the exception of the areas of spinal contact chosen to be fixed. Aside from the areas of fixed nodes, larger differences between two given nodes appear to be related to the distance from the spine-contacted nodes. For example, point 1.1 (from Table 1) is closer to the spinal contact than points 1.2 and 1.3, and it also has a larger MPS difference. The same occurs for points 2.1 and 2.4 from Table 1, with the MPS difference for point 2.1 being larger and the point occurring closer to the fixed nodes.

Further examination of the difference in MPS distribution was performed through histogram representation, as depicted in Fig. 5. The distribution of wall stress is very similar between methods. The differences are more evident in case 1, where there is a percentage of nodes with lower nodal stress. The relative shape of the distributions is otherwise extremely similar. Quantitative analysis of the differences between the two methods of obtaining MPS included the percentile comparison (Fig. 6), mean absolute difference, and root mean squared error (Table 2).

4 Discussion and Conclusions

The results show no clear disparity between the two maximum principal stress distribution contour maps of the two variant solutions. For both models, contour maps have identical areas of high stress in nodal regions that were not fixed. This suggests that

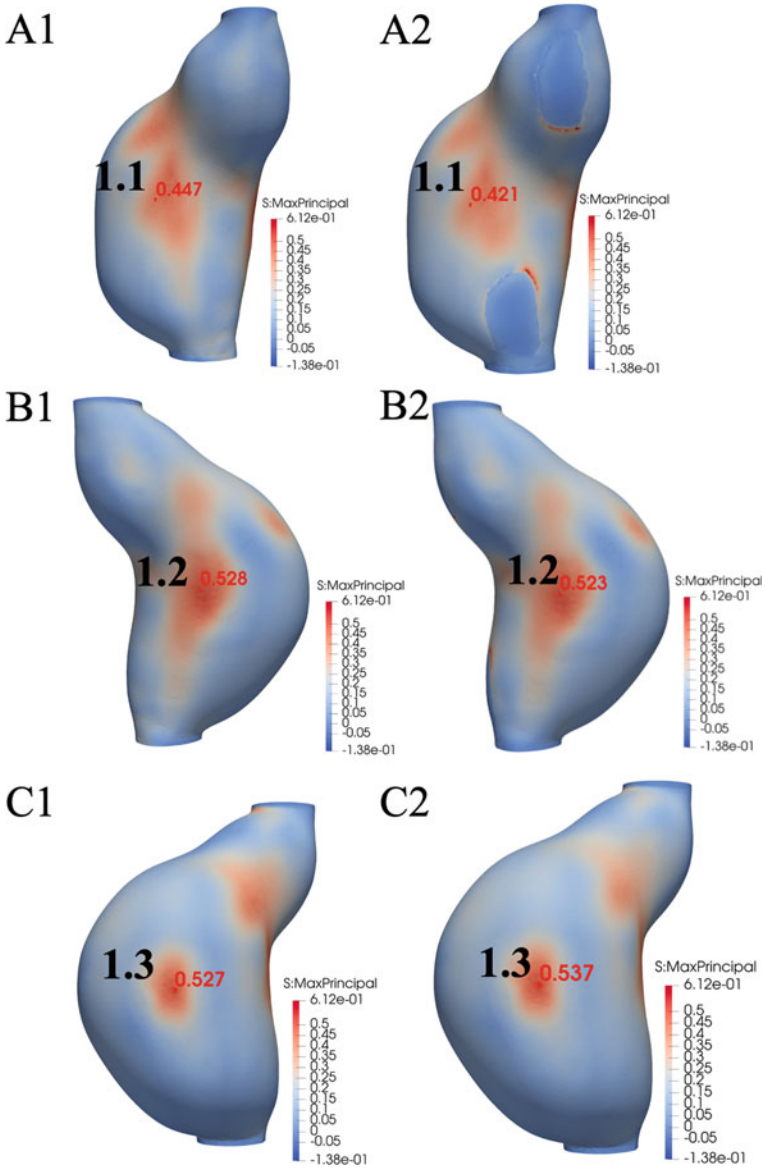


Fig. 3 Maximum principal stress (in MPa) contour plot for case 1, with specific areas of interest identified and labelled. **A** Posterior view showing MPS of 0.447 MPa versus 0.421 MPa. **B** Right view showing MPS of 0.528 MPa versus 0.523 MPa. **C** Left view showing MPS of 0.527 MPa versus 0.537 MPa. (1) Isolated AAA. (2) Spine-contacted AAA, with dark blue patches corresponding to fixed nodes. Contours are reasonably similar between cases. Specific nodes chosen in regions of high stress

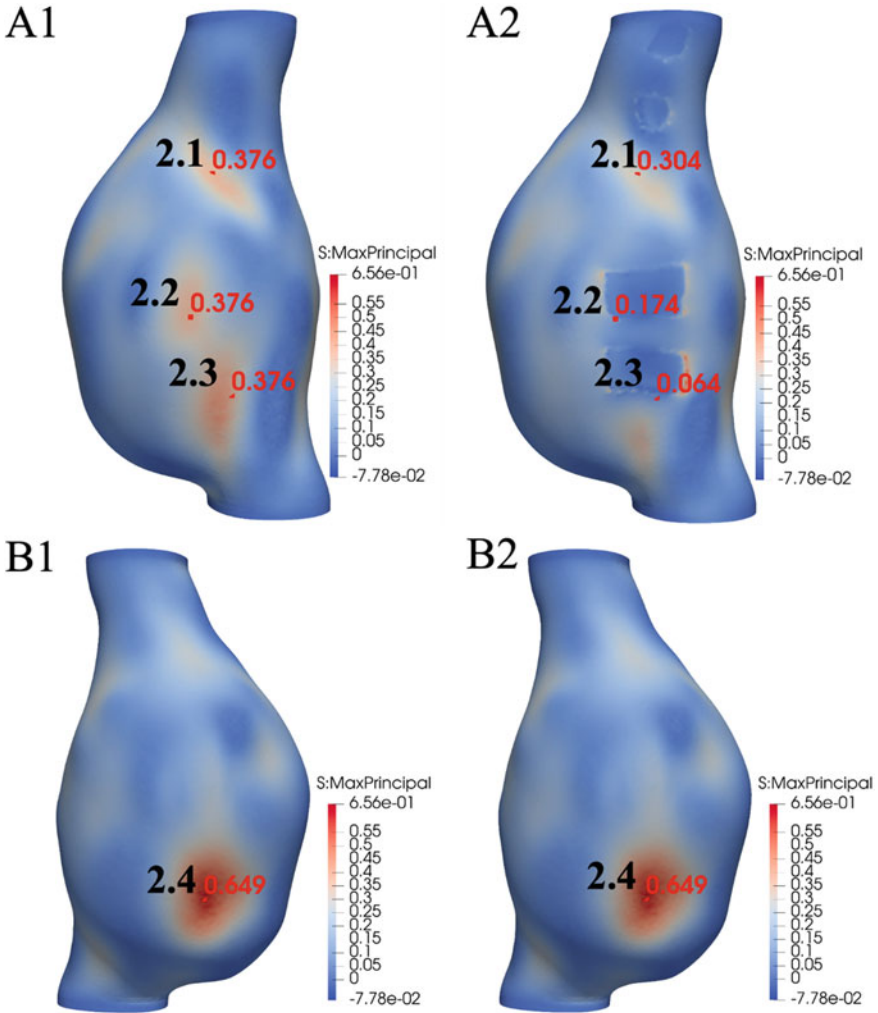


Fig. 4 Maximum principal stress (in MPa) contour plot for case 2, with specific areas of interest identified. **A** Posterior view showing MPS of 0.376 MPa versus 0.304 MPa, 0.376 MPa versus 0.174 MPa, and 0.376 MPa versus 0.064 MPa. **B** Anterior view showing MPS of 0.649 MPa versus 0.649 MPa. (1) Isolated AAA. (2) Spine-contacted AAA, with dark blue patches corresponding to fixed nodes. Contours are very similar between cases, besides the comparisons that fall within the fixed node regions. Specific nodes were chosen in regions of high stress in the isolated AAA model

fixing spinal contact nodes will result in negligible change to the calculated stress outside of the contacted areas. Meaning that the external tissue interaction assumption will not affect the accuracy of resultant clinical diagnoses, if the areas of high stress are away from the spinal contact. The negligible effects of the spinal contact

Table 1 Summary of maximum principal stress in areas of high stress in case 1 and case 2 for isolated and spine-contacted AAAs

Point	Isolated AAA wall MPS (MPa)	Spine-contacted AAA wall MPS (MPa)	Absolute difference (%)
<i>Case 1</i>			
1.1	0.447	0.421	5.8
1.2	0.528	0.523	1.0
1.3	0.527	0.537	1.9
<i>Case 2</i>			
2.1	0.376	0.304	19.2
2.2	0.376	0.174	53.7
2.3	0.376	0.064	83.0
2.4	0.649	0.649	0.0

Points were labelled as seen in Figs. 3 and 4. Almost negligible differences are seen at points 1.2, 1.3, and 2.4. Large differences were seen at areas of fixed nodes at points 2.2 and 2.3. Differences were seen at points 1.1 and 2.1 as these areas of high stress in the isolated method were near fixed nodes in the spinal contact method

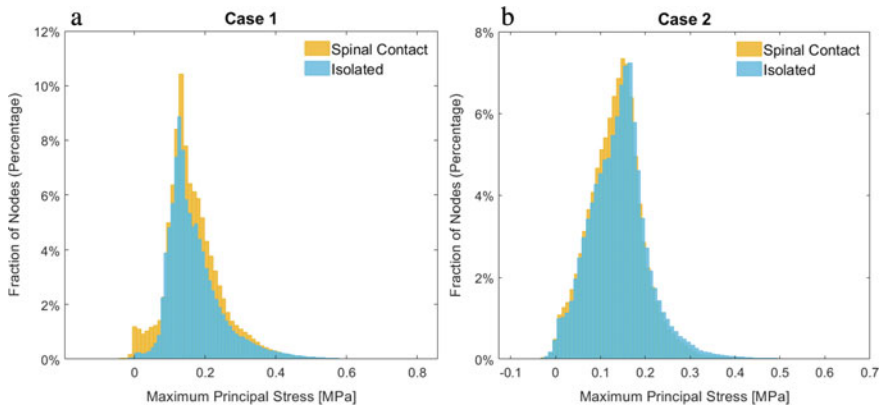


Fig. 5 Histogram of maximum principal stress in the aneurysm wall. Stress in the aneurysm with spinal contact is shown in yellow, and the stress in the isolated aneurysm is shown in blue. **A** Results for case 1. **B** Results for case 2. The distributions of the stress are very similar, except for the lower stress distribution in the model with spinal contact

interaction are seen in the comparison of percentile MPS. There is negligible difference between the 99th and 99.9th percentile of the two methods in both cases, and the percentile plots are virtually the same. As seen in Figs. 5 and 6, the isolated method produced a greater percentage of low stress area in case 1; however, this does not affect the areas of high stress. The mean absolute difference and root mean squared error had minimal difference, seen in Table 2. Despite the large changes in stress at the fixed contact node areas, these quantitative metrics support the negligible effects.

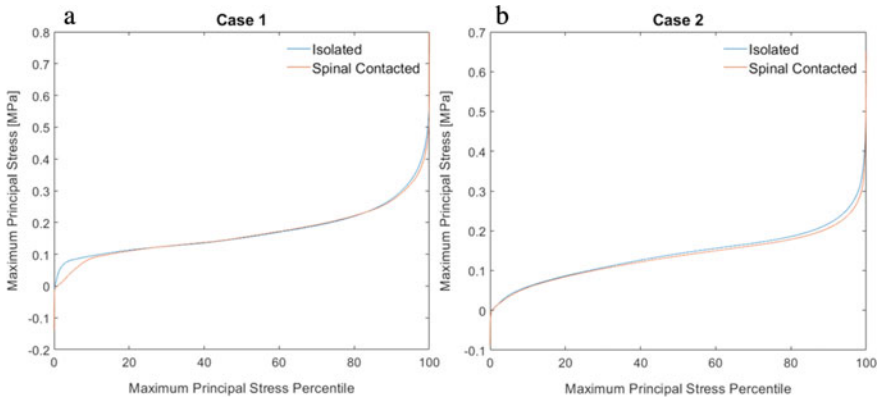


Fig. 6 Percentile plots of the maximum principal stress in the AAA wall for the two cases calculated for the spinal contact and isolated methods. **A** Case 1. **B** Case 2. The isolated method produced higher stresses in the low stress area for case 1, and the spinal contact method produced higher peak maximum principal stress in both cases. The overall distributions are very similar between methods

Table 2 Quantitative comparison of maximum principal stress

Case	99th percentile MPS (MPa)			99.9th percentile MPS (MPa)			MAD (MPa)	RMSE (MPa)
	Isolated	Spine contact	Difference (%)	Isolated	Spine contact	Difference (%)		
1	0.448	0.421	6.0	0.552	0.508	7.8	0.016	0.030
2	0.345	0.311	9.9	0.487	0.483	0.8	0.014	0.032

There is negligible difference between isolated and spine-contacted methods. MPS is maximum principal stress, MAD is mean absolute difference, and RMSE is root mean squared error.

Areas of high stress appear to be more similar the further away from the fixed spinal contact nodes. For example, from Table 1, point 2.1 has an MPS difference of 19.2% without being located in an area of spinal contact. Meanwhile, point 2.4 has no difference in MPS. This may be related to the fact that point 2.1 is in-between two contact areas, while point 2.4 is far away from them. This also occurs in case 1, since point 1.1 has a larger MPS difference than points 1.2 and 1.3 (5.8% compared to 1.0 and 1.9%) and point 1.1 is closer to the fixed nodes than points 1.2 and 1.3. This has implications on current isolated aneurysm biomechanical analyses, since both the top and bottom edges of AAA model are fully fixed. Therefore, if the aorta is not cropped sufficiently to leave enough space between the top/bottom of the lumen and the aneurysm, then the stress distributions in the aneurysm wall will be affected. Negative stresses were also seen in both methods for both cases; these negative indicate bending. The majority of the wall is in tension since the force from the blood pressure is acting on the inner surface of the ILT and thus pushing the wall outwards. The compressive forces are likely due to the irregularity in the wall

geometry. Surfaces that change angle drastically will cause the outward force to compress the part of the wall that is at a sharp angle.

The peak value of maximum principal stress was not taken since the peak stress occurs as stress concentrations at the edge of the spinal contact node areas, or at the top or bottom edges of the aneurysm wall. This is not reflective of actual high stress areas and are rather localised uncertainties due to the boundary conditions. Since fixed nodes have zero displacement, the degrees of freedom is decreased. The neighbouring nodes that are not fixed will have drastic changes in the degrees of freedom that causes these stress concentrations [31]. The same stress concentrations occur due to the top and bottom vessel fixations. Speelman et al. [31] found that the 99th percentile AAA wall stress improved reproducibility compared to the peak wall stress, due to localised uncertainties in computational grids. This correlates to the area of fixed nodes as they too would cause localised uncertainties, correlating to peaks in wall stress. Furthermore, Fillinger et al. [7] found that the majority of AAAs rupture posterolaterally or laterally, not posteriorly. The spine is posterior to the aorta, and therefore, this reduction in posterior rupture points may be due to the spinal support. Results from this study suggest that the posterior stress is overestimated when spinal contact is not included. However, as seen in the two cases, points 1.2 and 1.3 of Fig. 3 and point 2.4 of Fig. 4 are within the highest stress areas on the outer arterial wall. These points were on the lateral and anterior side of the AAA and therefore were not affected by the spinal contact. Thus, inclusion of the spinal contact may not affect the relevant areas of high stress.

There are a few limitations relating to the study that are important to consider. The first is that the fixed spinal contact nodes were chosen manually in relation to the spine. This means that they are not precisely reproducible. However, the exact size of the contact nodes is relatively not important in relation to the outcomes of this study since these contact nodes showed a near-negligible effect on the overall stress distributions. The second limitation with this study is the assumption of constant wall thickness (1.5 mm in this case), which is anatomically incorrect. This is an impactful assumption, since stress is approximately proportional to assumed thickness [22]. However, in practice it is very difficult to determine an accurate measurement of the patient-specific wall thickness using CT due to the low soft tissue contrast [12, 15]. Maximum principal stress is directly related to the aneurysm wall thickness, and constant thickness assumption causes uncertainty in the resultant stress. However, since the result of this assumption would occur in both methods of this study, the assumption will not affect the disparities in the results.

This study successfully analysed the biomechanics of the abdominal aortic aneurysm, incorporating the spine as a boundary condition interaction. Previous studies assume the effects of external tissues on AAA biomechanics to be negligible, without providing evidence to support it [8, 14, 15]. Conversely, other recent studies compute biomechanics on the isolated AAA, not including any external tissue boundary conditions, and do not mention the surrounding tissue non-contact assumption [2, 4, 9, 13, 20, 22, 24, 32]. The results from this study indicate the negligible

effects created by the spine on AAA stress distributions, supporting the common assumption in academic research to ignore such effects. The results provide the only substantial evidence to support this often-overlooked assumption. Thus, the external tissue interaction assumption is unlikely to affect the accuracy of resultant clinical diagnoses. However, any areas of posterior stress in the isolated method appear to be overestimated. Including the spine creates a lot of added manual input as contact nodes are not yet able to be automatically assigned. Thus, a recommendation may be to identify the areas of high stress on the AAAs examined, and further spinal boundary conditions may be necessary if the areas of high stress are on the posterior of the AAA.

Future studies should repeat the workflow presented in this paper on more AAA cases. This would increase the statistical validity of the results and thus create further evidence to confirm the reliability of the common assumption that spinal contact does not affect AAA biomechanics. The locations of areas of high stress should be identified to determine how often they occur on the posterior surface of the AAA. Fringe cases, such as patients with herniated discs, should also be examined to determine whether more extreme cases of contact would still result in little changes in wall stress. All external tissues could be added as boundary conditions. However, if there are more contact nodes fixed, then there are less nodes to compare, as per the second limitation of this study. The spinal contact model may be refined by including the patient-specific spine (extracted from the CT) as a rigid body in the model. This will eliminate the manual selection of the spinal contact nodes. The interaction between the aneurysm wall surface and spine will be seen if a proper contact was selected, and similar results should be expected.

Acknowledgements We gratefully acknowledge financial support from the National Health and Medical Research Council (NHMRC) Ideas Grant APP2001689. We would like to thank Tom Wilson from the University of Western Australia, Anatomy and Human Biology Department, for his advice on anatomical structures. We also thank the Fiona Stanley Hospital, Perth, Western Australia, for providing the patient scans. This research was carried out while the second author F. A. was in receipt of the Australian Government Research Training Program Scholarship at The University of Western Australia.

References

1. Badger, S.A., Harkin, D.W., Blair, P.H., Ellis, P.K., Kee, F., Forster, R.: Endovascular repair or open repair for ruptured abdominal aortic aneurysm: a cochrane systematic review. *BMJ Open* **6**(2), e008391 (2016). <https://doi.org/10.1136/bmjopen-2015-008391>
2. Doyle, B.J., McGloughlin, T.M., Miller, K., Powell, J.T., Norman, P.E.: Regions of high wall stress can predict the future location of rupture of abdominal aortic aneurysm. *CardioVasc. Interv. Radiol.* **37**(3), 815–818 (2014). <https://doi.org/10.1007/s00270-014-0864-7>
3. Droz, N.M., Miner, J., Pecchioni, L.: An 18-cm unruptured abdominal aortic aneurysm. *J. Vasc. Surg. Cases Innov Tech.* **3**(1), 16–19 (2017). <https://doi.org/10.1016/j.jvscit.2016.10.008>

4. Erhart, P., Hyhlik-Dürr, A., Geisbüsch, P., Kotelis, D., Müller-Eschner, M., Gasser, T.C., von Tengg-Kobligk, H., Böckler, D.: Finite element analysis in asymptomatic, symptomatic, and ruptured abdominal aortic aneurysms: in search of new rupture risk predictors. *Eur. J. Vasc. Endovasc. Surg.* **49**(3), 239–245. <https://doi.org/10.1016/j.ejvs.2014.11.010>
5. Fedorov, A., Beichel, R., Kalpathy-Cramer, J., Finet, J., Fillion-Robin, J.-C., Pujol, S., Bauer, C., Jennings, D., Fennessy, F., Sonka, M., Buatti, J., Aylward, S., Miller, J.V., Pieper, S., Kikinis, R.: 3D Slicer as an image computing platform for the quantitative imaging network. *Magn. Reson. Imaging* **30**(9), 1323–1341 (2012). <https://doi.org/10.1016/j.mri.2012.05.001>
6. Feller, L., Woodburne, R.T.: Surgical anatomy of abdominal aorta. *Ann. Surg.* **154**(Suppl 6), 239–252 (1961)
7. Fillinger, M.F., Racusin, J., Baker, R.K., Cronenwett, J.L., Teutelink, A., Schermerhorn, M.L., Zwolak, R.M., Powell, R.J., Walsh, D.B., Ruzicidlo, E.M.: Anatomic characteristics of ruptured abdominal aortic aneurysm on conventional CT scans: implications for rupture risk. *J. Vasc. Surg.* **39**(6), 1243–1252 (2004). <https://doi.org/10.1016/j.jvs.2004.02.025>
8. Gasser, T.C., Auer, M., Labruto, F., Swedenborg, J., Roy, J.: Biomechanical rupture risk assessment of abdominal aortic aneurysms: model complexity versus predictability of finite element simulations. *Eur. J. Vasc. Endovasc. Surg.* **40**(2), 176–185 (2010). <https://doi.org/10.1016/j.ejvs.2010.04.003>
9. Gasser, T.C., Nchimi, A., Swedenborg, J., Roy, J., Sakalihan, N., Böckler, D., Hyhlik-Dürr, A.: A novel strategy to translate the biomechanical rupture risk of abdominal aortic aneurysms to their equivalent diameter risk: method and retrospective validation. *Eur. J. Vasc. Endovasc. Surg.* **47**(3), 288–295 (2014). <https://doi.org/10.1016/j.ejvs.2013.12.018>
10. Glimåker, H., Holmberg, L., Elvin, A., Nybacka, O., Almgren, B., Björck, C.-G., Eriksson, I.: Natural history of patients with abdominal aortic aneurysm. *Eur. J. Vasc. Surg.* **5**(2), 125–130 (1991). [https://doi.org/10.1016/S0950-821X\(05\)80675-9](https://doi.org/10.1016/S0950-821X(05)80675-9)
11. Hoornweg, L.L., Storm-Versloot, M.N., Ubbink, D.T., Koelemay, M.J.W., Legemate, D.A., Balm, R.: Meta analysis on mortality of ruptured abdominal aortic aneurysms. *Eur. J. Vasc. Endovasc. Surg.* **35**(5), 558–570 (2008). <https://doi.org/10.1016/j.ejvs.2007.11.019>
12. Huynh, A.T., Miller, K.: Towards accurate measurement of abdominal aortic aneurysm wall thickness from CT and MRI. In: *Computational Biomechanics for Medicine—Towards Translation and Better Patient Outcomes*. Springer International Publishing (2022)
13. Hyhlik-Dürr, A., Krieger, T., Geisbüsch, P., Kotelis, D., Able, T., Böckler, D.: Reproducibility of deriving parameters of AAA rupture risk from patient-specific 3D finite element models. *J. Endovasc. Ther.* **18**(3), 289–298 (2011). <https://doi.org/10.1583/10-3384MR.1>
14. Joldes, G.R., Miller, K., Wittek, A., Doyle, B.: A simple, effective and clinically applicable method to compute abdominal aortic aneurysm wall stress. *J. Mech. Behav. Biomed. Mater.* **58**, 139–148 (2016). <https://doi.org/10.1016/j.jmbbm.2015.07.029>
15. Joldes, G.R., Miller, K., Wittek, A., Forsythe, R.O., Newby, D.E., Doyle, B.J.: BioPARR: a software system for estimating the rupture potential index for abdominal aortic aneurysms. *Sci. Rep.* **7**(1), 4641 (2017). <https://doi.org/10.1038/s41598-017-04699-1>
16. Kitware. VTK—The Visualization Toolkit. Retrieved 12 Mar 2022. <https://vtk.org/>
17. Long, A., Rouet, L., Lindholt, J.S., Allaire, E.: Measuring the maximum diameter of native abdominal aortic aneurysms: review and critical analysis. *Eur. J. Vasc. Endovasc. Surg.* **43**(5), 515–524 (2012). <https://doi.org/10.1016/j.ejvs.2012.01.018>
18. Madenci, E., Guven, I.: *The Finite Element Method and Applications in Engineering Using ANSYS®*. Springer, Berlin (2015)
19. Mahesh, M.: *The essential physics of medical imaging*, third edition. *Med. Phys.* **40**(7), 77301. <https://doi.org/10.1118/1.4811156>
20. Maier, A., Gee, M.W., Reeps, C., Pongratz, J., Eckstein, H.-H., Wall, W.A.: A comparison of diameter, wall stress, and rupture potential index for abdominal aortic aneurysm rupture risk prediction. *Ann. Biomed. Eng.* **38**(10), 3124–3134 (2010). <https://doi.org/10.1007/s10439-010-0067-6>
21. Martufi, G., Christian Gasser, T.: Review: the role of biomechanical modeling in the rupture risk assessment for abdominal aortic aneurysms. *J. Biomech. Eng.* **135**(2), 021010 (2013). <https://doi.org/10.1115/1.4023254>

22. Miller, K., Joldes, G.R., Qian, J., Patel, A.P., Jung, M.S., Tavner, A.C.R., Wittek, A.: Maximum principal AAA wall stress is proportional to wall thickness. In: Nielsen, P.M.F., Wittek, A., Miller, K., Doyle, B., Joldes, G.R., Nash, M.P. (eds.) *Computational Biomechanics for Medicine*, pp. 43–53. Springer International Publishing (2019). https://doi.org/10.1007/978-3-319-75589-2_5
23. Miller, K., Lu, J.: On the prospect of patient-specific biomechanics without patient-specific properties of tissues. *J. Mech. Behav. Biomed. Mater.* **27**, 154–166 (2013). <https://doi.org/10.1016/j.jmbbm.2013.01.013>
24. Miller, K., Mufty, H., Catlin, A., Rogers, C., Saunders, B., Sciarrone, R., Fourneau, I., Meuris, B., Tavner, A., Joldes, G.R., Wittek, A.: Is there a relationship between stress in walls of abdominal aortic aneurysm and symptoms? *J. Surg. Res.* **252**, 37–46 (2020). <https://doi.org/10.1016/j.jss.2020.01.025>
25. Moll, F.L., Powell, J.T., Fraedrich, G., Verzini, F., Haulon, S., Waltham, M., van Herwaarden, J.A., Holt, P.J.E., van Keulen, J.W., Rantner, B., Schlösser, F.J.V., Setacci, F., Ricco, J.-B.: Management of abdominal aortic aneurysms clinical practice guidelines of the European society for vascular surgery. *Eur. J. Vasc. Endovasc. Surg.* **41**, S1–S58 (2011). <https://doi.org/10.1016/j.ejvs.2010.09.011>
26. Nicholls, S.C., Gardner, J.B., Meissner, M.H., Johansen, K.H.: Rupture in small abdominal aortic aneurysms. *J. Vasc. Surg.* **28**(5), 884–888 (1998). [https://doi.org/10.1016/S0741-5214\(98\)70065-5](https://doi.org/10.1016/S0741-5214(98)70065-5)
27. Parkinson, F., Ferguson, S., Lewis, P., Williams, I.M., Twine, C.P.: Rupture rates of untreated large abdominal aortic aneurysms in patients unfit for elective repair. *J. Vasc. Surg.* **61**(6), 1606–1612 (2015). <https://doi.org/10.1016/j.jvs.2014.10.023>
28. Perry, R.J.T., Martin, M.J., Eckert, M.J., Sohn, V.Y., Steele, S.R.: Colonic ischemia complicating open vs endovascular abdominal aortic aneurysm repair. *J. Vasc. Surg.* **48**(2), 272–277 (2008). <https://doi.org/10.1016/j.jvs.2008.03.040>
29. Reeps, C., Gee, M., Maier, A., Gurdan, M., Eckstein, H.-H., Wall, W.A.: The impact of model assumptions on results of computational mechanics in abdominal aortic aneurysm. *J. Vasc. Surg.* **51**(3), 679–688 (2010). <https://doi.org/10.1016/j.jvs.2009.10.048>
30. Shigley, J.E.: *Shigley's Mechanical Engineering Design*. Tata McGraw-Hill Education (2011)
31. Speelman, L., Bosboom, E.M.H., Schurink, G.W.H., Hellenthal, F.A.M.V.I., Buth, J., Breeuwer, M., Jacobs, M.J., van de Vosse, F.N.: Patient-specific AAA wall stress analysis: 99-percentile versus peak stress. *Eur. J. Vasc. Endovasc. Surg.* **36**(6), 668–676 (2008). <https://doi.org/10.1016/j.ejvs.2008.09.007>
32. Tavner, A., Mufty, H., Catlin, A., Rogers, C., Saunders, B., Sciarrone, R., Joldes, G., Wittek, A., Miller, K.: Investigating the relationship between AAA wall stress and symptoms exhibited by patients, pp. 1–15. Research Report, The University of Western Australia, Intelligent Systems for Medicine Laboratory (2018)
33. Vande Geest, J.P., Wang, D.H.J., Wisniewski, S.R., Makaroun, M.S., Vorp, D.A.: Towards a noninvasive method for determination of patient-specific wall strength distribution in abdominal aortic aneurysms. *Ann. Biomed. Eng.* **34**(7), 1098–1106 (2006). <https://doi.org/10.1007/s10439-006-9132-6>
34. Wanhainen, A., Verzini, F., Van Herzele, I., Allaire, E., Bown, M., Cohnert, T., Dick, F., Van Herwaarden, J., Karkos, C., Koelemay, M., Kölbel, T., Loftus, I., Mani, K., Melissano, G., Powell, J. T., Szerberin, Z.: Editor's choice—European society for vascular surgery (ESVS) 2019 clinical practice guidelines on the management of abdominal aorto-iliac artery aneurysms. *Eur. J. Vasc. Endovasc. Surg.* **57**(1), 8–93 (2019)
35. Zhu, L., Kolesov, I., Gao, Y., Kikinis, R., Tannenbaum, A.: An effective interactive medical image segmentation method using fast GrowCut. In: *International Conference on Medical Image Computing and Computer-Assisted Intervention. Workshop on Interactive Methods*, vol. 17(9) (2014)

Analysis of Head Protection Performance of Bicycle Helmets by Full-Scale Computational Biomechanics Modelling of Real-World Car-to-Cyclist Accidents



Fang Wang, Ke Peng, Jiajie Yin, Shenghui Hu, Fan Li, and Lin Hu

Abstract Cyclist head injuries are common in car-to-cyclist accidents. Helmets remain the most commonly used protective equipment against such injuries. However, discussion about the effectiveness of bicycle helmets in actual car-to-cyclist accidents continues. In this study, we computationally reconstructed three real-world car-to-cyclist accidents using full-scale subject-specific cyclist models (i.e. representing cyclists involved in the reconstructed accidents) that consist of finite element models of the cyclist head-neck complex and multibody models of the remaining segments of the cyclist body. In all analysed accidents, the cyclists were not wearing helmets. To analyse helmet effectiveness, for each analysed accident, we also conducted computer simulations for cyclist wearing a helmet. The analysis was conducted for four different helmet types using previously validated finite element helmet models. Comparison between the results for cyclists wearing a helmet and cyclists without a helmet indicated that wearing a helmet appreciably reduces the skull fracture risk as measured by the head injury criterion (HIC). Evaluation using the maximum principal strain (MPS) brain injury criterion suggested that wearing a helmet could reduce the brain injury risk in cyclists.

Keywords Car-to-cyclist accident · Bicycle helmet · Finite element model · Multibody model · Head injury · Brain injury

F. Wang (✉) · K. Peng · J. Yin · S. Hu · L. Hu
School of Automotive and Mechanical Engineering, Changsha University of Science and Technology, Changsha 410114, China
e-mail: wangfang@csust.edu.cn

F. Li
State Key Laboratory of Advanced Design and Manufacturing for Vehicle Body, Hunan University, Changsha 410082, China

1 Introduction

Cyclists are vulnerable road users (VRU). Head injuries are the most common injury type in traffic accidents involving cyclists, and brain injuries are the leading cause of cyclist deaths resulting from such accidents [1–3]. Cyclists wear helmets as protection while riding. Investigation of performance of helmets in protecting cyclists' heads from injury has been traditionally conducted experimentally using headform impactor and crash-test dummies. Computational modelling has made such investigation more efficient and cost-effective allowing comprehensive analysis of helmet performance under various loading conditions [4–7]. Bourdet et al. [6] determined the initial impact conditions of cyclist heads in traffic accidents from the analysis of real-world bicycle accidents and computationally predicted the cyclist head/brain injury risk using the stand-alone finite element (FE) human head model (head-only). Using an approach similar to that of Bourdet et al. [6], Xiao et al. [7] investigated the effects of impact velocity, impact angle, and helmet usage on cyclist brain injury responses using finite element (FE) and multibody (MB) models and observed an apparent reduction in brain pressure and skull bone principal stress when using a helmet. The studies by Bourdet et al. [6], Xiao et al. [7], and many others [5, 8, 9] used head-only FE models for predicting the head and brain injury responses due to high computational cost of full-scale (using the entire human body models) FE simulations and time-consuming process required to adjust a FE model to represent a cyclist posture in the analysed accidents. However, the following important limitations of head-only models have been identified in the literature: disregarding the effects of other segments of the human body on the head kinematics and inability to simulate the head impact with the road surface (often referred to as a secondary impact) [10–13].

In car-to-cyclist accidents, a cyclist's head is often subjected to two impacts: the primary impact with the car windshield and secondary impact with the road surface. However, many studies have solely focused on the primary impact and ignored the secondary impact [14–16]. Some of them, such as the study by Chen et al. [14] who reconstructed real-world car-to-motorcycle impacts, predicted that helmets can remarkably reduce the risk of head injury. However, caution should be exercised when interpreting these results as it has been indicated in the literature that disregarding the secondary impact may underestimate the cyclists' (and other VRUs) brain injury severity and risk [13].

This paper aims to analyse the performance of bicycle helmets in protecting from head and brain injuries through the computer modelling reconstruction of four real-world car-to-cyclist impact accidents and comparison of the head and brain injury risk and severity when helmet is worn and when cyclist does not wear helmet. We used a previously developed and validated full-scale human body model that combines finite element (FE) model of the head-neck complex and multibody dynamics (MB) model

of the remaining segments of the human body [13, 17]. The model was anthropometrically scaled to represent a cyclist involved in the analysed accidents. Application of a model that combines advantages of FE and MB analyses allowed us to simulate the entire impact event and take into account both primary and secondary impacts without compromising the computational efficiency.

2 Materials and Methods

2.1 Analysis Process

First, full-scale MB subject-specific cyclist models were built using the information available in the accident database and subsequently applied in car-to-pedestrian impact accident reconstruction to obtain the kinematics of cyclists during the accidents. Then, detailed reconstruction of the biomechanical responses of the brain was conducted using cyclists FE–MB models (i.e. the models that consist of FE model of head-neck FE complex and MB model of the remaining segments of the human body) and car windshield FE models. Finally, the injury parameters of cyclist head and brain predicted for the situations when helmets are worn and when cyclists do not wear helmets were analysed to evaluate the protective performance of helmets. The workflow is shown in Fig. 1.

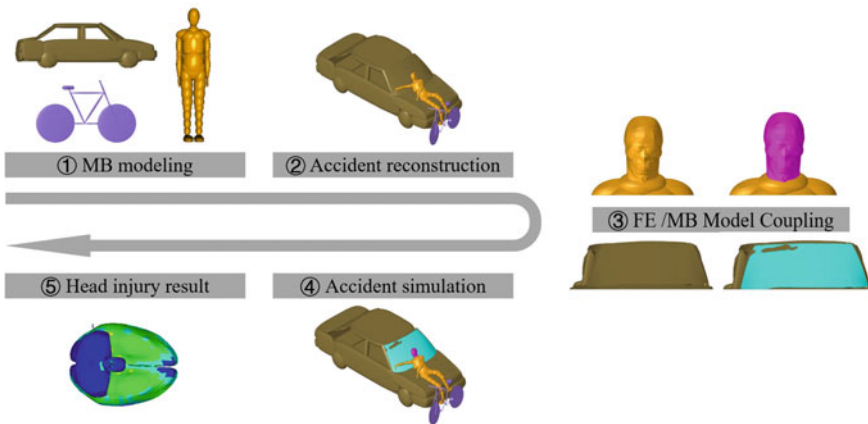





Fig. 1 Workflow of the current research

Table 1 Information about the analysed car-to-bicycle impact accidents

Accident number	Car impact speed (km/h)	Bicycle speed (m/s)	Cyclist injury	Impact location
Accident 1	32	1.5	Serious injury	
Accident 2	35	1.2	Death	
Accident 3	40	1.1	Serious injury	

2.2 Accident Information

In this study, three typical car-to-cyclist impact accidents were selected from the IVAC database (the In-Depth Investigation of Vehicle Accident in Changsha) [18] established by Hunan University (Changsha, China) in 2006 to collect the on-site data of traffic accidents involving VRUs in Changsha. The criteria for accident selection were

- (1) cyclist must be older than 18 and taller than 1.5 m;
- (2) the collected accident information is sufficient for accident reconstruction and its usage for research is permitted;
- (3) the cyclist head impacted the car windshield;
- (4) the car impact speed (i.e. car speed at the time of impact with the bicycle) was between 20 and 40 km/h;
- (5) cyclists did not wear helmets at the time of the accident.

Information about the three accidents analysed in this study is reported in Table 1.

2.3 Accident Reconstruction

We reconstructed the real-world car-to-cyclist impact accidents described in Sect. 2.2 using the subject-specific cyclist models, vehicle models, and bicycle models implemented in the MADYMO MB analysis package by TASS International Software and Services (Helmond, The Netherlands; <https://www.tassinternational.com/madyimo>)

Table 2 Information about mass and geometry of the cars involved in the analysed accidents

Accident number	Car manufacturer	Mass (kg)	Length (mm)	Width (mm)	Height (mm)
Accident 1	Shanghai Volkswagen	1500	4428	1660	1420
Accident 2	FAW Volkswagen	1565	4818	1843	1432
Accident 3	Shanghai Volkswagen	1540	4595	1750	1430

[17]. The specific accident reconstruction process was similar to that used in our previous research [19]. The models used in the MB reconstruction are described in the following subsections.

2.3.1 Car Models

The cars involved in the analysed real-world accidents are small passenger cars typical in China. Car MB models were created by geometrically modifying the small passenger car model validated and used in our previous studies [13, 19]. The modifications included car mass and geometry/dimensions of car front components to match the characteristics of cars involved in the analysed accidents (Table 2). Car stiffness parameters were derived from the previous research [20]. The main features of each car in the accidents are given in Table 2.

2.3.2 Bicycle Models

The bicycle models in this study include all key bicycle components: frame, front fork, front/rear wheels, pedal shaft, pedals, and seat. Each part of the model was defined as a rigid body with defined mass and inertia moment. The frame parts were rigidly connected using ‘bracket’ joints available in the MB system dynamics software package MADYMO V 7.7 [21]. Front fork and pedal board were connected with the frame by revolute joints. Information about the mass and geometry of the bicycles involved in the analysed accidents is in Table 3.

Table 3 Mass and key geometric characteristics of the bicycles involved in the accidents analysed in this study

Accident number	Mass (kg)	Wheel base (mm)	Tyre radius (mm)	Seat height (mm)
Accident 1	15	950	300	850
Accident 2	20	950	310	830
Accident 3	10.5	820	200	760

2.3.3 Multibody (MB) Cyclist Models

The 50% male and 5% female TNO (The Netherlands Organisation for Applied Scientific Research, <https://www.tno.nl/en/>) pedestrian models (Table 4) were scaled according to the information about anthropometry of the cyclists involved in the analysed accidents (Table 5) to obtain the subject-specific cyclist models. The models of male and female cyclists are obtained by scaling from the 50% and 5% male and female models, respectively. The scaling was conducted using the Generator of Body Data (GEBOD) [22] available in the MADYMO package.

Table 4 Anthropometric information about 50% male and 5% female multibody models (by The Netherlands Organisation for Applied Scientific Research TNO, <https://www.tno.nl/en/>) used in this study



	5% female	50% male
		
Height (m)	1.53	1.74
CG height (m)	0.843	0.958
Weight (kg)	49.8	75.7

Table 5 Key anthropometric information about the cyclists involved in the accidents analysed in this study

Accident	Cyclist information			
	Gender	Height (cm)	Weight (kg)	Age
Accident 1	Male	165	55	62
Accident 2	Male	165	60	65
Accident 3	Female	161	45	23

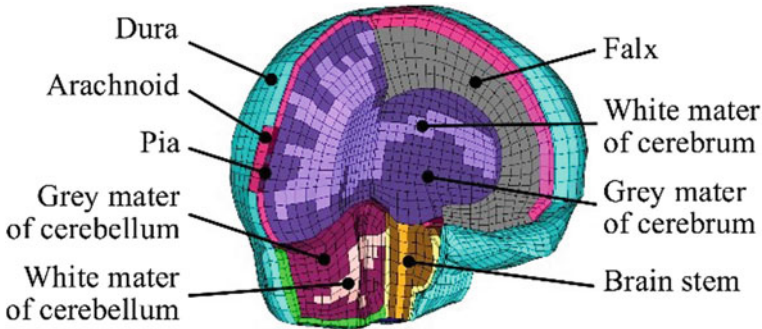


Fig. 2 THUMS Version 5.02 brain model used in this study (copied from our previous publication [24])

2.4 Models for Investigation of the Head and Brain Injury Risk and Severity




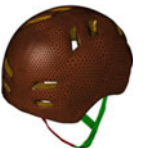
2.4.1 Finite Element (FE)–Multibody (MB) Cyclist Models

To obtain the information about the cyclist brain deformation during the car-to-cyclist impact accidents, we used a FE–MB pedestrian model developed and validated in our previous study [13]. The model was built by combining the head-neck complex from the Total Human Model for Safety THUMS Version 5.02 finite element human body FE model by Toyota Motor Corporation and Toyota Central R&D Labs [23] and the remaining human body segments from the full-scale MB model an adult pedestrian by The Netherlands Organisation for Applied Scientific Research TNO (The Netherlands Organisation for Applied Scientific Research, <https://www.tno.nl/en/>). The THUMS brain model includes representations of all key brain tissues and anatomical components: grey mater, white mater, falx, subarachnoidal cerebrospinal fluid (CSF), dura, arachnoid, and pia (Fig. 2). The two coupled models are simultaneously executed on their own software platforms. This approach combines computational efficiency of the MB models with the FE model capabilities in predicting the skull and brain tissue deformations due to impact.

2.4.2 Finite Element Helmet Models

We used FE models of four bicycle helmets created and validated in our previous study [17]. The helmets were selected to provide representation of low-cost (Helmet 2 and Helmet 4) and medium-cost (Helmet 1 and Helmet 3) helmets available in China. Each helmet model includes three key components of helmet structure: the outer shell made of ABS or PC plastic, energy-absorbing liner made of EPS foam material, and chin strap. The contact between the helmet and the head is defined with automatic surface to surface contact available in MADYMO FE code. Key

Table 6 Information about the helmets and helmet models analysed and used in this study

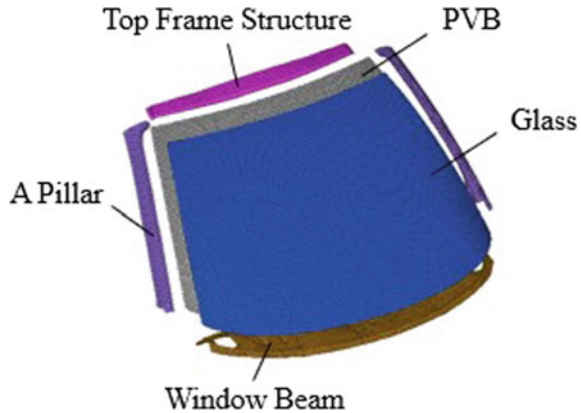
Helmet	Finite element model	Price (¥ RMB)	Mass (g)	Number of finite elements in FE helmet model		Number of nodes in FE helmet model
				Triangular elements	Tetrahedral elements	
Helmet 1		499	230	17,486	47,850	14,949
Helmet 2		89	275	16,350	42,020	12,079
Helmet 3		650	335	27,620	69,822	17,059
Helmet 4		79	390	16,652	45,541	13,276

information about the analysed helmets and helmet FE models used is in Table 6. The mechanical properties of the four helmets were obtained from material tests, and the readers are referred to our previous publication [17] to access the detailed information.

2.4.3 Finite Element Windshield Model

In the all simulation of car-to-cyclist impact accident the same FE windshield model was used (Fig. 3). The model includes the laminated safety glass (consisting of Polyvinyl butyral PVB and glass layers) and the surrounding metal frame (pillar, window beam, and top frame structure). The material parameters for the model were taken from the literature and the verification process can also be seen in the literature [8, 20].

Fig. 3 Finite element (FE) windshield model used in this study



2.4.4 Computer Simulation and Model Set-Up for Investigating Cyclist Head and Brain Injury

Accident reconstruction using MB cyclist and car models described in Sect. 2.3 was used to determine the initial and boundary conditions for more advanced simulations to investigate the risk and severity of cyclist head and brain injury resulting from the analysed car-to-cyclist impact accidents. In these simulations, the MB cyclist models were replaced with the FE–MB human body models (see Sect. 2.4.1 for more information about these models) (Fig. 4a). To more accurately represent interactions between the cyclist head (or helmet) and windshield, the MB car models were replaced with FE–MB models that use the FE windshield model (the model details are in Sect. 2.4.3) (Fig. 4b). The simulation set-up is shown in Fig. 5. All FE simulations in this study were conducted using the LS-DYNA 971 nonlinear explicit finite element code by Livermore Software Corporation (Livermore, CA, USA; <http://www.lstc.com>).

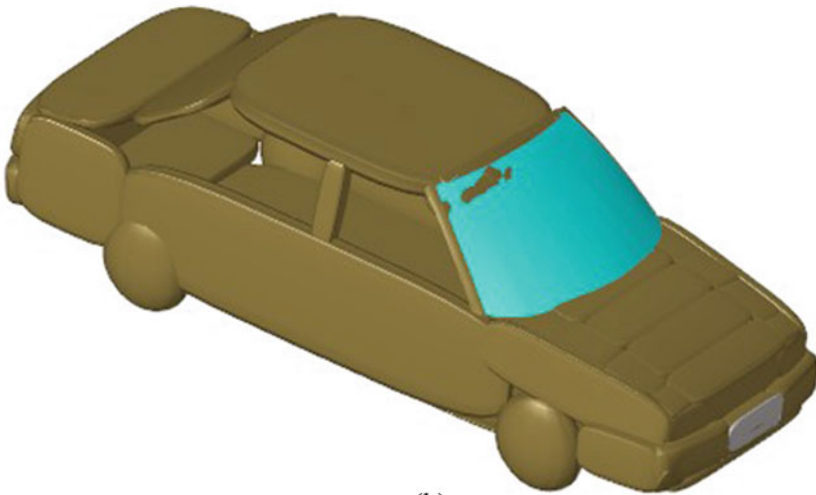
2.5 Simulation Matrix

In total, 18 computer simulations were performed in this study:

- Three simulations using the multibody cyclist (helmet not worn) and car models for reconstruction of three real-world car-to-pedestrian impact accident reconstruction.
- Three simulations of three real-world car-to-cyclist accidents using FE–MB cyclist (helmet not worn) and car models
- $3 \times 4 = 12$ simulations of three real-world car-to-cyclist accidents using FE–MB cyclist and car models with each cyclist wearing four different helmets. We followed the procedures previously used in [17] to ensure that the helmet models are properly secured to the cyclist head models.



(a)



(b)

Fig. 4 **a** Finite element (FE)—multibody system dynamics (MB) pedestrian model consisting of the FE model of the head-neck complex (pink area) and MB model of the remaining segments of the human body (orange areas). **b** Coupled FE–MB car model consisting of the FE windshield model (blue area) and MB model of the remaining components of the car structure (brown areas)

2.6 Injury Criteria

We relied on two commonly used head and brain injury criteria: (1) head injury criterion (HIC) [17, 25] and (2) maximum principal strain (MPS) brain injury criterion [26, 27].

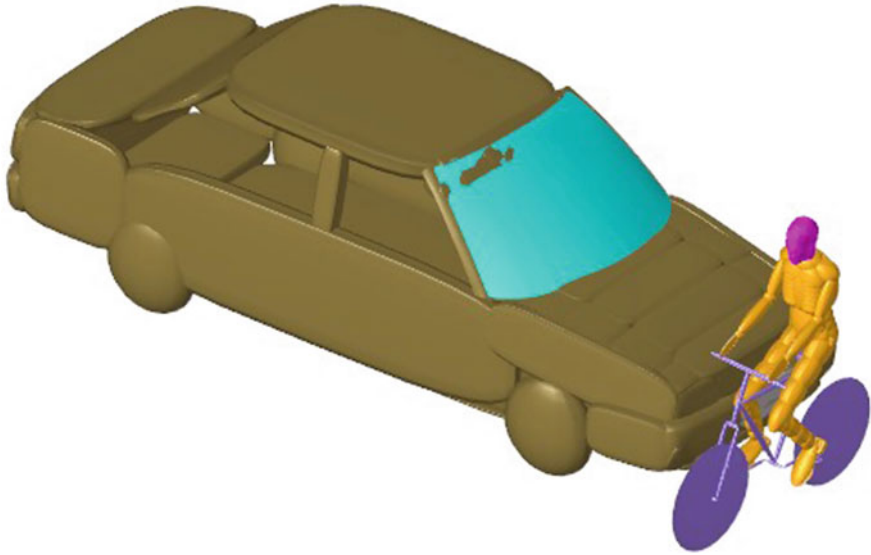


Fig. 5 Set-up of computer simulation of Accident 1 for investigation of injury risk and severity to cyclist head and brain FE–MB cyclist and car models. In this simulation, the cyclist does not wear a helmet

HIC is the most widely used head injury evaluation metric in car safety standards and regulations. It is associated with skull fractures and brain injury and calculated from the head centre of gravity (COG) resultant linear acceleration and acceleration pulse duration [28]:

$$HIC = \left\{ (t_2 - t_1) \left[\frac{1}{t_2 - t_1} \int_{t_1}^{t_2} a(t) dt \right]^{2.5} \right\}_{\max},$$

where $a(t)$ is the resultant linear acceleration of the head COG, and the time interval $(t_2 - t_1)$ is selected to maximise HIC over a maximum duration of 15 ms which is often referred to in the literature as maximise HIC₁₅ [13, 17].

Maximum principal strain (MPS) of brain tissue has been proposed for evaluation of severity of brain injuries associated with brain tissue deformation such as Diffuse Axonal Injury DAI [26]. As the peak MPS computed at a single Gauss integration point in the FE head model may be prone to modelling artefacts, we used the 98th percentile maximum principal strain (referred to as $MPS_{0.98}$).

3 Results

3.1 Kinematic of the Cyclists

Figures 6, 7, and 8 show the predicted cyclist kinematics in all analysed accidents. The cyclist’s lower limbs contacted the car first, then the cyclist’s head impacted the windshield. At 1000 ms, the head impacted the road surface. No significant differences in kinematics were found between the three simulations (MB accident reconstruction, simulation with FE–MB cyclist and vehicle models, and simulation with helmet 1) of Accident 3.




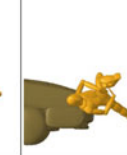
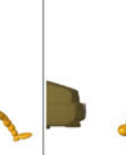




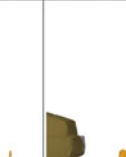
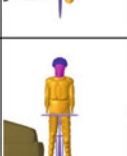
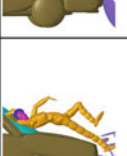
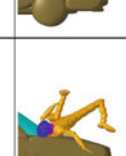
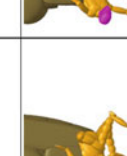

Accident 1	0 ms	200 ms	500 ms	800 ms	1000 ms
MB accident reconstruction					
Simulation using FE-MB cyclist and car models. Cyclist does not wear a helmet					
Simulation using FE-MB cyclist and car models. Cyclist wears helmet 1					

Fig. 6 Predicted cyclist kinematics in Accident 1





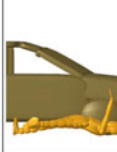



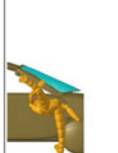




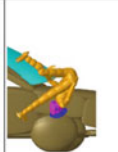

Accident 2	0 ms	200 ms	500 ms	800 ms	1000 ms
MB accident reconstruction					
Simulation using FE-MB cyclist and car models. Cyclist does not wear a helmet					
Simulation using FE-MB cyclist and car models. Cyclist wears helmet 1					

Fig. 7 Predicted cyclist kinematics in Accident 2














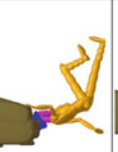

Accident 3	0 ms	200 ms	500 ms	800 ms	1000 ms
MB accident reconstruction					
Simulation using FE-MB cyclist and car models. Cyclist does not wear a helmet					
Simulation using FE-MB cyclist and car models. Cyclist wears helmet 1					

Fig. 8 Predicted cyclist kinematics in Accident 3

3.2 Head and Brain Injury Risk Analysis

3.2.1 Head Injury as Determined by Head Injury Criterion (HIC)

Reconstruction conducted using the MB cyclist and car models as well as the simulations conducted using the FE–MB models predicted that in all the analysed accidents, the cyclist heads impacted the car windshield (primary impact) and the road surface (secondary impact). We report the head injury criterion (HIC_{15}) separately for the primary and secondary impact (Fig. 9). Our computer simulation predicted that primary impact results in higher HIC_{15} than the secondary impact (Fig. 9). They also predicted that wearing a helmet appreciably reduces HIC_{15} in both primary and secondary impacts. Such reduction was more pronounced in Accident 1 and Accident 3 than in Accident 2. The predicted reduction in HIC_{15} varied between the helmets, with helmet 2 and helmet 4 providing larger reduction than helmet 1 and helmet 3.

To relate the predicted HIC_{15} to the risk of cyclist skull fracture, we used the skull fracture risk curve proposed by Yoganandan et al. [29]. We considered only the primary impact as our computer simulations predicted that it leads to higher HIC_{15} than the secondary impact (Fig. 9). Application of the skull fracture risk curve by Yoganandan et al. [29] to HIC_{15} predicted in this study indicates high risk of cyclist's skull fracture (over 95% for Accident 1 and over 80% for Accident 3) if a helmet is not worn (Fig. 10). Our results clearly predict that wearing a helmet can greatly reduce the skull fracture risk, with up to 70% reduction for Accident 1 and around 95% reduction for Accident 3.

To relate the predicted HIC_{15} to the cyclist brain injury risk, we used the risk curve by Yoganandan et al. [29] that links HIC_{15} with the risk of sustaining the injury of a given severity as defined by the Abbreviated Injury Scale (AIS). AIS is the most commonly used injury scale to quantify the injury severity [30]. We focused on severe brain injuries classified as AIS 4+ [30]. The risk of severe brain injuries predicted from HIC_{15} and injury risk curve by Yoganandan et al. [29] is similar to the risk of

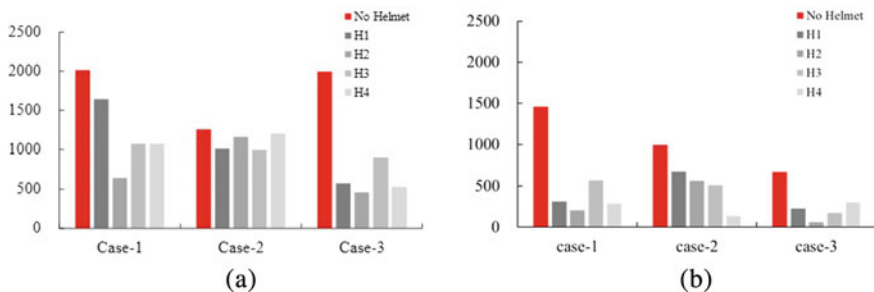


Fig. 9 Comparison of the predicted head injury criterion HIC_{15} in the analysed car-to-cyclist impact accidents for cyclists without a helmet (unhelmeted cyclists) and when wearing a helmet. Four different helmets (H1, H2, H3, and H4; Table 6) were analysed. **a** Primary impact; **b** secondary impact

Fig. 10 Reduction in the risk of cyclist skull fracture due to the helmet use in the analysed car-to-cyclist impact accidents. Skull fracture risk is calculated from HIC₁₅ using the injury risk curve by Yoganandan et al. [29]. Four different helmets (H1, H2, H3, and H4; Table 6) were analysed

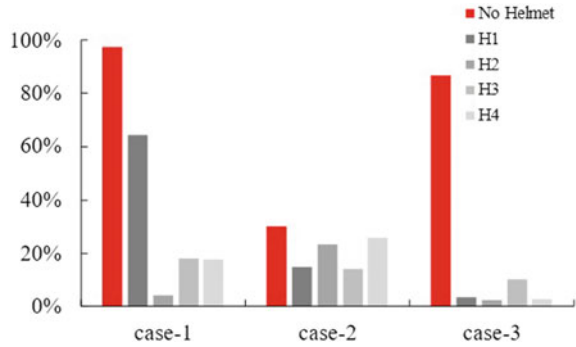
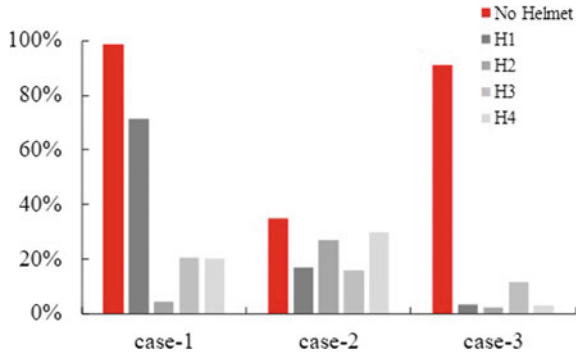


Fig. 11 Reduction in the risk of AIS 4+ brain injury when wearing helmet in the analysed car-to-cyclist impact accidents. AIS 4+ brain injury risk is determined from HIC₁₅ using the injury risk curve by Yoganandan et al. [29]. Four different helmets (H1, H2, H3, and H4; Table 6) were analysed



skull fracture (Figs. 10 and 11). As was with the skull fractures, our results predict that wearing a helmet can appreciably reduce in the AIS 4+ brain injury risk, with over 95% reduction for Accident 1 and Accident 3 (Fig. 11).

3.2.2 Brain Injury as Determined by Maximum Principal Strain Criterion

The predicted 98th percentile brain tissue maximum principal strain (MPS_{0.98}) was higher for Accident 3 than Accident 1 (Fig. 12). Opposite trend was observed for HIC₁₅ (Fig. 9a). With exception of helmet 3 in Accident 1, our results indicate that wearing a helmet reduces MPS_{0.98} (Fig. 12). However, the predicted protective effect of wearing a helmet is much less pronounced than that observed for HIC₁₅ (Figs. 9a and 12).

To relate the predicted MPS to the cyclist DAI risk, we used the risk curve by Takhounts et al. [26] that links MPS with the DAI risk. Clearly, the DAI risk predicted from MPS and injury risk curve by Takhounts et al. [26] is similar to the calculated MPS (Figs. 12 and 13). The results indicate that wearing a helmet can reduce the DAI risk of the cyclist (Fig. 13) although such reduction is much less significant than

Fig. 12 Comparison of the calculated 98th percentile brain tissue maximum principal strain ($MPS_{0.98}$) for cyclists without a helmet (unhelmeted cyclists) and when wearing a helmet. Four different helmets (H1, H2, H3, and H4; Table 6) were analysed

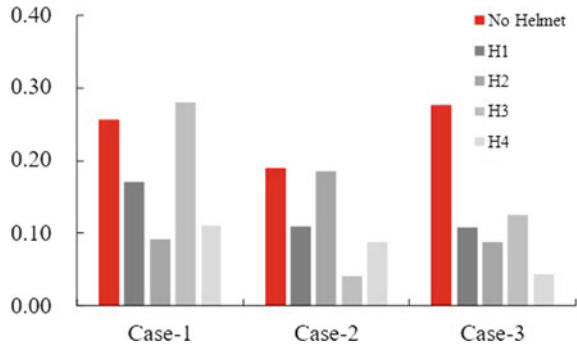
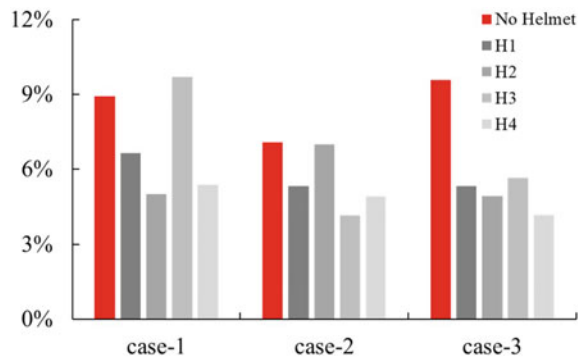


Fig. 13 Reduction in the DAI risk when wearing helmet in the analysed car-to-cyclist impact accidents. DAI risk is determined from $MPS_{0.98}$ using the injury risk curve by Takhounts et al. [26]. Four different helmets (H1, H2, H3, and H4; Table 6) were analysed



that when evaluating the risks of skull fracture and AIS 4+ brain injury with HIC (Figs. 10 and 11).

4 Discussion and Study Limitations

Results of our computer simulations of car-to-cyclist impact accidents suggest that wearing a helmet appreciably reduces the cyclist’s head injury criterion (HIC) and HIC-determined risk of skull fracture and severe (classified as Abbreviated Injury Scale AIS 4+) brain injury (Figs. 9, 10, and 11). These results are consistent with the observations made by other researchers [4, 5, 31–33].

Our results predict that helmets can reduce the maximum principal strain (MPS) of the brain tissue and MPS-based DAI risk in cyclists for almost all car-to-cyclist accidents analysed here (Figs. 12 and 13). However, this reduction is clearly less pronounced than that observed for HIC (Figs. 9, 10, and 11). Some previous studies have used brain tissue deformation to evaluate the effectiveness of helmets in protecting cyclists’ brain from injury. For example, Fahlstedt et al. [34] found, using the finite element (FE) head model, that helmets can reduce the predicted MPS by

up to 43%. This observation is consistent with the results of our study that predicted that wearing helmet can reduce the cyclist's brain tissue MPS by between 5 (helmet 2 in Accident 2) and 80% (helmet 4 in Accident 3) (Fig. 12).

Four helmets analysed in this study differed in weight and price (Table 6). No obvious correlation was found between the reduction in the skull fracture and brain injury risk and helmet weight (Figs. 10, 11, and 13). Less expensive helmets (helmet 2 and helmet 4) seemed to perform somewhat better in reducing cyclists' skull and brain injury risk (Figs. 10, 11, and 13). This observation is consistent with the results of our previous similar research [17] in which we investigated the performance of helmets in typical single bicycle accident scenarios (skidding and curb-impact) and found no relationship between the helmet price and helmet injury prevention potential.

We would like to point out the following three limitations of this study. First, we analysed only three car-to-cyclist impact accidents and four helmets. While this provides insight into the head (i.e. skull and brain) injury prevention performance of the analysed bicycle helmets, more comprehensive analysis that include more accidents and more helmet types would be required to derive more general conclusions about the performance of different helmets in car-to-cyclist impact accidents. Second, in all model used in this study, the lower section of the strap of the helmet was rigidly constrained to the chin. This totally prevents movement between the helmet strap and cyclist head. Third, for all analysed helmets and cyclists, we used the same characteristics/properties of contact interactions between the scalp and helmet and the same friction coefficient between the scalp and helmet.

5 Conclusions

In this study, we investigated the effectiveness bicycle helmets in protecting the cyclist's skull and brain from injury in selected typical real-world car-to-cyclist impact accidents using full-scale (i.e. representing the entire cyclist body) computational biomechanics models. We reconstructed three accidents, analysed four different bicycle helmets, and conducted a series of simulations using finite element (FE)—multibody dynamic (MB) cyclist models that consists of the FE model of the head-neck complex and MB model of the remaining segments of the human body. Based on the limited number of accidents analysed in the current study, comparison of the skull and brain injury responses of cyclists wearing a helmet and when helmet is not worn suggests the following:

- Bicycle helmets can appreciably reduce the risk of cyclist's skull fracture and severe brain injury as evaluated by the head injury criterion HIC. When the maximum principal strain MPS of the brain tissue is used as the brain injury criterion, the predicted protective effect of wearing a helmet is less pronounced than that observed for HIC.
- Performance of helmets in protecting the cyclist's skull and brain from injury varies between the accidents.

- Less expensive helmets seem to offer slightly better protection from injury, and the helmet price does not appear to be a decisive factor determining the helmet safety performance.

References

1. Chen, W.Y., Guo, J.: Characteristics analysis of traffic injury related to electric bicycle: a single hospital study. *Zhejiang J. Traum. Surg.* **18**(2), 157–159 (2013)
2. Nie, J., Yang, J.K.: A study on the dynamic response and injury of cyclist based on car-bicycle accident reconstruction. *Automot. Eng.* **37**(2), 160–167 (2015)
3. Hu, L., et al.: The injury epidemiology of adult riders in vehicle-two-wheeler crashes in China, Ningbo, 2011–2015. *J. Saf. Res.* **72**, 21–28 (2020)
4. Fahlstedt, M., Halldin, P., Kleiven, S.: Importance of the bicycle helmet design and material for the outcome in bicycle accidents. In: *International Cycling Safety Conference*, Gothenburg, Sweden (2014)
5. Levadnyi, I., et al.: Finite element analysis of impact for helmeted and non-helmeted head. *J. Med. Biol. Eng.* **38**(4), 587–595 (2018)
6. Bourdet, N., et al.: Experimental and numerical considerations of helmet evaluation under oblique impact. *J. Transp. Saf. Secur.* 1–14 (2019)
7. Xiao, Z., et al.: A study on motorcyclist head responses during impact against front end of vehicle. *Int. J. Crashworthiness* **27**(1), 147–159 (2022)
8. Yao, J.F., Yang, J.K., Otte, D.: Investigation of head injuries by reconstructions of real-world vehicle-versus-adult-pedestrian accidents. *Saf. Sci.* **46**(7), 1103–1114 (2008)
9. Fahlstedt, M., Halldin, P., Kleiven, S.: Comparison of multibody and finite element human body models in pedestrian accidents with the focus on head kinematics. *Traffic Inj. Prev.* **17**(3), 320–327 (2016)
10. Ghajari, M., et al.: Effects of the presence of the body in helmet oblique impacts. *Accid. Anal. Prev.* **50**(1), 263–271 (2013)
11. Feist, F., Klug, C.: A numerical study on the influence of the upper body and neck on head kinematics in tangential bicycle helmet impact. In: *International Research Council on Biomechanics of Injury (IRCOBI)*, Malaga, Spain (2016)
12. Meng, S.Y., Fahlstedt, M., Halldin, P.: The effect of impact velocity angle on helmeted head impact severity. In: *International Research Council on Biomechanics of Injury (IRCOBI)*, Athens, Greece (2018)
13. Wang, F., et al.: Prediction of pedestrian brain injury due to vehicle impact using computational biomechanics models: are head-only models sufficient? *Traffic Inj. Prev.* **21**(1), 102–107 (2020)
14. Sahoo, D., et al.: Development of skull fracture criterion based on real-world head trauma simulations using finite element head model. *J. Mech. Behav. Biomed. Mater.* **57**, 24–41 (2016)
15. Bourdet, N., et al.: In-depth real-world bicycle accident reconstructions. *Int. J. Crashworthines.* **19**(3), 222–232 (2014)
16. Chen, J.G., et al.: FEA of helmet-head injury protection based on motorcycle accident reconstruction. In: *Measuring Technology and Mechatronics Automation (ICMTMA)*. Institute of Electrical and Electronics Engineers, Hongkong, China (2013)
17. Wang, F., et al.: Evaluation of the head protection effectiveness of cyclist helmets using full-scale computational biomechanics modelling of cycling accidents. *J. Safety Res.* **80**, 109–134 (2022)

18. Nie, J., Yang, J.: A study of bicyclist kinematics and injuries based on reconstruction of passenger car–bicycle accident in China. *Accid. Anal. Prev.* **71**, 50–59 (2014)
19. Wang, F., et al.: Reconstruction of real-world car-to-pedestrian accident using computational biomechanics model: effects of the choice of boundary conditions of the brain on brain injury risk. In: *Computational Biomechanics for Medicine, MICCAI*. Springer, Quebec City, Canada (2017)
20. Li, F., Yang, J.K.: A study of head-brain injuries in car-to-pedestrian crashes with reconstructions using in-depth accident data in China. *Int. J. Crashworthiness* **15**(2), 117–124 (2010)
21. TNO: *Madymo Human Body Models Manual Release 7.7* (2017)
22. TNO: *MADYMO Utilities Manual, Version 7.7*. TASS International, Helmond, The Netherlands (2017)
23. Shigeta, K., Kitagawa, Y., Yasuki, T.: Development of next generation human FE model capable of organ injury prediction. In: *International Technical Conference on the Enhanced Safety of Vehicles (ESV)*. National Highway Traffic Safety Administration, Stuttgart, Germany (2009)
24. Wang, F., et al.: Prediction of brain deformations and risk of traumatic brain injury due to closed-head impact: quantitative analysis of the effects of boundary conditions and brain tissue constitutive model. *Biomech. Model. Mechanobiol.* **17**(4), 1165–1185 (2018)
25. King, A.I.: *The Biomechanics of Impact Injury. Biomechanical Response, Mechanisms of Injury, Human Tolerance and Simulation*, vol. 242. Springer Nature, Switzerland (2018)
26. Takhounts, E.G., et al.: Development of brain injury criteria (BrIC). *Stapp Car Crash J.* **57**, 243–266 (2013)
27. Giordano, C., Kleiven, S.: Evaluation of axonal strain as a predictor for mild traumatic brain injuries using finite element modelling. *Stapp Car Crash J.* **58**(58), 29–62 (2014)
28. Wang, F., et al.: Investigation of prediction effectiveness of brain injury criteria on injury risk through reconstruction of pedestrian impact accidents. *China J. Highw. Transp.* **31**(4), 235–244 (2018)
29. Yoganandan, N., Nahum, A.M., Melvin, J.W.: *Accidental Injury. Biomechanics and Prevention*, vol. 104. Springer, London (2015)
30. Gennarelli, T.A., Wodzin, E.: *Abbreviated Injury Scale 2005, Update 2008*. Association for Advancement of Automatic Medicine, Barrington, USA (2008)
31. McIntosh, A.S., Lai, A., Schilter, E.: Bicycle helmets: head impact dynamics in helmeted and unhelmeted oblique impact tests. *Traffic Inj. Prev.* **14**(5), 501–508 (2013)
32. McNally, D.S., Whitehead, S.: A computational simulation study of the influence of helmet wearing on head injury risk in adult cyclists. *Accid. Anal. Prev.* **60**, 15–23 (2013)
33. Cripton, P.A., et al.: Bicycle helmets are highly effective at preventing head injury during head impact: head-form accelerations and injury criteria for helmeted and unhelmeted impacts. *Accid. Anal. Prev.* **70**(70), 1–7 (2014)
34. Fahlstedt, M., Halldin, P., Kleiven, S.: The protective effect of a helmet in three bicycle accidents—a finite element study. *Accid. Anal. Prev.* **91**, 135–143 (2016)

Fluid Biomechanics

Modelling the Blood Flow and Drug Transport in an Anatomically Accurate Rat Liver



Harvey Ho, Chong Sheng Chuah, and Uta Dahmen

Abstract In this paper, we present an *in silico* model for the blood flow and drug transport in an anatomically accurate rat liver where the vascular geometry of the portal vein (PV) and hepatic vein (HV) was digitized from microCT images. Assuming Poiseuille flow in veins, we were able to compute the flow rate and blood pressure in each vascular segment of the PV and HV trees. With the pressure gradients in the PV and HV trees configured as 3 mmHg and 4 mmHg, respectively, the total flow rates in the PV and HV trees were calculated as 12 mL/min and 16 mL/min. In addition, we quantified the portal flow to the four rat liver lobes based on their supplying vessels. By solving a partial differential equation, we simulated the perfusion of a virtual drug across the PV tree over 1.3 s after a single dosage of 50 mg/Kg. In conclusion, we constructed simple computational models for hepatic flow and drug transport in a rat liver with realistic vascular geometries. The model may be used in conjunction with other *in silico* models or multiscale physiological, pharmacological and surgical platforms.

Keywords Rat liver · Blood flow · Portal vein · Drug transport · Model

1 Introduction

The rat liver is frequently used in various physiological, pharmacological and surgical experiments. For example, rat livers were used in hepatobiliary surgical experiments where different portions of liver mass were removed for regeneration analysis [1]. It was found that a rat might still survive after 95% of its parenchyma was removed. The rat liver is often used in metabolism experiments. Much of our knowledge of metabolic zones in liver lobules (the functioning units of a liver) were derived from experiments on rat or murine livers [2]. For example, it was found that the oxygen

H. Ho (✉) · C. S. Chuah

Auckland Bioengineering Institute, The University of Auckland, Auckland, New Zealand
e-mail: harvey.ho@auckland.ac.nz

U. Dahmen

Department of General, Visceral and Vascular Surgery Jena University, Jena, Germany

© The Author(s), under exclusive license to Springer Nature Switzerland AG 2023

M. P. Nash et al. (eds.), *Computational Biomechanics for Medicine*,

https://doi.org/10.1007/978-3-031-34906-5_8

and fatty acid uptake played a vital role in the zonation of carbohydrate metabolism and lipid distribution in rat livers [2, 3]. This is a typical example of heterogeneous zonation of metabolism in liver lobules.

The hepatic flow plays a central role in many liver functions such as regeneration after hepatectomy, oxygen and nutrient transportation and uptake. Although the macroscopical appearance of rat livers is quite different from that of human livers, the rat and human livers have similar supply and drainage patterns [4]. In brief, the parenchyma of rat livers is perfused by hepatic arteries (HAs) and portal veins (PVs) and drained by hepatic veins (HVs) [5]. In a study of the hepatic arterial buffer response (HABR) mechanism, i.e. the arterial flow buffers the changes in portal flow, the flow rates in rat livers were measured by ultrasonic perivascular flow probes [6]. It was found that in baseline conditions, i.e. without vessel ligations, the PV and HA inflows ranged between 8.6 ml/min –9.3 ml/min and 5.0 ml/min –5.5 ml/min, respectively. In another study, the portal pressure was measured from an inserted needle which was connected to a pressure measuring set [7]. The portal pressure was about 17.5 cmH₂O (~12.8 mmHg or ~1.7 kPa) in normal control rats.

These *in vivo* measurements provided us with great insights into the hepatic flow in rat livers. However, since the blood flow could only be measured *in vivo* in large vessels, it becomes much more technically challenging to investigate the flow in smaller intra-hepatic vessels that taper with every bifurcation. Alternatively, *in silico* models that incorporate the vascular geometry and haemodynamics principles could be applied [8]. In a previous work, a rat liver atlas was constructed from microCT images and was made available in the public domain [4]. The present work aims to make blood flow simulations based on the atlas, whilst making use of *in vivo* flow data mentioned above [6, 7].

2 Methods

2.1 The Vascular Geometry of PV and HV Trees

The rat liver consists of the left lateral lobe (LLL), median lobe (ML), right lobe (RL) and the caudate lobe (CL) [4]. The ML, RL and CL have two sub-lobes as shown in the rat liver atlas (Fig. 1). The PV and HV trees were constructed using one-dimensional (1D) cubic Hermite mesh [4]. Since the blood in hepatic veins empties into the inferior vena cava (IVC), a section of IVC is also included in the atlas. However, the atlas does not provide the geometry for hepatic arteries, because they could not be differentiated from the liver tissue in the microCT images due to limited enhancement from the contrast agent.

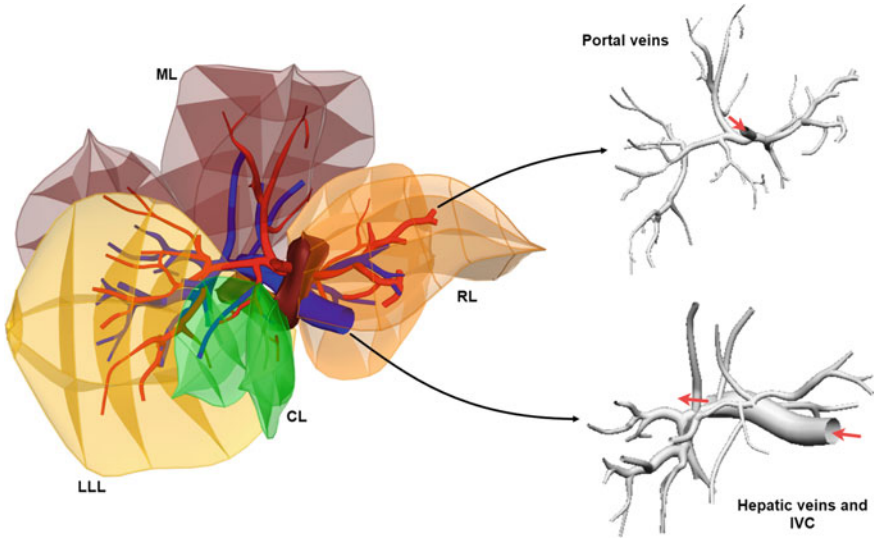


Fig. 1 Rat liver atlas [4] and the geometry of the PV and HV trees. The red arrows indicate the directions of blood flow. In portal veins, the inlet is the entry of the portal vein. The outlets are other terminals in the tree. In contrast, in hepatic veins and IVC, there are only one outlet, which is located at the IVC receiving the outflow from the liver. All other terminals in the HV tree are inlets. Abbreviations: LLL—right lateral lobe; RL—right liver; ML—median lobe; CL—caudate lobe; IVC—inferior vena cava

2.2 Blood Flow and Drug Transport Solver

A blood flow solver needs to be employed to quantify the hepatic flow in the vascular trees shown in Fig. 1. The three-dimensional (3D) Navier-Stokes equations governing fluid dynamics are very expensive to solve for such a vasculature. Alternatively, the 1D version of the Navier-Stokes equations is often used to assess the pulsatile arterial flow in a 1D vasculature [9]. Since the blood flow in the PV and HVs is quite steady [10], the governing equations can be further reduced by assuming Poiseuille flow in veins. Under this assumption, the resistance of a vessel to blood flow is characterized by its length and diameter based on the Hagen–Poiseuille equation. In essence, the blood flow solver needs to solve an algebraic equation system arranged as [11]

$$\begin{bmatrix} Q \\ P_e \\ 0 \end{bmatrix} = \begin{bmatrix} \kappa & \Gamma & \Psi \\ \Gamma^T & 0 & 0 \\ \Psi^T & 0 & 0 \end{bmatrix} \begin{bmatrix} P \\ \lambda_1 \\ \lambda_2 \end{bmatrix} \tag{1}$$

where Q , P , κ represent the flow rate, pressure gradient and resistance of blood vessels in vascular network, respectively. Γ is a permutation matrix indicating the connectivity of the vessels in a vasculature, i.e. in which way the vessels are

connected. Ψ is a matrix indicating internal nodes and terminal nodes. P_e is the prescribed pressure as boundary conditions. λ_1 and λ_2 are vectors of Laplacian multipliers. We refer the interested reader to more mathematical details and associated numerical methods of Eq. (1) in [12].

With prescribed pressure gradients between the inlets and outlets, the blood flow in each segment of a vascular tree can be determined. For the PV tree, the inlet is the portal vein (indicated by a red arrow in Fig. 1), and the outlets are the other terminals of the tree. For the HV tree and the IVC, the inlets are the entry sites of hepatic veins and the large inlet of the IVC. However, the hepatic veins and the IVC have only one outlet, i.e. the IVC that delivers the blood back to the heart (Fig. 1).

Another physiological simulation was made for the transport of a foreign species, e.g. a drug in the blood vessels. Here a partial differential equation is used[11]

$$\frac{\partial C}{\partial t} + U \frac{\partial C}{\partial x} = I(x, t) \quad (2)$$

where C is the concentration of the drug and U is the blood flow velocity. I is the dose of the drug. In terms of initial and boundary conditions, we assume that the drug arrives at the inlet of portal veins at time 0 and the initial drug concentration is $10 \mu\text{M}$. From pharmacokinetics' perspective, the concentration can be reached by intravenous injection with a bolus dose, e.g. 50 mg/Kg of phosphorothioate oligonucleotide [13]. After an intravenous injection, the drug enters the systemic circulation immediately and arrives in the portal vein within seconds. The slight delay, however, is not critical in our model since we only consider the hepatic flow not systemic circulation. Equation (2) was solved using a finite difference scheme. We used an implicit numerical scheme to solve Eq. (2)[11]

$$C_i^n = C_i^{n+1}(1 + \alpha) - \alpha C_{i-1}^{n+1} \quad (3)$$

where i denotes the position in space and n in time. $\alpha = \frac{U\Delta t}{\Delta x}$ is the Courant number. The scheme is unconditionally stable so that the constraints on the time step Δt are loosened.

The blood flow and transport solvers were developed in-house in MATLAB and Python languages [11]. An open-source software CMGUI was used for graphics processing. For more mathematical details of the solvers, we refer interested readers to literature [11] and [12].

3 Results

3.1 Flow Rates and Pressure in the PV and HV Trees

Based on the vascular geometry and the pressure and flow boundary conditions, the blood pressure (in mmHg) and flow rate (in mL/min) in the PV and HV trees were solved and shown in Fig. 2a and b. The flow rates in the PV and HV trees were 12 mL/min and 16 mL/min, respectively. In comparison, the flow rate in the IVC (~ 35 mL/min) is much higher because it receives the blood return from the lower body and internal organs.

In the context of hepatectomy, the blood flow to individual lobes of the rat liver is important but difficult to measure *in vivo*. In the *in silico* set-up, we could determine the flow rates at the supplying branches of these lobes. Figure 2a shows the sites (from S1 to S4) where the blood supplies to the RL, ML, LLL and CL were computed as 2.3 mL/min, 4.9 mL/min, 4.3 mL/min and 0.5 mL/min, respectively.

3.2 Drug Transport in the PV Tree

Assuming the drug concentration at the PV inlet at time 0 is $10 \mu\text{M}$ [13], Fig. 3 shows the transport of a virtual drug across the PV tree at three time points: 0.1s, 0.6s and 1.3s. Since the drug is not supplied continuously, the initial drug concentration at the portal inlet reduces sharply with time, and the drug was transported across the PV tree from time 0. When at bifurcations, more drug is distributed to the routes that have less resistance to the flow.

4 Discussion

We presented simple *in silico* models for the hepatic flow and drug transport in a rat liver in this paper. To our knowledge, this is the first time such simulations were made for the rat liver based on anatomically accurate vascular geometries. Furthermore, we made use of flow data measured *in vivo* from healthy rat livers [6, 7], which calibrated and indirectly validated our model. One advantage of such an *in silico* model is that it allows predictions for blood flow to be made which are otherwise difficult to measure *in vivo*, such as the flow rates to individual lobes shown in Fig. 2a.

A direct extension of the work is to apply the models to the assessment of hepatic flow under diseased conditions, e.g. cirrhosis, or flow variations after partial hepatectomy. For the former, it has been shown that the HBR mechanism still holds in a cirrhotic rat liver [6]. Specifically, after ligation of portal veins and with only 11% of baseline PV volume supplied, the PV and HA flow became 1.0 ml/min and 8.9 ml/min, respectively, versus 8.6 ml/min $-$ 9.3 ml/min and 5.0 ml/min $-$ 5.5 ml/min

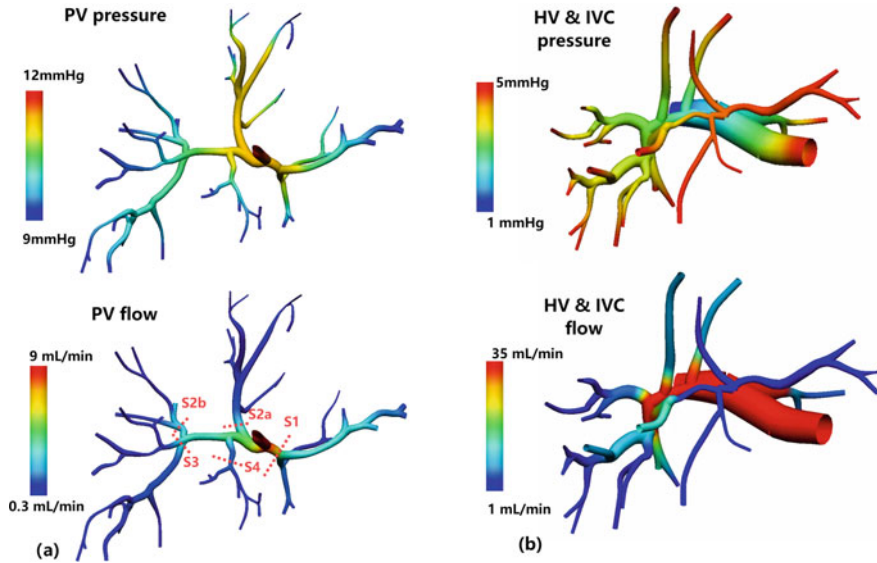


Fig. 2 Blood pressure and flow rate in **a** the PV tree and **b** the HV tree. The flow rates in the PV and HV trees were 12 mL/min and 16 mL/min, respectively. Blood supply to individual lobes was determined from the flow rates at sites S1 (2.3 mL/min), S2 (4.9 mL/min), S3 (4.9 mL/min) and S4 (0.5 mL/min) that supply the RL, ML, LLL and CL, respectively

before portal vein ligation [6]. For the latter, variations of the flow were reported in publications using different surgical methods. For instance, after two-thirds hepatectomy the portal pressure increased significantly (~ 13.5 cmH₂O vs. ~ 18.1 cmH₂O) [7]. The increased portal pressure was due to substantially increased perfusion in the remnant liver that could not be drained in a timely manner. The congestion in the vascular bed leads to higher resistance to flow and portal hypertension.

It should be stressed that the presented model simulates the blood flows in the PV and HV trees separately (Fig. 2a and b). To predict their variations after some basic conditions are changed, e.g. after portal vein ligation [6], it is necessary to couple the flows in PV, HA and HV. Towards that end, a different *in silico* model, e.g. an electrical analog or OD model that simulates the hepatic circulation as a whole should be utilized [10]. In this way, a multi-dimensional or multiscale model could be constructed, where the OD model is used to simulate the HABR mechanism, and then the simulation results are provided to 1D HA, HV and PV trees as boundary conditions as described in the paper.

The simulation for the drug transport in portal veins (Fig. 3) can be used in conjunction with pharmacokinetic models. For example, in physiologically based pharmacokinetic models, the blood flow rates to individual organs are required. The simulations in Fig. 2 showing flow rates in the liver and individual lobes become very relevant. The models may be more useful when combined with other microscale and micro-circulation models. For example, modelling for the small for size syndrome

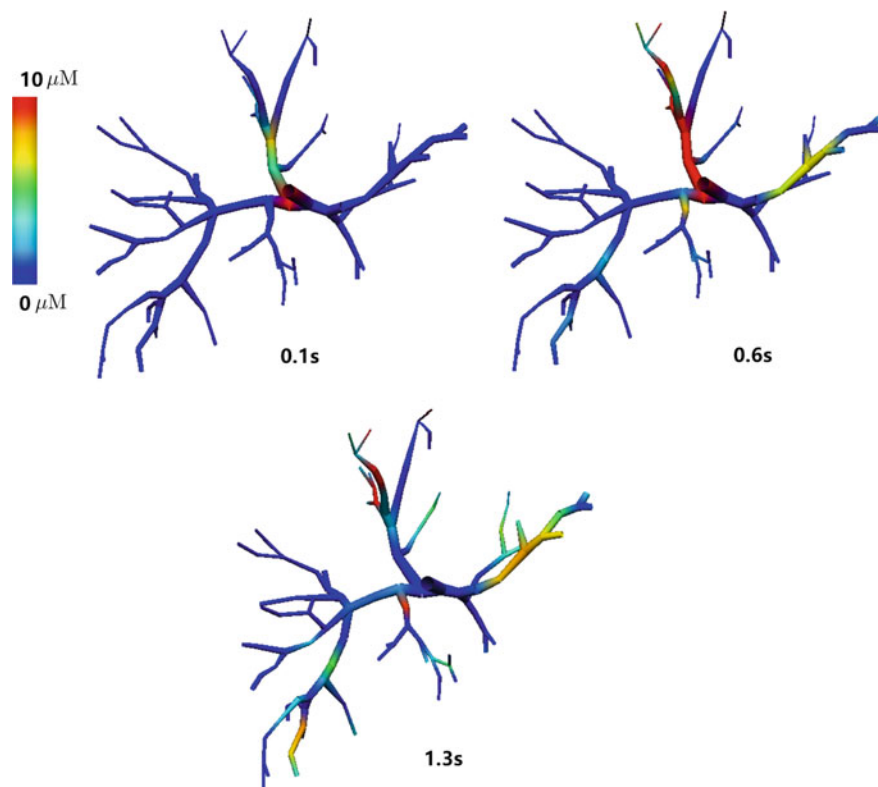


Fig. 3 Given an injection of drug (10 mg/L) that arrives at the entry point of PV, the figure shows the evolution of drug concentration across the tree at three time points (0.1s, 0.6s and 1.3s)

after liver transplantation requires considering the hepatic circulation from the whole-organ level (e.g. due to vessel ligation), as well as from micro-circulation at the lobule level [14]. Since the flow rates in sinusoids can be measured by intravital microscopy [15], the plasma concentrations of fatty acids and glucose at different zones of lobules could be estimated [2, 3] and be used in intracellular drug metabolism and toxicity models [3]. These *in silico* models of different spatial and temporal scales constitute a multiscale platform for the virtual liver [16–18].

5 Conclusion

We presented simple blood flow and transport models based on anatomically accurate vascular geometries of a rat liver. The resultant flow simulations are consistent with data measured *in vivo*. The presented model may be used in conjunction with various pharmacological or mechanistic models for multiscale modelling.

References

1. Madrahimov, N., Dirsch, O., Broelsch, C., Dahmen, U.: Marginal hepatectomy in the rat: from anatomy to surgery. *Ann. Surg.* **244**(1), 89 (2006)
2. Jungermann, K., Kietzmann, T.: Role of oxygen in the zonation of carbohydrate metabolism and gene expression in liver. *Kidney Int.* **51**(2), 402–412 (1997)
3. Schleicher, J., Guthke, R., Dahmen, U., Dirsch, O., Holzhuetter, H., Schuster, S.: A theoretical study of lipid accumulation in the liver-implications for nonalcoholic fatty liver disease. *Biochim. Biophys. Acta (BBA)-Mol. Cell Biol. Lipids* **1841**(1), 62–69 (2014)
4. Ho, H., Dahmen, U., Hunter, P.: An in silico rat liver atlas. *Comput. Methods Biomech. Biomed. Eng.* **23**(10), 597–600 (2020)
5. Kogure, K., Ishizaki, M., Nemoto, M., Kuwano, H., Makuuchi, M.: A comparative study of the anatomy of rat and human livers. *J. hepato-biliary-Pancreat. Surg.* **6**(2), 171–175 (1999)
6. Richter, S., Mucke, I., Menger, M.D., Vollmar, B.: Impact of intrinsic blood flow regulation in cirrhosis: maintenance of hepatic arterial buffer response. *Am. J. Physiol.-Gastrointest. Liver Physiol.* **279**(2), G454–G462 (2000)
7. Morsiani, E., Aleotti, A., Ricci, D.: Haemodynamic and ultrastructural observations on the rat liver after two-thirds partial hepatectomy. *J. Anat.* **192**(4), 507–515 (1998)
8. Barléon, N., Clarke, R., Ho, H.: Novel methods for segment-specific blood flow simulation for the liver. *Comput. Methods Biomech. Biomed. Eng.* **21**(15), 780–783 (2018)
9. Muller, A., Clarke, R., Ho, H.: Fast blood-flow simulation for large arterial trees containing thousands of vessels. *Comput. Methods Biomech. Biomed. Eng.* **20**(2), 160–170 (2017)
10. Ho, H., Sorrell, K., Bartlett, A., Hunter, P.: Modeling the hepatic arterial buffer response in the liver. *Med. Eng. Phys.* **35**(8), 1053–1058 (2013)
11. Coutey, C., Berg, M., Ho, H., Hunter, P.: Computational simulation of blood flow and drug transportation in a large vasculature. In: *Computational Biomechanics for Medicine*, pp. 133–142. Springer, Berlin (2016)
12. Wu, X., Allard, J., Cotin, S.: Real-time modeling of vascular flow for angiography simulation. In: *International Conference on Medical Image Computing and Computer-Assisted Intervention*, pp. 557–565. Springer, Berlin (2007)
13. Graham, M.J., Croke, S.T., Monteith, D.K., Cooper, S.R., Lemonidis, K.M., Stecker, K.K., Martin, M.J., Croke, R.M.: In vivo distribution and metabolism of a phosphorothioate oligonucleotide within rat liver after intravenous administration. *J. Pharmacol. Exp. Ther.* **286**(1), 447–458 (1998)
14. Vollmar, B., Menger, M.D.: The hepatic microcirculation: mechanistic contributions and therapeutic targets in liver injury and repair. *Physiol. Rev.* **89**(4), 1269–1339 (2009)
15. Marques, P.E., Oliveira, A.G., Chang, L., Paula-Neto, H.A., Menezes, G.B.: Understanding liver immunology using intravital microscopy. *J. Hepatol.* **63**(3), 733–742 (2015)
16. Debbaut, C., Vierendeels, J., Siggers, J.H., Repetto, R., Monbaliu, D., Segers, P.: A 3d porous media liver lobule model: the importance of vascular septa and anisotropic permeability for homogeneous perfusion. *Comput. Meth. Biomech. Biomed. Eng.* **17**(12), 1295–1310 (2014)
17. Fu, X., Sluka, J.P., Clendenon, S.G., Dunn, K.W., Wang, Z., Klaunig, J.E., Glazier, J.A.: Modeling of xenobiotic transport and metabolism in virtual hepatic lobule models. *PLoS one* **13**(9), e0198060 (2018)
18. Peeters, G., Debbaut, C., Cornillie, P., De Schryver, T., Monbaliu, D., Laleman, W., Segers, P.: A multilevel modeling framework to study hepatic perfusion characteristics in case of liver cirrhosis. *J. Biomech. Eng.* **137**(5) (2015)

Numerical Simulation of Blood Flow Under High Shear Forces in Experimental and Clinical Applications



Przemysław Kurtyka, Magdalena Kopernik, Ievgenii Altyntsev, Maciej Gawlikowski, Roman Kustosz, Małgorzata Pomorska, Christoph Hofstetter, Juergen M. Lackner, and Roman Major

Abstract The present study covers simulation of blood flow in a rough high speed vortex testing unit and in the RELIGA HEART ROT pump to anticipate the hemodynamic conditions and probability of adhesion of blood elements to the surface. The finite volume method and disperse particle method were applied to develop the target model of an operation of laboratory blood tester. The objective of the numerical calculation of the flow system of RH ROT pump with semi-open channel impeller is to determine the performance characteristics of the flow system and to assess the shear stresses acting on the pumped blood. The Ansys CFX, Ansys SpaceClaim, and ICEM CFD software were used for performing numerical calculations and for the preparation of the geometry for the calculations including the calculation grid, respectively. The shear stress calculations obtained from the numerical simulations of laboratory blood tester was found to be below critical level for blood morphotic elements. Simultaneously, the local increase in RBCs mass concentration was located in the middle part of the laboratory blood tester model, what can result in local deposition of red blood cells. At the same time, the flow system of the RH ROT pump

P. Kurtyka · I. Altyntsev · M. Gawlikowski · R. Kustosz
Foundation for Cardiac Surgery Development, Institute of Heart Prostheses, Wolności St. 345a,
41-800 Zabrze, Poland

M. Kopernik (✉)
AGH University of Krakow, al. Mickiewicza 30, 30-059 Cracow, Poland
e-mail: kopernik@agh.edu.pl

M. Pomorska · R. Major
Institute of Metallurgy and Materials Science, Polish Academy of Sciences, 25 Reymonta St.,
30-059 Cracow, Poland

C. Hofstetter
Lithoz GmbH, Mollardgasse 85a/2/64-69 1060, Vienna, Austria

J. M. Lackner
Joanneum Research Forschungsges.m.b.H., Institute of Surface Technologies and Photonics,
Functional Surfaces, Leobner Street 94, 8712 Niklasdorf, Austria

with semi-open channel impeller meets the performance, head and efficiency requirements. The use of the impeller with semi-open channels allows the shear stress on the impeller walls to be reduced and the residence time of blood in high stress areas to be shortened. The latter should have a beneficial effect on reducing the level of blood damage during operation of the RH ROT pump.

Keywords Finite volume method · Disperse particle method · Shear stress blood flow tester · Mechanical circulatory support

1 Introduction

Myocardial insufficiency is a complex clinical syndrome resulting from structural or functional impairment of filling or expelling blood from the heart. This may be due to multiple cardiac or large vessel abnormalities and some metabolic abnormalities, but most patients are suffering heart failure due to impaired left ventricular myocardial function [1]. Heart failure is an epidemic of the twenty-first century and affects 33% of the population over 55 and 22% over 40 [2]. There are an estimated 5.8 million heart failure cases in the USA with a 30-day mortality rate of 11%, hospitalization rates of ~ 25%, and a 5-year survival rate lower than most cancers [3]. Similarly, there are 15 million patients in Europe, of which 45% are the fatal ones [4].

The heart transplantation is the gold standard for end-stage heart failure, but it is limited by a small number of donors' hearts (covering < 0.5% of needs). An alternative is the use of mechanical cardiac assist systems (for example, left ventricular assist devices (LVADs)), which is capable to significantly reduce tissue stress during the drug-assisted recovery phase [5]. The LVADs are effective in the treatment of reduced stroke volume resulting primarily from acute decompensated, hemodynamically unstable myocardial dysfunction, both in the short term (hours to days) and in the long term (months to years). Particularly, for medium to long-term treatment, implantable centrifugal pumps for continuous flow have become the absolute leader (61% in 2016), with 459 implants registered worldwide in 2008, followed by 3 004 implants in 2015 (98.3% of all registered applications). Rotary LVAD generally consists of an impeller with embedded strong permanent magnets to suspend the impeller and a coil system in the pump housing. Its low energy consumption will enable replacement of the currently used an outside-of-the-body placed battery with a small implantable one [5–8]. The problem with the LVADs are twofold: Their cost is very high, and they can cause adverse events like strokes (due to the formation of blood clots in the pump), bleeding or infections [9]. In particular, the pump-induced thrombosis ailment is complex and undoubtedly multifactorial one [10]. A general medical solution of this problem is to adapt the adequate treatment protocol to the appropriate device overcoming in such a way current technological limitations [11]. A proper engineering, together with a better understanding of the utilized material hemocompatibility, is the key to reducing the problem of in-pump thrombosis, what eventually should enable the expansion of LVADs into wider patient groups [12].

Especially important role in this process passes to innovative hybrid materials and engineering methods based on the so-called Additive Manufacturing method. The latter allows for fabrication of the most complicated shapes of the rotor designed on the biomimetic basis for long-term contact with blood [13].

However, the most important physical phenomena observed in the cardiovascular devices are usually impossible to determine even by indirect methods. It is because, the application of particle image velocimetry methods for the measurement of local flow values is significantly hampered by limited visualization of the tested elements. At the same time, the Ultrasound Doppler Velocimetry (UDV) methods do not allow for precise measurements in small crevices and flow channels. Simultaneously, the direct measurement of local pressures is technically difficult and may disturb the measured process. That is why the computational fluid dynamics simulations are a valuable source of information on the course of flow phenomena in centrifugal pumps, as only they make it possible to calculate pressure fields and fluid flow velocities, shear stresses, and exposure times. On this basis, other mathematical models (e.g., Wurzinger model [14]) allow to assess the risk of hemolysis or platelet activation. However, numerical methods belong to a group of approximate methods based on simplified models of physical phenomena (e.g., blood rheology [15]) and mechanical properties (e.g., surface roughness [16]) of pump components. Therefore, these models of blood flow in mechanical heart assisted devices are only helpful in optimization construction parameters with respect to flow critical parameters, but not with respect to all the interactions among parts of the blood–material–tissue complex system.

As it concerns the devices planned to stay in contact with blood, it is important to better understand the relationship between shear stress, exposure time, and blood damage. It is so important as the blood damage is not only causing the hemolysis or activation of platelets, but also thrombosis and embolism as well as the destruction of von Willebrand factor (vWf). According to the literature, hemolysis occurs at shear stress level (SSL) > 150 Pa, activation of thrombocytes > 50 Pa, and degradation of von Willebrand factor > 9 Pa [17]. In vitro testing for hemocompatibility remains a challenge because the background of interactions between blood and foreign material is not fully explained [18]. It is generally acknowledged that initial and rapid adsorption of plasma proteins can improve biocompatibility of the material [19].

Taking into account the above, one may point that experimental and numerical tests simulating the phenomena on the blood–material contact in blood flow systems are still very much in need. Up till now the numerical modeling of the blood flow ensuring its good compliance with the experiment has used, inter alia, mixture theory [20], discrete particle method [21], and SST $k-\omega$ turbulence model [22]. Blood flow may also concern issues related to blood-contacting devices, which cause hemolysis [23]. Simultaneously, particle-based models are applied to simulate red blood cells (RBCs) membrane dynamics and platelets, as well as margination effects and heterogeneities of blood morphotic elements [24].

Thus, the goal of the present study is the numerical simulation of blood flow in the laboratory high speed vortex tester and in the clinical application—the RH ROT pump to anticipate the hemodynamic conditions and probability of adhesion of blood

elements to the surface applying finite volume method (FVM) and disperse particle method (DPM).

2 Applications

2.1 Laboratory Blood Tester

A self-designed device “Symmed” (Fig. 1a and b) allows to perform fundamental research to be carried out under laboratory conditions in order to determine the effect of high shear stress generated by the surface of a biomaterial moving against blood on the cells and plasma proteins of blood contacted under defined flow conditions and contact time with the surface of the biomaterial. The implemented research method is expected to help selecting a biomaterial dedicated to the pump design under this study. The tester is dedicated for specimens of low complexity, in particular for assessment of the hemocompatibility of materials in the form of thin films and flexible materials for micropump flaps, under strong shear forces, in direct contact with whole human blood.

The device is dedicated for testing platelet function under close to physiological conditions. The device is aimed at testing platelet adhesion and aggregation in an anti-coagulated whole blood (citrate buffer tubes) under arterial flow conditions (2000 s^{-1} for 2 min). The laminar flow over the polystyrene surface of the well is achieved according to the cone and plate principle [24]. The device can also give indication for patient response to drugs. Upon application of a blood sample (130 μl) into the polystyrene well, plasma proteins immediately adhere to the well surface and attract the platelets, causing their adhesion and aggregation on the well surface under flow conditions. The results are expressed as the percentage of the well surface covered by platelets aggregates representing platelet adhesion and the average size of the aggregates representing platelet aggregation.

2.2 Clinical Application

The aim of the work was therefore to optimize the Religa Heart ROT centrifugal blood pump with the use of FVM for fully hemocompatible rotors. This innovative device was developed at the Foundation of Cardiac Surgery Development (Zabrze, Poland). Eventually, it is planned to be used for patients with advanced myocardial dysfunction. It is a mechanical bearing-less pump, equipped with a contactless impeller suspended in a hybrid balanced magnetic and hydrodynamic bearing system, which provides a flow rate of up to 7 l/min with a capacity of 30–45%. To improve the properties of hemocompatibility, including the reduction of shear stresses, and follow global trends, a complete magnetic rotor suspension system was

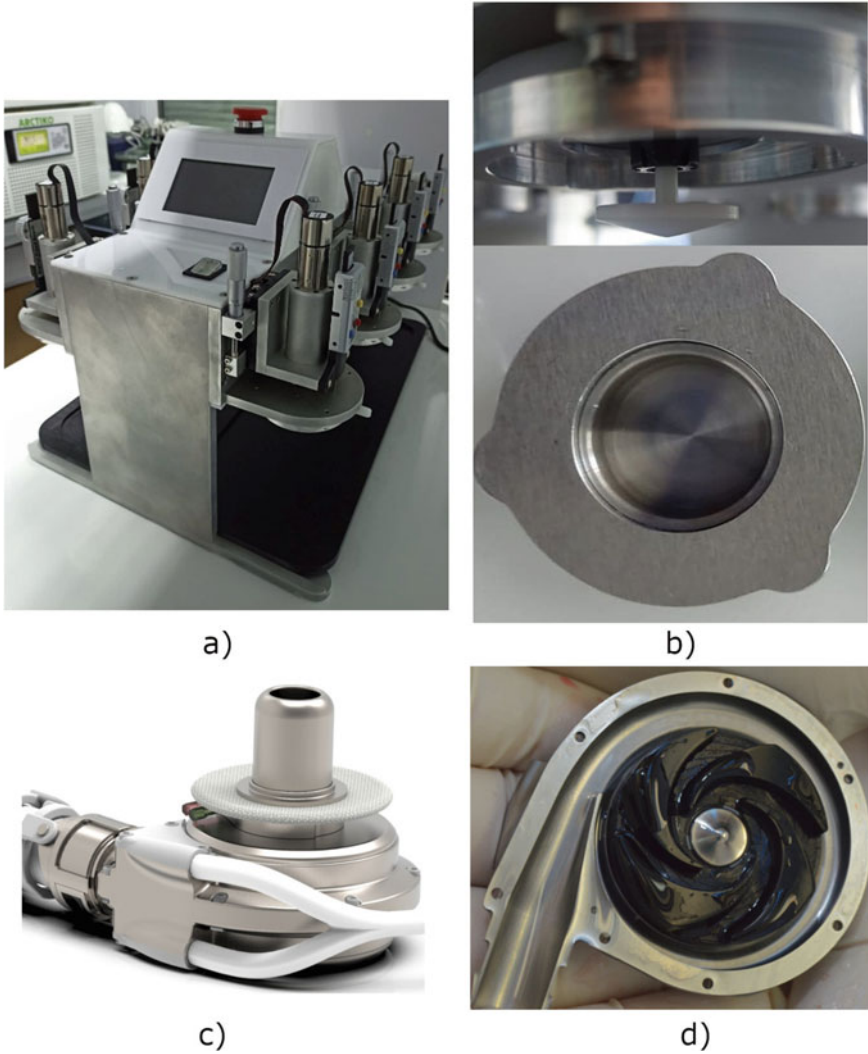


Fig. 1 Images of: **a** dynamic hematological test apparatus in the plate—cone system of Symmed blood tester, **b** cone and blood domain of part of Symmed blood tester, and the Religa Heart ROT **c** side view, and **d** cross section view of a model unit, respectively

developed. The bearing of the rotor using active magnetic levitation is intended to reduce the aforementioned shear stresses generated in contact with the flowing blood and to protect platelets and von Willebrand proteins from damage causing the risk of bleeding. For this reason, various impeller designs with both closed and partially open channels are considered in the paper. Figure 1c and d shows the geometry of the flow system.

3 Numerical Models

3.1 Blood Tester Model

The FVM model was developed using the Ansys Fluent 2022 R2 software to introduce the roughness in the Symmed system enabling to investigate its influence on blood velocity and shear stress. The developed simulations were run on a standard PC (Processor Intel® Core™ i7-3770 CPU, 3.40 GHz, 32 GB RAM). The simulations lasted for 0.03 s (1 000 iterations) with time step of $3 \cdot 10^{-5}$ s. The FVM mesh was composed of 497 557 cells and 147 379 nodes. The mesh quality parameters (skewness—0.09, orthogonal quality—0.9, element quality—0.8) were very good and there were six layers of prism elements near walls of the FVM model. The average element size was 0.276 mm. The developed FVM model uses non-Newtonian power law [25], and the following coefficients of blood are assumed to be density 1059 kg/m³ [26], specific heat 3617 J/kgK [27], and thermal conductivity 0.52 W/mK [28]. A cone made of Teflon with a radius of 6.5 mm and an angle of 88° rotated in blood at 2 000 rpm. The shape of the chamber in which the cone rotated corresponded to a polystyrene cylinder with a radius of 7 mm. The distance between the cone and the cylinder wall was 0.5 mm. The bottom wall of the FVM model has a sand-grain roughness described by a standard roughness model with parameters: height 100 nm and constant 0.5. This model was applied with parameters of roughness based on experimental observation and they are correlated with the size of tested parts. The pressure–velocity coupling scheme of solution was selected with spatial discretization using gradient (least squares cell based) and transient formulation was also used. Finally, the SST $k-\omega$ turbulence model was applied in all simulations.

The DPM model was developed to compute distributions of RBCs mass concentration and velocity magnitude, etc. It was applied to investigate the behavior of the RBCs from a Lagrangian view and a discrete perspective. Blood behavior in Lagrangian view was examined on the basis of a particle tracking of a RBC of blood plasma flow; whereas blood plasma behavior was considered in Eulerian view based on the assumption of a finite volume element in the fluid flow path. In modeling of RBC—primary blood plasma interaction a two way approach was considered, in which RBC fluid flow and carrier blood plasma flow interact with each other simultaneously. The diameter of RBCs was assumed to be 5–10 μm using the Rosin–Rammler diameter distribution method. The rotation of RBCs was enabled. The density of plasma was 1040 kg/m³, specific heat 3930 J/kgK, thermal conductivity 9.93 W/mK, and viscosity was 0.0015 kg/ms [29, 30]. The density of RBCs equaled to 1090 kg/m³ and specific heat equaled to 870 J/kgK [30]. Viscosity of red blood cells was set to 0.0075 kg/ms, and their surface tension was set to $5 \cdot 10^{-6}$ N/m [31].

Particles and plasma were injected in full volume, and the system had no other physical inlet. In simulation, particles were injected into the entire volume of the medium, just like in the Symmed system. This allowed the behavior of particles to be observed without imposing additional boundary conditions at the inlet, i.e., helped to eliminate it directly. The total flow rate of RBCs was $1 \cdot 10^{-10}$ kg/s. The

DPM model is characterized by an interaction with continuous phase and a particle track with fluid flow time step. The boundary condition of RBCs phase is assumed as escape; however, RBCs can be reflected from the ground.

3.2 Clinical Application Model

The numerical calculations of the model of the RH ROT pump were done with an ANSYS CFX software, while for setting-up of the geometry for the calculations and the calculation grid was performed with Ansys SpaceClaim and ICEM CFD software.

Structural meshes, consisting of hexagonal elements with good mesh resolution at the walls, were prepared for the inflow channel, spiral channel, and outflow channel. Simultaneously, an unstructured mesh, consisting of tetrahedral elements, with a wall layer with prismatic elements, was prepared for the slotted impeller. The used computational grid consisted of 16 708 380 elements and 6 469 518 nodes.

Figure 2 shows the computational grid for the entire model. The computational domain was divided into four parts, including three stationary (inflow channel, spiral channel, outflow channel) and one rotating (slotted impeller). The rotational speed was 3000 rpm (nominal speed).

The Frozen Rotor interfaces were used in the calculations for the domain connection. The calculations were performed for two positions (along the axis of rotation) of the impeller in the pump housing. In the first case, the impeller was at the geometric

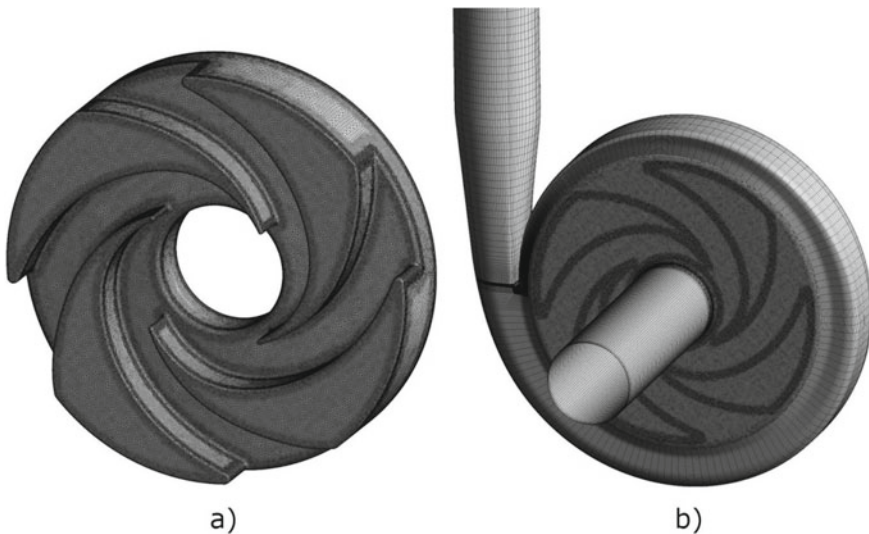


Fig. 2 Images of calculation grid of: **a** rotor and **b** whole device

center of the casing (the top gap (from the impeller inlet) and the bottom gap were equal (gap height 0.4 mm)). In the second case, the impeller was displaced by 0.2 mm toward the pump inlet. In this position, the top gap width was 0.2 mm and the bottom gap width was 0.6 mm. For each case, a series of calculations were performed to determine the performance characteristics of the flow system. During these calculations, the variable was the pump capacity Q , which varied from 1 to 7 l/min with a step of 1 l/min.

The calculations were carried out using the $k-\omega$ SST turbulence model. This model allows an accurate representation of the flow conditions both in the near-wall layers and in the center of the flow channel.

A non-Newtonian model of blood (Carreau-Yasuda model [32]), described by the formula, was used in the calculations:

$$\mu = \mu_{\infty} + \frac{\mu_0 - \mu_{\infty}}{(1 + (\lambda \cdot \dot{\gamma})^m)^{n-1/m}}, \quad (1)$$

where $\mu_{\infty} = 0.0035$ Pa s, $\mu_0 = 0.16$ Pa s, $\lambda = 8.2$ s, $m = 0.64$, $n = 0.2128$, $\dot{\gamma}$ —shear strain rate, μ —blood viscosity.

4 Results

4.1 Blood Tester Model Results

The results of simulations considering roughness of bottom wall of the Symmed system are analyzed against that of the values of velocity, shear stress, RBCs mass concentration, and turbulence kinetic energy. The rotating cone causes the formation of maximum values of the RBCs velocity over the cone (velocity of $2.25 \text{ m}\cdot\text{s}^{-1}$, Fig. 3a) and at its edges. The blood velocity on the plane under the cone (velocity of $0.92 \text{ m}\cdot\text{s}^{-1}$) is not the highest in the entire model, but it increases from the center to the edge and only there reaches the highest values. The rotation of the cone also results in the maximum values of the shear stress over the cone and especially at its edges (shear stress of 0.5 Pa, Fig. 3b). The blood shear stress on the plane under the cone (shear stress of 0.09 Pa) is not the highest in the entire model, but the shear stresses occur only on the circumference of the selected plane of blood domain. The distribution of RBCs mass concentration in the modeled Symmed system is the highest at the wall slightly below the outer edge of the cone (Fig. 3c). In contrast, the highest turbulence kinetic energy is computed under the outer edges of the rotating cone (Fig. 3d).

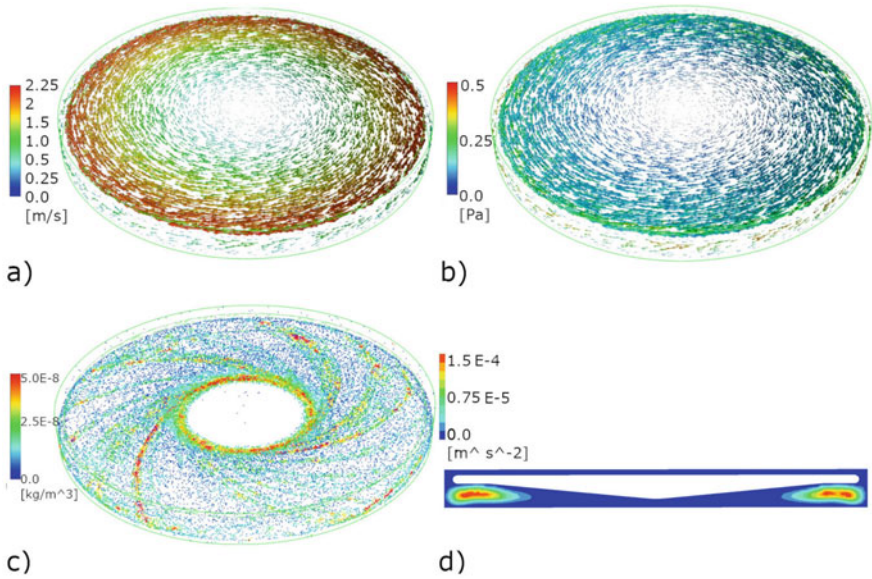


Fig. 3 Distributions of **a** velocity, **b** shear stress, **c** RBCs mass concentration, **d** turbulence kinetic energy (cross section) in Symmed model

4.2 Clinical Application Model Results

On the basis of the numerical calculations carried out, the performance characteristics of the RH ROT pump with semi-open impeller were developed for two impeller positions in the pump housing.

Figures 4, 5, 6, and 7 show the performance characteristics of the RH ROT pump with different impeller designs. The graphs show the characteristics for

- RH ROT X02 pump (closed impeller with fixed height inter-vane channels);
- RH ROT pump with “neck” impeller for different gap heights around the impeller ($h = 0.15 \text{ mm}$, $h = 0.3 \text{ mm}$, $h = 0.5 \text{ mm}$), impeller channel of variable height.
- RH ROT pumps with semi-open impeller (impeller channel with variable height, the total opening angle of the inter-vane channels is smaller than in the “neck” impeller design).

Figure 4 shows the headroom for different flow system designs presented in different units.

As can be seen, the highest lift values among the compared flow systems were obtained for the “necked” flow system. This result is due to the change in geometry of the impeller flow channels compared to the RH ROT X02 design.

The characteristics shown in Fig. 4 for the semi-open impeller flow system vary significantly depending on the position of the impeller in the pump housing. As the top gap decreases (the impeller moves toward the pump inlet), the pump head

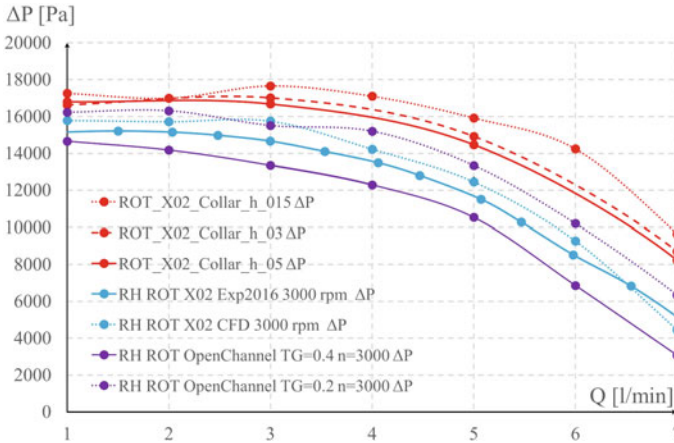


Fig. 4 $\Delta P(Q)$ characteristics for different rotor designs

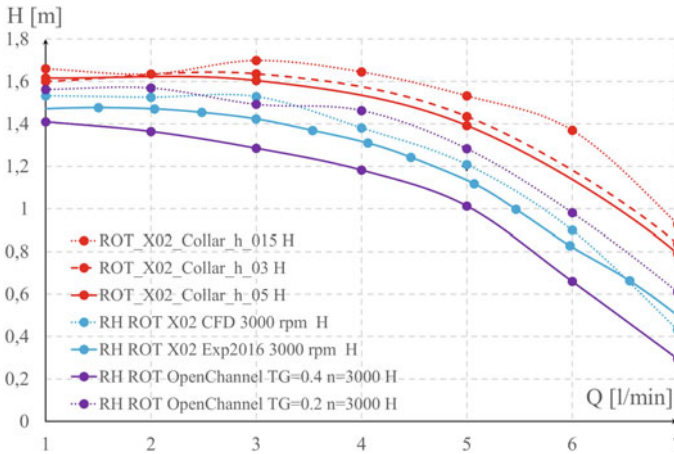


Fig. 5 Characteristics of $H(Q)$ for different rotor designs

increases. This effect can be explained by the “sealing” of the impeller, i.e., the closing of the impeller flow channels by the pump casing. A reduction in the top gap results in an increase in its resistance, which leads to a reduction in leakage and, consequently, energy loss.

Figure 5 shows the $H(Q)$ characteristics for the compared flow systems. Changing the position of the impeller in the pump housing affects the mechanical power required to drive the impeller. As the top gap decreases, an increase in mechanical power takes place. It should be noted that the increase is greater at higher pump capacities.

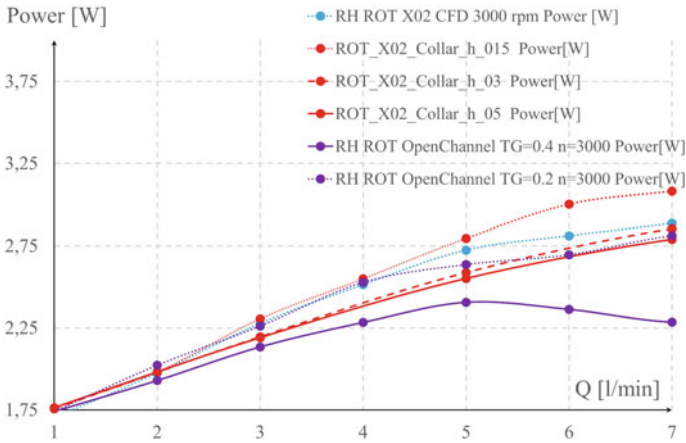


Fig. 6 Power characteristics $P(Q)$ for different pump impeller designs

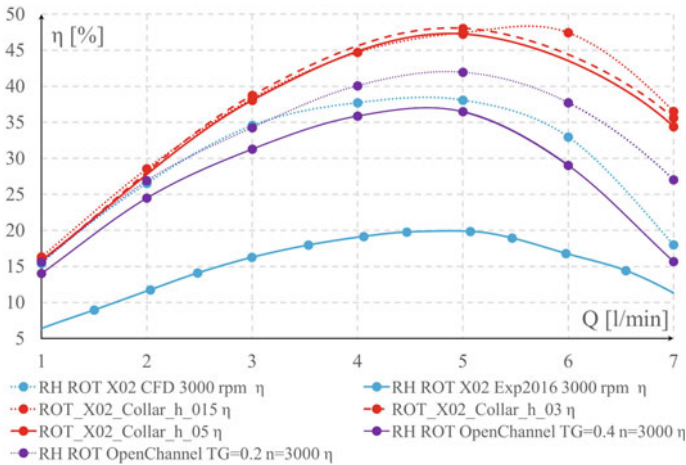


Fig. 7 Characteristics $\eta(Q)$ for different impeller designs determined by numerical calculations and the efficiency characteristics of the RH ROT X02 pump

Figure 6 shows the mechanical power characteristics for the compared flow system designs and the electrical power characteristics for the RH ROT X02 pump. The difference between mechanical power and electrical power is due to the losses generated within the electric motor.

Figure 7 shows the hydraulic efficiencies for the systems tested and the total efficiency of the RH ROT X02 pump.

As can be seen, a reduction in the top gap despite an increase in the power consumed by the impeller results in an improvement of hydraulic efficiency for the semi-open impeller pump. For the operating point ($Q = 5$ l/min), the flow system

reaches its maximum efficiency. The hydraulic efficiency at this point reaches approximately 5.5%. The “necked” flow system has the highest efficiency among the investigated set-ups. The maximum efficiency of this flow system for the nominal operating point is equal to 47.25%.

Figures 8 and 9 show the shear stress distributions for different flow rates through the pump for the two impeller positions. As can be seen from Figs. 8 and 9, the flow rate and the shear stress values increase simultaneously. It is because an increase in the fluid flow velocity and leads to higher shear stress on the impeller channel surfaces. As the top gap decreases, there is an increase in shear stress on the flat external surfaces of the impeller. As one can see in Figs. 8 and 9, these stresses exceed 100 Pa. Figure 9 shows better the stress distributions for a top gap height of 0.2 mm reaches up to 200 Pa. The stresses on the flat surfaces of the impeller are very little affected by the value of the flow through the pump. This is because they are a result of the impeller speed and the distance between the impeller and the casing. It should be noted that the residence time of the cells in the high stress area will be short, as the cells passing through the narrow area between the impeller and the pump casing will reach the main channel of the impeller, where the stresses will be lower.

5 Discussion and Conclusions

The simulations of the laboratory blood tester work predicted low values of the involved shear stresses. In the developed model, both, the hematocrit and the concentration of blood cells are high. Both parameters influenced on the value of the viscosity. The increased viscosity is a direct result of the shear stress reduction. In the case of no-slip boundary condition, similar to the originally designed Symmed system, one deals with shear stresses resulting from the interaction of cell adhesion molecules with surface. It has been also shown in other experiments published elsewhere [33]. The maximum wall shear stresses presented in literature for the similar tests are varied from 0.3 [34] to 7 Pa [35]. Therefore, the computed wall shear stress of 0.5 Pa in this work is in the range of data published up to date. In the present paper, the obtained tangential distributions of wall shear stress and velocity distributions are increasing from the center to the edge, which corresponds with other experimental and literature observations [34, 35]. The model of the originally developed test, Symmed, considers roughness of the sample and blood flow turbulence. Thus, the presented results show relatively complete blood–material interaction. The global model results (RBCs mass concentration and RBCs velocity magnitude) show the highest velocities and mass concentrations of RBCs on the upper surface of the rotating cone in the laboratory blood tester. Both, RBCs velocities and RBCs mass concentrations are lower under cone. The computed local RBCs mass concentration increases in the middle part of the model and in the zone close to inner wall. It might cause a local attachment of red blood cells, which was confirmed experimentally (SEM analysis). Local RBCs mass concentrations are most likely being the

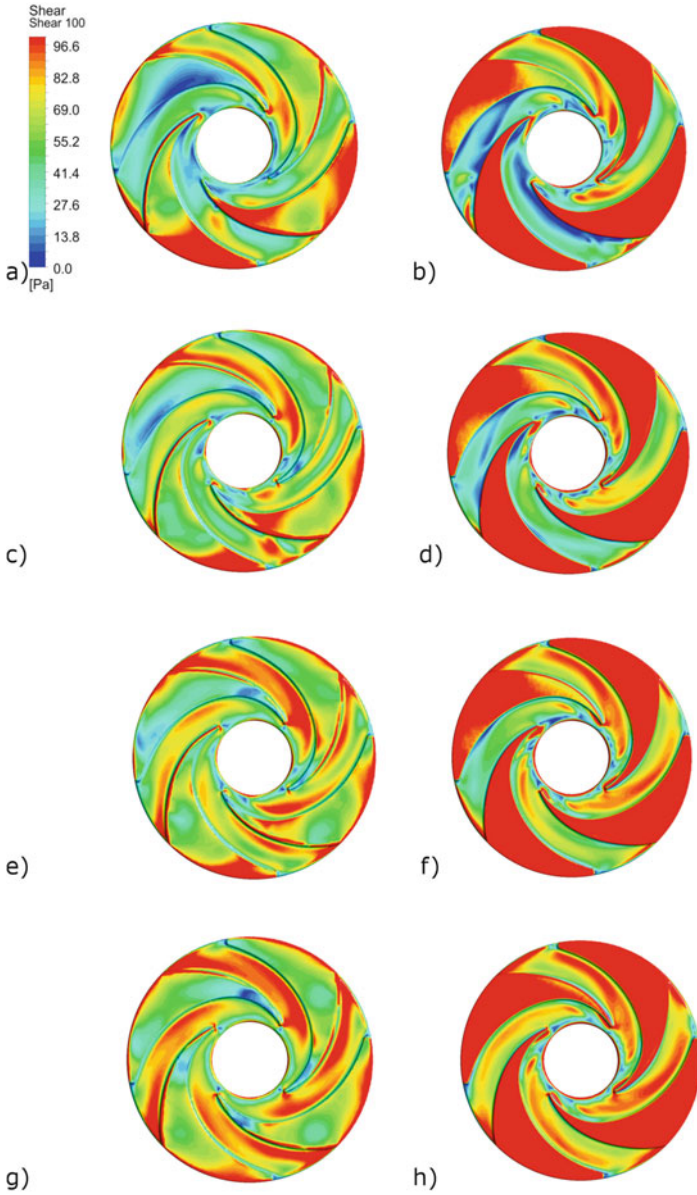


Fig. 8 Image presenting rotor shear stress distributions for different capacities: **a** top gap 0.4 mm, bottom gap 0.4 mm, $Q = 1$ l/min, **b** top gap 0.2 mm, bottom gap 0.6 mm, $Q = 1$ l/min, **c** top gap 0.4 mm, bottom gap 0.4 mm, $Q = 2$ l/min, **d** top gap 0.2 mm, bottom gap 0.6 mm, $Q = 2$ l/min, **e** top gap 0.4 mm, bottom gap 0.4 mm, $Q = 3$ l/min, **f** top gap 0.2 mm, bottom gap 0.6 mm, $Q = 3$ l/min, **g** top gap 0.4 mm, bottom gap 0.4 mm, $Q = 4$ l/min, **h** top gap 0.2 mm, bottom gap 0.6 mm, $Q = 4$ l/min, **i** top gap 0.4 mm, bottom gap 0.4 mm, $Q = 5$ l/min, **j** top gap 0.2 mm, bottom gap 0.6 mm, $Q = 5$ l/min, **k** top gap 0.4 mm, bottom gap 0.4 mm, $Q = 6$ l/min, **l** top gap 0.2 mm, bottom gap 0.6 mm, $Q = 6$ l/min, **m** top gap 0.4 mm, bottom gap 0.4 mm, $Q = 7$ l/min, **n** top gap 0.2 mm, bottom gap 0.6 mm, $Q = 7$ l/min

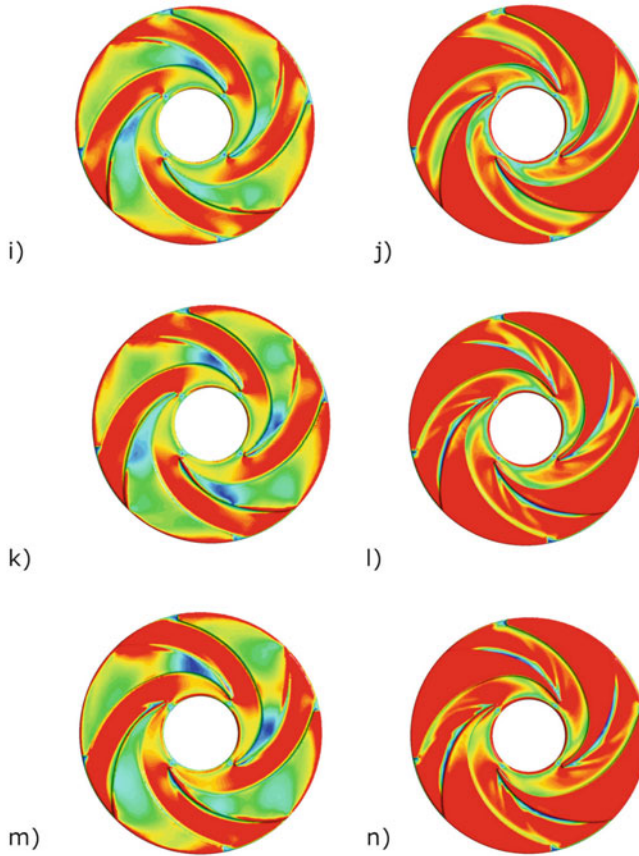


Fig. 8 (continued)

direct result of the flow itself. Despite of high rotation velocity, the shear stress level computed in the simulations of Symmed system was found to remain below critical values for blood morphotic elements and von Willebrand factor.

Centrifugal blood pumps are currently one of the few alternatives to heart transplantation and are often the only solution, giving patient's valuable time for treatment. Ventricular assist devices (VAD) are intended for long-term heart support at patient's home, without the need for permanent hospitalization. Improving biocompatibility with the use of state-of-the-art materials, reducing the size and complexity of MCS devices have led to a significant reduction in complications caused by their use. Despite many improvements, patients still experience high morbidity, many side effects, and mortality. The devices are characterized by a complicated construction consisting of many elements that may fail. Mechanical circulatory support (MCS) systems are currently quite invasive, technically difficult to implant, and still require systemic anticoagulation. Moreover, the patients themselves are becoming more

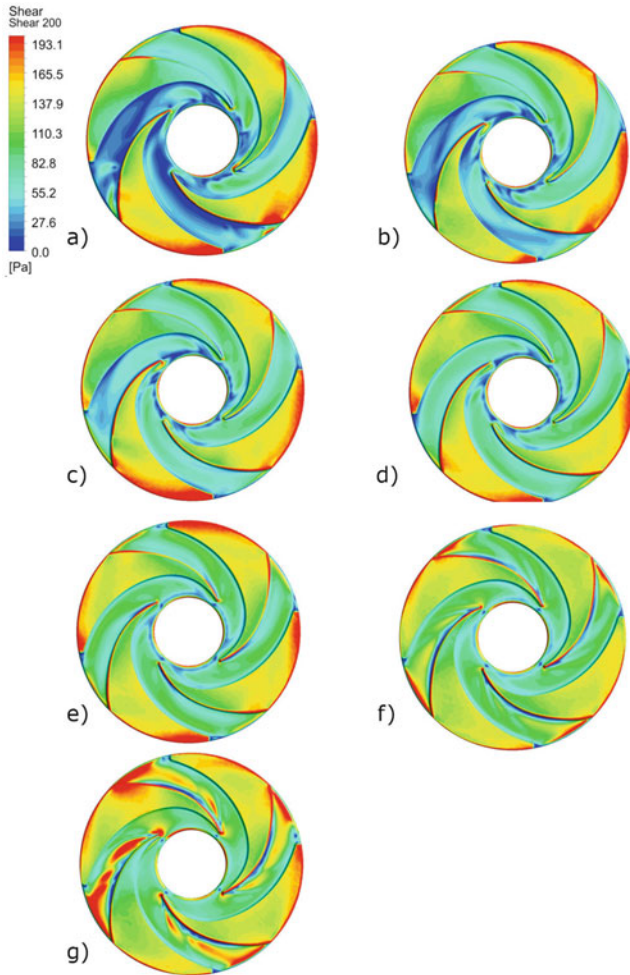


Fig. 9 Image presenting shear stresses on a scale up to 200 Pa: **a** top gap 0.2 mm, bottom gap 0.6 mm, $Q = 1$ l/min, **b** top gap 0.2 mm, bottom gap 0.6 mm, $Q = 2$ l/min, **c** top gap 0.2 mm, bottom gap 0.6 mm, $Q = 3$ l/min, **d** top gap 0.2 mm, bottom gap 0.6 mm, $Q = 4$ l/min, **e** top gap 0.2 mm, bottom gap 0.6 mm, $Q = 5$ l/min, **f** top gap 0.2 mm, bottom gap 0.6 mm, $Q = 6$ l/min, **g** top gap 0.2 mm, bottom gap 0.6 mm, $Q = 7$ l/min

complex and undergo MCS implantation in an increasingly critical form, which translates into the occurrence of many perioperative and support-related complications. Therefore, work is being carried out on new impeller designs that will allow increase biological safety, while maintaining high hydraulic efficiency. The VAD-type pump is equipped with an impeller, which is the only moving element of the whole device. In the currently used constructions of the III generation, non-contact and effective work without wear is ensured by means of a hybrid bearing or active

magnetic levitation. In both cases, the mechanical bearing was abandoned in relation to generation II due to many cases of complications occurring during support. In the hybrid system, i.e., in the HeartWare pump, the levitation of the rotor is ensured by the balance of forces of the hydrodynamic and magnetic bearings. On the upper surface of the impeller, there is a specially designed slope—a component of the hydrodynamic bearing, which generates a repulsive force, during the operation of the impeller, creating a gap between the impeller and the pump housing. The permanent magnetic bearing is responsible for the axial stabilization of the rotor. In the case of fully magnetic levitation, we are dealing with an active levitation system (Full Mag-Lev), on the example of the HeartMate III device, provided by a designed system of coils and permanent magnets. Due to the trend toward solutions with active levitation, analyses are being carried out around the world to optimize the design of the rotor and more attention is paid to the generated shear stresses [36]. Khoo et al. analyzed in their simulations parameters such as flow velocity, shear stress fields, washout, and hemolysis index of the three pumps [37]. The CH-VAD hemolysis index was two times lower than the HVAD and HeartMate II pumps under the same conditions. The CH-VAD pump was characterized by the least percentage volume with shear stress larger than 100 Pa (i.e., normal condition: 0.4% versus HVAD 1.0% and HeartMate II 2.9%). Zhang et al. showed that the rotational chamber support devices have the following normal stresses: fluid volumes with normal stress above 10 Pa were 0.011 ml (0.092%) and 0.027 ml (0.39%) for HeartWare HVAD and HeartMate II, respectively (HMII), and normal stresses of more than 100 Pa were present [38]. The shear stress volumes were up to two orders of magnitude greater than normal stress volumes. Considering the deformation thresholds of red blood cells and von Willebrand factor under normal and shear stress, the volumes of fluid causing deformation under normal stress were 2.5–5 times greater than the volumes causing deformation under shear stress.

In the case of RH ROT semi-open impeller it can be seen that as the gap between the impeller and the pump casing diminishes, there is an increase both in the delivery head (at a constant flow) and in the capacity of the pump at a constant delivery head (the characteristic curve moves to the right of the initial curve). At the same time there is a rise in the hydraulic power and efficiency of the pump. These changes are caused by a reduction in the gap height between the impeller and the pump casing and therefore a reduction in volume loss in the pump (leakage from the high pressure area to the lower pressure areas). It is likely that, at a constant speed, the axial displacement of the impeller will succeed in generating circulating system pressure pulsations. Changing the rotational speed may further enhance the effect in question. On the basis of an analysis of the shear stresses on the impeller surfaces, it can be concluded that there is an increase in shear stress values as the distance between the impeller and the pump casing decreases. However, in contrast to the closed-channel impeller design, in a semi-open-channel impeller the residence time of the blood cells in the high shear stress region will be much shorter, which should translate into a lower level of blood damage in a pump with such an impeller.

In conclusion, the experiments performed presently proved the flow system of the RH ROT pump with semi-open channel impeller, meet efficiency requirements.

The design of the impeller with semi-open channels allows to control the pump by changing the position of the impeller in the casing, i.e., without altering the impeller speed. The use of the impeller with semi-open channels allows the shear stress on the impeller walls to be reduced and the residence time of blood in high stress areas to be shortened. Both of them will have a beneficial effect on reducing the level of blood damage during operation of the RH ROT pump.

Acknowledgements The work was supported by the Polish National Centre of Research and Development (Grant no. M-ERA.NET2.2017/4/2019, “4 Dimensional Single Piece Miniaturized Blood Rotor”) and by the Austrian Federal Ministry of Climate Action, Environment, Energy, Mobility, Innovation and Technology through the program Production of the Future, FFG grant number 865877, in connection with cooperation in M.ERA-NET, Nanostructured Materials, Biomaterials and Additive Manufacturing.

References

1. Birks, E.J., Tansley, P.D., Hardy, J., et al.: Left ventricular assist device and drug therapy for the reversal of heart failure. *NEJM* **355**, 1873–1874 (2006)
2. Yearly Statistics Overview Eurotransplant.: (2021). https://statistics.eurotransplant.org/index.php?search_type=&search_organ=heart&search_region=by+country&search_period=2021&search_characteristic=&search_text. Accessed 30 May 2022
3. Molina EJ et al (2021) The society of thoracic surgeons intermacs 2020 annual report. In: The Society of Thoracic Surgeons Intermacs Annual Report. <https://doi.org/10.1016/j.athoracsur.2020.12.038>
4. Timms, D.: A review of clinical ventricular assist devices. *Med. Eng. Phys.* **33**, 1041–1047 (2011)
5. Strüber, M., Sander, K., Lahpor, J., Ahn, H., Litzler, P.Y., Drakos, S.G., Musumeci, F., Schlensak, C., Friedrich, I., Gustafsson, R., Oertel, F., Leprince, P.: HeartMate II left ventricular assist device; early European experience. *Eur. J. Cardiothorac. Surg.* **34**, 289–294 (2008)
6. Popov, A.F., Hosseini, M.T., Zych, B., Mohite, P., Hards, R., Krueger, H., Bahrami, T., Amrani, M., Simon, A.R.: Clinical experience with HeartWare left ventricular assist device in patients with end-stage heart failure. *Ann. Thorac. Surg.* **93**, 810–815 (2012)
7. Higgins, R.S., Kilic, A., Tang, D.G.: Surgical treatment of heart failure. *Surg. Clin. North Am.* **97**, 923–946 (2017)
8. John, R., Pagani, F.D., Naka, Y., Boyle, A., Conte, J.V., Russell, S.D., Klodell, C.T., Milano, C.A., Rogers, J., Farrar, D.J., Frazier, O.H.: Post-cardiac transplant survival after support with a continuous-flow left ventricular assist device: impact of duration of left ventricular assist device support and other variables. *J. Thorac. Cardiovasc. Surg.* **140**, 174–181 (2010)
9. Sheikh, F.K., Russel, S.D.: HeartMate® II continuous-flow left ventricular assist system. *Expert Rev. Med. Devices* **8**, 11–21 (2011)
10. Lahpor, J.R., et al.: State of the art: implantable ventricular assist devices. *Curr. Opin. Organ Transplant.* **14**, 554–559 (2009)
11. Naftel, D.C., et al.: Use of an intrapericardial, continuous-flow, centrifugal pump in patients awaiting heart transplantation. *Circulation* **125**, 3191–3200 (2012)
12. Carrel, T., et al.: Continuous flow left ventricular assist devices: a valid option for heart failure patients. *Swiss Med. Wkly* (2012). <https://doi.org/10.4414/smw.2012.13701>
13. Slaughter, M.S., Rogers, J.G., Milano, C.A., et al.: HeartMate II investigators. Advanced heart failure treated with continuous-flow left ventricular assist device. *N. Engl. J. Med.* **361**, 2241–2251 (2009)

14. Wurzinger, L.J., Opitz, R., Eckstein, H.: Mechanical blood trauma. An overview. *Angeologie* **38**, 81–97 (1986)
15. Kopernik, M., Kruczek, D., Kurtyka, P., Pomorska, M., Major, R.: Experimental and numerical analysis of blood flow in roughness impact-R test. *Acta Bioeng. Biomech.* **24**, 119–133 (2022). <https://doi.org/10.37190/ABB-02134-2022-02>
16. Kopernik, M., Dyrda, K., Kurtyka, P., Major, R.: Discrete phase model of blood flow in a roughness microchannel simulating the formation of pseudointima. *Acta Bioeng. Biomech.* **24**, 131–144 (2022). <https://doi.org/10.37190/ABB-01989-2021-02>
17. Fraser, K.H., Zhang, T., Taskin, M.E., Griffith, B.P., Wu, Z.J.: A quantitative comparison of mechanical blood damage parameters in rotary ventricular assist devices: shear stress, exposure time and hemolysis index. *J. Biomech. Eng.* (2012). <https://doi.org/10.1115/1.4007092>
18. Harrison, P.: Progress in the assessment of platelet function. *Br. J. Hematol.* **111**, 733–744 (2000)
19. Gemmel, C.H.: Activation of platelets by in vitro whole blood contact with materials: increases in microparticle procoagulant activity, and soluble P-selectin blood levels. *J. Biomater. Sci. Polym.* **12**, 933–943 (2001)
20. Kim, J., Antaki, J.F., Massoudi, M.: Computational study of blood flow in microchannels. *J. Comput. Appl. Math.* **292**, 174–187 (2016)
21. Yu, Z., Tan, J., Wang, S.: Enhanced discrete phase model for multiphase flow simulation of blood flow with high shear stress. *Sci. Prog.* (2021). <https://doi.org/10.1177/00368504211008064>
22. James, M.E., Papavassiliou, D.V., O’Rear, E.A.: Use of computational fluid dynamics to analyze blood flow, hemolysis and sublethal damage to red blood cells in a bileaflet artificial heart valve. *Fluids* (2019). <https://doi.org/10.3390/fluids4010019>
23. Beris, A.N., et al.: Recent advances in blood rheology: a review. *Soft Matter* **17**, 10591–10613 (2021)
24. Sucusky, P., Padala, M., Elhammali, A., Balachandran, K., Jo, H., Yoganathan, A.P.: Design of an ex vivo culture system to investigate the effects of shear stress on cardiovascular tissue. *J. Biomech. Eng.* (2008). <https://doi.org/10.1115/1.2907753>
25. Major, R., Wilczek, G., Więcek, J., Gawlikowski, M., Plutecka, H., Kasperkiewicz, K., Kot, M., Pomorska, M., Ostrowski, R., Kopernik, M.: Hemocompatible Thin Films Assessed under Blood Flow Shear Forces. *Molecules.* **27**, 5696 (2022). <https://doi.org/10.3390/molecules27175696>
26. El-Aragi, G.M.: Effect of electrohydraulic discharge on viscosity of human blood. *Phys. Res. Int.* (2013). <https://doi.org/10.1155/2013/203708>
27. Karaki, W., Rahul, L.C.A., Borca-Tasciuc, D.A., De, S.: A continuum thermomechanical model of in vivo electrosurgical heating of hydrated soft biological tissues. *Int. J. Heat Mass Transf.* **127**, 961–974 (2018)
28. Vaidya, N., Baragona, M., Lavezzo, V., Maessen, R., Veroy, K.: Simulation study of the cooling effect of blood vessels and blood coagulation in hepatic radiofrequency ablation. *Int. J. Hyperther.* **38**, 95–104 (2021)
29. Blake, A.S.T., Petley, G.W., Deakin, C.D.: Effects of changes in packed cell volume on the specific heat capacity of blood: implications for studies measuring heat exchange in extracorporeal circuits. *Br. J. Anaesth.* **84**, 28–32 (2000)
30. Ponder, E.: The specific heat and the heat of compression of human red cells, sickled red cells, and paracrystalline rat red cells. *J. Gen. Physiol.* **38**, 575–580 (1995)
31. Alimohamadi, H., Smith, A., Nowak, R., Fowler, V., Rangamani, P.: Non-uniform distribution of myosin-mediated forces governs red blood cell membrane curvature through tension modulation. *PLoS Comput. Biol.* (2020). <https://doi.org/10.1371/journal.pcbi.1007890>
32. Liu, H., Lan, L., Abrigo, J., et al.: Comparison of newtonian and non-newtonian fluid models in blood flow simulation in patients with intracranial arterial stenosis. *Front. Physiol.* (2021). <https://doi.org/10.3389/fphys.2021.718540>
33. Derakhti, S., Hamid Safiabadi-Tali, S., Amoabediny, G., Sheikhpour, M.: Attachment and detachment strategies in microcarrier-based cell culture technology: a comprehensive review. *Mater. Sci. Eng. C* (2019). <https://doi.org/10.1016/j.msec.2019.109782>

34. Buschmann, M.H., Dieterich, P., Adams, N.A., Schnittler, H.-J.: Analysis of flow in a cone-and-plate apparatus with respect to spatial and temporal effects on endothelial cells. *Biotechnol. Bioeng.* **89**, 493–502 (2005)
35. Spruell, C., Baker, A.B.: Analysis of a high-throughput cone-and-plate apparatus for the application of defined spatiotemporal flow to cultured cells. *Biotechnol. Bioeng.* **110**, 1782–1793 (2013)
36. Chen, Z., Sun, A., Wang, H., Fan, Y., Deng, X.: Non-physiological shear stress-induced blood damage in ventricular assist device. *DOAJ* (2019). <https://doi.org/10.1016/j.medntd.2019.100024>
37. Khoo, D.P.Y., Cookson, A.N., Gill, H.S., Fraser, K.H.: Normal fluid stresses are prevalent in rotary ventricular assist devices: a computational fluid dynamics analysis. *IJAO* **41**, 738–751 (2018)
38. Zhang, J., Chen, Z., Griffith, B.P., Wu, Z.J.: Computational characterization of flow and blood damage potential of the new maglev CH-VAD pump versus the HVAD and HeartMate II pumps. *IJAO* **43**, 653–662 (2020)

Effect of Mechanical Aortic Valves on Coronary Artery Flow in a Patient Suffering from Ischemic Heart Disease



Anna Nieroda, Krzysztof Jankowski, and Marek Pawlikowski

Abstract Coronary artery disease is the most common cardiovascular condition and one of the leading causes of death worldwide. Coronary artery disease is caused by a narrowing or complete occlusion of the coronary artery lumen. Early diagnosis and correct assessment of the existing stenosis are essential. In our study, a pilot study in this regard, we present a method of non-invasive FFR estimation based on 3D numerical simulations of blood flow through coronary arteries in a 50-year-old man with coronary artery stenosis. Our study considered patient-specific coronary artery geometry. The study determined the effect of blood pressure gradient in flow across mechanical trileaflet (TRI) and bileaflet (BIL) and natural aortic valves on the fractional coronary flow reserve (FFR) value. The predicted value of the FFR ratio for the natural valve is 82% while the FFR value from coronarography is 83%. The predicted FFR values for BIL and TRI mechanical valves are 77% and 75%, respectively.

Keywords Aortic valve · Mechanical valve · Coronary artery · Blood flow · FFR

1 Introduction

One of the most common diseases of the cardiac system is ischemic heart disease (IHD) also called coronary heart disease (CHD). It still remains the main cause of mortality in the world [1, 2]. Patients suffering from IHD are treated either conservatively by means of medications [3] or invasively by means of percutaneous revascularization [4] or coronary artery bypass surgery [5]. An invasive intervention must be preceded by an accurate examination of patients which will give a clear indication of whether or not they may be qualified for a surgical procedure. To detect ischemia caused by artery stenosis fractional flow reserve (FFR) ratio is commonly measured [6–8]. FFR, which is the gold standard for diagnosis of the functional

A. Nieroda · K. Jankowski · M. Pawlikowski (✉)

Institute of Mechanics and Printing, Warsaw University of Technology, Narbutta 85, 02-524 Warszawa, Poland

e-mail: marek.pawlikowski@pw.edu.pl

severity of coronary lesions, is calculated as the ratio between the averaged blood flow pressure measured distally to that measured proximally to the stenosis. FFR is obtained invasively by measurement of both pressure values by means of a guiding catheter and a sensor-tipped pressure wire. For some years now non-invasive methods of ischemia diagnosis have been developing. The method of FFR calculation based on computer tomography (FFR-CT) is commonly used. FFR-CT incorporates computational fluid dynamics to estimate the functional data (FFR values) from anatomic images obtained by means of CT coronary angiography. A systematic review of the diagnostic performance of FFR-CT compared to FFR as the reference standard was presented in [9]. The authors reported very high compliance of diagnoses based on FFR-CT with those based on invasive FFR, especially in the cases of patients whose coronary arteries were minimally diseased or normal ($FFR > 0.80$) and the patients qualified for stenting ($FFR < 0.60$). The FFR-CT gave less certainty of diagnosis in the case of patients with FFR between 0.60 and 0.80. The study showed that the diagnostic accuracy of FFR-CT varied across the spectrum of disease. In general, FFR-CT shows a significant correlation with invasive FFR; however, additional studies are required to determine its diagnostic performance [10–13].

Stress cardiovascular magnetic resonance imaging (CMR) is another non-invasive method to diagnose myocardial ischemia. It is also widely used to document ischemia in qualification for coronary revascularization [14]. An attempt to evaluate the agreement of CMR with FFR as the gold standard in assessing the severity of stenoses in IHD has been made by Siastała et al. [15]. The authors analysed 25 consecutive patients who underwent both CMR and FFR to diagnose possible stenosis. They concluded that CMR was clinically useful mostly in patients with stable IHD. Whereas, for patients with a high pretest probability of IHD, CMR method may be applied as a confirmatory test. Recent study shows that CMR seems to be an excellent tool for the assessment of IHD [16]. However, the utilisation of CMR is hampered by several factors, such as claustrophobic and obese patients may not be able to tolerate the examination, patients with implantable ferromagnetic material-made devices should not be examined by means of CMR, relatively high cost compared to invasive FFR method.

It is acknowledged that invasive FFR will remain an important determinant of the treatment indication of IHD. Nevertheless, newer less- and non-invasive techniques are expected to play an increasingly important role in the diagnosis. In our paper, a pilot study in this regard, we present a method of non-invasive FFR estimation based on 3D numerical simulations of blood flow through coronary arteries. It is expected that such simulations will give reliable value of FFR and in future will be utilised in qualification for a surgical procedure. Once the method is fully developed and validated, it can be utilised to assess FFR value in patients with, e.g. implanted an artificial (mechanical) aortic valve (AV). We have not found any studies which undertake the problem of possible FFR value change after an AV implantation. There is some research dealing with FFR estimation after transcatheter aortic valve implantation (TAVI) [17–19]. It has to be underlined that during a TAVI procedure a natural aortic valve is implanted, i.e. pork or beef pericardium on a metallic stent is inserted.

In our study, we aim to assess the difference in FFR values in patients with a mechanical valve implanted. Nowadays, mainly mechanical aortic valves with two leaflets (bileaflet (BIL) AVs) are implanted. However, also studies on AVs with three leaflets (trileaflet (TRI) AVs) are also carried out [20–22]. Analyses of blood flow through BIL and TRI are presented in our previous paper [23]. The analyses are based on numerical simulations performed by means of finite element method (FEM) where boundary conditions play a significant role [24]. A few words regarding this matter are presented in the last section. In the present paper, we estimate a possible change in FFR value in patients who underwent an implantation of BIL valve and a TRI valve [23]. Simulation of blood flow in the coronary arteries in a patient with the natural aortic valve is also carried out. The results of the simulations are compared and analysed.

2 Methods

2.1 Study Design

The main objective of this study was to analyse the effect of mechanical heart valves on coronary artery blood flow. Comparison of flow across BIL, TRI and natural aortic valves (Fig. 1) in a patient with CHD will allow us to estimate the impact of mechanical valve geometry on FFR values. The FFR value measured at coronarography was 83%.

Modelling blood flow through blood vessels, which form a branching structure, requires truncation of the model of this structure. Thus, a problem of proper boundary conditions at the distal ends of the vessels arises. The smaller vessels beyond the truncation point must be substituted by boundary conditions to make the simulations more realistic. In our studies, we defined a combination of flow velocity and pressure at the inlet and outlet. Measurement of blood flow velocity (Doppler ultrasound) was used to determine the boundary conditions. To reflect the physiological blood flow, especially in the region of the sinuses where vortices form, we assumed turbulent blood flow and used the $k-\epsilon$ model to determine its turbulent characteristics. Blood was modelled as an incompressible fluid. We assumed the density $\rho = 1060 \text{ [kg/m}^3\text{]}$

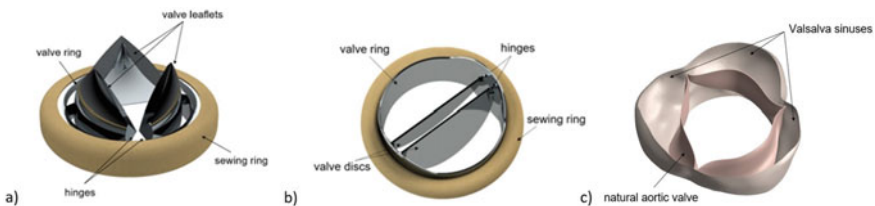


Fig. 1 Aortic valves: **a** TRI, **b** BIL, **c** natural

and viscosity $\mu = 0.0035$ [kg/(m·s)] [25]. The Navier–Stokes equations defined the flow.

2.2 Geometry and Meshing

The geometrical model of blood was generated in Mimics software from CT images of a 50-year-old man with coronary artery stenosis. The CT scan was performed on a 384 Slice Cardiac CT scanner (spatial resolution is 0.24 [mm]). Blood in the coronary arteries is visible on CT images due to the contrast medium added during the coronarography. The model consisted of the aortic root (with Valsalva sinuses) and coronary arteries (Fig. 2). The inner diameter of the ascending aorta is about 30 [mm], the diameter of the inlet is about 23 [mm].

In our study, we considered two types of mechanical valves, i.e. BIL and TRI valves and natural aortic valve. The design of the mechanical valve rings and BIL valve discs was modelled in our previous study [23]. Following the conclusions of our recent study, we modified the shape of the TRI valve leaflets to increase the effective orifice area E_{OA} (Fig. 3). The geometry of the natural valve was modelled based on the anatomical structure of the valve leaflets.

The dynamics of blood circulation were determined using ANSYS 2020 R2 software. The use of the Fluent Flow module allowed the determination of accurate flow

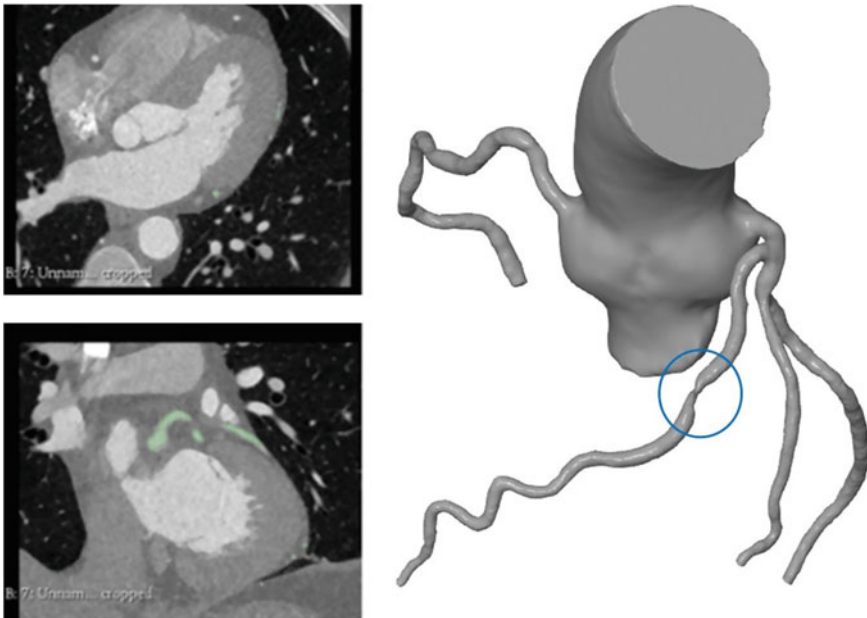


Fig. 2 Model of the whole analysed system

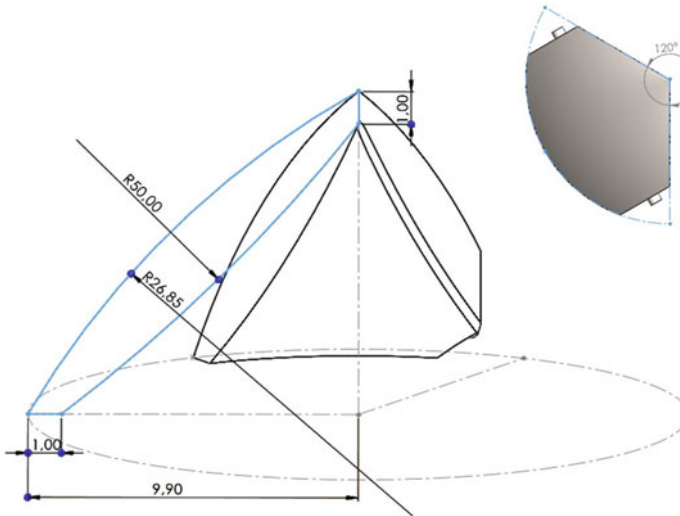


Fig. 3 Shape of the TRI valve leaflet

characteristics. A pressure-based solver was used for the calculations. The numerical model showed the blood model (Fig. 4a) without considering the tissues. The whole blood system was discretised into 2.5 million finite elements. The mesh is made of tetrahedron elements.

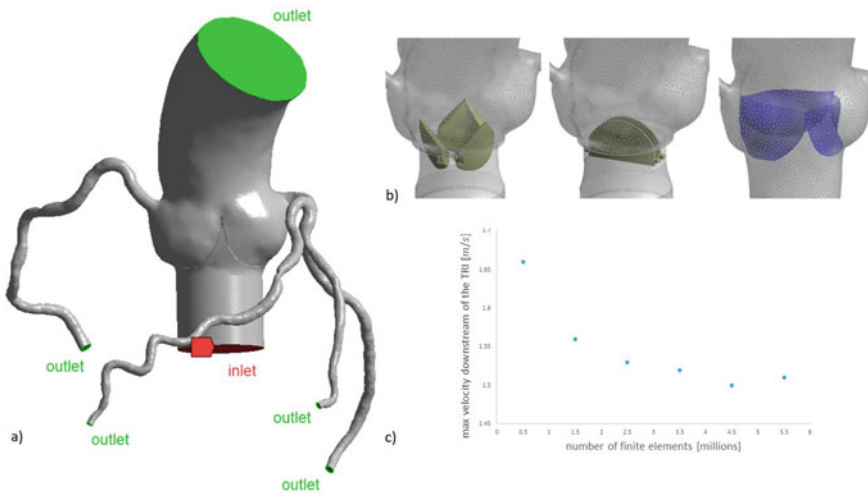


Fig. 4 **a** Fluid domain with the inlet and outlets, **b** TRI, BIL (mechanical valves) and natural valve location in numerical model (from left to right), **c** Influence of the number of the finite elements on maximal velocity downstream of the TRI valve

We confirmed the mesh independence of the flow model solution by comparing the max velocities (Fig. 4c). In addition, the quality of the mesh representing blood was checked. The Orthogonal Quality is about 0.79, and the Skewness is about 0.21. The values obtained indicate a grid of good quality.

Numerical analyses were performed on a workstation with the following parameters: AMD Ryzen 7 3700X 8-Core Processor, 32 GB RAM, 64-bit operation system, and NVIDIA Quadro graphic card.

2.3 Boundary Conditions

The correlation of the flow velocity and valve opening time was determined by Doppler ultrasound and described by Eqs. (1)-(3) [23]. The length of one cycle is 0.8 [s]. Numerical measurement of FFR was performed during the hyperemia (for $t = 0.29$ [s]).

for $t \in < 0; 0.36$ s)

$$v = 10259.13 \cdot t^6 - 13602.92 \cdot t^5 + 6827.23 \cdot t^4 - 1500.76 \cdot t^3 + 90.61 \cdot t^2 + 9.54 \cdot t \quad (1)$$

for $t \in < 0.36; 0.38$ s)

$$v = 2.5 \cdot t - 0.95 \quad (2)$$

for $t \in < 0.38; 0.8$ s)

$$v = 0 \quad (3)$$

Flow velocity values were determined at the inlet, which was defined at the aortic inlet. At the outlet of the coronary arteries, a pressure of 1.3 [kPa] was defined, allowing for consideration of vascular resistance and normal myocardial perfusion.

Figure 4a illustrates the boundary conditions, and Fig. 4b shows a scheme of valve locations in the model.

3 Results

The FFR is defined as the ratio of mean pressure measured distally behind the stenosis location (P_d) to mean pressure measured proximally (P_a) during hyperemia Eq. (4). The $FFR < 0.8$ determines surgical treatment.

$$FFR = \frac{P_d}{P_a} \tag{4}$$

Using data from the results of pressure distribution, the FFR ratio for the natural valve, BIL valve and TRI valve was calculated and compared with the results of coronarography (Table 1). The pressure (P_d and P_a) was calculated at a distance of five stenosis diameters from the maximum coronary artery stenosis as it is measured during the examination.

In Figs. 5 and 6, the flow velocity magnitude changes in the aortic root and ascending aorta, and the velocity distribution are shown, respectively.

In Fig. 7, the geometry of the aortic root is presented. The Valsalva sinuses can be clearly seen. In geometrical modelling of the aorta and coronary arteries it is crucial to model accurately the sinuses geometry as it significantly influences the results of blood flow simulation. In addition, correct location of the sinuses in the model determines the orientation of the mechanical valve placement. During building the assembly models of the aorta and mechanical valves we paid special attention to the leaflet position in terms of a possible obstruction of blood flow into coronary arteries.

We also calculated the effective orifice area E_{OA} and geometric flow area of the fluid through the valves (Table 2). Determination of E_{OA} allows assessment of the pressure gradient through the valve. In this way, it evaluates whether the flow area

Table 1 FFR ratio

	FFR [%]
Coronarography	83
Natural valve	82
BIL valve	77
TRI valve	75

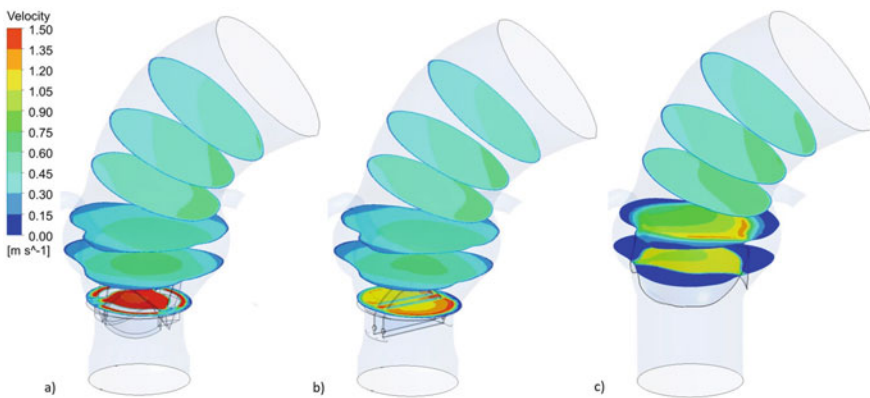


Fig. 5 Flow velocity magnitude change in the aortic root and ascending aorta for the valve: **a** TRI, **b** BIL, **c** natural

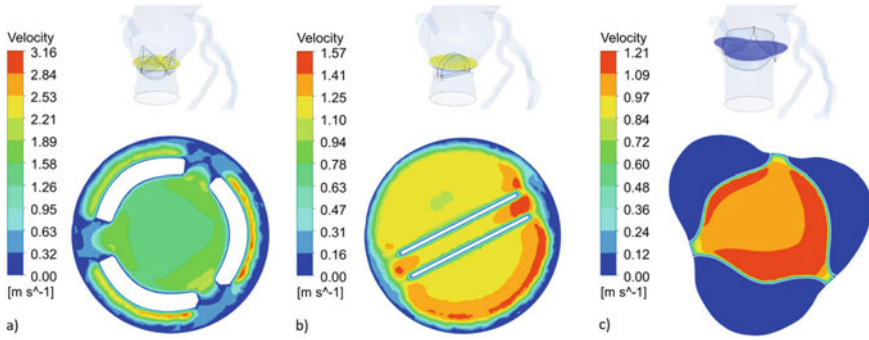


Fig. 6 Velocity magnitude distribution for the valve: **a** TRI, **b** BIL, **c** natural

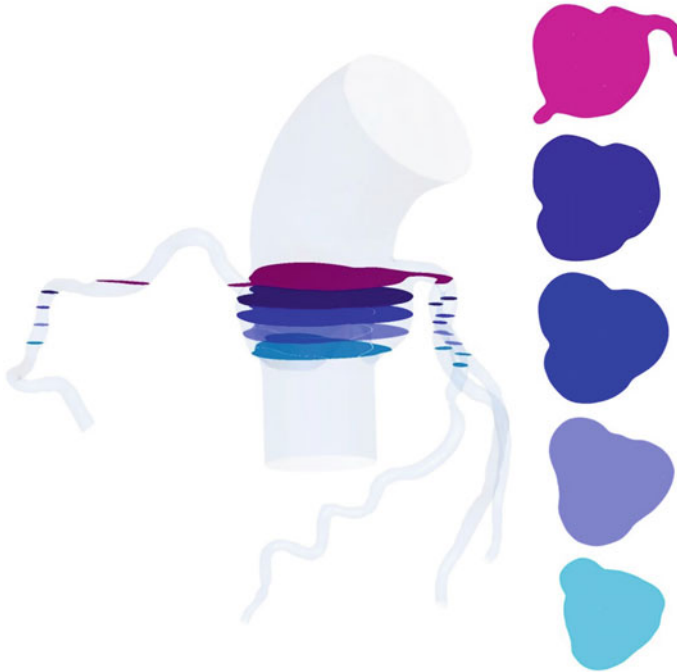


Fig. 7 Patient-specific aortic root geometry

is large enough to prevent the pressure gradient from increasing, which can lead to heart failure. To calculate E_{OA} , we used the corrected Gorlin formula in the form [26]:

$$E_{OA} = \frac{Q}{51.6 \sqrt{\frac{\Delta p}{\rho}}} \quad (5)$$

Table 2 E_{OA} and geometric valves flow area

	E_{OA}	Geometric flow area [cm ²]
Natural valve	2.85	3.74
BIL valve	1.53	2.88
TRI valve	0.73	1.61

where Q is the volume flow rate in [mL/s], Δp is the average pressure difference through the valve in [mmHg], and ρ is the blood density in [g/cm³]. The number 51.6 is the gravitational acceleration constant.

The calculations were based on $Q = 110$ [mL/s] (the value obtained from the study for the analysed patient) and $\rho = 1.06$ [g/cm³].

4 Discussion

Modern high-resolution CT enables obtaining exact images converted into precise 3D models of blood. These models can be used in simulations of blood flow. The value of the FFR ratio (Table 1) for the natural valve predicted in our numerical simulation (82%) is near to the FFR value from coronarography (83%). The obtained results confirm the validity of the simulations. Since the predicted and measured FFR values for natural valve are almost the same, we hypothesise that the numerical model is accurate enough to reliably predict the FFR values for the artificial valves. The FFR values for BIL and TRI mechanical valves are 77 and 75%. The difference in FFR values for the natural valve compared to the BIL and TRI valves is 5 and 7%, accordingly. The differences in the results may be due to the smaller E_{OA} of the mechanical valves (Table 2). Although the E_{OA} for the TRI valve (0.73 [cm²]) is smaller than that for the BIL valve (1.53 [cm²]), the FFR value differs slightly. This is probably due to the shape of the TRI valve leaflets, which point towards the sinuses of Valsalva at the maximum opening and allow unobstructed blood flow into the coronary arteries.

Studies suggest that geometric parameters of the coronary artery are essential in the final haemodynamic results of the simulations. This issue is critical because coronary branches' number, length, irregularity, and given boundary conditions at the ends influence the pressure value behind the stenosis. Defining distal boundary conditions is particularly challenging, as circulatory conditions in the coronary microcirculation are heterogeneous in health and disease. Consequently, their underestimation or omission may distort the FFR ratio determined by us. The values of pressure in a coronary artery, and consequently those of FFR, strongly depend on boundary conditions, especially those defined in the truncated ends of the arteries at the outlets [27]. Identification of the outlet boundary conditions is not trivial as measurement of reliable blood flow, pressure, or resistance at each outlet is practically impossible [28]. However, there are methods which make it possible to estimate the outlet resistance according to myocardial perfusion territory. One of the newest approaches

in the outlet boundary conditions definition is reported in [29]. The authors developed a personalised CT-based coronary blood flow model to estimate coronary outlet resistance and distributed outlet coronary blood flow based on myocardial perfusion territory. Although their method seems to be reliable, they stated that it still requires further validation.

Our study considered patient-specific coronary artery geometry (Fig. 2). Carvalho et al. [30] use an idealised geometry, which may impact fluid dynamics. Researchers use different blood viscosity models and flow conditions to study flow. It is generally accepted that blood behaves as a Newtonian fluid in large coronary vessels [31, 32]. However, it should be noted that in areas of constriction, due to the ability of red blood cells to form aggregates, blood should be defined as a non-Newtonian fluid [33, 34]. Only a few studies have evaluated the impact of different inlet and outlet boundary conditions. Researchers use velocity, pressure or flow rate combinations at the inlet while at the outlet constant pressure outlet, Windkessel model or zero gauge pressure [30, 31, 35]. In our study, we assumed velocity at the inlet, which was determined by Doppler ultrasound, and pressure at the outlet allowing for consideration of vascular resistance (Fig. 4a). In future studies, we will focus on analysing the effect of preset boundary conditions on the corresponding behaviour of blood flow in coronary arteries. There is no substantial evidence that it is necessary to reflect the movement of the vessel wall to calculate FFR. Typically, rigid wall conditions are used [32, 33]. Our future studies will also focus on examining the effect of considering coronary artery walls on flow and FFR.

Our model takes into account the sinuses of Valsalva, which have individually defined shapes and dimensions. Consideration of the real geometry allows for accurate results. De Tulio et al. conducted numerical simulations of blood flow after a mechanical aortic valve and studied the influence of the aortic root geometry on blood behaviour in the region of sinuses [36]. They considered three models, i.e. three sinuses, one sinus in the form of an axisymmetric bulb, and a simple aorta without sinuses. Their results indicate that the aortic root's geometry only marginally affects the kinematic features of blood flow downstream of a mechanical valve. Only minor changes in velocities were observed. However, differences in the dynamics of blood flow resulting from the aortic root geometry are noticeable. The authors of [37] observed the formation of vortices in the region of the sinuses. Their numerical results show a presence of negative velocities that they interpreted as blood recirculation in the sinuses. However, researchers do not consider coronary arteries, which have their origins in the sinuses and may significantly affect fluid dynamics in the aortic root. In consequence, the wall boundary condition is imposed on the inner surfaces of the sinuses. This is a factor that benefits vortex formation in the region. In [36], the authors modelled the aortic root geometry with coronary arteries truncated at a close distance from the aorta and defined boundary conditions that “are limiting in that, in general, they do not accurately replicate vascular impedance of the downstream vasculature”. This means that they did not consider the inertia of the fluid of all the neglected parts of the vascular network, nor did they consider the compliance of the arteries. The primary characteristics of coronary flow were analysed by Querzoli et al. [38]. They concluded that 75% of the flow in coronary arteries occurs during

diastole. During systole, no distinct effects were observed, except for a secondary vortex region located at the inlet of the coronary vessel. In future studies, we will focus on comparing the behaviour of blood in systole and diastole.

The flow distribution in the ascending aorta is determined by the curvature of the aortic arch (Fig. 5). Maximum flow velocities occur in the TRI valve because a gap between the leaflet and the valve ring remains during maximal leaflet opening (Figs. 5 and 6a). Analysis of fluid behaviour indicates that implanting the valve before the aortic root does not cause vortices in the sinuses of Valsalva and reduces turbulent flow. However, this may have a negative effect on the closure of the valve leaflets. Analysis of Fig. 6 allows us to note the impact of the non-idealised shape of the sinuses on flow. The patient-specific aortic root geometry shows in Fig. 7. There are higher flow velocities in the sinus where the left coronary artery is located, 3.16 [m/s] for TRI, 1.57 [m/s] for BIL and 1.21 [m/s] for the natural valve (Fig. 6).

The study determined the effect of blood pressure gradient in flow across mechanical (TRI and BIL) and natural aortic valves on the fractional coronary flow reserve (FFR) value. Due to their geometry and location, mechanical heart valves have a smaller flow area, so there is a change in the pressure gradient upstream and downstream of the valve. It is worth analysing the location of the implanted artificial heart valve and its effect on the pressure change and optimising the mechanical valve's shape.

References

1. Fossan, F.E., Sturdy, J., Muller, L.O., et al.: Uncertainty quantification and sensitivity analysis for computational FFR estimation in stable coronary artery disease. *Cardiovasc. Eng. Technol.* **9**(4), 597–622 (2018)
2. Knuuti, J., Wijns, W., Saraste, A., et al.: 2019 ESC guidelines for the diagnosis and management of chronic coronary syndromes. *Eur. Heart J.* **41**, 407–477 (2020)
3. Rezende, P.C., Scudeler, T.L., Alves da Costa, L.M., et al.: Conservative strategy for treatment of stable coronary artery disease. *World J. Clin. Cases* **3**, 163–170 (2015)
4. Perera, D., Clayton, T., O’Kane, P.D., et al.: Percutaneous revascularization for ischemic left ventricular dysfunction. *N. Engl. J. Med.* **387**, 1351–1360 (2022)
5. Bojar, R.M.: Cardiovascular management. In: *Manual of Perioperative Care in Adult Cardiac Surgery*. Wiley. ISBN 978-1-119-58255-7 (2021)
6. Li, M., Zhou, T., Yang, L.-F., et al.: Diagnostic accuracy of myocardial magnetic resonance perfusion to diagnose ischemic stenosis with fractional flow reserve as reference: systematic review and meta-analysis. *JACC Cardiovasc. Imaging* **7**, 1099–1105 (2014)
7. Yang, Z., Zheng, H., Zhou, T., et al.: Diagnostic performance of myocardial perfusion imaging with SPECT, CT and MRI compared to fractional flow reserve as reference standard. *Int. J. Cardiol.* **190**, 103–105 (2015)
8. Qayyum, A., Kastrup, J.: Measuring myocardial perfusion: the role of PET, MRI and CT. *Clin. Radiol.* **70**, 576–584 (2015)
9. Cook, C.M., Petraco, R., Shun-Shin, M.J., et al.: Diagnostic accuracy of computed tomography-derived fractional flow reserve. A systematic review. *JAMA Cardiol.* **2**(11), 803–810 (2017)
10. Sonck, J., Nagumo, S., Norgaard, B.L., et al.: Clinical validation of a virtual planner for coronary interventions based on coronary CT angiography. *JACC Cardiovasc. Imaging* **15**, 1242–1255 (2022)

11. Serruys, P.W., Hara, H., Garg, S., et al.: Coronary computed tomographic angiography for complete assessment of coronary artery disease. *J. Am. Coll. Cardiol.* **78**, 713–736 (2021)
12. Tanigaki, T., Emori, H., Kawase, Y., et al.: QFR versus FFR derived from computed tomography for functional assessment of coronary artery stenosis. *JACC Cardiovasc. Interv.* **12**, 2050–2059 (2019)
13. Peper, J., Becker, L.M., van den Berg, H., et al.: Diagnostic performance of CCTA and CT-FFR for the detection of CAD in TAVR work-up. *JACC Cardiovasc. Interv.* **15**, 1140–1149 (2022)
14. Costa, M.A., Shoemaker, S., Futamatsu, H., et al.: Quantitative magnetic resonance perfusion imaging detects anatomic and physiologic coronary artery disease as measured by coronary angiography and fractional flow reserve. *J. Am. Coll. Cardiol.* **50**, 514–522 (2007)
15. Siastala, P., Kądziela, J., Małek, Ł.A., et al.: Do we need invasive confirmation of cardiac magnetic resonance results? *Adv. Interv. Cardiol.* **13**(1), 26–31 (2017)
16. Patel, A.R., Salerno, M., Kwong, R.Y., et al.: Stress cardiac magnetic resonance myocardial perfusion imaging: JACC review topic of the week. *J. Am. Coll. Cardiol.* **78**, 1655–1668 (2021)
17. Scarsini, R., Lunardi, M., Venturi, G., et al.: Long-term variations of FFR and iFR after transcatheter aortic valve implantation. *Int. J. Cardiol.* **317**, 37–41 (2020)
18. Scarsini, R., Pesarini, G., Lunardi, M., et al.: Observations from a real-time, iFR-FFR “hybrid approach” in patients with severe aortic stenosis and coronary artery disease undergoing TAVI. *Cardiovasc. Revasc. Med.* **19**, 355–359 (2018)
19. Ahmad, Y., Götzberg, M., Cook, C., et al.: Coronary hemodynamics in patients with severe aortic stenosis and coronary artery disease undergoing transcatheter aortic valve replacement: implications for clinical indices of coronary stenosis severity. *JACC Cardiovasc. Interv.* **11**, 2019–2031 (2018)
20. Nowak, M., Divo, E., Adamczyk, W.P.: Fluid-structure interaction methods for the progressive anatomical and artificial aortic valve stenosis. *Int. J. Mech. Sci.* **227**, 1–20 (2022)
21. Zhou, H., Wu, L., Wu, Q.: Structural stability of novel composite heart valve prostheses—fatigue and wear performance. *Biomed. Pharmacother.* **136**, 1–8 (2021)
22. Cavallo, A., Gasparotti, E., Losi, P., et al.: Fabrication and in-vitro characterization of a polymeric aortic valve for minimally invasive valve replacement. *J. Mech. Behav. Biomed. Mater.* **115**, 1–9 (2021)
23. Pawlikowski, M., Nieroda, A.: Comparative analyses of blood flow through mechanical trileaflet and bileaflet aortic valves. *Acta Bioeng. Biomech.* **24**, 141–152 (2022)
24. Vignon-Clementel, I.E., Figueroa, C.A., Jansen, K.E., et al.: Outflow boundary conditions for 3D simulations of non-periodic blood flow and pressure fields in deformable arteries. *Comput. Methods Biomech. Biomed. Eng.* **13**, 625–640 (2010)
25. Ali, A., Kazmi, R.: High performance simulation of blood flow pattern and transportation of magnetic nanoparticles in capillaries. *Intell. Technol. Appl.* **1198**, 222–236 (2020)
26. Hui, S., Mahmood, F., Matyal, R.: Aortic valve area-technical communication: continuity and Gorlin equations revisited. *J. Cardiothorac. Vasc. Anesth.* **32**(6), 2599–2606 (2018)
27. Taylor, C.A., Figueroa, C.: Patient-specific modeling of cardiovascular mechanics. *Ann. Rev. Biomed. Eng.* **11**, 109–134 (2009)
28. Morris, P.D., van de Vosse, F.N., Lawford, P.V., et al.: “Virtual”(computed) fractional flow reserve: current challenges and limitations. *JACC: Cardiovasc. Interv.* **8**(8), 1009–1017 (2015)
29. Xue, X., Liu, X., Gao, Z., et al.: Personalized coronary blood flow model based on CT perfusion to non-invasively calculate fractional flow reserve. *Comput. Methods Appl. Mech. Eng.* **404**, 115789 (2023)
30. Carvalho, V., Rodrigues, N., Ribeiro, R., et al.: Hemodynamic study in 3D printed stenotic coronary artery models: experimental validation and transient simulation. *Comput. Methods Biomech. Biomed. Eng.* **24**(6), 623–636 (2020)
31. Lo, E.W.C., Menezes, L.J., Torii, R.: Impact of inflow boundary conditions on the calculation of CT-based FFR. *Fluids* **4**(2), 60 (2019)
32. Carvalho, V., Rodrigues, N., Ribeiro, R., et al.: 3D printed biomodels for flow visualization in stenotic vessels: an experimental and numerical study. *Micromachines* **11**(6), 549 (2020)

33. Kashyap, V., Arora, B.B., Bhattacharjee, S.: A computational study of branch-wise curvature in idealized coronary artery bifurcations. *Appl. Eng. Sci.* **4**, 100027 (2020)
34. Pandey, R., Kumar, M., Srivastav, V.K.: Numerical computation of blood hemodynamic through constricted human left coronary artery: pulsatile simulations. *Comput. Methods Program. Biomed.* **197**, 105661 (2020)
35. Zhao, Y., Ping, J., Yu, X.: Fractional flow reserve-based 4D hemodynamic simulation of time-resolved blood flow in left anterior descending coronary artery. *Clin. Biomech.* **70**, 164–169 (2019)
36. de Tullio, M.D., Pedrizzetti, G., Verzicco, R.: On the effect of aortic root geometry on the coronary entry-flow after a bileaflet mechanical heart valve implant: a numerical study. *Acta Mech.* **216**(1), 147–156 (2011)
37. Belkhiri, K., Boumeddane, B.: A Cartesian grid generation technique for 2-D non-Newtonian blood flow through a bileaflet mechanical heart valve. *Int. J. Comput. Methods Eng.* **22**(4), 297–315 (2021)
38. Querzoli, G., Fortini, S., Espa, S., et al.: A laboratory model of the aortic root flow including the coronary arteries. *Exp. Fluids* **57**(8), 1–9 (2016)

New Applications

Stump Length Effect on Pelvic Tilt in Transfemoral Amputees Assessed by Statistical Parametric Mapping



Vít Nováček, Simona Bartošová, Bohumír Chládek, Pavel Jedlička, Alberto Sanchez-Alvarado, Ondřej Vyhna, Tomáš Železný, Jiří Křen, and Luděk Hynčík

Abstract There are limited objective data on the effects of transection levels in transfemoral amputees on gait patterns. The small sample size is frequently a limiting factor. Indeed, it may prove difficult to enroll enough volunteers sharing common aspects, e.g., the same model of the prosthetic knee articulation. The small sample size might be compensated by using advanced data analysis techniques. Statistical Parametric Mapping (SPM) allows analyzing n-dimensional data in contrast to standard techniques comparing sets of scalar values, which leads to data compression and information loss. The SPM technique was used to compare pelvic rotation angles in three knee disarticulation amputees with three mid-femur amputees under slow, normal, and fast walking instruction. SPM allowed identifying gait cycle intervals with significant differences in pelvic rotation angles. Stump length affected the gait pattern: The longer the stump, the higher the gait stability with less variability in pelvic tilt and shorter time spent on the healthy limb. These results suggest differences in compensatory mechanisms between knee disarticulation and mid-femur amputees. A detailed understanding of these mechanisms should help optimize the prosthesis design and settings and the therapy preventing low back pain and other complications associated with unilateral overloading.

V. Nováček (✉) · L. Hynčík
New Technologies - Research Centre, University of West Bohemia, Plzeň, Czech Republic
e-mail: vnovacek@ntc.zcu.cz

S. Bartošová · B. Chládek
Protetika Plzeň s.r.o., Plzeň, Czech Republic

P. Jedlička · T. Železný
New Technologies for the Information Society, University of West Bohemia, Plzeň, Czech Republic

A. Sanchez-Alvarado
Institute of Human Movement Science, University of Hamburg, Hamburg, Germany

O. Vyhna
Otto Bock ČR s.r.o., Zruč-Senec, Czech Republic

J. Křen · L. Hynčík
Faculty of Applied Sciences, University of West Bohemia, Plzeň, Czech Republic

Keywords Transfemoral amputees · Gait · Pelvic tilt · Statistical parametric mapping

1 Introduction

The main causes of lower limb amputation are vascular disease (54%) including diabetes and peripheral arterial disease, trauma (45%), and cancer (less than 2%) [1]. There were 1.6 million amputees in the United States in 2005, and approximately 185,000 amputations were performed per year [2]. There were 57.7 million people with lower limb amputation due to traumatic causes worldwide in 2017 [3].

Lower-limb amputees present an asymmetrical gait pattern. Their functional level after surgery is thought to be affected by the length of the remaining limb structure, commonly known as the stump [4, 5]. The amputees usually spend more time on the intact limb and less time on the amputated side during the stance phase. Their stance phase duration varies according to the level of amputation and walking speed as compensation to protect their residual limb [6]. Moreover, the prosthetic components are known to influence their gait parameters [7].

The effect of the stump length on the gait pattern has been previously evaluated [4, 5, 8]. In the study of 26 military personnel with a trauma-related unilateral transfemoral amputation, the results showed that the gait speed of the shorter residual limb group was statistically lower than the longer residual limb group (1.22 ± 0.10 m/s vs. 1.37 ± 0.13 m/s, respectively) [4]. The step lengths, step widths, stance, and swing phases were not significantly different between groups.

In a recent mixed-method of scoping review and expert opinions, the authors concluded that a longer residual limb length has a positive effect on the gait parameters of transfemoral amputees, providing a greater mechanical lever arm, and better prevention of contractures [8].

In contrast, no correlation between the stump length and either knee (involved and non-involved sides), nor in the involved leg during the sit-to-stand or stand-to-sit transitions was shown [5]. However, a weak correlation between the hip torque on the sound side and the residual limb height was found [5].

Most of the available studies evaluating the gait kinematics in lower limb amputees are limited by small sample sizes and a lack of the inclusion of other influencing factors such as the orientation of the stump [4]. Other limitations are that part of these studies were based on military personnel or evaluated the correlation between the level of the femoral transaction and joint moments during sitting and standing transitions.

Finally, the studies mentioned above performed the discrete statistical analysis, limiting the results to a single time point throughout the continuous variables change over time. This may lead to excessive data compression and information loss. To the best of our knowledge, there is a lack of studies analyzing the effect of the stump length by the use of continuous waveform analysis. Therefore, the current research was aimed at assessing the effect of the stump length using an alternative

method known as Statistical Parametric Mapping [9, 10], with a particular focus on the pelvic rotation angles. Continuous waveform analysis allows us to identify the gait cycle intervals with significant differences in pelvic rotation angles between the studied groups. This analysis helps to better understand the underlying compensatory mechanisms employed by transfemoral amputees and amputees with knee disarticulation. A detailed understanding of these mechanisms should help optimize the prosthesis design and settings and also the therapy preventing low back pain and other complications associated with unilateral overloading.

2 Materials and Method

2.1 Participants

The study was approved by the Ethical Committee of the University of West Bohemia (request number NTC/477/2020 approved on 15th July 2020). The volunteers with knee disarticulation or transfemoral amputation were enrolled within the region to limit their travel. The purpose of the study and the test protocol was explained to the volunteers and they provided written consent for the study before the testing.

The participants had either knee disarticulation (A) or transfemoral amputation (B). All the volunteers were required to walk independently without any walking aid at the time of testing. Exclusion criteria included age above 70 years, diabetes, surgery within one year before the testing, injuries or comorbidities to the intact limb, or other areas of the body that might affect their gait, and finally, they had to avoid excessive physical activity one day before the testing.

In total 6 volunteers were enrolled, 3 in group A and 3 in group B. Groups A and B were further subdivided into subgroups L (left) and R (right) according to the side of amputation. The anthropometric details are summarized in Table 1. Both height and weight were measured with the prosthesis and shoes on. Stump length is expressed as a percentage of the intact limb length.

The length of the intact limb was measured from the ischial tuberosity to the medial femoral condyle. The length of the residual limb was measured from the ischial tuberosity to the distal end. Then, the stump length was considered a percentage of the sound limb. Personal and anthropometric data were collected by three professionals from the field of orthotics/prosthetics.

All the amputees used the C-Leg (Otto Bock, Germany) microprocessor knee unit in conjunction with the foot they usually use (not the same for everyone). Due to low numbers of amputees within the region meeting the inclusion criteria and willing to participate, stricter inclusion/exclusion criteria with more specific foot prosthesis design, time from injury, prosthetic experience, and other parameters, were not used.

Table 1 Anthropometric characteristics

Group	A: Knee disarticulation			B: Transfemoral amputation		
	1	2	3	4	5	6
Subject's ID						
Gender	Man	Woman	Man	Man	Man	Man
Age (years)	46	48	46	60	46	38
Time from injury (years)	18	26	8	35	12	12
Height (cm)	183	170	175	180	194	164
Weight (kg)	115	56	82	80	95	71
Prosthesis weight (kg)	4.5	4.0	5.0	4.1	5.0	5.4
Side of amputation	Right	Left	Left	Right	Left	Left
Etiology	Accident	Sarcoma	Accident	Accident	Accident	Accident
Stump length (%)	100	100	100	65	54	61

2.2 Gait Analysis

Conventional 3D gait analysis was performed for all subjects, employing spherical reflective markers with a diameter of 8 mm, placed according to the Conventional Gait Model 2 (CGM version 2.4). The same professional placed markers for all kinematic measurements. The Vicon motion tracking system (Vicon, Oxford, UK) was used to record kinematic data. The system consisted of eight Vicon T-20 cameras with a resolution of 2 Megapixels and the software Vicon Nexus v.2.11. The kinematic data acquisition frequency was set to 200 Hz. A calibration of the system was performed before the testing using a standard calibration tool.

The kinetic data were recorded with two Kistler (Kistler, Winterthur, Switzerland) portable force plates (model 9286BA, nominal capacity 10 kN). The kinetic data recording was hard-synchronized with the optical system. The kinetic data were collected at 10 kHz. Both force plates were integrated into a modular wooden walkway. The design of the walkway allows the force plates to be placed so that the first landing limb can be either right or left. To visually unify the surfaces and prevent slipping, the walkway and force plates were covered with a 2 mm thin dark blue carpet. The length of the walkway in front of and behind the force plates was between 4 and 5 m, and its total length was approximately 10 m.

A static measurement was performed with the subject standing on one force plate. The subject had the upper extremities lifted under the angle of approximately 45 degrees concerning the body and the elbows bent with forearms pointing forward. This position allowed us to check if all markers were correctly placed and visible. The static test was also used to record the subject's weight and to define a frame of reference for the calculation of pelvic angles.

The right force plate was placed closer to the subject in the initial walkway setup. Before a dynamic (walking) test, each subject performed several familiarization trials to estimate the starting point to hit both force plates correctly, without modifying their normal gait pattern. Then, the walkway setup was modified so that the left force

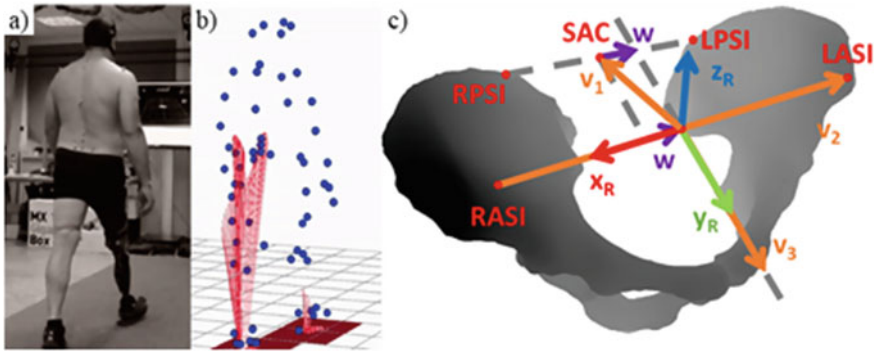


Fig. 1 **a** Illustration of a dynamic trial. **b** Corresponding markers (blue dots) and reaction forces (red butterfly graph). Force plates are shown in dark red. **c** A scheme illustrating how the frame of reference (origin and base vectors) is defined using four pelvic markers.

plate was closer to the subject and the entire procedure was repeated including the familiarization trials. The subjects took five minutes of rest or more if needed every five trials.

Each subject was asked to walk at three self-selected speeds: normal, fast, and slow. Normal speed was considered a self-selected speed both comfortable and safe for the volunteers. Fast and slow speeds were faster and slower than the normal speed, respectively, both still comfortable and safe for the volunteers. Five successful trials were recorded for each speed and force plate location. A trial was considered successful when the subject walked without missteps, all reflective markers were visible and the gait was smooth. A dynamic trial is illustrated in Fig. 1a. Corresponding markers and reaction forces are illustrated in Fig. 1b.

2.3 Data Processing

The kinetic and kinematic data were processed for all measurements first on the Nexus software. In case of temporary loss of reflective markers, an interpolation of their missing trajectory was used. Then, the data was exported to the C3D biomechanical data format. Finally, a custom code in the MATLAB R2019b software package (© The MathWorks, Inc., Natick, Massachusetts, USA) was used for further data processing. Body weight (measured in Newtons) recorded in the static trial was used to normalize the reaction forces measured by the force plates. The static trial was used to define the reference coordinate system (reference origin and base vectors) using the coordinates of four reflective markers: left anterior sacroiliac marker (LASI), right anterior sacroiliac marker (RASI), left posterior sacroiliac marker (LPSI), and right posterior sacroiliac marker (RPSI) (Fig. 1c).

The full gait cycle was considered from the first stepping limb foot contact until the toe-off of the contralateral limb. The dynamic trials were normalized to the interval

0% to 100% of the gait cycle with 1% step resulting in 101 data points for each pelvic rotation angle. The beginning of the gait cycle (first stepping limb foot contact) was defined when the normal component of the reaction force exceeded the value of 30 N. The end of the gait cycle (toe-off of the second lifting limb) was defined when the normal component of the reaction force fell below the value of 30 N. This is a widely accepted and frequently applied threshold used to identifying heel contact and toe-off [11].

The actual origin and base vectors were determined, as functions of the gait cycle, in dynamic trials from the coordinates of the same reflective markers as in the static trial. Rigid body movements were removed preserving only the rotations of the coordinate system. The average walking speed was determined for all dynamic trials as the ratio of the total trajectory of the origin's y coordinate and the total duration of the gait cycle.

The rotation matrix was determined from the reference and actual base vectors in the sense of least squares. The MATLAB rotation matrix function *absor* was used. This was written by Matt Jacobson and is freely available on the File Exchange service provided by MathWorks® [12]. The corresponding Euler angles were then determined from the rotation matrix. They represent rotations around the axes of the reference coordinate system. Thus, the angle labeled U_x is the angle of rotation about the “left–right” or “medio-lateral” x-axis, U_y is the angle of rotation about the “front-back” or “anterio-posterior” y-axis, and U_z is the angle of rotation about the “longitudinal” or “cranio-caudal” z-axis.

2.4 Statistical Analysis

To compare the scalar data, a one-tailed Student's t-test was used in case of data normality with a significance level of $\alpha = 0.05$; otherwise, a non-parametric Wilcoxon paired test was used. To compare more than two groups of data, ANOVA was used in the case of normality; otherwise, the Kruskal–Wallis nonparametric test was used. The Lilliefors test was used to evaluate normality. The SPM technique was used to compare kinetic and kinematic one-dimensional data with a significance level of $\alpha = 0.01$. Differences in pelvic angles between groups AL versus BR and AL versus BL were analyzed.

SPM is a generalization of classical statistical tests for use on n-dimensional data in general [9, 10]. Its MATLAB implementation was used and applied on 1D pelvic angles as functions of the gait cycle. Specifically, an SPM two-tailed paired t-test was used. The scalar output test statistic, $SPM\{t\}$, was calculated separately at each gait cycle data point in the normalized time series. The calculation of $SPM\{t\}$ indicates the magnitude of the differences between groups AL and BL or AR and BR.

To test the null hypothesis, a critical threshold is calculated at which only α -percent (1%) of smooth random curves would be expected to traverse. This threshold is based upon estimates of trajectory smoothness via temporal gradients [13] and, based

on that smoothness, Random Field Theory expectations regarding the field-wide maximum [14].

Conceptually, an SPM-paired t-test is similar to the calculation and interpretation of a scalar paired t-test; if the SPM{t} trajectory crosses the critical threshold at any data point, the null hypothesis is rejected. Typically, due to waveform smoothness and the inter-dependence of neighboring points, multiple adjacent points of the SPM{t} curve often exceed the critical threshold. These neighboring points are called “supra-threshold clusters.” SPM then uses Random Field Theory expectations regarding supra-threshold cluster size to calculate cluster-specific p-values which indicate the probability with which supra-threshold clusters could have been produced by a random field process with the same temporal smoothness [14].

3 Results

Gait cycle times were the total gait cycle time, the time spent on the healthy limb, the time spent on the amputated limb, and the time spent on both limbs at the same time. The values of these times averaged over all subjects and corresponding standard deviations are summarized in Table 2 for all three walking speeds. The results are consistent with the walking speed instruction; the times decrease with increasing walking speed. The total gait cycle time of slow walking is approximately 1.6 s. At normal speed, the gait cycle time is approximately 1.4 s and at fast walking, it is 1.2 s. On average, the subjects spend slightly more time on the healthy limb. The time spent on both limbs at the same time represents approximately 10–13% of the total duration of the walking cycle, and this ratio increases with decreasing walking speed. All subjects spent significantly ($p < 0.05$) more time on the healthy limb except for subject 6 performing slow and fast motion ($p = 0.285$).

The walking speed was 0.895 ± 0.100 m/s, 1.070 ± 0.109 m/s, and 1.346 ± 0.228 m/s in slow, normal, and fast walking speed instruction. With few exceptions, the data showed a statistically significant increase in walking speed between the slow and normal walking instruction and normal and fast walking instruction. The analysis of walking speed served as a control demonstrating that the increase in walking speed did exist.

Figure 2 illustrates the SPM comparison of pelvic rotation about the antero-posterior axis under normal walking speed instruction. Figure 2a shows a comparison

Table 2 Gait cycle time (s). Average \pm standard deviation

	Total	Healthy limb	Amputated limb	Both limbs
Fast	1.188 \pm 0.079	0.681 \pm 0.054	0.632 \pm 0.074	0.125 \pm 0.063
Normal	1.387 \pm 0.073	0.799 \pm 0.049	0.739 \pm 0.050	0.152 \pm 0.028
Slow	1.611 \pm 0.125	0.944 \pm 0.085	0.879 \pm 0.105	0.212 \pm 0.098

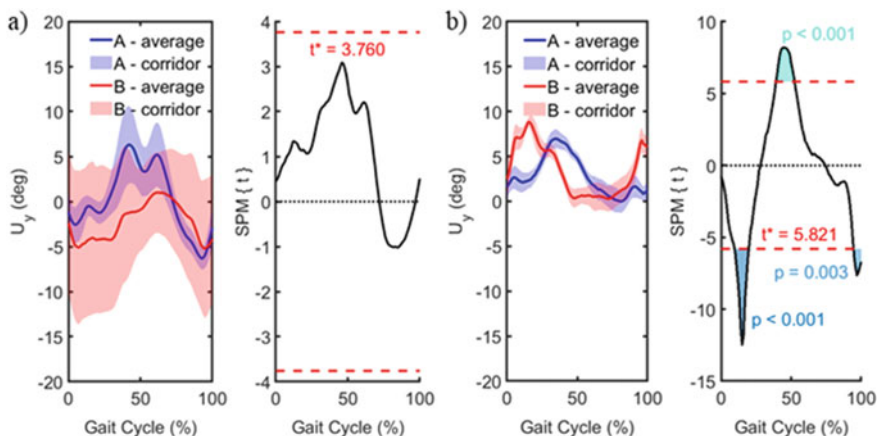


Fig. 2 Illustration of SPM comparison of pelvic rotation about the antero-posterior axis under normal walking speed instruction. **a** Comparison of left-leg amputees. The red dashed line shows the critical threshold. SPM{t} curve does not cross the threshold indicating no significant difference between the groups' AL and BL. **b** Comparison of right-leg amputees. SPM{t} curve crosses the threshold creating three clusters associated with different p-values indicating a significant difference between the groups' AR and BR

between the groups' AL and BL. Large corridors demonstrate large standard deviations, especially that of the BL group. SPM{t} curve does not cross the threshold indicated in red meaning no significant difference between the groups' AL and BL. Figure 2b shows the comparison between the groups' AR and BR. SPM{t} curve crosses the threshold indicated in red. It creates three clusters associated with different p-values indicating a significant difference between the groups' AR and BR in corresponding intervals of the gait cycle.

SPM results are further summarized in Fig. 3. Statistically significant differences in pelvic angles are shown between groups AL and BL and between groups AR and BR. Red areas show gait cycle intervals of statistically significant differences with a p-value lower than 0.001. Orange areas show gait cycle intervals of statistically significant differences with a p-value between 0.01 and 0.001. There is no statistically significant difference in pelvic angles in green areas.

4 Discussion and Conclusion

The effect of stump length on pelvic tilt in transfemoral amputees was assessed using SPM. The group of three mid-femur amputees was compared to the group of three amputees with knee disarticulation. This study suffers from a small sample size due to a limited number of lower limb amputees in our region willing to participate. The situation is even more complex due to heterogeneity within the groups. Indeed, both

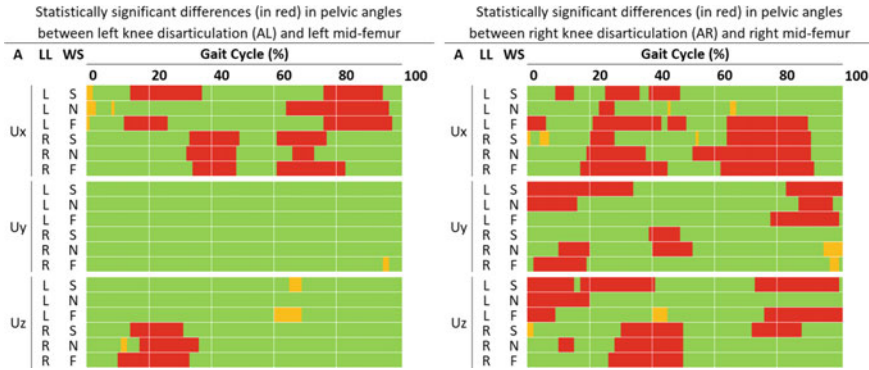


Fig. 3 Red and orange areas show intervals of statistically significant differences in pelvic angles (A) for left (L) and right (R) leading leg (LL) and slow (S), normal (N), and fast (F) walking speed (WS) within the gait cycle. The p-value was between 0.01 and 0.001 in the orange areas and less than 0.001 in the red areas, respectively. Ux is the angle of rotation about the “left–right” or “medio-lateral” x-axis, Uy is the angle of rotation about the “front-back” or “anterio-posterior” y-axis, and Uz is the angle of rotation about the “longitudinal” or “cranio-caudal” z-axis

groups include one right-leg amputee and two left-leg amputees. This makes the analysis even more difficult.

Standard techniques assessing gait cycle parameters usually rely on sets of scalar values. Complex waveforms are reduced to only several numbers. This may result in excessive data compression and information loss. SPM can analyze n-dimensional data in general [9]. It may lead to more insight despite the small sample size compared to standard techniques. Other researchers have suggested that relative small samples of 10 subjects can detect one-dimensional effects with a proper statistical power [15]. Even though our sample size is smaller, the statistical power of SPM differs from regular scalar statistics, highlighting another advantage of this statistical method.

Gait cycle times and walking speed were analyzed to confirm that the subjects respected the walking speed instruction. In a few cases, the increase in walking speed was not statistically significant but all subjects respected the walking speed instruction.

SPM allowed us to identify gait cycle intervals with statistically significant differences in pelvic angles between the groups. In left-leg amputees, there were two subjects with mid-femoral amputation (group AL) and two subjects with knee disarticulation (group BL). In right-leg amputees, there was only one subject with mid-femoral amputation (group AR) and one subject with knee disarticulation (group BR). The data in AL and BL groups exhibited larger variations compared to AR and BR groups as illustrated in Fig. 2. These variations may be directly related to the number of subjects in the respective groups. The data exhibited excellent repeatability and consistency with low variations for every single subject. Inter-subject variations seem to exceed the intra-subject variations. Large inter-subject variations may hide possible differences between the groups. This is confirmed by our findings.

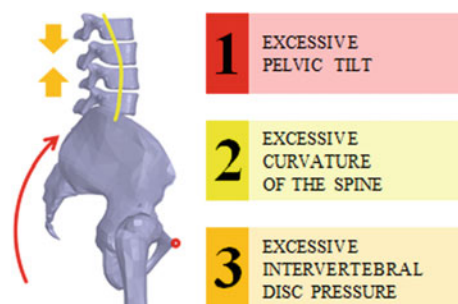
More statistically significant differences were found between the groups AR and BR exhibiting lower variations.

Significant differences were found in clusters (intervals) within the gait cycle. Two types of qualitatively different clusters were found: shorter intervals with a p-value between 0.01 and 0.001 spanning less than 10% of the gait cycle and larger intervals with a p-value less than 0.001. A thorough analysis of the data unveiled that shorter intervals were not associated with any unusual mechanisms of the gait. In contrast, larger intervals demonstrated interesting phenomena discussed below.

The range of rotation about the medio-lateral axis in group A was close to that of the healthy population while in group B it was almost 8 degrees larger [16, 17]. There was a difference of 4–5 degrees between the groups under fast walking instruction. The rotation angle was higher in group B. Correlation between stump length and pelvic rotation in the sagittal plane was previously reported [16] supporting our observations. Pelvic anteversion was previously observed in the phase of pre-swing and initial swing [17]. It was related to the support provided by the socket to the ischial tuberosity. The extended femur would create pressure in this area resulting in pelvic anteversion. This was not confirmed in our study as none of the subjects specifically described pressure on the ischial tuberosity. The anteversion might be attributed to the insufficient muscle strength of the back of the thigh responsible for pelvic retroflexion or their compression during extension. Three to five degrees of pelvic anteversion was also observed in group B at the end of the stance phase. It may be related to the impossibility to pre-flexion the knee joint shifting the center of gravity forward [18]. This pre-flexion functionality is already available on the market in electronically controlled knee joints providing four degrees of pre-flexion at initial contact which promotes increased stance flexion and shock absorption, reciprocal ramp and stair descent [19]. These functions are important in preventing low back pain. Pelvic anteversion may lead to excessive curvature of the spine and, as a consequence excessive pressure applied to the intervertebral disks as illustrated in Fig. 4.

In terms of the rotation about the antero-posterior axis, group A subjects had a maximum pelvic tilt range of 7 degrees, and group B subjects of 10 degrees were within the range (6–11 degrees) reported for the healthy population [17, 20]. No significant difference in the frontal plane rotation was found between groups AL

Fig. 4 Illustration of the mechanism leading from excessive pelvic tilt to excessive intervertebral disk pressure possibly resulting in low back pain



and BL. This is very likely due to large inter-subject variations. Group AR demonstrated pelvic tilt toward the amputated limb in a healthy limb heel strike causing a pelvic drop. Pelvic drop is caused by both gravity and weakened hip stabilizers [21]. Increased hip abductor atrophy has been observed in transfemoral amputees [22]. In slowly walking group BR, the pelvis tilted to the side of the healthy limb. It could be a compensatory mechanism tilting the trunk above the standing leg. This would shift the center of gravity and drop the pelvis to the side of the healthy limb allowing the amputated limb to swing more easily [23]. This phenomenon is known as hip-hiking and is very common in people with transfemoral amputation [24, 25].

The range of pelvic rotation in the transverse plane, i.e., about the cranio-caudal axis was up to 3 degrees externally and 6 degrees internally. It was within the range observed in a healthy population [20, 26]. Significant differences between AL and BL groups were found only in right leading leg trials within 10–30% of the gait cycle. Group BL demonstrated rotation toward the neutral position in contrast to group AL. Significant differences between AR and BR groups were found in right leading leg trials within 30–50% of the gait cycle and in the left leading leg at the beginning and end of the gait cycle. Internal rotation is natural in a healthy limb heel strike. Rotation of the pelvis should change against the swing limb in the toe-off. This trend was visible in group A, but in group B, after the lift-off of the preserved limb, the pelvis tilted to the opposite side. This is attributed to the rotation of the pelvis in the two other planes since it functions as a whole and the rotations about the three axes are not independent.

The application of SPM does not compensate small sample size. Comparison of continuous waveforms requires further fragmentation of the subjects into subgroups according to the amputation side. Using more than two force plates would accelerate the testing and facilitate data post-processing. On one hand, additional fragmentation to left and right leading leg trials makes the comparison even more difficult. On the other hand, SMP allows the identification of gait cycle intervals with unusual phenomena. This allows us to better interpret the data concerning the gait cycle phase.

A larger sample size would probably lead to larger inter-subject variations. It is difficult to draw any reasonable conclusion about a small and heterogeneous population. The gait patterns of the lower limb amputees are affected by many different parameters and may be considered highly subject-specific. It would make more sense to compare individuals with data sets from healthy people. This could help to better understand patient-specific compensatory mechanisms to adjust the prosthesis settings and/or propose adequate therapy. Further work will focus on the analysis of individual gait patterns of the amputees compared to available data sets acquired on healthy volunteers [27–29].

Acknowledgements This work was supported by /the European Regional Development Fund-Project “Application of Modern Technologies in Medicine and Industry” (No. CZ.02.1.01/0.0/0.0/17_048/0007280).

References

1. Ziegler-Graham, K., MacKenzie, E.J., Ephraim, P.L., Trivison, T.G., Brookmeyer, R.: *Arch. Phys. Med. Rehabil.* **89**, 422 (2008)
2. Stern, J.R., Wong, C.K., Yerovinkina, M., Spindler, S.J., See, A.S., Panjaki, S., Loven, S.L., D'Andrea, R.F., Nowygrod, R.: *Ann. Vasc. Surg.* **42**, 322 (2017)
3. McDonald, C.L., Westcott-McCoy, S., Weaver, M.R., Haagsma, J., Kartin, D.: *Prosthet. Orthot. Int.* **45**, 105 (2021)
4. Bell, J.C., Wolf, E.J., Schnall, B.L., Tis, J.E., Tis, L.L., Benjamin, M.A.J., Potter, K, *JBSJ* **95**, 408 (2013)
5. Highsmith, M.J., Lura, D.J., Carey, S.L., Mengelkoch, L.J., Kim, S.H., Quillen, W.S., Kahle, J.T., Miro, R.M.: *Prosthet. Orthot. Int.* **40**, 522 (2016)
6. Nolan, L., Wit, A., Dudziński, K., Lees, A., Lake, M., Wychowański, M.: *Gait Posture* **17**, 142 (2003)
7. Uchytíl, J., Jandacka, D., Zahradník, D., Farana, R., Janura, M.: *Prosthet. Orthot. Int.* **38**, 199 (2014)
8. Geertzen, J.H.B., de Beus, M.C., Jutte, P.C., Otten, E., Dekker, R.: *Med. Hypotheses* **129**, 109238 (2019)
9. Pataky, T.C.: *J. Biomech.* **43**, 1976 (2010)
10. Pataky, T.C.: *Comput. Methods Biomech. Biomed. Engin.* **15**, 295 (2012)
11. Tirosh, O., Sparrow, W.A.: *J. Appl. Biomech.* **19**, 178 (2003)
12. Jacobson, M.: *Absolute Orientation—Horn's Method* (2023)
13. Friston, K., Ashburner, J., Kiebel, S., Nichols, T., Penny, W. (ed) In: *Statistical Parametric Mapping*, p. iii. Academic Press, London (2007)
14. Adler, R.J., Taylor, J.E.: *Random Fields and Geometry*. Springer, New York (2007)
15. Pincheira, P.A., De La Maza, E., Silvestre, R., Guzmán-Venegas, R., Becerra, M.: *Clin. Biomech. (Bristol, Avon)* **62**, 7 (2019)
16. Murray, M.P., Kory, R.C., Sepic, S.B.: *Arch. Phys. Med. Rehabil.* **51**, 637 (1970)
17. Kadaba, M.P., Ramakrishnan, H.K., Wootten, M.E.: *J. Orthop. Res.* **8**, 383 (1990)
18. Fatone, S., Stine, R., Gottipati, P., Dillon, M.: *Am. J. Phys. Med. Rehabil.* **95**, 438 (2016)
19. Mileusnic, M.P., Rettinger, L., Highsmith, M.J., Hahn, A.: *Disabil. Rehabil. Assist. Technol.* **16**, 453 (2021)
20. Stokes, V.P., Andersson, C., Forsberg, H.: *J. Biomech.* **22**, 43 (1989)
21. Powers, C.M.: *J. Orthop. Sports Phys. Ther.* **40**, 42 (2010)
22. Jaegers, S.M., Arendzen, J.H., de Jongh, H.J.: *Clin. Orthop. Relat. Res.* 276 (1995)
23. Neumann, D.: *Kinesiology of the Musculoskeletal System* (Mosby, 2016)
24. Michaud, S.B., Gard, S.A., Childress, D.S.: *J. Rehabil. Res. Dev.* **37**, 1 (2000)
25. Castiglia, S.F., Ranavolo, A., Varrecchia, T., De Marchis, C., Tatarelli, A., Magnifica, F., Fiori, L., Conte, C., Draicchio, F., Conforto, S., Serrao, M.: *Gait Posture* **80**, 280 (2020)
26. Crosbie, J., Vachalathiti, R., Smith, R.: *Gait Posture* **5**, 13 (1997)
27. Horst, F., Lapuschkin, S., Samek, W., Müller, K.-R., Schöllhorn, W.I.: **2** (2019)
28. Horst, F., Lapuschkin, S., Samek, W., Müller, K.-R., Schöllhorn, W.I.: *Sci. Rep.* **9**, 2391 (2019)
29. Schreiber, C., Moissenet, F.: *Sci. Data* **6**, 111 (2019)

Assessment of Obstructive Sleep Apnea Phenotypes from Routine Sleep Studies: A New Approach to Precision Medicine



Raichel M. Alex, Khosrow Behbehani, and Donald E. Watenpaugh

Abstract Obstructive sleep apnea (OSA) is the most common breathing disorder where a patient repeatedly stops breathing during sleep. The treatment of choice for OSA is continuous positive airway pressure therapy; however, not all OSA patients benefit from a prescribed standard therapeutic intervention, and multiple alternative treatment options exist for OSA. Success of therapeutic interventions may depend on identifying multifactorial pathophysiological mechanisms of OSA to further classify the patient subtypes that may respond better to specific therapeutic approaches. Indeed, recent research shows that OSA is a heterogenous disorder caused by variable combinations of craniofacial features, obesity, and deficits in several pathophysiological traits known as endotypic traits. The key endotypic traits include respiratory control system instability (high loop gain), low arousal threshold (easily aroused from sleep), increased upper airway collapsibility, and decreased neuromuscular compensation of airway musculature. Quantifying these traits in a clinical setting may provide targeted individualized treatment options to OSA patients. In this regard, new automated methods have been developed to reliably estimate endotypic traits of OSA from routine diagnostic sleep studies, without the need for any invasive procedures. These collective observations support the notion that automated noninvasive estimation of endotypic traits can be widely used as a valuable tool to both clinicians and researchers involved in sleep health care.

R. M. Alex (✉)

Division of Sleep and Circadian Disorders, Brigham and Women's Hospital and Harvard Medical School, 221 Longwood Ave, BLI-225, Boston, MA 02115, USA

e-mail: ralex@bwh.harvard.edu

K. Behbehani · D. E. Watenpaugh

Department of Bioengineering, University of Texas at Arlington, Arlington, TX, USA

D. E. Watenpaugh

Department of Anatomy and Physiology, University of North Texas Health Science Center, Fort Worth, TX, USA

1 Control of Breathing During Normal Ventilation

Breathing is crucial for staying alive, as it has the vital role of supplying oxygen to the body and removing excess carbon dioxide. Normal breathing is cyclic and has two distinct and easily identifiable phases: (1) inspiration and (2) expiration [1, 2]. The supply of oxygen to the lungs takes place during inspiration and removal of the carbon dioxide is achieved during exhalation. The plurality of inspiration and expiration is called respiration [1, 2]. A physiologically significant and useful measure of respiration is the volume of air that is inhaled during natural breathing in each inspiration, called tidal volume. Additionally, the term ventilation refers to the mechanical flow of air in and out of the lungs. A common measure of ventilation is minute ventilation, which equals the number of respiratory cycles in one minute multiplied by the average tidal volume of breaths over that minute [1, 2].

The rate of respiration is controlled by the respiratory centers in the brain that are located in medulla oblongata and pons [1, 3]. These centers regulate breathing based on stimuli received from central chemoreceptors, peripheral chemoreceptors, and somatic mechanoreceptors. Central chemoreceptors are co-located in the medulla and are sensitive to changes in blood pH caused by CO₂ levels: A decrease in pH—induced by a rise in CO₂ (i.e., hypercapnia)—will stimulate the respiratory centers to increase breathing rate [4, 5]. Peripheral chemoreceptors consist of aortic bodies and carotid bodies which are predominantly sensitive to low levels of oxygen (hypoxia), though they can also monitor changes in pH or PCO₂ [4, 6]. Mechanoreceptors or the stretch receptors found in the airway, trachea, walls of bronchi and bronchioles relay information on lung volume to the respiratory center via vagus nerve to increase breathing rate, volume of breath and to initiate coughing in response to foreign respiratory irritants [3, 7].

During inspiration, the inspiratory center in medulla stimulates the contraction of the diaphragm and the intercostal muscles to initiate breathing [1, 2]. Diaphragm moves down and external intercostal muscles move the rib cage out, thereby increasing the volume of thoracic cavity. This results in a decrease in alveolar pressure to a level below atmospheric pressure causing the lungs to expand and air flows into the lungs. When the lungs expand to their physical limit, stretch receptors send signals to medulla to inhibit the inspiratory muscles and to start expiration, thereby preventing over inflation of lungs. During expiration, diaphragm and intercostal muscles relax, chest wall moves in, and air flows out of the lungs [1–3]. As the lungs empty due to return of diaphragm to its un-extended position, the stretch receptors send stimulus to the inspiratory center to commence a new inspiration. Additionally, the breathing rate and volume are modified by the metabolic needs—hypercapnia and hypoxia will lead to an increase in respiration whereas hyperventilation (increased elimination of CO₂ and greater intake of O₂) will depress the inspiratory drive from the respiratory centers, thereby by reducing breathing [1–3]. A healthy adult has a breathing rate of 12–20 breaths per minute at rest and 40–60 breaths per minute during exercise [8].

2 Ventilatory Control During Sleep

Sleep is essential for normal childhood growth and development, musculoskeletal tissue maintenance, cardiovascular health, removal of potentially toxic metabolites from the brain, nervous system homeostasis, all aspects of cognitive function, immune function, healing from injury, and health in general [9, 10]. Interestingly, breathing and sleep are among the very few basic bodily processes that we cannot voluntarily terminate without external means. No matter how hard we try to hold our breath, our autonomic nervous system will within seconds to minutes force us to breathe. No matter how hard we try to stay awake, our central nervous system will within a few days involuntarily cease wakeful function and go to sleep.

Sleep attenuates breathing rate, tidal volume, and thus minute ventilation compared to the awake state. This occurs because inspiratory drive decreases during sleep [11]. One reason for sleep-related changes in respiration is the absence of wakeful stimuli. During wakefulness, breathing is regulated by both metabolic needs and the wake state *per se*. Wakeful respiratory stimuli consist of the tonic influence on ventilation arising from a state of alertness and phasic influences on ventilation from behavioral control of ventilation (talking, swallowing, laughing, physical activity, etc.) [12]. The influence of these stimuli on breathing supersedes simple metabolic control. Hence during wakefulness, a rhythmic breathing pattern can be maintained regardless of metabolic status (e.g., breathing rhythmicity can be maintained even after hyperventilation in healthy humans when awake) [12, 13].

Breathing during sleep is solely determined by basal metabolic needs [12, 13]. Moreover, sleep causes significant reduction in the neuromuscular compensation, which is usually present during awake state and helps with compensating for changes in ventilation due to negative intrathoracic pressure oscillations and reduced motor output [13]. Another change in the upper airway during sleep is reduction of airway muscle tone thereby increasing airflow resistance due to reduced cross-sectional area of airway. Some data suggest that airway resistance increases ~ 230% during non-rapid eye movement (NREM) sleep [13]. Reduced muscle tone also makes the airway flaccid which in turn increases probability of reduced ventilation, upper airway collapse, and may lead to subsequent breathing cessation (apnea) [13]. The increased airway resistance and collapsibility can lead to increased ventilatory drive (effort to breath) to maintain ventilation. Such an event can cause occurrence of repeated cortical microarousals (i.e., brief awakening) throughout the sleep which, in turn, results in ventilatory overshoots and hyperventilation leading to depression of inspiratory drive [4].

Ventilatory patterns vary with different sleep stages [11, 13, 14]. Compared to wakefulness, tidal volume decreases about 25% during rapid eye movement (REM) sleep, whereas only 6–16% reduction in tidal volume occurs in NREM. Similarly, compared to awake state, minute ventilation reductions of 16% during REM and 6–7% during NREM are observed [13]. Hence, tidal volume and minute ventilation are considerably lower during REM sleep compared to NREM sleep [11, 13]. Mean inspiratory flow rate—a measure of ventilatory drive—is significantly reduced

during REM relative to NREM and wakeful levels, which are similar [11, 13]. Furthermore, the two different subtypes of REM sleep—tonic and phasic REM—can exhibit different ventilatory patterns. Tonic REM sleep is similar to wakefulness and can exert an excitatory influence on the ventilatory control system resulting in a rapid, irregular, shallow breathing pattern and hypoventilation [14]. Phasic REM exhibits the greatest reduction in ventilation due to significant reduction in inspiratory drive and, in some instances especially in patients with a flaccid airway, can lead to a loss of muscle tone in respiratory muscles resulting in hypoxia [11, 14].

3 Breathing Disorders During Sleep

One of the most common (yet often underdiagnosed) breathing disorders during sleep is sleep apnea, a term coined from the Greek word “apnea” meaning “absence of breathing.” Sleep apnea is characterized by partial (hypopnea) or complete cessation (apnea) of breathing during sleep [15]. Apnea–hypopnea events result in reduced or zero air flow to the lungs causing hypercapnia and hypoxia, which trigger microarousals from sleep to resume breathing. Breathing normalizes blood gases, sleep resumes, and the cycle continues with another episode of restricted breathing. In severe cases, these disruptive respiratory events can occur several hundred times during a single night of sleep resulting in extreme sleep fragmentation. The duration of apneas and hypopneas can vary from a few seconds to over one minute [15, 16]. Diagnosis and severity of sleep apnea are determined by computing the average number of apneas and hypopneas per hour of sleep, which equals the apnea–hypopnea index (AHI). For adults, an AHI of < 5 events/h is considered normal, 5–15 events/h constitutes mild sleep apnea, 15–30 events/h is moderate, and ≥ 30 events/h is severe [15].

Sleep apnea is classified into obstructive sleep apnea (OSA), central sleep apnea (CSA), and mixed apnea based on the underlying physiological cause(s) of breathing cessation [15, 17, 18]. OSA is most common with an estimated 84% of patients with sleep apnea suffering from OSA [15, 19]. OSA occurs due to partial or complete closure of the upper airway thereby restricting or preventing air flow to the lungs. The *sine qua non* of OSA is excessive muscle relaxation in the posterior oropharynx which causes the tongue to fall back into the airway during sleep [15, 18]. Current estimates suggest that OSA affects as many as 22% of men and 17% of women worldwide [20]. However, estimates also suggest that 85% of OSA patients go undiagnosed [21].

CSA is characterized by cyclically reduced or absent ventilation resulting from repetitive temporary attenuation or cessation of brainstem inspiratory neural center signals to respiratory muscles [17]. As a result, there will be minimal or no diaphragmatic or other inspiratory motor activity and thus ventilation. This occurs most commonly in infants with prematurity or congenital neurologic disorders, and in adults with heart failure or with use of medications that depress brainstem respiratory drive [18]. Such medications include both prescribed and illicit opiates such as fentanyl. Healthy subjects may also experience temporary CSA at higher altitudes

[17]. The prevalence of CSA in adults over 40 years of age is about 0.9% [22]. In some instances of sleep apnea, breathing cessations begin with absence of central respiratory drive and motor activity (CSA) followed by re-initiation of respiratory efforts against upper airway closure (OSA). Such respiratory events are known as mixed apneas [18].

This chapter focuses primarily on OSA since it is the most common form of sleep apnea, yet as suggested above, significant crosstalk exists between the various manifestations of sleep apnea.

4 Underlying Mechanisms of Obstructive Sleep Apnea

During the past three decades, research documents that OSA causes repetitive hypoxia and hypercapnia throughout the night resulting in hypertension, heart failure, stroke, brain atrophy, memory impairments, excessive daytime sleepiness, and reduced quality of life [23, 24]. The US National Commission on Sleep Disorders Research estimates that approximately 38,000 people die annually from cardiovascular problems associated with sleep apnea (hypertension, stroke) and at least 1400 people die from sleep apnea-related automobile accidents [25]. OSA can lead to occupation-related accidents for train operators, ship captains, power-plant operators, pilots, surgeons, and other critical occupations.

The mechanism underlying the manifestation of OSA depends on the balance between upper airway patency, negative intrathoracic pressure swings, and chemoreflex stimulation. The upper airway is primarily a soft muscular structure not supported by bones and hence can collapse under certain conditions such as OSA [26]. Oropharyngeal muscles such as the genioglossus and those in the soft palate play an important role in maintaining airway patency by actively dilating the airway to keep it open [26, 27]. However, during sleep, upper airway dilator muscle tone is markedly reduced in OSA patients compared to healthy controls [28]. In the presence of other anatomical deficits (e.g., narrow airway that is common in OSA), this reduced dilator muscle activity can lead to significant increases in airway resistance and even airway closure [26]. Attempted breathing against a restricted or closed airway reduces intrathoracic pressure, ventilation, and arterial oxygen saturation, and increases CO₂ levels. The peripheral and central chemoreceptors might try to compensate for the airway closure by increasing the dilator muscle activity [29]. However, in most cases this compensatory mechanism might not be sufficient to reopen the airway fully and the resulting increase in ventilatory drive accentuates respiratory muscle contractions leading to further upper airway narrowing [30]. This continues until the patient wakes up from sleep to resume breathing.

OSA is usually treated using continuous positive airway pressure (CPAP) therapy, which pressurizes the airway to prevent airway collapse and obstruction [31]. However, CPAP use is inconsistent and problematic [32, 33]. The major barriers to CPAP use include air leaks, nasal congestion, dry throat, sleep disturbances, and

inconvenience of sleeping with a pressurized mask strapped on the head [34]. Alternative treatments include mandibular advancement with oral appliances (to prevent the tongue from falling back and blocking the airway), airway or bariatric surgery, supplemental oxygen, hypoglossal nerve stimulation, preventing supine sleep, and pharmacological interventions [32, 35, 36]. OSA patients with mild to moderate sleep apnea gain the most benefit from these alternative therapies; severe OSA patients still require CPAP to effectively eliminate obstruction [34].

5 Understanding the Heterogenous Mechanisms of OSA Pathogenesis—A Step Toward Precision Medicine

Important questions sleep physicians currently confront include why certain individuals develop OSA, what drives its severity, and which therapeutic options will be most effective for specific patients. Research suggests OSA is a heterogenous disease with multifactorial pathophysiologic mechanisms. They can be classified into anatomic and non-anatomic traits [32, 37, 38]. Patients may exhibit singular or multiple contributing factors. Early research on OSA focused entirely on anatomic traits such as impairments in pharyngeal anatomy (a narrow upper airway, increased airway length, airway lumen shapes, etc.), obesity, and craniofacial characteristics [32]. Measuring some of these traits is challenging since they require airway imaging procedures and pharyngeal catheterization during sleep that are impractical as routine procedures.

Non-anatomic traits include unstable ventilatory control during sleep (high loop gain) and low arousal threshold (which contributes to premature awakening from sleep in response to mild airway restriction). These cause sleep fragmentation and impaired upper airway neuromuscular compensation [32, 37]. These traits are collectively referred to as OSA endotypic traits or endotypes. Recent studies show that non-anatomic features are important in the progression of OSA [32, 37, 38]. Roughly 69% of OSA patients exhibit one or more of the traits: high loop gain, low arousal threshold, and increased upper airway collapsibility [38]. Hence, measuring these traits in the clinical setting can help predict therapeutic responses in OSA patients and avoid complications associated with treatment failure. As examples: (1) patients with high loop gain will probably not benefit from oral appliances or surgical intervention. Supplemental oxygen may treat them successfully and should be a primary option; (2) oral appliances are futile in patients with severe upper airway collapsibility; (3) reduced upper airway muscle compensation can be corrected by hypoglossal nerve or genioglossus muscle stimulation leading to improved airway patency; (4) low arousal threshold can be addressed with sedative pharmacological interventions; these patients may not tolerate neuromuscular stimulation and device therapies since they are easily aroused from sleep [36, 38–41]. The following sections describe the endotypes and a computational model to calculate them in an automated fashion in the sleep clinic.

5.1 Loop Gain

The ventilatory control system maintains homeostatic CO₂ levels using a negative feedback loop, and the term loop gain reflects the degree of the feedback response when a deviation from homeostatic level occurs [13, 32]. It is defined as the ratio of the changes in ventilation that occurs in response to a ventilatory disturbance such as apnea–hypopnea events. Loop gain determines the magnitude and speed of ventilatory response, and hence, it affects the overall stability and sensitivity of the ventilatory feedback control system [13, 32, 42]. Loop gain may be thought of as the combined effect of plant gain, circulatory delay, and controller gain. Plant gain includes lung volume and gas exchange rates and represents the changes in partial pressure of CO₂ (PaCO₂) for corresponding changes in ventilation [13]. Circulatory delay represents the time delay before peripheral and central chemoreceptors sense changes in CO₂ levels in blood and cerebrospinal fluid, respectively. Controller gain represents the degree of amplification or reduction in ventilation for the corresponding change in PaCO₂. It is the magnitude of feedback from the respiratory control in medulla in response to changes in PaCO₂ to adjust ventilation [42].

Medical conditions such as heart failure can alter loop gain measures. A patient with higher loop gain will have an unstable ventilatory control and will produce an elevated ventilatory response and hyperventilation in response to a small change in CO₂ levels [43]. In sleep clinics, CPAP manipulations are used to quantify loop gain. Transient oscillations in CPAP create controlled disturbances to ventilation [44, 45]. The corresponding ventilatory response is measured via pneumotachograph, and this process is repeated several times throughout the night. The ratio of ventilatory response to varying levels of ventilatory disturbance is used to calculate loop gain. Approximately, 30% of OSA patients have pathologically high loop gain [38].

5.2 Arousal Threshold

Cortical arousals help wake the OSA patient from sleep to open the upper airway and resume breathing when an apnea or hypopnea event occurs [32]. To be classified as a respiratory event-related arousal, this increased electroencephalogram activity must continue for 3 s or more and occur within ± 5 s after termination of an apnea or hypopnea event. These arousals reestablish airflow quickly following a respiratory event [12, 46, 47]. However, having a low arousal threshold—defined as increased arousability from sleep from stimuli such as respiratory events—can be detrimental, as about 20% or more of such events often terminate without measurable cortical arousal [32]. Arousals per se exacerbate the cyclic breathing patterns characteristic of OSA, sleep fragmentation, and thus sleep quality degradation. The premature awakening from sleep does not provide sufficient time to activate the upper airway dilator muscles to normalize airway patency [48, 49]. Subsequent unstable

breathing contributes to worsening of OSA pathogenesis. Indeed, an estimated 30–50% of OSA patients have low arousal threshold [32, 49]. Quantification of arousal threshold during overnight sleep studies requires an invasive procedure of inserting an esophageal catheter to measure intrathoracic pressure swings. The nadir of the pressure swing prior to the cortical arousal quantifies the arousal threshold [32].

5.3 Pharyngeal Collapsibility

OSA is characterized by narrowing or complete closure of the upper airway during sleep. Airway collapse can occur at one or more sites along the length of upper airway. The most common sites of collapse include the soft palate, lateral pharyngeal walls, genioglossus and epiglottis [32]. Obesity, tongue fat and increased neck circumference increase the probability of collapse [50]. Pharyngeal collapsibility is defined as the measure of ventilation observed at critical closing pressure (Pcrit) of the airway. Pcrit is usually measured using CPAP dial-downs and a pharyngeal pressure catheter [32, 51, 52]. In this procedure, CPAP pressure is decreased during stable sleep before dialing back up to therapeutic pressure. This is repeated until airflow limitation and airway collapse occur [53]. The mask pressure where collapse occurs is measured and the pressure at which the inspiratory flow becomes zero is used to obtain Pcrit.

There are two types of Pcrit, passive and active, depending on the levels of pharyngeal muscle activation in response to reduced ventilation [52]. Passive Pcrit is determined by measuring ventilation while lowering CPAP abruptly and then returning to the therapeutic level within very few respiratory cycles. This process does not give sufficient time for activation of pharyngeal dilator muscles in response to airway collapse. Active Pcrit is determined by lowering CPAP slowly and steadily to give sufficient time for activation of dilator muscles [32]. In OSA patients, Pcrit can vary from $-5 \text{ cmH}_2\text{O}$ to $+5 \text{ cmH}_2\text{O}$ with an average of $0 \text{ cmH}_2\text{O}$ relative to atmospheric pressure [32]. A Pcrit of $0 \text{ cmH}_2\text{O}$ indicates that airway collapse occurs at $0 \text{ cmH}_2\text{O}$. Positive Pcrit values indicate a severely collapsible airway whereas negative values indicate the necessity of suction to collapse the airway during sleep.

5.4 Neuromuscular Compensation

In addition to anatomical deficits, impairments in neuromuscular activity can play a major role in compromising airway patency and ventilation during sleep in OSA patients [54, 55]. During wakefulness, upper airway dilator muscles remain activated, and this neuromuscular tone stabilizes the airway. With sleep onset, dilator muscle activation decreases, and this combined with an anatomically collapsible airway can lead to apnea–hypopnea events. Hence, the neuromuscular compensation is defined as the increase in ventilation due to dilator muscle activation in response to airway

collapse [29]. Measurement of dilator muscle activity requires insertion of wire electrodes to the base of the tongue or the use of transcutaneous electrodes [32, 55]. To complicate matters, different dilator muscles can exhibit different patterns of activity. The genioglossus, located at the base of the tongue, is the largest pharyngeal dilator muscle. Hypercapnia and reflex inputs from mechanoreceptors stimulate phasic activation of the genioglossus (i.e., increased activation during inspiration and lesser activation during expiration) to prevent airway collapse [32, 54]. On the other hand, the palatal muscle—tensor palatini—exhibits tonic activation (i.e., constant activity during inspiration and expiration) in response to negative intrathoracic pressure swings, hypercapnia, and hypoxia [56]. Reduced neural input to the dilator muscles, reduced muscle responsiveness, and mismatched neural input and muscle activation contribute to OSA pathogenesis. In many OSA patients, low neuromuscular compensation also results in part from a higher recruitment threshold for dilator muscles which can be achieved only with arousals from sleep [57]. Individuals with relatively high compensation are somewhat protected from developing OSA even in the presence of an anatomically compromised airway [32].

6 An Automated Non-invasive Approach to Estimate Endotypic Traits in OSA

Identifying endotypic traits of a given sleep apnea patient can lead to effective treatment(s) optimized for that patient. Hence, it is highly desirable to devise a feasible method of identifying these traits. In particular, it would be highly attractive to be able to identify the endotypic traits from data that is obtained as part of routine sleep apnea diagnostic tests. However, endotypic traits are historically determined by invasive or sophisticated procedures, thereby limiting their widespread clinical use [38, 58]. Recently, an automated computational model was proposed to extract the endotypic traits (loop gain, arousal threshold, airway collapsibility, and respiratory neuromuscular compensation) from a routine diagnostic sleep study [29, 42, 49]. This recent development is the first automated approach of its kind to translate the endotypic traits from physiological laboratories to clinical practice. The method uses a first order control system model that incorporates chemoreflex stimulations and wakefulness drive (the ventilatory response to cortical arousal) to quantify ventilatory drive during sleep. Because this method does not require imaging or invasive techniques, it enables application of precision sleep medicine to OSA, CSA, and mixed sleep apnea endotypes. The original computational model was custom-coded using MATLAB software (Phenotyping Using Polysomnography; MATLAB, Mathworks, Natick, MA). An independent implementation of the model using Python programming provides a scalable cloud-based approach to make endotypic trait analysis more widely available to researchers and clinicians [59].

The computational method estimates breath-by-breath ventilation and ventilatory drive throughout the night to assign and quantify endotypic traits [29, 42, 49]. The

key to understanding the model is that apnea and hypopnea events repeatedly limit or stop ventilation, increase CO_2 , and reduce O_2 . Such chemoreflex stimulation, or chemical drive, causes an increase of ventilatory drive. Another factor that affects the ventilatory drive is “wakefulness drive,” the additional drive to breath caused by arousal from sleep. Hence, ventilatory drive at any time point can be defined as the sum of chemical drive and wakefulness drives [42]. Chemical drive can be determined from a first order system that incorporates a circulatory delay (time delay between lungs and chemoreceptors), time constant (time taken for the buffering of CO_2 in lungs), and steady-state loop gain. Wakefulness drive equals the increase in ventilation during a cortical arousal not attributable to chemoreflex inputs. A detailed description of the model is provided below under the subheading of Control Theory Basis for Endotypic Trait Estimation.

Inputs to the computational model include changes in ventilation derived from the nasal pressure signal and the degree to which those changes were impacted by arousal from sleep [42]. For this purpose, the nasal pressure signal is linearized and integrated to estimate breath-by-breath ventilation (uncalibrated tidal volume \times respiratory rate). The ventilation signal is normalized such that a value of 100% equals eupneic (healthy unobstructed) ventilation. For any given level of ventilation, the model parameters (steady-state loop gain, delay, time constant, and response to arousal) are adjusted to best fit the ventilatory drive that matched the ventilation during unobstructed breathing. The assumption is that during unobstructed breaths, ventilatory drive (intended ventilation) can be directly estimated from the observed ventilation based on chemical and arousal parameters. During obstructed breaths (apnea–hypopnea events), the observed ventilation will be less than the ventilatory drive, i.e., the intended level of ventilation. For this purpose, the sleep data is divided into 7-min analysis windows, and the computational models are fit separately for each available window containing sleep to estimate ventilatory drive [33]. Ventilation and ventilatory drive estimates are subsequently used to quantify the endotypic traits (loop gain, arousal threshold, pharyngeal collapsibility, and neuromuscular compensation) for an OSA patient. Figure 1 illustrates a basic workflow of the process.

6.1 Control Theory Basis for Endotypic Trait Estimation

To understand the computational model, one needs to consider the physiological control of respiration. This control is achieved by means of multiple sensing entities such as chemoreceptors, respiratory tissue mechanoreceptors, and thermoreceptors providing feedback input to the brain, which in turn controls the upper airway muscles and diaphragm. Figure 2 shows a simplified diagram of the closed loop structure of the respiratory control system. For simplicity and due to its preeminent effect on respiration, only the respiratory control loop associated with chemoreceptors is shown. Mudiaga et al. provide a more complete illustration [60]. As Fig. 2 shows, chemoreceptors sense the level of partial pressure of CO_2 in blood (PCO_2) and transmit that to the brain. During this transmission, the sensed level of PCO_2 is affected

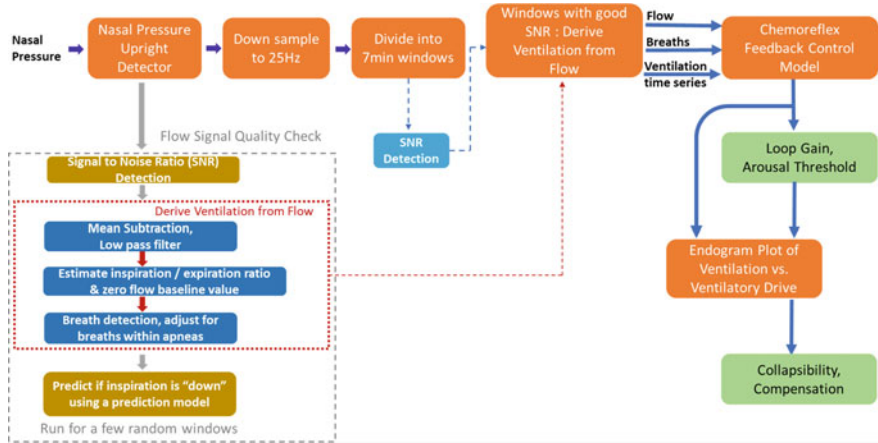


Fig. 1 Flow diagram of the computational Model for endotypic trait estimation. The model consists of several segments, the details of them have been explained elsewhere [29, 42, 49]. In brief, first, a prediction model is used to determine if the inspiration is upright or not (i.e., to check if the polarity of inspiration is positive or negative) using the nasal pressure upright detector. This segment also performs a quality check on the flow signal to determine overall signal-to-noise ratio, presence of filtering, amplitude clipping or spikes in the flow signal. To speed up the process this step is initially done on a few ($n = \sim 21$) 7-min windows randomly selected from the overnight data. After determining if the overall signal quality is good, overnight nasal pressure is down sampled, divided into seven-minute windows and SNR is recalculated for all the available windows. Only those windows with good SNR are used for deriving ventilation from nasal pressure signal. Breath detection algorithm is used to detect individual breaths and apply correction for apnea breaths (since apnea has almost zero flow, breaths cannot be easily detected based on flow amplitude during this period; hence, a specialized correction method is applied for all possible breaths that might occur during an apnea period). This creates a ventilation time series for the entire night which can be used to estimate endotypic traits using the first order feedback control system model. *SNR*—signal-to-noise ratio.

by a gain factor, here referred to as “controller gain.” Based on the measured vs. target (homeostatic) PCO_2 level (35–45 mmHg), the brain signals respiratory pump (i.e., diaphragm) and upper airway muscles to modulate breathing rate and depth, and airway caliber, respectively. These centrally issued commands are modified by gains associated with the upper and lower respiratory musculature, here referred to collectively as “plant gain.”

The physiological feedback control system of ventilation (Fig. 2) forms a basis for analyzing the dynamics of breathing during sleep as affected by respiratory events. In particular, some fundamental concepts of control theory [61] can be utilized to gain a better understanding of dynamic response of the respiration in presence of OSA. Consider the basic feedback control system components shown in Fig. 3. The desired output can be viewed as a target range of arterial PCO_2 (i.e., the homeostatic level of 35–45 mmHg) and the actual output as the actual level of PCO_2 in the blood which as determined by metabolism and respiration. The sensor can be considered to be the chemoreceptors sensing the PCO_2 level. The summing junction

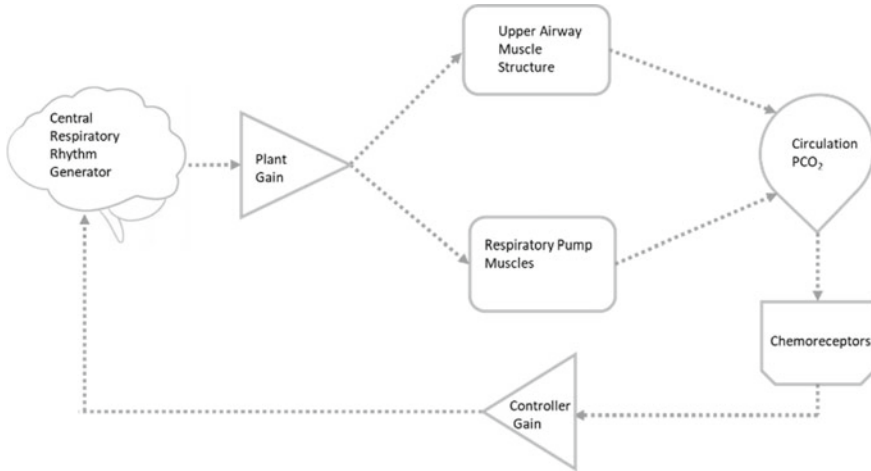


Fig. 2 Simplified diagram of the respiratory control system showing how chemoreceptors mediate motor output to upper airway and thoracic musculature

and controller together provide central control of respiration. The plant represents the lungs, musculature, and structural elements involved in air movement and gas exchange.

Based on feedback control theory, Terrill et al. [42] proposed a system to quantify the dynamics of respiration when airflow obstruction occurs (e.g., sleep apnea). The system aims to model the effect of ventilatory drive on the respiration as shown in Fig. 4.

In this model, ventilation is activated based on the net effect of chemical drive, arousal response, and airflow obstruction. In turn, ventilation with some finite time delay (δ s) affects PCO₂, or chemical drive. The dynamics of the system may be described using concepts from dynamic system modeling and automatic control theory, as proposed by Terrill et al.

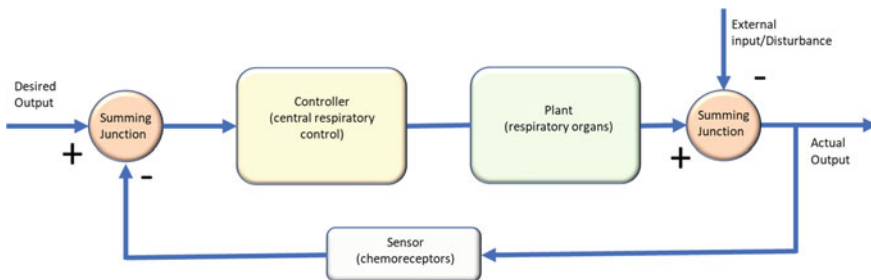


Fig. 3 Elements of basic feedback control loop system and their comparable respiratory feedback control subsystems

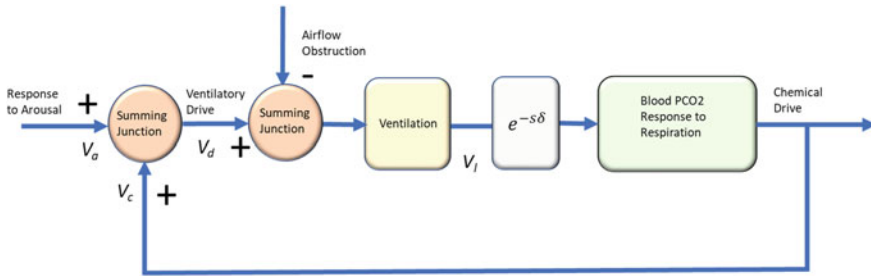


Fig. 4 Conceptual model of the feedback system governing the ventilation drive in presence of sleep apnea

$$V_d = V_c + V_a, \tag{1}$$

where V_d signifies the total ventilatory drive, V_c represents the chemical drive to breath from PCO_2 , and V_a denotes the drive to breath elicited by arousal from sleep (modeled as a nonzero constant (e.g., γ) when arousal is present and zero otherwise).

Based on the proposed model, when a reduction in the ventilation occurs (e.g., due to an obstructive sleep apnea event), after a finite time delay (i.e., δ), the chemical drive to breath begins to rise at a rate governed by time constant of τ . During the rise in V_c , V_a has a null value and the total ventilatory drive, V_d , is simply equal to V_c (Eq. 1). However, when V_c reaches its steady-state level (i.e., LG_0) and an arousal from sleep occurs, V_a assumes the value of γ and hence $V_d = V_c + \gamma$. With the arousal and subsequent opening of the airway, the breathing/ventilation is restored causing V_c and consequently V_d to decay to the pre-obstruction levels.

The dynamic response of V_c is determined by a first order linear differential equation as

$$\tau \frac{dV_c}{dt} = -V_c - LG_0 \times V_l(t - \delta), \tag{2}$$

where τ is the time constant reflecting the buffering of CO_2 in the lungs and tissues, LG_0 is the steady loop gain defining the steady-state level V_c after an obstruction occurs, and V_l equals the level of ventilation at δ s before the present time (i.e., t). Since some parameters of Eq. (2) (i.e., τ , LG_0 , and δ) are unknown, a model parameter identification is needed. In this case, the model parameters, τ , LG_0 , and δ , are adjusted until V_d best fits V_l measured during unobstructed breaths. Once the model parameters are identified, one can obtain the transfer function between V_c and V_l (i.e., $\frac{V_c(s)}{V_l(s)}$) as

$$\tau s V_c(s) = -V_c(s) - LG_0 V_l(s) e^{-s\delta}, \tag{3}$$

or

$$\frac{V_c(s)}{V_l(s)} = \frac{-\text{LG}_0 e^{-s\delta}}{1 + \tau s}. \quad (4)$$

The relation in Eq. (4) is the transfer function for the closed loop relating the ventilation and PCO_2 drive variations as function of ventilation.

6.2 Loop Gain

Since the transfer function in general is a complex variable, it needs to be analyzed in terms of its magnitude and phase at various frequencies. By substituting for $s = j2\pi f$, where j is the complex variable indicator and f is the frequency one can examine the magnitude and phase of $\frac{V_c(s)}{V_l(s)}$. Of interest is the magnitude of the transfer function in Eq. (4) which is given by

$$\left| \frac{V_c(j2\pi f)}{V_l(j2\pi f)} \right| = \text{LG}_f = \frac{\text{LG}_0}{\sqrt{1 + (2\tau\pi f)^2}}, \quad (5)$$

where LG_f signifies the dynamic gain of the closed loop relation between V_c and V_l for frequency of f . Note that LG_f is a function of frequency, f , and it reflects that the different frequency of variations in ventilation (i.e., V_l) result in different magnitude of change in V_c . The computational model calculates LG_f at $f = 1$ cycle/min ventilatory disturbance termed as LG_1 (measure of ventilatory sensitivity). If the natural cycling frequency of respiratory events specific to the subject is considered then, LG_f is shown as LG_n . LG_n can be considered as a measure of ventilatory instability and if its value is higher than 1, it is usually associated with cyclic CSA.

6.3 Arousal Threshold

For calculating the arousal threshold, ventilatory response to arousal (VRA) is first determined [49]. VRA represents the additional rise in ventilatory drive in the presence of a cortical arousal that is independent of increases in ventilatory drive due to chemical inputs. The ventilatory drive immediately preceding each of the respiratory event-related arousals is quantified for each 7-min analysis window of sleep data. The mean of these ventilatory drive values is used to calculate arousal threshold (ArThresh) for each window [49]. To provide a single summary value for each patient, the median value of the arousal threshold across all available 7-min sleep windows is used. Lower arousal threshold values indicate increased arousability and susceptibility to sleep disruption.

6.4 *Pharyngeal Collapsibility and Compensation*

To estimate collapsibility and neuromuscular compensation traits, first, ventilation level during each breath is determined and the corresponding ventilatory drive is estimated [29]. For this process, breaths during wake, arousals and breaths that occur immediately after arousals and sleep onset are excluded. Second, based on the ventilatory drive, breath-by-breath data are sorted into 10 bins (deciles). The median values of ventilation and ventilatory drive for each bin during sleep are obtained. Next, the ventilation levels are plotted against the estimated ventilatory drive [29]. Lastly, a linear interpolation between bins is used to obtain the ventilation at normal ventilatory drive represented by V_{passive} or the passive collapsibility. Ventilation levels at the arousal threshold is used to estimate V_{active} or the active collapsibility. The difference between V_{passive} and V_{active} is used to estimate the pharyngeal muscle compensation (V_{comp}).

6.5 *Reliability of the Endotypic Trait Estimation*

Without establishing the reliability and reproducibility of sleep apnea endotypic traits, they cannot be used as a clinical tool for successful individualized sleep apnea treatments. A recent study examined within-night repeatability and long-term consistency of these endotypic traits to enable their use in large-scale epidemiological studies [37]. Correlation coefficients (R) for within-night repeatability ranged from 0.69 to 0.83 when recommended amounts of data were available (20–35 seven-min sleep windows) [37]. The investigators of the study state that this level of repeatability means that any measurement error caused by this technique is unlikely to reduce its utility. Repeatability was similar for collapsibility, loop gain, and arousal threshold ($R = 0.79\text{--}0.83$), but lower for compensation ($R = 0.69$).

Long-term consistency (measured at two time points 6.5 ± 0.7 years apart) in aging men was more modest ($R = 0.36\text{--}0.63$) [37]. The reduced long-term consistency relative to within-night data may be due to multiple age-related factors (e.g., changes in body mass index, loss of muscle tone, circadian rhythm disruption, comorbidities) impacting sleep apnea pathophysiology [62]. Analysis of body position and sleep state variations revealed modest reduction in loop gain during REM and reduction in collapsibility during stage 3 sleep. The effects of body position and sleep state on AHI exceeded effects of endotypic traits. This study provided overall guidance on how to increase endotypic trait reliability in a clinical setting. Their results support use of endotypic traits for precision medicine in clinical and research arenas.

6.6 *Clinical Implications*

One of the major issues facing the sleep health care is that all new sleep apnea treatments, both drugs and devices, are only suitable for certain subtypes of sleep apnea, because different people acquire the disorder for different reasons. Hence, the field of sleep medicine needs to evolve from a “one-size-fits-all” approach to interventions targeting to each patient’s unique pathophysiology. The concepts proposed here offer such a patient-specific treatment paradigm using data from established and routine sleep recordings. The proposed computational model estimates individual patient endotypic traits to identify sleep apnea subtypes. The significance of this computational model is that it is based on a technique that requires nothing more than routine sleep study recordings. That is, laboratory-based physiological studies may be easily translated to the clinical arena to guide clinical decision. This approach will enable clinicians to individualize and optimize sleep apnea treatment according to patient subtype, which in turn will improve outcomes and reduce costs by steering patients to therapies that most appropriately address their unique pathophysiology.

6.7 *Limitations*

The estimation of endotypic traits by the proposed model requires a sizeable number of spontaneous ventilatory perturbations caused by apnea–hypopnea events. As a result, the model has been validated in a large sample of OSA patients with moderate to severe OSA. Further studies must be conducted to validate its usefulness in pediatric and mild OSA patients. The computational process is based on several validated assumptions: use of a linearized nasal pressure signal to derive ventilation, a data collection period with unobstructed breathing, and airway patency between respiratory events [63]. A “gold standard” approach to quantify ventilation and ventilatory drive would require additional potentially invasive signals and use of pneumotachograph that are not part of routine polysomnography and thus would prevent widespread use for precision sleep medicine. Also, studies have shown that endotypic traits obtained from pneumotachography are very similar to those estimated from nasal pressure ($R > 0.95$ for all traits) [29]. Another limitation is that this computational model in no way incorporates the many complex human behavioral factors that contribute to sleep apnea pathogenesis and exacerbation. Discussion of these inputs is well beyond the scope of this chapter. Countless such factors, known and yet unknown, remain the responsibility of the educated and attentive sleep/circadian rhythm practitioner to understand and incorporate into individual patient’s care plans.

7 Conclusions

Sleep apnea patients vary significantly in disease pathogenesis and response to therapeutic interventions. Individualizing therapy to patients according to their pathophysiology is crucial to successful treatment outcomes. This work presents new and simplified methods to address this opportunity by enabling targeted individualized treatment of sleep apnea patients based on their unique etiology.

References

1. Levitzky, M.G.: Control of breathing. In: Pulmonary Physiology, 9th edn. McGraw-Hill Education, New York, NY (2017)
2. Macklem, P.T.: The act of breathing. In: Aliverti, A., Pedotti, A. (eds.) *Mechanics of Breathing: New Insights from New Technologies*, pp. 3–10. Springer Milan, Milano (2014)
3. Brinkman, J.E., Toro, F., Sharma, S.: Physiology, respiratory drive. In: StatPearls. Treasure Island (FL). StatPearls Publishing LLC (2022)
4. Dempsey, J.A., Smith, C.A., Blain, G.M., Xie, A., Gong, Y., Teodorescu M. (eds.): Role of central/peripheral chemoreceptors and their interdependence in the pathophysiology of Sleep Apnea. In: *Arterial Chemoreception*. Springer Netherlands, Dordrecht (2012)
5. Loeschcke, H.H.: Central chemoreceptors. In: Pallot, D.J. (ed.) *Control of Respiration*, pp. 41–77. Springer, US, Boston, MA (1983)
6. Prabhakar, N.R., Peng, Y.J.: Peripheral chemoreceptors in health and disease. *J. Appl. Physiol.* **96**(1), 359–366 (2004)
7. Hazari, M.S., Farraj, A.K.: Chapter 15—Comparative control of respiration. In: Parent, R.A. (ed.) *Comparative Biology of the Normal Lung*, 2nd edn., pp. 245–288. Academic Press, San Diego (2015)
8. Chourpiliadis, C., Bhardwaj, A.: Physiology, Respiratory Rate. StatPearls. Treasure Island (FL) (2022)
9. Malhotra, R.K., Desai, A.K.: Healthy brain aging: what has sleep got to do with it? *Clin. Geriatr. Med.* **26**, 45–56 (2010)
10. Xie, L., Kang, H., Xu, Q., Chen, M.J., Liao, Y., Thiyagarajan, M., et al.: Sleep drives metabolite clearance from the adult brain. *Science* **342**(6156), 373–377 (2013)
11. Douglas, N.J., White, D.P., Pickett, C.K., Weil, J.V., Zwillich, C.W.: Respiration during sleep in normal man. *Thorax* **37**(11), 840–844 (1982)
12. Phillipson, E.A.: Control of breathing during sleep. *Am. Rev. Respir. Dis.* **118**(5), 909–939 (1978)
13. Sowho, M., Amatoury, J., Kirkness, J.P., Patil, S.P.: Sleep and respiratory physiology in adults. *Clin. Chest Med.* **35**(3), 469–481 (2014)
14. Orem, J.M., Kubin, L. (ed.): Chapter 17—Respiratory physiology: central neural control. *Principles and Pract. Sleep. Med.* (2000)
15. Young, T., Peppard, P.E., Gottlieb, D.J.: Epidemiology of obstructive sleep apnea: a population health perspective. *Am. J. Respir. Crit. Care Med.* **165**(9), 1217–1239 (2002)
16. Young, T., Palta, M., Dempsey, J., Skatrud, J., Weber, S., Badr, S.: The occurrence of sleep-disordered breathing among middle-aged adults. *N. Engl. J. Med.* **328**(17), 1230–1235 (1993)
17. Javaheri, S., Dempsey, J.A.: Central sleep apnea. *Compr. Physiol.* **3**(1), 141–163 (2013)
18. Dempsey, J.A., Veasey, S.C., Morgan, B.J., O'Donnell, C.P.: Pathophysiology of sleep apnea. *Physiol. Rev.* **90**(1), 47–112 (2010)
19. Somers, V.K., White, D.P., Amin, R., Abraham, W.T., Costa, F., Culebras, A., et al.: Sleep apnea and cardiovascular disease: an American Heart Association/American College of Cardiology

- Foundation Scientific Statement from the American Heart Association Council for High Blood Pressure Research Professional Education Committee, Council on Clinical Cardiology, Stroke Council, and Council On Cardiovascular Nursing. In collaboration with the National Heart, Lung, and Blood Institute National Center on Sleep Disorders Research (National Institutes of Health). *Circulation*. **118**(10), 1080–1111 (2008)
20. Franklin, K.A., Lindberg, E.: Obstructive sleep apnea is a common disorder in the population—a review on the epidemiology of sleep apnea. *J. Thorac. Dis.* **7**(8), 1311–1322 (2015)
 21. Motamedi, K.K., McClary, A.C., Amedee, R.G.: Obstructive sleep apnea: a growing problem. *Ochsner. J.* **9**(3), 149–153 (2009)
 22. Donovan, L.M., Kapur, V.K.J.S.: Prevalence and characteristics of central compared to obstructive sleep apnea: analyses from the sleep heart health study cohort. *Sleep* **39**(7), 1353–1359 (2016)
 23. Somers, V.K., White, D.P., Amin, R., Abraham, W.T., Costa, F., Culebras, A., et al.: Sleep apnea and cardiovascular disease: an American Heart Association/American College Of Cardiology Foundation Scientific Statement from the American Heart Association Council for High Blood Pressure Research Professional Education Committee. *Circulation* **118**(10), 1080–1111 (2008)
 24. Alex, R.M., Mousavi, N.D., Zhang, R., Gatchel, R.J., Behbehani, K.: Obstructive sleep apnea: brain hemodynamics, structure, and function. *J. Appl. Biobehav. Res.* **22**(4), e12101 (2017)
 25. National Commission on Sleep Disorders R, United States Department of H, Human S. Wake up America: a national sleep alert: report of the National Commission on Sleep Disorders Research. Washington, DC. The Commission; (1993)
 26. Jordan, A.S., White, D.P.: Pharyngeal motor control and the pathogenesis of obstructive sleep apnea. *Respir. Physiol. Neurobiol.* **160**(1), 1–7 (2008)
 27. Pierce, R., White, D., Malhotra, A., Edwards, J.K., Kleverlaan, D., Palmer, L., et al.: Upper airway collapsibility, dilator muscle activation and resistance in sleep apnoea. *Eur. Respir. J.* **30**(2), 345–353 (2007)
 28. Fogel, R.B., Trinder, J., White, D.P., Malhotra, A., Raneri, J., Schory, K., et al.: The effect of sleep onset on upper airway muscle activity in patients with sleep apnoea versus controls. *J. Physiol.* **564**(Pt 2), 549–562 (2005)
 29. Sands, S.A., Edwards, B.A., Terrill, P.I., Taranto-Montemurro, L., Azarbarzin, A., Marques, M., et al.: Phenotyping pharyngeal pathophysiology using polysomnography in patients with obstructive sleep apnea. *Am. J. Respir. Crit. Care Med.* **197**(9), 1187–1197 (2018)
 30. Smith, P.L., Kirkness, J.P., Patil, S., Schneider, H., Schwartz, A.R.: Biomechanics of the upper airway during sleep. In: Pack, A.I. (ed.) *Sleep Apnea: Pathogenesis, Diagnosis and Treatment*, 2nd edn., pp. 27–52. CRC Press, Boca Raton, FL (2011)
 31. Spicuzza, L., Caruso, D., Di Maria, G.: Obstructive sleep apnoea syndrome and its management. *Therap. Adv. Chron. Dis.* **6**(5), 273–285 (2015)
 32. Osman, A.M., Carter, S.G., Carberry, J.C., Eckert, D.J.: Obstructive sleep apnea: current perspectives. *Nat. Sci. Sleep* **10**, 21–34 (2018)
 33. Rotenberg, B.W., Murariu, D., Pang, K.P.: Trends in CPAP adherence over twenty years of data collection: a flattened curve. *J. Otolaryngol. Head Neck Surg. (Le Journal d'oto-rhinolaryngologie et de chirurgie cervico-faciale)*. **45**(1), 43 (2016)
 34. Durgan, D.J., Bryan, R.M., Jr.: Cerebrovascular consequences of obstructive sleep apnea. *J. Am. Heart Assoc.* **1**(4), e000091 (2012)
 35. Lavie, P.: Treatment of sleep apnea: unmet needs. *Chest* **116**(6), 1501–1503 (1999)
 36. Joosten, S.A., Leong, P., Landry, S.A., Sands, S.A., Terrill, P.I., Mann, D., et al.: Loop gain predicts the response to upper airway surgery in patients with obstructive sleep apnea. *Sleep*. **40**(7), zsx094, (2017). <https://doi.org/10.1093/sleep/zsx094>
 37. Alex, R.M., Sofer, T., Azarbarzin, A., Vena, D., Gell, L.K., Wellman, A., et al.: Within-night repeatability and long-term consistency of sleep apnea endotypes: the multi-ethnic study of atherosclerosis and osteoporotic fractures in men study. *Sleep*. **45**(9), zsa129, (2022). <https://doi.org/10.1093/sleep/zsa129>
 38. Eckert, D.J., White, D.P., Jordan, A.S., Malhotra, A., Wellman, A.: Defining phenotypic causes of obstructive sleep apnea. Identification of novel therapeutic targets. *Am. J. Respir. Crit. Care Med.* **188**(8), 996–1004 (2013)

39. Edwards, B.A., Andara, C., Landry, S., Sands, S.A., Joosten, S.A., Owens, R.L., et al.: Upper-airway collapsibility and loop gain predict the response to oral appliance therapy in patients with obstructive sleep apnea. *Am. J. Respir. Crit. Care Med.* **194**(11), 1413–1422 (2016)
40. Subramani, Y., Singh, M., Wong, J., Kushida, C.A., Malhotra, A., Chung, F.: Understanding phenotypes of obstructive sleep apnea: applications in anesthesia, surgery, and perioperative medicine. *Anesth. Analg.* **124**(1), 179–191 (2017)
41. Bamagoos, A.A., Cistulli, P.A., Sutherland, K., Madronio, M., Eckert, D.J., Hess, L., et al.: Polysomnographic endotyping to select patients with obstructive sleep apnea for oral appliances. *Ann. Am. Thorac. Soc.* **16**(11), 1422–1431 (2019)
42. Terrill, P.I., Edwards, B.A., Nemati, S., Butler, J.P., Owens, R.L., Eckert, D.J., et al.: Quantifying the ventilatory control contribution to sleep apnoea using polysomnography. *Eur. Respir. J.* **45**(2), 408 (2015)
43. Eckert, D.J.: Phenotypic approaches to obstructive sleep apnoea—new pathways for targeted therapy. *Sleep. Med. Rev.* **37**:45–59, (2016). <https://doi.org/10.1016/j.smrv.2016.12.003>
44. Wellman, A., Eckert, D.J., Jordan, A.S., Edwards, B.A., Passaglia, C.L., Jackson, A.C., et al.: A method for measuring and modeling the physiological traits causing obstructive sleep apnea. *J Appl Physiol.* **110**(6), 1627–1637 (2011)
45. Wellman, A., Edwards, B.A., Sands, S.A., Owens, R.L., Nemati, S., Butler, J., et al.: A simplified method for determining phenotypic traits in patients with obstructive sleep apnea. *J. Appl. Physiol.* **114**(7), 911–922 (2013)
46. Eckert, D.J., Younes, M.K.: Arousal from sleep: implications for obstructive sleep apnea pathogenesis and treatment. *J. Appl. Physiol.* **116**(3), 302–313 (2014)
47. Jordan, A.S., O’Donoghue, F.J., Cori, J.M., Trinder, J.: Physiology of arousal in OSA and potential impacts for sedative treatment. *Am. J. Respir. Crit. Care Med.* **196**, 814–821 (2017)
48. Younes, M.: Role of arousals in the pathogenesis of obstructive sleep apnea. *Am. J. Respir. Crit. Care Med.* **169**(5), 623–633 (2004)
49. Sands, S.A., Terrill, P.I., Edwards, B.A., Taranto Montemurro, L., Azarbarzin, A., Marques, M., et al.: Quantifying the arousal threshold using polysomnography in obstructive sleep apnea. *Sleep.* **41**(1), zsx183, (2018). <https://doi.org/10.1093/sleep/zsx183>
50. Young, T., Peppard, P.E., Taheri, S.: Excess weight and sleep-disordered breathing. *J. Appl. Physiol.* **99**(4), 1592–1599 (2005)
51. Patil, S.P., Schneider, H., Marx, J.J., Gladmon, E., Schwartz, A.R., Smith, P.L.: Neuromechanical control of upper airway patency during sleep. *J. Appl. Physiol.* **102**(2), 547–556 (2007)
52. Azarbarzin, A., Sands, S.A., Taranto-Montemurro, L., Oliveira Marques, M.D., Genta, P.R., Edwards, B.A., et al.: Estimation of pharyngeal collapsibility during sleep by peak inspiratory airflow. *Sleep.* **40**(1), zsw005, (2017). <https://doi.org/10.1093/sleep/zsw005>
53. Morrison, D.L., Launois, S.H., Isono, S., Feroah, T.R., Whitelaw, W.A., Remmers, J.E.: Pharyngeal narrowing and closing pressures in patients with obstructive sleep apnea. *Am. Rev. Respir. Dis.* **148**(3), 606–611 (1993)
54. Pham, L.V., Schwartz, A.R.: The pathogenesis of obstructive sleep apnea. *J. Thorac. Dis.* **7**(8), 1358–1372 (2015)
55. McGinley, B.M., Schwartz, A.R., Schneider, H., Kirkness, J.P., Smith, P.L., Patil, S.P.: Upper airway neuromuscular compensation during sleep is defective in obstructive sleep apnea. *J Appl Physiol.* **105**(1), 197–205 (2008)
56. Nicholas, C.L., Jordan, A.S., Heckel, L., Worsnop, C., Bei, B., Saboisky, J.P., et al.: Discharge patterns of human tensor palatini motor units during sleep onset. *Sleep* **35**(5), 699–707 (2012)
57. Loewen, A.H., Ostrowski, M., Laprairie, J., Maturino, F., Hanly, P.J., Younes, M.: Response of genioglossus muscle to increasing chemical drive in sleeping obstructive apnea patients. *Sleep* **34**(8), 1061–1073 (2011)
58. Wellman, A., Eckert, D.J., Jordan, A.S., Edwards, B.A., Passaglia, C.L., Jackson, A.C., et al.: A method for measuring and modeling the physiological traits causing obstructive sleep apnea. *J. Appl. Physiol.* **110**(6), 1627–1637 (2011)

59. Finnsson, E., Ólafsdóttir, G.H., Loftsdóttir, D.L., Jónsson, S., Helgadóttir, H., Ágústsson, J.S., et al.: A scalable method of determining physiological endotypes of sleep apnea from a polysomnographic sleep study. *Sleep*. **44**(1), zsa168, (2021). <https://doi.org/10.1093/sleep/zsaa168>
60. Mudiaga Sowho, M., Amatoury, J., Kirkness, J.P., Patil, S.P.: Sleep and respiratory physiology in adults. *Clin. Chest Med.* **35**, 469–481 (2014)
61. Ogata, K.: *Modern Control Engineering*, 5th ed. Pearson, Upper Saddle New Jersey (2010)
62. Li, J., Vitiello, M.V., Gooneratne, N.S.: Sleep in normal aging. *Sleep Med. Clin.* **13**(1), 1–11 (2018)
63. Mann, D.L., Terrill, P.I., Azarbarzin, A., Mariani, S., Franciosini, A., Camassa, A., et al.: Quantifying the magnitude of pharyngeal obstruction during sleep using airflow shape. *Eur. Respir. J.* **54**(1), 1802262, (2019). <https://doi.org/10.1183/13993003.02262-2018>

Index

A

- Abdominal Aortic Aneurysm, 3, 4, 6, 7, 10, 16, 19, 63, 75, 79, 80, 90
- Aneurysms, 3–9, 11–17, 63–65, 80, 82, 83, 85, 88–91
- Aortic valve, 145–148, 154, 155
- Assumption, 74, 79, 80, 87, 90, 91, 119, 130, 182, 188

B

- Bicycle helmet, 95, 96, 101, 111
- Biomechanics, 23, 24, 36, 65, 79–81, 90
- Blood flow, 117–123, 125, 127, 136, 145–147, 151, 153, 154
- Brain injury, 95, 96, 101, 103, 105, 106, 108–111

C

- Canny edges, 74, 75
- Car-to-cyclist accident, 95, 96, 103, 110
- Computational biomechanics, 4, 12, 63, 65, 80, 111
- Computed tomography, 6, 7, 9, 80
- Coronary artery, 145–148, 150, 151, 153–155

D

- Disperse particle method, 125, 128
- Drug transport, 117, 119, 121, 122

E

- Epilepsy, 33, 34, 36, 43

- External tissues, 80, 81, 87, 90, 91

F

- Finite element method, 3, 4, 33, 41, 50, 147
- Finite element model, 4, 12, 13, 16, 17, 67, 95, 102
- Finite volume method, 125, 128
- Fractional Flow Reserve (FFR), 145–147, 150, 151, 153–155
- Framework, 33–36, 42, 43, 50, 51, 54, 58

H

- Head injury, 95, 96, 105, 108, 110, 111

M

- Maximum Principal stress (MPS), 12–18, 70, 72–74, 79, 81, 84–90, 95, 105, 106, 109–111
- Mechanical circulatory support, 138
- Mechanical valve, 145, 147–149, 151, 153–155
- Model, 5, 11–16, 18, 23–31, 33–43, 49–59, 63, 65–67, 72, 73, 80, 81, 83, 85, 89, 91, 95–106, 108, 110, 111, 117, 118, 120–123, 125, 127, 129–133, 136, 147–151, 153, 154, 161, 164, 178, 181–186, 188
- Modeling, 33–35, 43, 96, 127, 130, 184
- Multi-body model, 24–26, 29, 31, 95, 100

P

Patient-specific, 3–7, 12, 16, 33–40, 42, 43, 63–65, 68, 69, 74, 80, 81, 83, 84, 90, 91, 145, 152, 154, 155, 171, 188

Patient-specific aneurysm wall, 3, 4

Patient-Specific Modelling (PSM), 80

Portal vein, 117–122

Principal stresses, 17, 69, 70, 96

R

Rat liver, 117–119, 121, 123

S

Segmentation variability, 65, 70, 75

Structured hexahedral elements, 5